Improving grid based quantum dynamics:

From the inclusion of solvents to the utilization of machine learning

Julius Philipp Paul Zauleck

München 2017

Dissertation zur Erlangung des Doktorgrades
der Fakultät für Chemie und Pharmazie
der Ludwig–Maximilians–Universität München

Improving grid based quantum dynamics:

From the inclusion of solvents to the utilization of machine learning

Julius Philipp Paul Zauleck

aus

Berlin, Deutschland

2017

Erklärung:

Diese Dissertation wurde im Sinne von §7 der Promotionsordnung vom 28. November 2011 von Frau Prof. Dr. Regina de Vivie-Riedle betreut.

Eidesstattliche Versicherung:

Diese Dissertation wurde eigenständig und ohne unerlaubte Hilfe erarbeitet.

Julius Philipp Paul Zauleck, München, den 29.01.2018

Dissertation eingereicht am:	15.12.2017
1. Gutachterin:	Prof. Dr. Regina de Vivie-Riedle
2. Gutachter:	Prof. Dr. Hubert Ebert
Tag der mündlichen Prüfung:	23.1.2018

Contents

Abstract

In this work the development and refinement of methods that allow for a more efficient use of quantum dynamics calculations with the dynamic Fourier method (DFM) and the extension of the DFMs applicability to solvated systems are presented. The systems studied with these methods are primarily molecular reactions. The contents of this thesis can be divided in three parts. In the first, approaches to automate the necessary and difficult construction of reactive coordinates are developed. The reactive coordinates constructed are linear combinations of the Cartesian coordinates of the atoms in two cases and nonlinear combinations in one case. Of the two linear approaches, one uses points along the minimum energy path of the reaction to span a reactive subspace and the other uses classical trajectories that are run along the reaction path to extract essential motions. The nonlinear approach uses an autoencoder that learns an efficient low-dimensional description of the reactive space by using large amounts of trajectory data. All three methods are presented in detail and applied to example systems. The advantages of each method and the immense potential of the nonlinear approach are discussed.

In the second part, the inclusion of dynamic solvent effects on the reactive solute is studied. This is important, because dynamic interactions can significantly alter the outcome of reactions. Three methods were developed in the course of this work. The first one treats the solvent implicitly as a continuum that causes frictional forces acting on the solute. This is computationally convenient but, as it cannot describe certain interactions – such as collisions – it is not suited for all systems. The second and third method treat the solvent particles explicitly, using frozen and classically propagated environments, respectively. Here, the third approach extends the second to a much larger field of application by means of a quantum-classical TDSCF. The three methods are applied to the practically important problems of the photogeneration of diphenylmethyl cations as reactive intermediates and the photorelaxation of uracil as a way to prevent photodamage in RNA.

The third part is comprised of two minor improvements. The first deals with errors that can be introduced due to an incorrect treatment of an approximation within the Wilson G-matrix formalism, a formalism that offers a simple way to perform coordinate transformations. This not only applies to some implementations of the DFM method, but to all methods that use the G-matrix formalism with nonlinear coordinates. The second studies the use of undersampling in the DFM method to reduce the number of grid points and thus computational time. Its potential savings are demonstrated using a model system.

List of publications

This thesis is based on the following five publications and one draft listed in chronological order. They are reprinted in the chapters 1 (**3, 5**), 2 (**1, 2, 4**) and 3 (**6**).

1 S. Thallmair, M. Kowalewski, J. P. P. Zauleck, M. K. Roos, R. de Vivie-Riedle:
Quantum Dynamics of a Photochemical Bond Cleavage Influenced by the Solvent Environment: A Dynamic Continuum Approach.
J. Phys. Chem. Lett. **5**, 3480–3485 (2014).
Contributions: The author of this thesis contributed important parts to the derivation of the working equations, i.e. eqs. 5 and 6.

2 S. Thallmair, J. P. P. Zauleck, R. de Vivie-Riedle:
Quantum Dynamics in an Explicit Solvent Environment: A Photochemical Bond Cleavage Treated with a Combined QD/MD Approach.
J. Chem. Theory Comput. **11**, 1987–1995 (2015).
Contributions: The author of this thesis developed most of the theory of section 2.2 as well as the choice of relative coordinates as shown in fig. 1.

3 J. P. P. Zauleck, S. Thallmair, M. Loipersberger, R. de Vivie-Riedle:
Two new methods to generate internal coordinates for molecular wave packet dynamics in reduced dimensions.
J. Chem. Theory Comput. **12**, 5698–5708 (2016).

4 J. P. P. Zauleck, M. T. Peschel, F. M. Rott, S. Thallmair, R. de Vivie-Riedle:
Reactive quantum dynamics coupled to classical solvent dynamics using an extended quantum-classical TDSCF approach.
Submitted to *J. Phys. Chem. A* (2017).

5 J. P. P. Zauleck, R. de Vivie-Riedle:
Constructing grids for molecular quantum dynamics using an autoencoder.
J. Chem. Theory Comput. **14**, 52–62 (2018).

6 J. P. P. Zauleck, S. Thallmair, R. de Vivie-Riedle:
Revisiting an approximation in the Wilson G-matrix formalism and its impact on molecular quantum dynamics.
Draft.

Additional publications listed in chronological order:

7 S. Thallmair, J. P. P. Zauleck, R. de Vivie-Riedle:
Quantum Dynamics of Molecular Reactions Directed by Explicit Solvent Environment.
in: Ultrafast Phenomena XIX, K. Yamanouchi, S. Cundiff, R. de Vivie-Riedle, M. Kuwata-Gonokami, L. S. DiMauro (Eds.), Springer Proceedings in Physics 162, Springer, 2015, 373–377.

8 D. Keefer, S. Thallmair, J. P. P. Zauleck, R. de Vivie-Riedle:
A multi target approach to control chemical reactions in their inhomogeneous solvent environment.
J. Phys. B: At. Mol. Opt. Phys. **48**, 234003 (2015).

9 D. Keefer, S. Thallmair, J. P. P. Zauleck, R. de Vivie-Riedle:
Optimal Control Theory for Molecular Reactions in Atomistic Surroundings.
in: Ultrafast Phenomena XX, OSA Technical Digest (online) (Optical Society of America, 2016).

Introduction

Models and theoretical methods that explain experimental observations and make predictions are a fundamental part of all natural sciences. In theoretical chemistry the focus lies on the description and prediction of properties of chemical compounds on the one hand and of chemical reactions on the other hand. Of these two similarly important topics, the latter is key to understanding the chemical processes around us and is an important tool to devise new synthesis routes and strategies. This produces an enormous momentum towards the development of ever more powerful methods to simulate reactive processes. While there are some instances where completely new methods are developed [1, 2], usually most progress is made by improving the existing ones and extending them to new applications [3, 4].

Some of the recent extensions and improvements made to one of the methods for the quantum dynamical description of molecular processes are the topic of this thesis. The method in question is the dynamic Fourier method (DFM) [5–7], a type of pseudo-spectral method [8, 9]. The DFM produces very accurate results [6], is widely applicable and is conveniently implemented regardless of the system. It uses a discretized representation of the wavefunction by employing a spatial grid as basis. The action of the kinetic energy operator on the wavefunction, which is required to propagate the system in time, is evaluated using the fast Fourier transform [10, 11]. Since the potential energy operator can simply be multiplied with the wavefunction in this basis, this results in the computation scaling $O(n \log n)$ with the number of basis functions or grid points n.

However, since the number of grid points scales exponentially with the number of degrees of freedom or dimensions and since it requires a relatively large number of grid points per degree of freedom, it is limited to a relatively small number of degrees of freedom. The number of degrees of freedom is in practice limited to less than 10 in contrast to the most high-dimensional, but less general and strongly approximated methods. A prominent example of this is the multilayer MCTDH [4, 12] that is limited to the low thousands for the most benign systems [13]. It is based on the MCTDH [2], which can treat up to a few dozen degrees of freedom, but requires the studied system's Hamiltonian to be expandable in a very specific form and typically works well for systems with low correlation between the different degrees of freedom [12]. In its multilayer variant, this dependency on low correlation is furthered and engrained in a tree structure, making it computationally very powerful but also far less general. Alternatively, for the DFM the degrees of freedom of realistic systems are reduced to the most essential ones. Even though there are many systems that can be well described with a few dimensions due to the low intrinsic dimensionality of their reactive behaviour [14, 15], increasing the number of degrees of freedom that can be treated is still important to extend the scope of the DFM. A way to do this can be to reduce the number of grid points needed per dimension [16–18]. Additionally, for the systems that can be treated with few dimensions, it is of major importance to efficiently identify these dimensions, which will in this work also be referred to as reactive coordinates.

In this thesis, the chapters 1 and 2 each contain one of the two main developments of this work, namely the identification of reactive coordinates and the inclusion of dynamic solvent effects, and chapter 3 contains two additional minor improvements to the accuracy and efficiency of

the calculations. Specific examples of the aforementioned improvements constitute the majority of the contents of this thesis. Chapter 1 deals with the dimensionality reduction necessary for virtually every application of the DFM. Usually, a high amount of chemical intuition is involved and the strategies vary with the system studied [15, 19, 20]. This often results in tedious work, when the reactive dynamics of a system are complex, include collective motions of many atoms or simply are unusual. Hence, progress in the automation of this task is very valuable. Concerning dimensionality reduction, one can distinguish linear from nonlinear approaches, which lead to linear and nonlinear reactive coordinates, respectively. While the former ones are simpler and computationally less demanding, the latter ones can construct far more general and more efficient reactive coordinates [21–23]. For the present work, two linear and one nonlinear dimensionality reduction method have been developed and will be presented. The two linear methods use points along the minimum energy path of the reaction studied and classical molecular dynamics (MD) trajectories run along the reaction path. Out of the wide variety of machine learning algorithms that exist for nonlinear dimensionality reduction [24], an autoencoder [25] learning from large amounts of MD trajectory data was chosen.

Chapter 2 is dedicated to extending the scope of the DFM to include the dynamic effects of solvent environments. The fact that a majority of important reactions take place in solution emphasizes the relevance of the correct description of the solvent influence. For many reactions, this can be modeled well using static effects and the corresponding methods are fairly complete [26]. However, the inclusion of dynamic effects relies stronger on the use of approximations on the one hand, usually limiting the description of the solvent to classical mechanics due to the large number of degrees of freedom involved. On the other hand, the solvent's influence on the dynamics of the solute is less obvious, because the dynamic picture of a system is more complicated to obtain. Nevertheless, it has been shown that the dynamic influence can be very consequential [27–29]. In this thesis, three developed methods are presented. One treats the solvent implicitly by employing its viscosity to construct a Stokes' force acting on the solute. The other two treat the solvent particles explicitly with increasing accuracy. The interaction potential between the solute and the solvent is evaluated for each pair of particles.

In contrast to the first two chapters, the contents of the third and last chapter are less ubiquitous within the DFM, but the developments come with significant benefits where they apply. The first topic is a re-evaluation of an approximation in the Wilson G-matrix formalism [30–32]. This formalism is very useful for the DFM and other methods because it enables the construction of the Hamiltonian in arbitrary coordinates. As a result, one may consider to use the G-matrix formalism by default to allow for more automation. It is thus of interest to maintain its quality. The approximation discussed seems to be an example of techniques, that need to be re-examined time and time again in order to avoid the introduction of errors, as has been the case here. An illustration of the possible errors and ways to avoid them are given in the first part of chapter 3.

A method that may prove valuable is introduced in the second part of chapter 3. It uses undersampling to reduce the number of grid points necessary for systems with localized wavepackets in momentum space. The associated reduction in computation time may ultimately lead to the ability to treat the systems in question using a higher number of reactive coordinates and thus pushes the computational limits of the DFM.

It should be understood that the entirety of this thesis focuses on the time-dependent quantum mechanics, from hereon referred to as quantum dynamics (QD), of reactive chemical systems using the DFM. While parts can be directly transferred to other fields, this was always the context in which these were researched. All equations, unless explicitly stated otherwise, are given in atomic units.

Chapter 1

Automating reactive coordinate construction

The DFM [5] produces very accurate results [6] that come at some computational cost. This cost is the reason the dimensionality has to be reduced considerably for most systems. As a consequence, finding the subspace and reactive coordinates that describe the studied reactions most efficiently becomes one of the central challenges for this kind of QD calculations [14, 15]. This is reflected in the considerable effort invested in this task. A few examples of the developed approaches are the use of spherical and hyperspherical coordinates [14, 33, 34], selected normal modes [35–37], Jacobi or Jacobi-like coordinates [15, 19, 38, 39], dissociative coordinates and umbrella modes [40–43] and other hand-build combinations describing the reactive subspace [15, 20, 44–46]. The last two often use coordinates related to the intrinsic reaction coordinate (IRC), the minimum energy path of a reaction.

All these efforts illustrate the importance of every bit of progress in automating the construction of reactive coordinates. While the aforementioned methods rely significantly on chemical intuition, there are alternative approaches, which can be applied here that rather fall in the range of mathematical optimizations and machine learning. For example, one such application is the reaction plane approach [47, 48], where a reactive linear subspace is spanned by critical points of a reaction such as reactant and product minima and transition states. This has also been extended to include more degrees of freedom in a harmonic approximation [49].

In this chapter, three newly developed methods are presented that automate coordinate construction. The first two are examples of the aforementioned linear dimensionality reduction schemes and are described in section 1.1. The IRC-based approach (IBA) spans a number of subspaces, using points along the IRC, and compares them to find the most suited one. The trajectory-based approach (TBA) uses MD trajectories that are run along the reaction path and applies a principal component analysis (PCA) to the resulting trajectory data points to find the coordinates that describe the trajectories the most. Since both work on linear subspaces, the corresponding coordinates can be found by constructing any orthonormal basis that spans this subspace. The IBA and TBA are applied to the proton transfer in (Z)-hydroxyacryloyl chloride and to the methylization reaction of cyclohexanone using trimethylaluminum. The third approach uses an autoencoder [25], a type of neural network, to achieve a nonlinear dimensionality reduction. In the resulting subspace a set of nonlinear coordinates is found using a projection from a linear subspace. It is presented in section 1.2. As an example system, the same proton transfer in (Z)-hydroxyacryloyl chloride is used as for the other two methods.

This third method is an example of the large field of machine learning. Advancements in this field and increasing computational power made it accessible for applications to chemical systems. For example, extensive work has been done in the calculation of the potential energy surface (PES) of molecular systems [50–53], the prediction of the binding interactions of proteins [54–56],

the prediction of a number of properties of chemical compounds [57–60] and the automated grouping, classification and naming of chemicals [61–64].

There is also the option to apply machine learning to search for nonlinear reactive subspaces [21–23] and while they do not seem to have been applied to the construction of reactive coordinates used in grid based QD prior to this work, a number of powerful algorithms have been developed for related purposes. The most closely related methods stem from the low-dimensional reconstruction of geometries obtained by classical MD calculations of medium to large sized molecules [23, 65–68]. The required nonlinear dimensionality reduction algorithms exist in a large variety and many of them have been applied to molecular structures. A few examples of the algorithms are Isomap [69], locally linear embedding [70], diffusion maps [71], self-organizing maps [72] and the aforementioned autoencoders [25], whose application to the DFM will be the focus of section 1.2.

1.1 Two linear dimensionality reduction schemes

Linear dimensionality reduction has a long history in the molecular context. The main reason for this is the need to analyze the dynamics of large molecules. Especially for the dynamics of biomolecules, where thousands of degrees of freedom could be involved in reactions, it is practically impossible to naively determine the essential motions one wishes to study without reducing the dimensionality. This is reflected by a large amount of associated literature [21, 23, 73–85]. In addition, dimensionality reduction can also be used to increase the efficiency of MD calculations [23, 86–91].

In this chapter, a method is presented, which uses PCA, one of the most widely applied methods in this field [21–23, 87] for the purpose of dimensionality reduction. The PCA is a mathematical tool that allows the extraction of a set of orthogonal degrees of freedom of a system ordered according to the variance of a given set of data points in that system. The degrees of freedom found are the same as would be found by manually identifying the degree of freedom in the system with the biggest variance in the data points and then identifying the next one that is orthogonal to the first one and so on. A two-dimensional illustration is shown in fig. 1.1. u and v represent the first and second principal component of the Cartesian coordinates x and y of the green data points, respectively. The PCA has been applied to refine free energy calculations [87, 92, 93], to analyze the dynamics of proteins [94–97] and to many more topics [98–101].

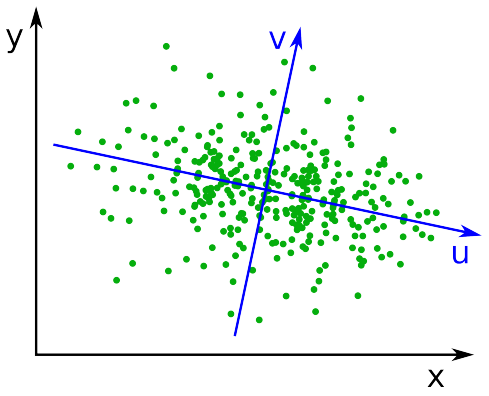

Figure 1.1: Results of a PCA. u and v are the principal components of the green data points.

The article "Two New Methods To Generate Internal Coordinates for Molecular Wave Packet Dynamics in Reduced Dimensions" published in *The Journal Chemical Theory and Computation* presents two approaches using points along the IRC and MD trajectory data to span a subspace suited for QD, using the examples of the proton transfer in (Z)-hydroxyacryloyl chloride and the methylization of cyclohexanone using trimethylaluminum [102]. The key points of the article are:

- To create an N-dimensional subspace, the IBA uses $N+1$ geometries (points) or M geometries and K predefined degrees of freedom (vectors) with $M + K = N + 1$. For the $N + 1$ (or M) geometries, critical points of the studied reactions are used first. Then, for the remaining geometries, the IRC is segmented and combinations of the resulting points along the IRC are used. The resulting subspaces are compared by their ability to reproduce the IRC and the energy profile of the IRC and the best subspace is obtained, accordingly.

- The TBA uses MD trajectories that are run from a point of high energy, e.g. a transition state, approximately along the reaction path. While fulfilling the Eckart conditions [31, 103, 104] to remove translation and rotation, the trajectory data points are used to construct a data matrix $\mathbf{X}$, with each row being build from the Cartesian coordinates of a single geometry and each column being shifted to ensure a column mean of 0. Applying the PCA to this matrix, i.e. calculating the eigenvectors of $\mathbf{X}^T \cdot \mathbf{X}$, the principal components containing the degrees of freedom with the most variance are obtained and used together with the critical points of the studied reaction to construct the subspace.

- A similarity measure is developed to compare the resulting subspaces produced by the two approaches. It is defined in way that removes most of the influence of the system size and

thus allows a comparison of the similarity between the two approaches for systems of different size.

- Both approaches are applied to two example systems and for both systems a three-dimensional subspace is constructed. The first is the proton transfer in (Z)-hydroxyacryloyl chloride. Two degrees of freedom are predetermined by three critical points and after applying both methods to construct a third, the IRC is accurately reconstructed. The second system is the methylization of cyclohexanone using trimethylaluminum. Two degrees of freedom are predetermined by two critical points and a predefined coordinate. Due to the much bigger system size, the reconstruction of the IRC using a subspace of same size is worse. However, since for this system each degree of freedom is more important, both approaches yield more similar results, as they should.

Altogether, it is shown that the results indicate that both approaches work satisfactory. It is also concluded that in contrast to the proton transfer reaction, three linear degrees of freedom are not enough to give an accurate description of the methylization system. Additionally, the different application scenarios of the two approaches are discussed.

In the following, the article "Two New Methods To Generate Internal Coordinates for Molecular Wave Packet Dynamics in Reduced Dimensions" published in *The Journal Chemical Theory and Computation* is reprinted with permission from *J. Chem. Theory Comput.* **12**, 5698-5708 (2016);

JCTC Journal of Chemical Theory and Computation Article
pubs.acs.org/JCTC

Two New Methods To Generate Internal Coordinates for Molecular Wave Packet Dynamics in Reduced Dimensions

Julius P. P. Zauleck, Sebastian Thallmair, Matthias Loipersberger, and Regina de Vivie-Riedle*

Department Chemie, Ludwig-Maximilians-Universität München, D-81377 München, Germany

ABSTRACT: The curse of dimensionality still remains as the central challenge of molecular quantum dynamical calculations. Either compromises on the accuracy of the potential landscape have to be made or methods must be used that reduce the dimensionality of the configuration space of molecular systems to a low dimensional one. For dynamic approaches such as grid-based wave packet dynamics that are confined to a small number of degrees of freedom this dimensionality reduction can become a major part of the overall problem. A common strategy to reduce the configuration space is by selection of a set of internal coordinates using chemical intuition. We devised two methods that increase the degree of automation of the dimensionality reduction as well as replace chemical intuition by more quantifiable criteria. Both methods reduce the dimensionality linearly and use the intrinsic reaction coordinate as guidance. The first one solely relies on the intrinsic reaction coordinate (IRC), whereas the second one uses semiclassical trajectories to identify the important degrees of freedom.

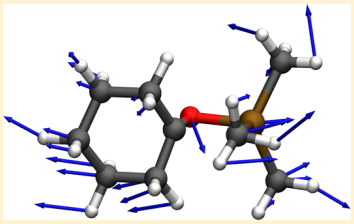

INTRODUCTION

In molecular quantum dynamical calculations the dimensionality issue is generally the decisive factor on which approximations have to be used for a practical implementation and in turn which degree of accuracy can be achieved. This is due to the exponential scaling of the calculation time and storage with the number of included dimensions. One way then is to avoid parts of the quantum mechanics of the dynamics by using approximations. Examples for this are Tully's surface hopping,[1] which takes part of the statistical behavior of quantum mechanics into account and has done very well over the decades, and focusing on efficient representations and calculations of the potential energy surface (PES) to then use semiclassical approaches to describe the dynamics.[2] However, these approaches are not an option when quantum effects that are important to describe a system cannot be reproduced. A popular approach that works well with up to a few dozen degrees of freedom while remaining quantum mechanical in nature is the multiconfiguration time-dependent Hartree (MCTDH) method.[3,4] It has been successfully applied to the calculation of absorption spectra of large molecules[5,6] and photophysical processes[7] and can with extensions like the multilayer MCTDH be applied to even bigger systems.[8] This approach is highly efficient when the potential and kinetic part of the Hamiltonian can be expressed as a small sum of products of operators that act on a single degree of freedom of the system. If this is not intrinsically the case for the PES of a system, it can be fitted accordingly with the POTFIT method.[9] The dynamics of chemical reactions however often leave the regions of the PES where this is efficient. Since reactive scenarios will be our main focus here we chose to explore grid-based approaches that also allow us to assess the relevance of the degrees of freedom for the reactions we are describing. It is based on a pseudospectral representation making use of the fast Fourier transform.[10] As a result the number of degrees of freedom often has to be significantly reduced, which leaves us with the choice of an affine configuration subspace to describe our reaction. This will be the topic of this paper.

One common way to reduce the number of degrees of freedom is the transformation from Cartesian coordinates to a set of internal coordinates describing bond distances, bond angles, and dihedral angles.[11−14] Ultrafast chemical reactions can often be approximated by a small number of internal coordinates providing an efficient description is found, exemplary shown by the reactive coordinates derived for the dissociation of diphenylmethyl systems by Thallmair et al.[15] On the other hand there exist many reactions with complex deformation of the molecular structure. A possible scenario is the relaxation of a conjugated π system due to a change in the bond order of a reactive coordinate. It is clear that most of these relaxations cannot be described by a single internal coordinate of the set formulated above, even though it may possibly be described with very few degrees or even a single degree of freedom. The key idea we followed was to replace the manual search for the most efficient set of coordinates by easily implemented algorithms.

Our approaches can be classified as linear dimensionality reduction, since they detect affine subspaces of the complete molecular configuration space. Their advantages are the relative ease to construct and evaluate linear subspaces. Additionally, the kinetic energy operator can be constructed diagonally with respect to the configurational degrees of freedom reducing the calculation time of the quantum dynamical propagation. The drawback is of course that in general fewer curvilinear coordinates are needed than linear ones for the same quality of results.

For the dimensionality reduction we devised two approaches. One uses points of the intrinsic reaction coordinate (IRC)[16,17] to span the reduced subspaces and will in the following be

Received: August 12, 2016
Published: November 7, 2016

DOI: 10.1021/acs.jctc.6b00800
J. Chem. Theory Comput. 2016, 12, 5698−5708

called the IRC-based approach (IBA). The other one uses a swarm of semiclassical trajectories starting from the transition state (TS) and extracts the most important dimensions in addition to those connecting the critical points of the reaction and will therefore be called trajectory-based approach (TBA).

The IBA basically guarantees to reproduce much of the IRC since the construction of its subspace is based on it. This makes it very reliable as long as the IRC describes the reaction reasonably well. The drawback is that with increasing dimensions of the subspaces many of them have to be constructed and tested. The method is intrinsically coupled to linear dimensionality reduction since it always uses N points to construct subspaces of $N - 1$ dimensions. Since the use of curvilinear coordinates is in many cases more efficient it is desirable to extend algorithms to nonlinearity. This is one of the two major advantages of the TBA. Here semiclassical trajectories are started from higher lying critical points toward the lower lying ones. These readily produce large data sets which can directly be used by dimensionality reduction algorithms. In our case this is done by principal component analysis (PCA) but could also be done by a nonlinear dimensionality reduction algorithm. The second advantage is the independence of calculation time on the number of dimensions extracted, which makes the TBA very efficient for higher dimensional models. However, due to accumulating momentum this method can have difficulties to reproduce the IRC well in some cases. It might also suggest subspaces which are suboptimal due to the lack of quantum effects such as barrier tunneling in the trajectories. In the following section both methods will be explained in detail. Thereafter the application of both methods to two examples and their evaluation is presented.

THEORY

The IRC is used as an evaluation tool for both methods, because it represents a minimum energy path between reactant and product, which would be the path followed by the system from the TS if the accumulation of momentum could be neglected. Even though the momentum induced in chemical reactions will lead to deviation from it, the IRC is a good starting point from which to derive the reactive coordinates. Furthermore, for a reaction steered by IR-light the IRC seems to be a reasonable path of choice.[18] This leads to our assumption that suitable subspaces have to reproduce the IRC reasonably well. The idea of the reaction path Hamiltonian also supports this assumption since it highlights the impact of the IRC on the reaction dynamics of a system.[19]

Because of the importance of the IRC of the subspace—which will from hereon be called IRC_{sub}—as quality criterion for the subspaces it should be pointed out that it is not to be confused with the projection of the IRC onto the subspace. This difference is shown in Figure 1, which illustrates for an exemplary potential the projection of a three-dimensional IRC onto the two-dimensional subspace as well as the IRC of the subspace. It also shows three critical points—the points where the IRC intersects the plane, shown as red circles—defining the subspace. It should be noted that the example is a simplified case and our molecular examples require a much higher dimensionality reduction. For visualization Figure 1 also overdraws the difference between the two curves since usually the IRC lies closer to the subspace and therefore its projection often is close to the IRC_{sub}. Still, there tend to be significant deviations motivating our decision to calculate the IRC_{sub}. Since

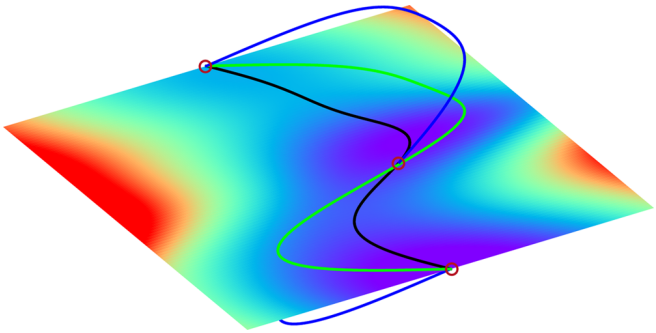

Figure 1. Two-dimensional affine subspace of a three-dimensional potential. The slice is the plane of the three-dimensional potential defined by the three intersection points. The potential energy is indicated by color ranging from blue (low) to red (high). The blue curve illustrates the full dimensional IRC and the green curve its projection onto the plane. The black curve illustrates an IRC inside the plane. Three critical point are highlighted by red circles.

we are focusing on affine subspaces the minimal dimensionality of the problem will in general be equal to the number of critical points minus one.

In this minimal case this approach is closely related to the reaction plane approach by Yagi et al.[20,21] This has been extended to cases that require more degrees of freedom in an approach similar to ones by Matanović et al.[22] They also construct linear subspaces to reproduce the IRC of a reaction, in their case the double proton transfer reaction in the formic acid dimer. However, there are a few key differences. The first one is their goal to construct subspaces which leave the kinetic energy operator diagonal with respect to the degrees of freedom. This on the one hand limits the solution space but on the other hand opens the way for different quantum dynamics approaches. Since we restricted ourselves to grid-based wave packet dynamics using algorithms that can deal with nonlinear kinetic energy operators, we can in general reduce the dimensionality of the subspace farther. Another key difference is the evaluation of the possible subspaces. Matanović et al. do this by projecting the IRC onto the subspace and calculating the deviation from the full dimensional one, while we calculate the deviation between the IRC_{sub} and the full dimensional one as illustrated in Figure 1. Using the IRC_{sub} requires additional calculations, but it also shifts the focus from a subspace just being close to the IRC to reconstructing it well. That being said, our approaches could also be run with the same projection of the IRC as done by Matanović et al. in order to be accelerated. There also remains a bit of a question toward the generalization of the evaluation of the subspaces done by Matanović et al. which relies on iterative kinematic rotations until self-consistency is reached. This process can lead to relative optima that are not guaranteed to be global ones. This can also happen for our IRC based approach (IBA), but as the feature of a good subspace here is its ability to reconstruct the IRC well, it seems likely that an approach using points along the IRC to construct an initial subspace has a good chance to find a local optimum that is close to the global one. Additionally, Matanović et al. choose a set of initial coordinates, which then is symmetrized. As a result we consider our approaches to be more automated.

IRC-Based Approach. The procedure of the IRC-based approach (IBA) is schematically shown in Figure 3. It begins by identifying the degrees of freedom that are necessary to connect the critical points of the reaction and have to be included in the

DOI: 10.1021/acs.jctc.6b00800
J. Chem. Theory Comput. 2016, 12, 5698−5708

model. One of the critical points is chosen as a reference and origin of the subspace. A typical set of critical points could be the reactant state, the TS and the product state, which would lead to the construction of a two-dimensional subspace. Next the IRC is calculated in full dimensions. Usually, this is done by following the gradient in both directions (toward reactant and product) from the TS. The tangent vectors of the IRC in configuration space are given by

$$\left.\frac{\mathrm{d}\mathbf{x}(s')}{\mathrm{d}s'}\right|_{s'=s} = \frac{\mathbf{g}[\mathbf{x}(s)]}{|\mathbf{g}[\mathbf{x}(s)]|} \tag{1}$$

Here s is the intrinsic reaction coordinate, $\mathbf{x}(s)$ is a position vector pointing to the IRC path at s and $\mathbf{g}[\mathbf{x}(s)]$ and $|\mathbf{g}[\mathbf{x}(s)]|$ are the gradient vector and its norm respectively at s. All vectors corresponding to the full configuration space have the dimension of $3N_{\mathrm{at}}$ since every atom is contributing three degrees of freedom. The first three entries correspond to the first atom, the second three entries to the second atom, and so on. There are a number of algorithms to calculate the IRC. We use the Gonzales−Schlegel method.[23]

The next step is to define the number of dimensions needed in addition to those predetermined by the critical points. For each additional dimension an extra point of the IRC has to be chosen leading to a segmentation of the IRC-based on the number of subspaces that are feasible to evaluate. A suggested strategy is to begin with a coarse segmentation and optimize the best subspaces by finer segmentation in the vicinity of points yielding good subspaces. In general the number of possible subspaces N_{ss} with N_{IRC} points on the IRC and D dimensions is given by

$$N_{\mathrm{ss}} = \frac{N_{\mathrm{IRC}}!}{(N_{\mathrm{IRC}} - D)!} \tag{2}$$

Although this number can be significantly reduced by avoiding points near the critical points as well as points being close together in the case of more than one additional dimension, it is clear that the number of subspaces to evaluate grows rapidly with dimensionality. Once a set of points defining a subspace is determined, the basis vectors of this subspace, corresponding to the internal coordinates for the reaction, can be created. There are several possibilities to construct the basis vectors. We chose to create the vectors $\mathbf{a}_i$ pointing from the reference point to all the other points of the subspace; for example, $\mathbf{a}_1$ could be constructed by creating the vector pointing from the TS to the reactant in the $3N_{\mathrm{at}}$ dimensional configuration space. Figure 2 illustrates one way to construct the vectors $\mathbf{a}_i$.

As a third step we minimize the translational and rotational degrees of freedom in the subspace by satisfying the Eckart conditions, which are given by

$$\sum_{b=1}^{N_{\mathrm{at}}} M_b \mathbf{d}_b = 0 \tag{3}$$

for translation and

$$\sum_{b=1}^{N_{\mathrm{at}}} M_b (\mathbf{d}_b \times \mathbf{R}_b) = 0 \tag{4}$$

for rotation.[24] Here b runs over the number of atoms and the vectors $\mathbf{d}_b$ and $\mathbf{R}_b$ are three-dimensional vectors corresponding to the individual atoms, M_b is the atom mass and × corresponds to the cross product of two vectors. $\mathbf{R}_b$ is the vector of atom b of a reference structure. A possible choice for our examples is the structure of the TS. $\mathbf{d}_b$ is a displacement vector of atom b and therefore related to the vectors $\mathbf{a}_i$ containing all atoms. A vector $\tilde{\mathbf{a}}_i$ satisfying the Eckart conditions would fulfill eq 3 if the first three entries comprise $\mathbf{d}_1$, the second triple $\mathbf{d}_2$, etc. The same is the case for eq 4 with the vectors $\mathbf{R}_b$ being structured like vectors $\mathbf{d}_b$.

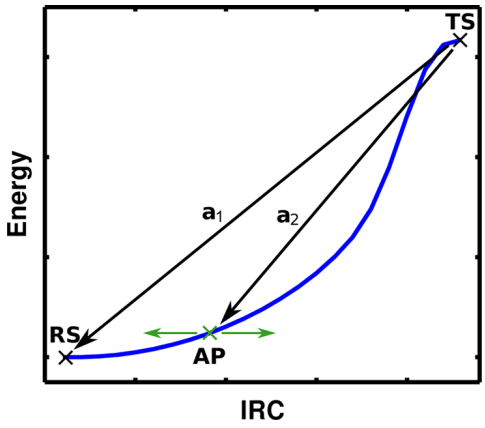

Figure 2. A possible way to construct the subspaces. The additional point (AP) is picked by moving along the IRC—here shown with its potential energy—and using the corresponding geometry. Then the vectors $\mathbf{a}_i$ are constructed by creating the vectors pointing from the TS to the other two points, reactant state (RS) and AP, in configuration space, symbolically shown by the black arrows.

Removing the translational degrees of freedom is straightforward. Given a set of displacement vectors $\mathbf{d}'_b$ a transformation to $\mathbf{d}_b$ is required that satisfies eq 3. This is done by

$$\mathbf{d}_b = \mathbf{d}'_b - \frac{\sum_{c=1}^{N_{\mathrm{at}}} M_c \mathbf{d}'_c}{\sum_{c=1}^{N_{\mathrm{at}}} M_c} \tag{5}$$

The rotation of a molecule cannot in general be fully eliminated from a displacement vector but there exist different algorithms to minimize it.[25] We use an approach by Dymarsky et al. that calculates the pseudorotation matrix for a structure so that it satisfies eq 4.[26] Once the vectors $\tilde{\mathbf{a}}_i$ are constructed they are orthonormalized yielding the basis vectors $\mathbf{b}_i$.

At this point all the subspaces to be tested can be created and evaluated. For this we need the $\mathrm{IRC}_{\mathrm{sub}}$. To construct it, we calculate the gradients and the Hessian of the PES in full dimensions. These are then projected onto the subspace, where the same algorithms as in the full dimensional problem follow the $\mathrm{IRC}_{\mathrm{sub}}$. For the projection a connection between the basis vectors $\mathbf{b}_i$ and the transformation matrix $\mathbf{A}$ between the Cartesian coordinates x_i and the internal coordinates b_i must be formulated. This is required, because we can use $\mathbf{A}$ to project quantities onto the subspace. The difference between the vectors $\mathbf{b}_i$ with elements $(\mathbf{b}_i)_j$ and $\mathbf{b}$ with elements b_i should be emphasized. They are named similarly because they are closely related. However, the former is the vector of the ith internal coordinate in Cartesian coordinates and the latter is a vector in the internal coordinate space. Let us define the transformation between Cartesian and internal coordinates ($\mathbf{x}$ and $\mathbf{b}$ respectively) as

$$\mathbf{b} = \mathbf{A}\mathbf{x} \quad \text{and} \quad \mathbf{x} = \mathbf{A}^{-1}\mathbf{b} \tag{6}$$

Now, the standard basis vectors for $\mathbf{b}$ ((1,0,0,...), (0,1,0,...) etc.) correspond to the internal coordinates. As a result, when $\mathbf{b}$ becomes the ith standard basis vector $\mathbf{x} = \mathbf{b}_i$, since it represents

DOI: 10.1021/acs.jctc.6b00800
J. Chem. Theory Comput. 2016, 12, 5698−5708

the displacement of the ith internal coordinate in Cartesian coordinates. In other words, $\mathbf{b}_i$ is the representation of an internal coordinate vector $\mathbf{b}$ in Cartesian coordinates. Additionally, eq 6 tells us that in this case $\mathbf{x}$ is equal to the ith column of the matrix $\mathbf{A}^{-1}$. As a result the ith column of the matrix $\mathbf{A}^{-1}$ has the same entries as the vector $\mathbf{b}_i$. Since the $\mathbf{b}_i$ are orthonormalized $\mathbf{A}^{-1} = \mathbf{A}^T$. From this we obtain the following derivatives as

$$\frac{\partial b_j}{\partial x_i} = \mathbf{A}_{ji} = (\mathbf{b}_j)_i \quad \text{and} \quad \frac{\partial x_k}{\partial b_j} = \mathbf{A}_{jk} = (\mathbf{b}_j)_k \tag{7}$$

With this and the multidimensional chain rule we can transform the elements of the gradient $\frac{\partial E}{\partial x_i}$ and the Hessian $\frac{\partial^2 E}{\partial x_i \partial x_j}$ from the $\mathbf{x}$ frame to the $\mathbf{b}$ frame and back again while taking into account only the coordinates we want to project onto. The projected gradient $\overline{\frac{\partial E}{\partial x_i}}$ of the PES is thus given by

$$\begin{aligned}\overline{\frac{\partial E}{\partial x_i}} &= \sum_{j=1}^{n}\sum_{k=1}^{3N_{at}} \frac{\partial b_j}{\partial x_i}\frac{\partial x_k}{\partial b_j}\frac{\partial E}{\partial x_k} \\ &= \sum_{j=1}^{n}\sum_{k=1}^{3N_{at}} \mathbf{A}_{ji}\mathbf{A}_{jk}\frac{\partial E}{\partial x_k}\end{aligned} \tag{8}$$

and the projected Hessian $\overline{\frac{\partial^2 E}{\partial x_i \partial x_j}}$ is given by

$$\begin{aligned}\overline{\frac{\partial^2 E}{\partial x_i \partial x_j}} &= \sum_{k=1}^{n}\sum_{l=1}^{n}\sum_{m=1}^{3N_{at}}\sum_{o=1}^{3N_{at}} \frac{\partial b_k}{\partial x_i}\frac{\partial x_o}{\partial b_k}\frac{\partial b_l}{\partial x_j}\frac{\partial x_m}{\partial b_l}\frac{\partial^2 E}{\partial x_o \partial x_m} \\ &= \sum_{k=1}^{n}\sum_{l=1}^{n}\sum_{m=1}^{3N_{at}}\sum_{o=1}^{3N_{at}} \mathbf{A}_{ki}\mathbf{A}_{ko}\mathbf{A}_{lj}\mathbf{A}_{lm}\frac{\partial^2 E}{\partial x_o \partial x_m}\end{aligned} \tag{9}$$

The indices running over n belong to the n coordinates of the subspace. From this point on, the usual algorithms to calculate the $\mathrm{IRC}_{\mathrm{sub}}$ can be employed as neither Hessian nor gradient leaves the subspace.

After the $\mathrm{IRC}_{\mathrm{sub}}$s are calculated they can be compared to the complete IRC in order to find the subspace that reproduces the IRC best. We propose two quantities to measure the quality of the $\mathrm{IRC}_{\mathrm{sub}}$s. The first one is a distance measure. For each $\mathrm{IRC}_{\mathrm{sub}}$ point the closest point of the IRC is determined (again satisfying the Eckart conditions). Thus, a distance function $\Delta r(\mathrm{IRC}^i_{\mathrm{sub}})$ of the subspace reaction coordinate for the ith subspace is obtained. The first quantity ΔA^i is then defined by

$$\Delta A^i = \int \Delta r(\mathrm{IRC}^i_{\mathrm{sub}})\, \mathrm{dIRC}^i_{\mathrm{sub}} \tag{10}$$

For the second quantity the energy difference of the same closest points is calculated. As the result an energy difference function $\Delta E(\mathrm{IRC}^i_{\mathrm{sub}})$ of the subspace reaction coordinate is obtained. The second quantity ΔB^i is then defined by

$$\Delta B^i = \int \Delta E(\mathrm{IRC}^i_{\mathrm{sub}})\, \mathrm{dIRC}^i_{\mathrm{sub}} \tag{11}$$

Those two can be used to calculate a combined quality criterion Q^i:

$$Q^i = \frac{N\Delta A^i}{\sum_{j=1}^{N}\Delta A^j} + \frac{N\Delta B^i}{\sum_{j=1}^{N}\Delta B^j} \tag{12}$$

Q^i is an average over both quantities and is also in a sense normalized over all subspaces so distance and energy differences are weighted equally. It can directly be used to compare the subspaces where the smallest Q^i indicates the best subspace i. It should be noted that these criteria are constructed for a relative comparison between the subspaces in order to identify the best one. They—especially ΔB^i—can also be used to get an idea of the absolute quality of the subspace with respect to the IRC. However, we suggest the use of the average distance or difference by dividing by the total length of the respective $\mathrm{IRC}_{\mathrm{sub}}$.

Trajectory-Based Approach. The procedure of the trajectory-based approach (TBA) is schematically shown in Figure 3. It requires at least one semiclassical trajectory approximately following the part of the reaction to be calculated. In a simple case this could be the part between TS and product which could be described by a trajectory starting from a point slighty displaced from the TS toward the product. Since the data set composed of the trajectory points has the most influence on the result, swarms of trajectories are recommended as data sets, because irregularities will have a smaller weight this way. The basic idea is then to use a PCA to extract the degrees of freedom with the biggest variance. PCA is already being applied to trajectories. This is generally done to extract the so-called essential dynamics of larger systems, in particular proteins. Two typical goals are then dimensionality reduction for interpretation and reduction of calculational cost of trajectory calculations.[27−29] An overview is given by Stein et al.[30] To our knowledge, the application of the PCA to trajectories for the construction of PESs for quantum dynamical calculations is new.

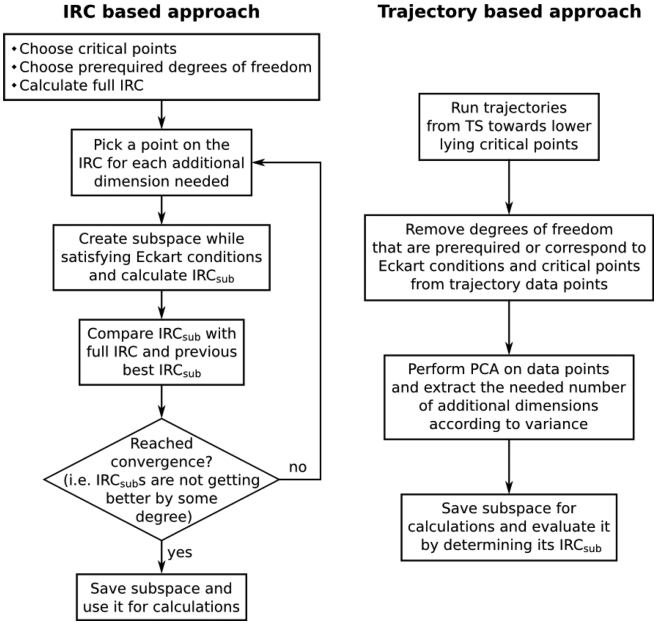

Figure 3. Basic process structures of the IBA and the TBA.

The first step after creating the data set is to satisfy the Eckart conditions (eq 3 and 4) for all points of the trajectories that are in this data set with respect to the reference point. Then a data matrix $\mathbf{Y}$ is created whose row vectors are the coordinate vectors of the data points. As a result, the element $\mathbf{Y}_{i,j}$ is the value of the jth coordinate of the ith data point. From this the matrix $\tilde{\mathbf{Y}}$ can be created by shifting the values of the column vectors to set their arithmetic means to zero. Before extracting the degrees of freedom with the biggest variance, the subspace

DOI: 10.1021/acs.jctc.6b00800
J. Chem. Theory Comput. 2016, 12, 5698−5708

containing the critical points has to be removed. To do so, the orthonormal basis vectors of the subspace that contains the critical points are assembled as rows in a matrix $\mathbf{V}$. Accordingly $\mathbf{V}_{i,j}$ is the value of the jth coordinate for the ith basis vector. The final data matrix $\mathbf{x}$ can then be constructed by

$$\mathbf{X} = \tilde{\mathbf{Y}} - (\tilde{\mathbf{Y}} \cdot \mathbf{V}^T)\mathbf{V} \tag{13}$$

At this point the PCA can be invoked. This means that the eigenvectors and -values of the matrix $\mathbf{x}^T \cdot \mathbf{x}$ are calculated where the eigenvector corresponding to the largest eigenvalue is the degree of freedom with the biggest variance, the eigenvector corresponding to the second largest eigenvalue is the degree of freedom with the second largest variance, and so on. These eigenvectors and the row vectors of the matrix $\mathbf{V}$ can directly be used as the basis vectors $\mathbf{b}_i$ of the final subspace. It is this last step at which the number of additional dimensions has to be chosen, and it is obvious that the scaling of the calculation of basis vectors with the number of additional dimensions is not relevant compared to quantum dynamical calculations in those subspaces.

This approach also delivers a way to test how well the trajectories can reproduce the critical points on their own. To do this, the PCA is used on the matrix $\tilde{\mathbf{Y}}$ instead of $\mathbf{x}$. Then the distance of the critical points—except for the reference point—to the subspace can be calculated. This simple test will later be very useful, because it tells us how closely the trajectories follow the IRC. The evaluation tools introduced together with the IBA are also applicable here, ultimately leading to the combined quality criterion Q^i (compare eq 12).

Similarity of the Results of Both Approaches. Additionally, the similarity of the results of the IBA and the TBA is of interest. This is mainly due to its importance for the evaluation of the quality of the produced subspaces. Since the two approaches are very different with respect to the information and the algorithms they use, it is expected that their results are not biased much to each other. This in return gives information about both approaches if the results are similar anyway. There are a few approaches to define a measure for similarity, and we suggest to use the canonical angles α_i between the subspaces. The canonical angles can be constructed by finding the pair of basis vectors—each from one of the subspaces—that have the smallest angle α_1 between each other. Then the second pair of basis vectors that fulfills the same condition has to be constructed with the requirement that each basis vector is orthogonal to the respective first. This is repeated until all the canonical angles are determined, their number equaling the number of dimensions of the subspaces.

Our goal is now to construct a parameter that is a measure of the similarity of the subspaces. Since the canonical angles themselves depend on the dimensionality of the system, we derive the variance σ by use of a distribution that recreates the subspaces as expected outcome. To overcome the enormous impact of the dimensionality on the probabilities, we decided to use a distribution that can easily be separated in a part dependent on the dimensionality and a part independent of it that incorporates σ. The independent part of the distribution of the two approaches can then either be compared directly for different systems using σ or the systems can be compared in a corresponding lower dimensional situation. However, in order to do that, an assumption has to be made on what makes the results of both approaches similar. Since the direct tool of comparison is the canonical angles, we chose to use some pseudoforce keeping the basis vectors together and the angles small. The most natural choice seemed a harmonic potential, resulting in a normal distribution along the angle between both vectors for a single relative degree of freedom. The dimensionality dependent part then enters in the form of degeneracy factors. The unnormalized probability density can be given by

$$f(\alpha_i; N) = \sin(\alpha_i)^{N-2}\, e^{-\alpha_i^2/(2\sigma_i^2)} \tag{14}$$

Here N is the number of degrees of freedom of the system and $\sin(\alpha_i)^{N-2}$ is the dimension dependent degeneracy factor. It gives the relative number of possible configurations with an angle α_i between two unit vectors in N dimensional space. As an example one can consider the three-dimensional case as shown in Figure 4. While fixing one vector the other can move along a circle with radius $\sin(\alpha_i)$ for a fixed α_i. Since the number of possible configurations is proportional to the circumference of this circle which in turn is proportional to the radius, $\sin(\alpha_i)$ can be used as an unnormalized degeneracy factor.

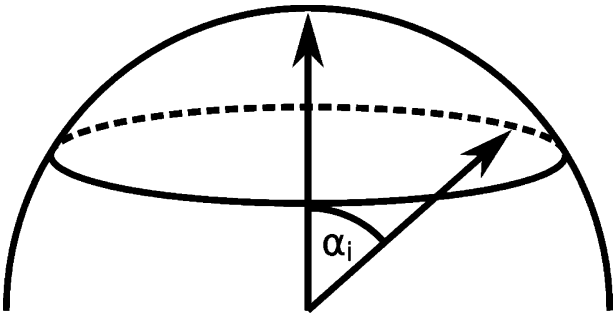

Figure 4. Illustration of the degeneracy factor of eq 14 in three dimensions. The number of possible orientations of two vectors with an angle α_i in three dimensions is proportional to the mapped circumference on the sphere.

The standard deviation σ_i of α_i is unknown but can be approximated to allow a comparison between different systems. Since two approaches are compared, there are two vectors for each degree of freedom. This can be approximated by the actual vector being located between the two vectors from both approaches. These vectors lie at the expected value of half of the canonical angle $E\left[\frac{\alpha_i}{2}\right]$ apart from the actual vector. As a result, the standard deviation σ_i can be calculated, as $E\left[\frac{\alpha_i}{2}\right]$ is given by

$$E\left[\frac{\alpha_i}{2}\right](\sigma_i) = \frac{\int_0^{\pi/2} \frac{\alpha_i}{2} f\left(\frac{\alpha_i}{2}; N\right) \mathrm{d}\alpha_i}{\int_0^{\pi/2} f\left(\frac{\alpha_i}{2}; N\right) \mathrm{d}\alpha_i} \tag{15}$$

Notice that we use half of the canonical angle α_i for the distribution f. Since the expected canonical angle is an injective function of the standard deviation, the standard deviation for a certain expected angle can be determined by iteratively refining its grid until a convergence criterion for the expected angle has been met. Assuming that all canonical angles are created independently a standard deviation for each one can be calculated. The average of the standard deviations can then either be compared directly for different systems or a lower dimensional canonical angle can be constructed to give a more intuitive criterion for comparison. We will use a corresponding

DOI: 10.1021/acs.jctc.6b00800
J. Chem. Theory Comput. 2016, 12, 5698−5708

two-dimensional canonical angle α_i^{2D} for comparison since the degeneracy factor in two dimensions can be ignored.

EXAMPLES

We tested both approaches on two examples. The first one is the proton transfer reaction between the two oxygen atoms in (*Z*)-hydroxyacryloyl chloride. Since this molecule has only nine atoms and the reaction can be approximated well by two dimensions[31] this is a benign problem for dimensionality reduction. The second example is the methylization of cyclohexanone using trimethylaluminum.[32] It has its origin in the more practical question whether this reaction can be triggered by IR-light and involves 30 atoms moving in all three spatial dimensions. This makes it obviously a much more challenging system. Both examples are ground-state reactions that are typically slower and therefore involve more motion compared to fast photochemical reactions. As a result they will generally require more degrees of freedom. For both systems our goal was to construct three-dimensional affine subspaces.

Proton Transfer. In the proton transfer reaction[31,33,34] we included the reactant state defined as the formyl configuration, the TS as reference point, and the product state with the chlorocarbonyl configuration in the subspace. This leaves one additional dimension to be determined. All quantum chemical calculations for this example were done with the program package Gaussian 09 at the DFT (M06-2X,cc-pVTZ) level of theory.[35] The IRC as well as the structures of the critical points are shown in Figure 5. For the IBA the IRC was segmented

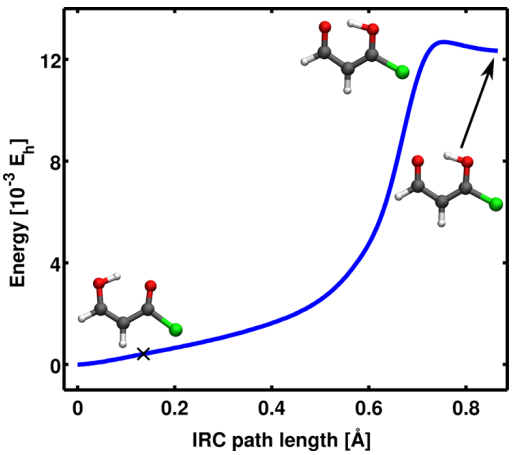

Figure 5. PES along the IRC for the proton transfer in (*Z*)-hydroxyacryloyl chloride. The reactant is shown on the left side in the formyl configuration. The part between the reactant and the TS, shown here as the maximum of the curve along with the structure in the middle, was recreated in the subspaces. The cross marks the 166th IRC point which turned out to produce the best subspace in the IBA.

using 245 points between the reactant and the TS. We searched for the best subspace describing this region to focus on the activation of a reaction thus picking the additional point in this section. The distance between the IRC points was set to about 0.0028 Å and every 10th point starting with the sixth and ending with the 196th point after the TS was used to define a subspace to be tested.

The resulting 20 IRC$_{sub}$s were then calculated between the TS and the reactant state. Extending the procedure to the second part of the IRC$_{sub}$ would be straightforward. The distance $\Delta r(\mathrm{IRC}_{sub}^i)$ and energy difference functions $\Delta E(\mathrm{IRC}_{sub}^i)$ of the IRC$_{sub}$s with respect to the full IRC were calculated as well as the quality criterion Q^i introduced in eqs 10−12. However, since the problem can be modeled very well with a three-dimensional subspace which in turn reproduces a very good IRC, our calculation produced some IRC$_{sub}$ points with an energy slightly below the energy of the closest full dimensional IRC point due to discretization errors. To avoid problems, we therefore shifted all the ΔB^i until the lowest was equal to zero. The best subspace due to Q^i was the one of the 166th IRC point after the TS. The values of the quality criteria for the subspaces of all IRC points are given in Table 1.

Table 1. Comparison of the Different Subspaces for the Proton Transfer in (*Z*)-Hydroxyacryloyl Chloride According to the Quality Criteria ΔA^i, ΔB^i, and Q^i Given in eqs 10−12[a]

IRC point	ΔA^i [10^{-4} Å^2]	ΔB^i [10^{-5} ÅE$_h$]	Q^i
6	9.758	6.04	4.822
16	8.387	9.31	5.319
26	7.743	9.51	5.173
36	6.364	7.95	4.289
46	3.783	6.79	3.137
56	2.164	3.05	1.558
66	1.951	2.15	1.233
76	1.850	1.99	1.154
86	1.726	1.88	1.084
96	1.635	1.70	1.004
106	1.556	1.62	0.956
116	1.506	1.27	0.840
126	1.471	1.31	0.842
136	1.466	1.52	0.900
146	1.482	1.70	0.954
156	1.522	0.63	0.665
166	1.605	0.00	0.510
176	1.750	1.00	0.840
186	2.005	2.83	1.444
196	2.963	6.65	2.837
TBA	3.393	4.77	2.438

[a]Listed are the results of the IBA using the IRC points 6 through 196 in steps of 10 as well as the results of the TBA. The values of the ΔB^i have been shifted so the smallest is equal to zero.

For the TBA, 50 semiclassical trajectories were calculated. To start the trajectories the geometry of the molecule was displaced in steps of 0.002 Å from the TS along the mode with imaginary frequency toward the reactant state, launching a trajectory from each geometry. No initial momentum was given. The trajectories were calculated with time steps of 0.5 fs using the program package NEWTON-X 1.4.[36] During the overall propagation time of 100 fs all trajectories passed by the reactant state. The PCA was then applied to obtain the corresponding subspace.

$\Delta E(\mathrm{IRC}_{sub}^i)$ and $\Delta r(\mathrm{IRC}_{sub}^i)$ for the IRC$_{sub}$ derived from the two approaches are shown in Figure 6. The results for the subspace derived from the 166th IRC point and from the TBA are colored green and red, respectively. For comparison, also the functions for the 66th IRC point is shown in blue. The values of the quality criteria of eqs 10−12 for the TBA are also shown in Table 1.

There are two important observations to be made from these functions. First, the values of the distance function $\Delta r(\mathrm{IRC}_{sub}^i)$ of the trajectory-based subspace are a bit bigger than for the best subspaces of the IBA. This is to be expected since the IBA

DOI: 10.1021/acs.jctc.6b00800
J. Chem. Theory Comput. 2016, 12, 5698−5708

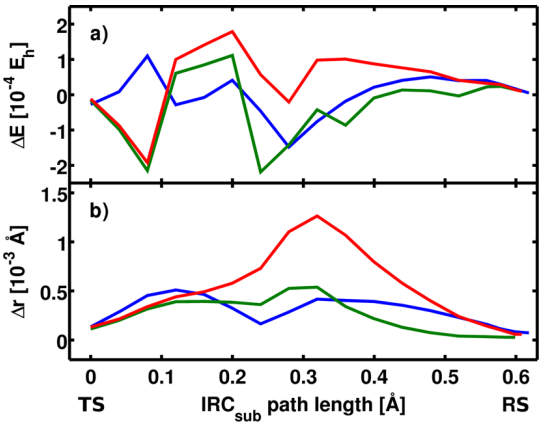

Figure 6. Energy difference functions $\Delta E(\mathrm{IRC}^i_{\mathrm{sub}})$ (a) and distance functions $\Delta r(\mathrm{IRC}^i_{\mathrm{sub}})$ (b) for the proton transfer in (*Z*)-hydroxyacryloyl chloride. In contrast to the IRC plots, the TS is here to the left. The blue graph belongs to the subspace of the 66th IRC point, the green one to the 166th point, and the red one to the subspace determined by the TBA.

uses an additional point of the IRC forcing its subspace closer to it. The other observation is that the energy difference functions $\Delta E(\mathrm{IRC}^i_{\mathrm{sub}})$ seem to be dominated by noise. This is indicated by fluctuation above and below the line of 0 E_h. Otherwise there are no big differences between the $\Delta E(\mathrm{IRC}^i_{\mathrm{sub}})$, because the three dimensions can describe the proton transfer very well resulting in $\mathrm{IRC}_{\mathrm{sub}}$s that are energetically very close to the full dimensional IRC. The main reason for an energy difference between an IRC point and an $\mathrm{IRC}_{\mathrm{sub}}$ point stems in this case from the discretization of both IRCs. Differences in discretization can lead to noise around an energy difference of zero. This noise can be reduced by finer discretization of the IRCs.

We also calculated the distance of the product and reactant state from the subspace obtained with the TBA by applying the PCA to $\tilde{\mathbf{Y}}$. This is interesting because the data matrix $\tilde{\mathbf{Y}}$ still contains all degrees of freedom except the ones corresponding to the Eckart conditions. As a result the distances can be viewed as a measure of how well the trajectories reproduce the critical points. The distance between reactant state and subspace is 0.040 Å, and the distance between product state and subspace is 0.074 Å. These distances give useful information if considered in relation to other distances of the system. For example, the distance between the reactant and the TS is 0.66 Å, and the distance between the product and the TS is 0.17 Å. Since the approaches both focused on reconstructing the IRC part toward the reactant, the product is not reconstructed very well because the distance between the product state and the subspace is about 44% of the distance between product state and TS. The other part of the IRC is much better reproduced, and the distance of the reactant state to the subspace is about 6% of the distance between the reactant state and the TS. Since 0% would correspond to the subspace containing the respective point, this is a good result and shows that in this case, the three-dimensional subspace obtained by the PCA includes the reaction pathway well. In general, the more curvature along different coordinates the trajectories contain, the worse linear approximations become, and the bigger the distance of the reactant state from the subspace should be, even if the trajectories all cross this point. These scenarios that may result in subspaces poorly describing the IRC are the major limitations of the TBA.

Additionally, the similarity of the subspaces generated by the two approaches can now be examined. The standard deviation given in eq 15 can be calculated and used as a similarity measure. Since the two approaches have two identical coordinates (compare Figure 7) the only relevant canonical

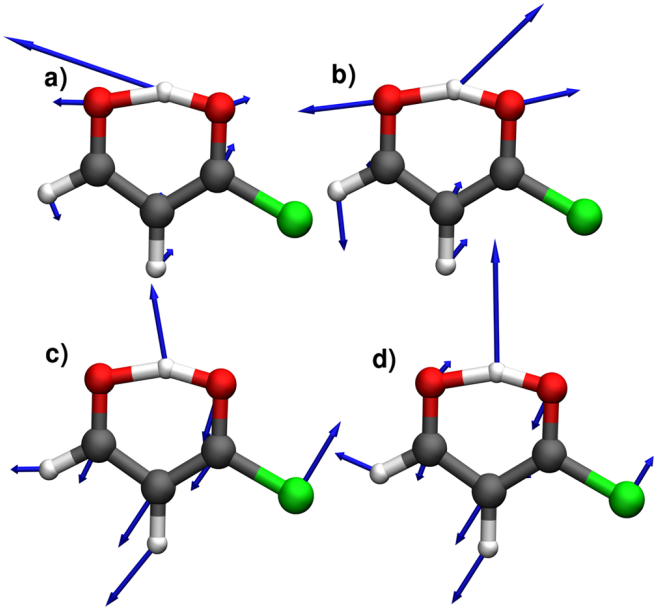

Figure 7. Basis vectors of the subspaces of the proton transfer in (*Z*)-hydroxyacryloyl chloride: (a and b) first and second coordinate which are identical for all subspaces since they are defined by the critical points; (c) third coordinate of the best subspace of the IBA; (d) third coordinate of the subspace of the TBA.

angle is the angle between the remaining third coordinate pair. The angle α_3 between these two coordinates is approximately 17.7°. In 13 available internal degrees of freedom (nine atoms, planar molecule, two translational and one rotational degree of freedom and two fixed degrees of freedom due to critical points) this corresponds to a standard deviation σ of 2.62° and an two-dimensional angle α_i^{2D} of 2.09° according to eq 15. The similarity of the third coordinate implied by these values is illustrated in Figure 7c and Figure 7d along with the first (a) and second (b) coordinate. The first two coordinates show the movement of the proton in the molecular plane as well as a variation of the oxygen−oxygen distance. The third coordinate from both approaches also includes part of the in-plane motion of the proton but also noteworthy contributions of the seemingly less relevant atoms for the reaction, illustrating the possible unintuitive nature of the best coordinates to describe a reaction.

Methylization. The methylization reaction is a much more challenging task. Many diverse motions contribute to the IRC. When reduced to three dimensions a decision on the importance of the degrees of freedom will be necessary. Therefore, an interesting point is whether both approaches will come to the same solution. We started by calculating the IRC from the TS of the reaction toward the reactant state. The last IRC point is chosen a little less than 0.0256 eV above from the energy of the reactant state. It will in the following be referred to as reactant. This was done because the PES in the vicinity of the reactant is very flat and causes the IRC to become overly

DOI: 10.1021/acs.jctc.6b00800
J. Chem. Theory Comput. 2016, 12, 5698−5708

lengthy and difficult to be calculated. Without significant loss of information the IRC was cut off at the first point where the energy level is reachable with 1 k_BT from the actual reactant state at room temperature. Both points—the reactant state and the TS—were included in the subspace with the TS as reference point. As the subspace should be generated for an IR driven reaction[32] the infrared active carbonyl mode of the reactant state was included as a second coordinate. It can be normalized and included as a basis vector given that neither translational nor rotational degrees of freedom are included. This again left one additional dimension to be determined.

All quantum chemical calculations for this example were done with the program package Gaussian 09 at the DFT (M06-2X, 6-31G(d)) level of theory.[35] For the IBA the IRC was calculated with 107 points between the TS and the reactant. Again we search for the best subspace between TS and reactant. The distance between the IRC points was set to about 0.052 Å and every fourth point starting with the 35th point after the TS up to the 67th point was used to define a subspace to be tested. The IRC is shown in Figure 8 with the structures of the

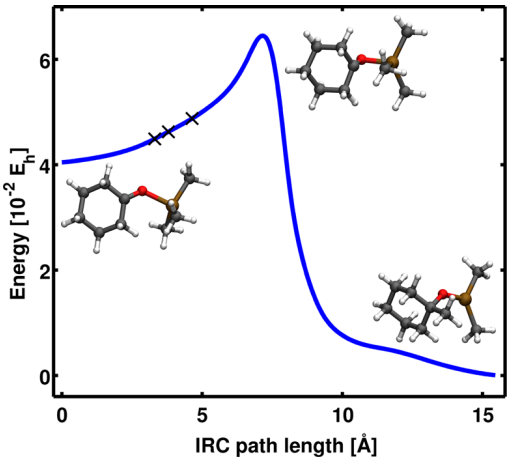

Figure 8. PES along the IRC for the methylization. The reactant is shown on the left side with all three methyl groups bound to the aluminum. The part between the reactant and the TS, shown here as the maximum of the curve along with the structure in the middle, was recreated in the subspaces in order to be optimized. To the right the product is shown with one of the methyl groups now attached to the carbon ring. Once the maximum of the barrier is reached, most of the molecules will likely be moved to the product by their momentum. The crosses mark the 63rd, 55th, and 43rd IRC point from used in the IBA from left to right.

reactant, TS, and product. The IRC$_{sub}$s have then been calculated between the TS and the reactant state. As expected these calculations proved more difficult due to the higher dimensionality of the system. Most subspaces develop a second, artificial TS which can be understood as the area least well described in the subspace. This artificial TS is located between the additional point for subspace construction and the reactant and gets energetically lower the further the point is moved toward the reactant. For our algorithms to calculate the complete IRC$_{sub}$s we had to locate this artificial TS and start another IRC$_{sub}$ calculation in both directions. As a final step all three IRC$_{sub}$ paths were connected by linear interpolation. The distance $\Delta r(\mathrm{IRC}^i_{sub})$ and energy difference functions $\Delta E(\mathrm{IRC}^i_{sub})$ of the IRC$_{sub}$s with respect to the full IRC were calculated as well as the quality criterion Q^i. The best subspace was the one of the 55th IRC point after the TS with an average deviation of about 0.086 eV from the full dimensional IRC. The values of the quality criteria for the subspaces of all IRC points are given in Table 2.

Table 2. Comparison of the Different Subspaces for the Methylization Reaction According to the Quality Criteria ΔA^i, ΔB^i, and Q^i given in eqs 10−12[a]

IRC point	ΔA^i [Å^2]	ΔB^i [10^{-2} ÅE$_h$]	Q^i
35	1.276	2.97	2.073
39	0.963	2.35	1.610
43	0.779	2.18	1.407
47	0.696	2.00	1.280
51	0.677	2.06	1.288
55	0.678	1.90	1.228
59	0.718	1.85	1.237
63	0.812	1.93	1.335
67	0.896	1.97	1.411
TBA	6.238	6.71	7.130

[a]Listed are the results of the IBA using the IRC points 35 through 67 in steps of 4 as well as the results of the IBA.

As in the first example 50 semiclassical trajectories were calculated for the TBA. Therefore, the geometry of the molecule was again displaced in steps of 0.002 Å from the TS along the mode with imaginary frequency toward the reactant state, again launching a trajectory from each point. The trajectories were calculated with time steps of 0.5 fs and over a time of 300 fs using the program package NEWTON-X 1.4.[36] Since most of the trajectories reach a deep local potential minimum quickly, parts of the trajectories were cut off. This was done by eliminating all points after a second local minimum was reached. Then the PCA was applied and the subspace retrieved. The values of the quality criteria of eqs 10−12 for the TBA is also shown in Table 2.

$\Delta E(\mathrm{IRC}^i_{sub})$ and $\Delta r(\mathrm{IRC}^i_{sub})$ for selected IRC$_{sub}$s are shown in Figure 9. The functions from the TBA are shown in blue, the ones of the 43rd IRC point in green, of the 55th in red, and of the 63rd in cyan. As expected the deviations are much larger compared to those in the first example. Now, the energy difference function $\Delta E(\mathrm{IRC}^i_{sub})$ does not fluctuate around zero

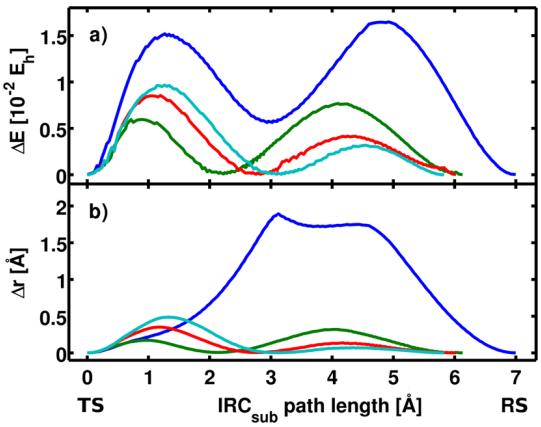

Figure 9. Energy difference functions $\Delta E(\mathrm{IRC}^i_{sub})$ (a) and distance functions $\Delta r(\mathrm{IRC}^i_{sub})$ (b) for the methylization reaction example. In contrast to the IRC plots, the TS is here to the left. The blue graph belongs to the TBA, the green one to the subspace of the 43rd IRC point, the red one to the one of the 55th point, and the cyan one to the one of the 63rd point.

DOI: 10.1021/acs.jctc.6b00800
J. Chem. Theory Comput. 2016, 12, 5698−5708

but shows two maxima in both approaches. In the case of the IBA, the functions of the earlier IRC points (e.g., 43) have their highest maximum for later parts of the IRC around 4 to 4.5 Å, whereas the later IRC points (e.g., 55,63) have higher maxima for smaller IRC values around 1 to 1.5 Å. This can be explained by the position of the additional point selected along the IRC used to span the subspace. This point will often lie very close to the IRC_{sub}, and there the IRC will be reproduced relatively well. As another result, of the two parts of the IRC_{sub} between the TS, the additional point and the reactant, the longer one will generally be a worse reproduction of the full IRC; hence, there the distance and energy difference will be bigger. $\Delta r(IRC^i_{sub})$ of the trajectory-based subspace again takes on much bigger values due to the same reason as in the first example. It also seems likely that the TBA subspace has a flat potential with respect to at least one of the degrees of freedom orthogonal to the IRC_{sub} in the region of the maxima of $\Delta r(IRC^i_{sub})$. This is because a large deviation in the IRC path can then lead to a small deviation in $\Delta E(IRC^i_{sub})$ as is seen in Figure 9. Additionally, this means that a relatively big deviation in the IRC path could have only a small impact on dynamics in that subspace.

We again calculated the distance of the reactant state from the subspace obtained by applying the PCA to the data matrix $\tilde{\mathbf{Y}}$. The distance between the reactant and the subspace is 3.86 Å compared to the distance of 4.68 Å between the reactant state and the TS, thus making up 82%, with again, 0% being the optimum for the reactant that is included in the subspace. This is an expected result since the trajectories do not completely follow the minimum energy path. This also directly reflects the increase in complexity of the reaction. The IRC is longer and more curved which results in trajectories becoming disconnected from it. However, the 82% still shows a dependence between the trajectories and the coordinate from the TS toward the reactant state in contrast to the description of the carbonyl mode, of which 99.4% are not included in the subspace.

The similarity of the subspaces generated by the two approaches can also be examined. Again, the two approaches have two identical coordinates and the only relevant canonical angle is the angle between the remaining third coordinate pair. The angle α_3 between these two coordinates is approximately 37.0°. In 82 available internal degrees of freedom (30 atoms, 3 translational, and 3 rotational degrees of freedom and 2 fixed degrees of freedom due to critical points and carbonyl mode) this corresponds to a standard deviation σ of 2.10° and an angle α_i^{2D} of 1.67° according to eq 15. The similarity of those coordinates is illustrated in Figure 10a and Figure 10b. It is apparent that both coordinates have very similar displacements for almost all atoms, the biggest differences being generated by the uppermost methyl group as well as the groups of both α-carbons (the carbon atoms next to the carbon with the functional group) of the ring. In comparison with the first example (σ of 2.62° and α_i^{2D} of 2.09) the generated coordinates are more similar. This can be understood by the fact that the methylization reaction requires more degrees of freedom to be approximated which leaves less room for deviations. In other words, if one has an algorithm that tries to improve the description of a system by determining additional degrees of freedom and all available degrees of freedom offer little improvement, the result will be more susceptible to the influence of the imperfections of the algorithm. In contrast, if there are degrees of freedom that offer a significantly bigger improvement than others, a functioning algorithm will be more likely to discover them. Since we already have a relatively good description with the two-dimensional subspace we predefined for the first example, there simply is not much room for improvement in contrast to the methylization reaction. Additionally, in contrast to the first system, the results here suggest that additional degrees of freedom would improve the quality of the subspace with respect to the deviations of the IRC.

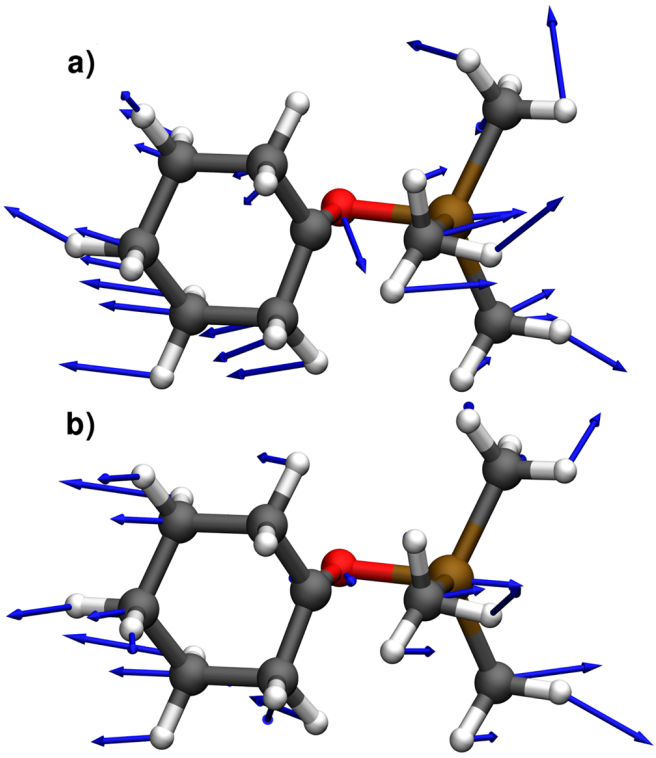

Figure 10. Basis vectors of the third coordinate of the subspaces for the methylization reaction example: (a) the coordinate of the TBA; (b) the coordinate of the best subspace of the IBA.

SUMMARY AND DISCUSSION

We presented two approaches for semiautomated linear dimensionality reduction of the configuration space of reactive chemical systems. After choosing a number of critical points that one wishes to be included in the simulation, both methods create the lowest dimensional affine subspace containing those points. The IRC-based approach (IBA) then uses additional points of the IRC to construct a number of subspaces which are evaluated. The subspaces are tested on their ability to reproduce the IRC by means of two criteria. The first one is based on the spatial distance between the IRC of the full dimensional and the reduced space. The second one uses the difference in potential energy between those two. In an ideal scenario the subspace would contain the complete IRC and both differences would be zero. Both measures can than be combined and the subspace that is best suited can be determined. Second, the trajectory based approach (TBA) uses principal component analysis on semiclassical trajectories to find the additional dimensions that describe the reaction best. The trajectories are started from the transition state of a reaction and are run until they pass by reactant and/or product state. The data points created can then be used to extract the degrees of freedom with the largest variance, hence being the most relevant for the trajectories and therefore being similarly relevant for the reaction itself.

DOI: 10.1021/acs.jctc.6b00800
J. Chem. Theory Comput. 2016, 12, 5698−5708

Both approaches were tested on two example systems for which the part of the IRC between the reactant and the transition state was considered. The first one is the proton transfer reaction between the two oxygen atoms in (Z)-hydroxyacryloyl chloride reduced to three degrees of freedom. Both methods produced subspaces whose subspace IRCs were very similar to the full dimensional IRC. In fact, both approaches yielded almost the same subspaces, supporting the results for this example. The other example is the methylization of cyclohexanone using trimethylaluminum. This system was reduced to three degrees of freedom as well. One of these degrees of freedom was reserved for an IR active carbonyl mode for optical steering at a later point. This example showcases the two approaches in a scenario for which the chosen number of linear degrees of freedom is barely enough to describe the system. As a result, the IRC of the best subspace produced by the IBA deviates significantly more from the complete IRC than in the first example. The TBA, which is intrinsically less connected to the IRC, reproduces a subspace IRC which deviates further. This however illustrates the stability of the two approaches, which still yield very similar subspaces for this example. In combination with the similar results for the first example, this is also a statement about the range of applicability of our approaches, since both examples are extremes with respect to the numbers of degrees of freedom that are required for a certain level of accuracy. Considering that both approaches are relatively free of biases and use very different inputs the quality of the identified third degree of freedom with regards to the studied reaction is evident.

Altogether both methods seem to have slightly different fields of application. The IBA will be most efficient if it is likely that the reaction can be described by a small number of coordinates with small curvature, which are difficult to be constructed intuitively. The relaxation of a conjugated π system during the course of a reaction is a good example, since it can often be described by a small number of linear combinations of Cartesian atomic coordinates. The TBA is useful if the dimensionality chosen for a description is relatively high, because the number of dimensions extracted does not influence the computational effort. It might also be suited to construct more complex subspaces, if the approach can be extended to nonlinear dimensionality reduction as the data points created by semiclassical trajectories can often be generated in large amounts.

Additionally, the trajectory calculations can be altered in order to focus on different aspects of the system. To begin with, there are a few things that can be fine-tuned in order to optimize the results. One is the running time of the trajectories. We chose to use simple stopping criteria such as a set propagation time or a cutoff after the overall motion became erratic. One could also use criteria that for the last data point of the trajectory use a clearer defined compromise of proximity to the optimal goal that the trajectory could reach and propagation time. Another parameter to be optimized is the initial distribution of starting points for the trajectories. Further improvement could be a deceleration to reduce the accumulation of momentum. This in turn would result in subspaces more similar to the IBA. One could also consider replacing the semiclassical trajectories with something that already includes many the effects that the full dimensional quantum dynamical description would, such as the G-MCTDH approach.[37] This could be done with very few basis functions, while still including quantum effects such as tunneling. Overall, the TBA seems to offer more room for growth and exploration.

AUTHOR INFORMATION

Corresponding Author

*E-mail: regina.de_vivie@cup.uni-muenchen.de.

Funding

Financial support by the Deutsche Forschungsgemeinschaft through the SFB749 and the excellence cluster Munich-Centre for Advanced Photonics (MAP) is acknowledged.

Notes

The authors declare no competing financial interest.

REFERENCES

(1) Tully, J. C. Trajectory Surface Hopping Approach to Non-adiabatic Molecular Collisions: The Reaction of H+ with D_2. *J. Chem. Phys.* **1971**, *55*, 562.
(2) Bowman, J. M.; Czakó, G.; Fu, B. High-dimensional ab initio potential energy surfaces for reaction dynamics calculations. *Phys. Chem. Chem. Phys.* **2011**, *13*, 8094−8111.
(3) Meyer, H.-D.; Manthe, U.; Cederbaum, L. S. The multi-configurational time-dependent Hartree approach. *Chem. Phys. Lett.* **1990**, *165*, 73−78.
(4) Meyer, H.-D.; Worth, G. A. Quantum molecular dynamics: propagating wavepackets and density operators using the multi-configuration time-dependent Hartree method. *Theor. Chem. Acc.* **2003**, *109*, 251−267.
(5) Raab, A.; Worth, G. A.; Meyer, H.-D.; Cederbaum, L. S. Molecular dynamics of pyrazine after excitation to the S[sub 2] electronic state using a realistic 24-mode model Hamiltonian. *J. Chem. Phys.* **1999**, *110*, 936.
(6) Vendrell, O.; Gatti, F.; Meyer, H.-D. Strong Isotope Effects in the Infrared Spectrum of the Zundel Cation. *Angew. Chem.* **2009**, *121*, 358−361.
(7) Hammerich, A. D.; Manthe, U.; Kosloff, R.; Meyer, H.-D.; Cederbaum, L. S. Time-dependent photodissociation of methyl iodide with five active modes. *J. Chem. Phys.* **1994**, *101*, 5623.
(8) Xie, Y.; Zheng, J.; Lan, Z. Full-dimensional multilayer multiconfigurational time-dependent Hartree study of electron transfer dynamics in the anthracene/C60 complex. *J. Chem. Phys.* **2015**, *142*, 084706.
(9) Peláez, D.; Meyer, H.-D. The multigrid POTFIT (MGPF) method: Grid representations of potentials for quantum dynamics of large systems. *J. Chem. Phys.* **2013**, *138*, 014108.
(10) Kosloff, D.; Kosloff, R. A Fourier Method Solution for the Time Dependent Schrödinger Equation as a Tool in Molecular Dynamics. *J. Comput. Phys.* **1983**, *52*, 35−53.
(11) Schlegel, H. B. A Comparison of Geometry Optimization with Internal, Cartesian and Mixed Coordinates. *Int. J. Quantum Chem.* **1992**, *44*, 243−252.
(12) Hofmann, A.; de Vivie-Riedle, R. Quantum dynamics of photoexcited cyclohexadiene introducing reactive coordinates. *J. Chem. Phys.* **2000**, *112*, 5054.
(13) Kowalewski, M.; Mikosch, J.; Wester, R.; de Vivie-Riedle, R. Nucleophilic Substitution Dynamics: Comparing Wave Packet Calculations with Experiment. *J. Phys. Chem. A* **2014**, *118*, 4661−4669.
(14) Thallmair, S.; Roos, M. K.; de Vivie-Riedle, R. Design of specially adapted reactive coordinates to economically compute potential and kinetic energy operators including geometry relaxation. *J. Chem. Phys.* **2016**, *144*, 234104.
(15) Thallmair, S.; Roos, M. K.; de Vivie-Riedle, R. Molecular features in complex environment: Cooperative team players during excited state bond cleavage. *Struct. Dyn.* **2016**, *3*, 043205.
(16) Fukui, K. A Formulation of the Reaction Coordinate. *J. Phys. Chem.* **1970**, *74*, 4161−4163.

DOI: 10.1021/acs.jctc.6b00800
J. Chem. Theory Comput. 2016, 12, 5698−5708

(17) Crehuet, R.; Bofill, J. M. The reaction path intrinsic reaction coordinate method and the Hamilton-Jacobi theory. *J. Chem. Phys.* **2005**, *122*, 234105.
(18) Gollub, C.; Kowalewski, M.; Thallmair, S.; de Vivie-Riedle, R. Chemoselective quantum control of carbonyl bonds in Grignard reactions using shaped laser pulses. *Phys. Chem. Chem. Phys.* **2010**, *12*, 15780.
(19) Miller, W. H.; Handy, N. C.; Adams, J. E. Reaction path Hamiltonian for polyatomic molecules. *J. Chem. Phys.* **1980**, *72*, 99.
(20) Yagi, K.; Taketsugu, T.; Hirao, K. Generation of full-dimensional potential energy surface of intramolecular hydrogen atom transfer in malonaldehyde and tunneling dynamics. *J. Chem. Phys.* **2001**, *115*, 10647.
(21) Giese, K.; Kühn, O. The all-Cartesian reaction plane Hamiltonian: Formulation and application to the H-atom transfer in tropolone. *J. Chem. Phys.* **2005**, *123*, 054315.
(22) Matanović, I.; Došlić, N.; Johnson, B. R. Generalized approximation to the reaction path: The formic acid dimer case. *J. Chem. Phys.* **2008**, *128*, 084103.
(23) Gonzalez, C.; Schlegel, H. B. Improved algorithms for reaction path following: Higher-order implicit algorithms. *J. Chem. Phys.* **1991**, *95*, 5853.
(24) Eckart, C. Some Studies Concerning Rotating Axes and Polyatomic Molecules. *Phys. Rev.* **1935**, *47*, 552.
(25) Kurtz, L.; Hofmann, A.; de Vivie-Riedle, R. Ground state normal mode analysis: Linking excited state dynamics and experimental observables. *J. Chem. Phys.* **2001**, *114*, 6151.
(26) Dymarsky, A. Y.; Kudin, K. N. Computation of the pseudorotation matrix to satisfy the Eckart axis conditions. *J. Chem. Phys.* **2005**, *122*, 124103.
(27) García, A. E. Large-Amplitude Nonlinear Motions in Proteins. *Phys. Rev. Lett.* **1992**, *68*, 2696−2700.
(28) Abseher, R.; Nilges, M. Efficient Sampling in Collective Coordinate Space. *Proteins: Struct., Funct., Genet.* **2000**, *39*, 82−88.
(29) David, C. C.; Jacobs, D. J. Principal component analysis: a method for determining the essential dynamics of proteins. *Methods Mol. Biol.* **2014**, *1084*, 193−226.
(30) Stein, S. A. M.; Loccisano, A. E.; Firestine, S. M.; Evanseck, J. D. In *Principal Components Analysis: A Review of its Application on Molecular Dynamics Data*; Spellmeyer, D. C., Ed.; Elsevier: Amsterdam, North Holland, Netherlands, 2006; Vol. 2; pp 233−262.
(31) Ruf, B. A.; Miller, W. H. A New (Cartesian) Reaction-path Model for Dynamics in Polyatomic Systems, with Application to H-atom Transfer in Malonaldehyde. *J. Chem. Soc., Faraday Trans. 2* **1988**, *84*, 1523−1534.
(32) Keefer, D.; Thallmair, S.; Zauleck, J. P. P.; Vivie-Riedle, R. D. A multi target approach to control chemical reactions in their inhomogeneous solvent environment. *J. Phys. B: At., Mol. Opt. Phys.* **2015**, *48*, 234003.
(33) Karlström, G.; Wennerström, H.; Jönsson, B.; Forsén, S.; Almlöf, J.; Roos, B. An Intramolecular Hydrogen Bond. Ab Initio MO Calculations on the Enol Tautomer of Malondialdehyde. *J. Am. Chem. Soc.* **1975**, *97*, 4188−4192.
(34) Isaacson, A. D.; Morokuma, K. Molecular Orbital Studies of Hydrogen Bonds. VIII. Malonaldehyde and Symmetric Hydrogen Bonding in Neutral Species. *J. Am. Chem. Soc.* **1975**, *97*, 4453−4457.
(35) Frisch, M. J.; Trucks, G. W.; Schlegel, H. B.; Scuseria, G. E.; Robb, M. A.; Cheeseman, J. R.; Scalmani, G.; Barone, V.; Mennucci, B.; Petersson, G. A.; Nakatsuji, H.; Caricato, M.; Li, X.; Hratchian, H. P.; Izmaylov, A. F.; Bloino, J.; Zheng, G.; Sonnenberg, J. L.; Hada, M.; Ehara, M.; Toyota, K.; Fukuda, R.; Hasegawa, J.; Ishida, M.; Nakajima, T.; Honda, Y.; Kitao, O.; Nakai, H.; Vreven, T.; Montgomery, J. A., Jr.; Peralta, J. E.; Ogliaro, F.; Bearpark, M.; Heyd, J. J.; Brothers, E.; Kudin, K. N.; Staroverov, V. N.; Kobayashi, R.; Normand, J.; Raghavachari, K.; Rendell, A.; Burant, J. C.; Iyengar, S. S.; Tomasi, J.; Cossi, M.; Rega, N.; Millam, J. M.; Klene, M.; Knox, J. E.; Cross, J. B.; Bakken, V.; Adamo, C.; Jaramillo, J.; Gomperts, R.; Stratmann, R. E.; Yazyev, O.; Austin, A. J.; Cammi, R.; Pomelli, C.; Ochterski, J. W.; Martin, R. L.; Morokuma, K.; Zakrzewski, V. G.; Voth, G. A.; Salvador, P.; Dannenberg, J. J.; Dapprich, S.; Daniels, A. D.; Farkas, O.; Foresman, J. B.; Ortiz, J. V.; Cioslowski, J.; Fox, D. J. *Gaussian 09*, revision A.02; Gaussian, Inc.: Wallingford, CT, 2009.
(36) Barbatti, M.; Granucci, G.; Ruckenbauer, M.; Plasser, F.; Crespo-Otero, R.; Pittner, J.; Persico, M.; Lischka, H. *NEWTON-X: a package for Newtonian dynamics close to the crossing seam*; 2013.
(37) Worth, G. A.; Burghardt, I. Full quantum mechanical molecular dynamics using Gaussian wavepackets. *Chem. Phys. Lett.* **2003**, *368*, 502−508.

DOI: 10.1021/acs.jctc.6b00800
J. Chem. Theory Comput. 2016, 12, 5698−5708

1.2 Nonlinear dimensionality reduction using an autoencoder

While linear dimensionality reduction schemes are simple and computationally inexpensive, the constructed linear subspaces are clearly inferior compared to their nonlinear counterparts [21–23]. This becomes clear in the example of reactions, where angular coordinates play an important role. Angular coordinates are nonlinear and in the case of a single angle, two linear coordinates are required to allow an exact reconstruction of all points along the angle. This requirement of a higher number of linear coordinates to achieve the same precision as nonlinear ones is pervasive throughout reactive molecular systems and the advantage of nonlinear dimensionality reduction has long been noted [23, 67, 85, 105, 106].

However, optimizing nonlinear subspaces is significantly more difficult, as the topography and possibly the topology enters as an additional optimization criterion. Generally, machine learning algorithms use a large number of full-dimensional data points to find these subspaces. There are several strategies to accomplish this, for example via methods that attempt to conserve the distances between close points in the full-dimensional space and thereby find a low-dimensional embedding like the Isomap algorithm [69] and the locally linear embedding [70]. These are usually most efficient when the data is in fact restricted to a few nonlinear degrees of freedom that are to be found. For these methods however, it might be difficult to deal with data with a bigger intrinsic dimensionality, because of the unavoidable reconstruction error associated with the additional degrees of freedom, which cannot be reconstructed and which enter as a type of noise [107, 108].

For the purposes of this section, the full-dimensional data points are created by MD calculations. Other than for a few exceptions, the active degrees of freedom of molecules in these calculations are not significantly restricted to a small number [23]. This makes noise resistant dimensionality reduction schemes more suited. One approach, which has been studied for its noise resistance, are autoencoders and will be used in the following [23, 25, 109]. This type of neural network employs a bottleneck structure in order to find a low-dimensional representation of the full-dimensional data as is outlined in fig. 1.2. Here, the example of the reconstruction of the coordinates x_i is used. As each of the five layers of nodes has to contain the approximate information of each input sample (a combination of the four coordinates x_i), the autoencoder is forced to find a two-dimensional representation of the 4-dimensional data.

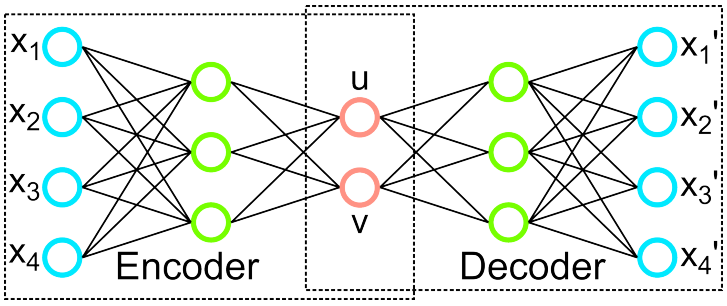

Figure 1.2: Schematic representation of a small autoencoder. Given samples with the coordinates x_i, the autoencoder creates a reconstruction of those coordinates as x_i' by finding a low-dimensional representation in the coordinates u and v.

The article "Constructing grids for molecular quantum dynamics using an autoencoder" published in *The Journal Chemical Theory and Computation* presents the steps necessary to automate the grid construction for QD using an autoencoder on the example of the proton transfer in (Z)-hydroxyacryloyl chloride. The key points of the article are:

- The setup and functionality of an autoencoder is explained using the example of molecular geometries. After a nonlinear subspace is found, a way to use the autoencoder to project points onto it is derived. This is used to project a grid in a linear subspace created using the PCA onto the nonlinear subspace discovered by the autoencoder. It is shown, how the

Wilson G-matrix formalism [30–32] can be used to construct a Hamiltonian for this grid to enable QD calculations.

- The generation of training data is illustrated. Generally, any kind of MD trajectory data that uses a similar subspace as would be expected for the QD can be used. A special case using the IRC as guidance is presented in detail. For this, a strategy is presented to only allow for MD trajectories to move perpendicular to the IRC. After starting many trajectory calculations from a number of different points along the IRC with a constant total energy, the generated trajectory data points can be used to train the autoencoder.

- These steps are applied to the example system of the proton transfer in (Z)-hydroxyacryloyl chloride. Three different grids are constructed using an autoencoder. Two of them are two-dimensional using a high and a low grid point density and the last one is three-dimensional. Dynamic calculations are performed on all three grids leading to similar results. The grids are shown to perform without notable unphysical behavior. Additionally, the nonlinear subspaces are compared to linear subspaces constructed using the PCA and it is shown that for the same accuracy three linear or two nonlinear degrees of freedom have to be used, emphasizing the quality of the approach.

In the following, the article "Constructing grids for molecular quantum dynamics using an autoencoder" published in *The Journal Chemical Theory and Computation* is reprinted with permission from *J. Chem. Theory Comput.* **14**, 52-62 (2018); The Supporting Information is reprinted in appendix A.

JCTC Journal of Chemical Theory and Computation Article
Cite This: J. Chem. Theory Comput. 2018, 14, 55−62 pubs.acs.org/JCTC

Constructing Grids for Molecular Quantum Dynamics Using an Autoencoder

Julius P. P. Zauleck and Regina de Vivie-Riedle*

Department Chemie, Ludwig-Maximilians-Universität München, D-81377 München, Germany

Supporting Information

ABSTRACT: A challenge for molecular quantum dynamics (QD) calculations is the curse of dimensionality with respect to the nuclear degrees of freedom. A common approach that works especially well for fast reactive processes is to reduce the dimensionality of the system to a few most relevant coordinates. Identifying these can become a very difficult task, because they often are highly unintuitive. We present a machine learning approach that utilizes an autoencoder that is trained to find a low-dimensional representation of a set of molecular configurations. These configurations are generated by trajectory calculations performed on the reactive molecular systems of interest. The resulting low-dimensional representation can be used to generate a potential energy surface grid in the desired subspace. Using the **G**-matrix formalism to calculate the kinetic energy operator, QD calculations can be carried out on this grid. In addition to step-by-step instructions for the grid construction, we present the application to a test system.

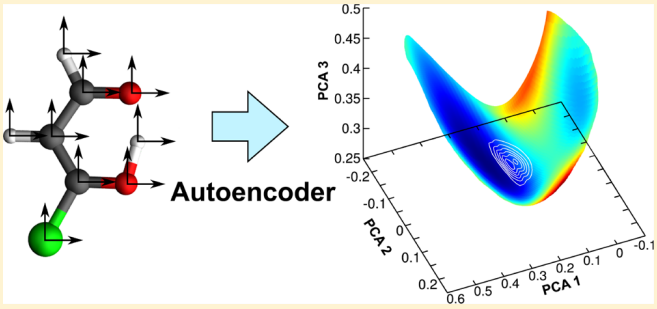

INTRODUCTION

The search for an efficient basis probably remains as the central challenge in molecular wavepacket quantum dynamics (QD). Several different approaches have been developed, each with its most efficient field of application. They all, in one way or another, have to deal with the exponential growth of their basis and therefore scaling of computation time with the number of degrees of freedom. The probably most successful approach, the multiconfiguration time-dependent Hartree method,[1,2] finds a powerful basis while requiring the potential part of the Hamiltonian to take on a certain form. This is highly efficient for many systems but in cases where the wave function moves far away from potential minima, like in reactive scenarios, grid-based approaches that are restricted to fewer degrees of freedom can be more practical. In this case, choosing the degrees of freedom of a subspace that best describe the reaction is one of the most important steps to produce reliable predictions. Though we recently presented two ways to automate the search for linear subspaces,[3] the identification of even more powerful nonlinear subspaces is still to a large degree driven by intuition. In this work we present an approach to automate this identification based on the data produced by trajectory calculations, replacing human intuition by a machine learning algorithm.

The search for nonlinear subspaces is generally much more difficult than for linear ones. For them a mathematical tool exists to extract the dimensions of biggest variance of a data set, namely, the principal component analysis. For a nonlinear generalization, the shape of the subspace now enters as an additional optimization task and there is no exact mathematical solution. Nevertheless, there are a number of approximate solutions that have gained popularity in recent years and many of them have been applied to molecular problems.[4−11] These methods can all be summarized with the concept of nonlinear dimensionality reduction. Due to its demonstrated efficiency for molecular data[4] as well as the promising prospect of further development,[12,13] we chose to use an autoencoder, a type of neural network, for our problem.

Neural networks have been extensively applied to the direct calculation of potential energy surface (PES)s in the last few decades and have signficantly improved the system sizes that can be described.[14−27] In our case, we use an autoencoder to learn a low-dimensional representation of a reaction, in which we then calculate a PES. For this, an autoencoder takes high-dimensional input in the form of data points corresponding to molecular geometries and finds a low-dimensional embedding that describes them well. We can then use this embedding to extract reactive coordinates and to span a grid, on which the time-dependent Schrödinger equation can be solved. Using trajectories is one way to generate input data points to train the autoencoder. Although these will generally miss the quantum effects we wish to include, they still can give meaningful information about the parts of molecular configuration space used to describe the reaction.

Once the grid in the desired subspace is created, the PES can be calculated for each grid point, completing the potential part of the Hamiltonian. Constructing the kinetic energy operator is more complicated, but the **G**-matrix formalism[28] that has

Received: October 12, 2017
Published: December 13, 2017

DOI: 10.1021/acs.jctc.7b01045
J. Chem. Theory Comput. 2018, 14, 55−62

proven useful for QD in reactive coordinates[29−31] can be applied here, too.

In the following section the construction, training and use of the autoencoder describing the subspace will be explained in detail. This includes the construction of a training data set from a chosen set of trajectories and a step-by-step explanation how to construct a grid that is ready for QD simulations. For completeness, we also give a short overview over the **G**-matrix formalism. Thereafter an application to the example system of the proton transfer in (*Z*)-hydroxyacryloyl chloride is presented. Our approach will be explained in detail using the example of a pseudospectral grid representation, making use of the fast Fourier transform on rectangular grids.[32] However, it is generally applicable for any scenario where a set of nonlinear coordinates is needed and a data set of trajectory points can be created that is approximately contained in those coordinates.

METHODOLOGY

There are several approaches to find a nonlinear subspace in the context of molecular dynamics. For grid-based QD this is often referred to as the search for reactive coordinates and we will refer to the nonlinear subspace in which the QD is performed as reactive coordinates throughout this work. Although there exist a few approaches like **Z**-matrix coordinates or Jacobi coordinates that are straightforward and describe some chemical reactions relatively well using very few coordinates, often linear combinations of them are more efficient.[33−35] Finding those combinations is mostly driven by experience and intuition and even then, there are many cases where the reactive coordinates best suited are simply of a more general kind. This behavior can already be observed in the intrinsic reaction coordinate (IRC) for a chemical transformation. The IRC rarely consists of a single linear combination of *Z*-matrix or Jacobi Coordinates and arguably are very close to the best one-dimensional subspace to describe a reaction.

As a result, our goal is to find a generalization that can recreate the aforementioned special cases of reactive coordinates as well as the IRC, but that is also not limited to any specific form. We will present such an approach using an autoencoder. In the molecular context we usually think of a reactive coordinate as a change of relative orientations of atoms. As we search for a generalized nonlinear subspace, these relations between the atoms become less intuitive, because we do not bias the algorithms toward our intuitions. Although the autoencoder will generate a number of "raw" reactive coordinates that span the subspace, they will usually be overly nonlinear and thus not very useful for understanding molecular motions or creating a PES grid. However, we will be left with a mapping between the subspace and the full-dimensional configuration space and vice versa. These mappings will then allow us to project configuration points onto the subspace and in turn give us the ability to create a PES spanned by more useful reactive coordinates.

In the next section, we will introduce the setup and functionality of an autoencoder in some detail to ensure comprehensibility for readers that are less familiar with the topic.

Autoencoder. The growth of computer performance and the development of new algorithms have caused an explosion in the applicability of machine learning methods. Probably, the recently most influential methods come from the field of artificial neural networks and an important type of neural networks are autoencoders.

Figure 1 illustrates the setup of an autoencoder on the example of molecular configurations, including restricted

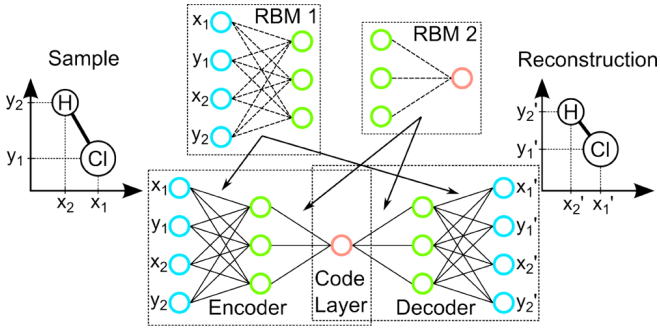

Figure 1. Schematic of an autoencoder reproducing molecular configurations of hydrochloric acid. Each Cartesian coordinate of each atom is represented by an input node. The restricted Boltzmann machines' (RBMs') architectures are chosen according to the autoencoder's. Their weights (here shown as dashed connections) can then be used as initial weights for the autoencoder.

Boltzmann machines (RBMs) used for pretraining, which will be shortly introduced in the following. If each Cartesian coordinate of the shown molecule is represented by an input node and the autoencoder architecture bottleneck is made of a single node, one can use the autoencoder to reproduce molecular geometries according to their interatomic distances. Here we refer to the number of layers of the network with their respective numbers of nodes as the architecture. In our case, autoencoders consist of an encoder and a decoder, where the encoder has an input layer of nodes, zero or more hidden layers (green nodes in Figure 1) and a layer of output nodes that represent the code (red). The decoder takes this code layer as input, has the same number of hidden layers with the same numbers of nodes as the encoder in opposite order and has an output layer with the same number of nodes as the input layer of the encoder. With respect to the complete autoencoder, coming from the input layer, all nodes of a following layer i starting with $i = 1$ take the function values $\mathbf{z}_{i-1}$ of the nodes of the previous layer $i - 1$ as variables $\mathbf{x}_i$ to calculate their function values $\mathbf{z}_i$:

$$\mathbf{z}_i = \sigma_i(\mathbf{W}_i\mathbf{x}_i + \mathbf{b}_i) \quad \text{with} \quad \mathbf{x}_i = \mathbf{z}_{i-1} \tag{1}$$

These in turn becomes the input arguments of the next layer. In the example of Figure 1, $\mathbf{x}_1$ corresponds to the Cartesian coordinates of the sample geometries and $\mathbf{z}_4$ corresponds to the Cartesian coordinates of the reconstructed geometries. Given an input vector with P dimensions $\mathbf{W}_i$ is a weight matrix of dimensionality $Q \times P$ and $\mathbf{b}_i$ a bias vector of dimensionality P, producing an output vector with Q dimensions. $\sigma_i(\mathbf{u})$ is an element-wise activation function of $\mathbf{u}$ introducing nonlinearity between the layers. In our examples σ_i will always be the logistic function $\sigma_{i,l}(\mathbf{u}) = 1/(1 + \exp(\mathbf{u}_l))$ except for the calculation of the output layer of the encoder, i.e., the code layer, for which it will be the identity function. Here the lth element of the output vector is calculated from the lth element of the input vector. The autoencoder can be trained by providing a sufficiently large number of input samples and correcting weights and biases so the input samples are better reproduced.

DOI: 10.1021/acs.jctc.7b01045
J. Chem. Theory Comput. 2018, 14, 55−62

However, for practical autoencoders with many hidden layers training can be difficult when the initial weights and biases are not close to a good solution. It has been demonstrated that finding such initial weights can be done by layer-by-layer pretraining using a RBM.[36] A RBM consists of a visible and a hidden layer and learns a probability distribution over its possible inputs (in the visible layer) by calculating gradients of its weights and biases to increase the probabilities of the input samples. These weights and biases can be initialized with normal distributions and zero values, respectively. After the set of activations of the hidden layer corresponding to the set of input samples is trained, they can be used to train the next RBM. If the architectures of the RBMs are chosen according to the architecture of the autoencoder, the weights and biases of the RBMs can be used as the initial weights and biases of the respective layers of the encoder and decoder. After this, the complete autoencoder can be trained by calculating the gradients of the weights and biases to produce more accurate results using the chain rule, which is known as back-propagation.[37] This is equivalent to minimizing the mean reconstruction error $\frac{1}{N}\sum_k^N ||\mathbf{x}_1^k - \mathbf{z}_{M+1}^k||$ given N training samples, M hidden layers, and subscript 1 representing the input layer. Here, the superscript index k is not to be mistaken for an exponent. For the example given in Figure 1, this corresponds to the distance vectors between the sampled and reconstructed Cartesian coordinates of the atoms. In this work, we used a version of conjugate gradient to minimize the reconstruction error with a modified version of the code provided by Hinton et al.[36] The training steps in machine learning are usually counted in epochs, where one epoch refers to a machine training over the whole set of training data once.

Once successfully trained, the final weights and biases are determined and the autoencoder can approximately reproduce input data in its output layer. This allows us to choose a bottleneck architecture where the code layer of the autoencoder only has very few nodes, equaling the number of degrees of freedom aimed for. In this case, the autoencoder learns an approximate reconstruction of the learning data using the number of variables equal to the number of nodes in the code layer. We can use this approximate reconstruction to create an approximate projection of full-dimensional data points onto the low-dimensional subspace defined by the code layer and then refine this projection iteratively using the decoder part of the autoencoder.

To obtain the refined projection, we can start with two mappings between the full-dimensional space and the subspace best describing the training data points. These are similar to the encoder and decoder but behave optimally in a way that will be described in the following. The first mapping $\mathbf{y}' = \mathbf{F}(\mathbf{y})$ takes a full-dimensional vector $\mathbf{y}$ as input and returns a vector $\mathbf{y}'$ with the dimensionality of the subspace as output. The second, inverse mapping $\mathbf{y}'' = \mathbf{H}(\mathbf{y}')$ takes such a vector of subspace dimensionality as input and returns a full-dimensional vector $\mathbf{y}''$. Let these two mappings with $\mathbf{y}'' = \mathbf{H}(\mathbf{F}(\mathbf{y}))$ have optimal behavior in the sense that if a full-dimensional vector $\mathbf{y}$ lies within the subspace, then $\mathbf{y}'' = \mathbf{y}$ and that if $\mathbf{y}$ does not lie within the subspace, the distance $||\mathbf{y}'' - \mathbf{y}||$ is the smallest possible for the subspace. We can then use the encoder $\tilde{\mathbf{F}}$ and the decoder $\tilde{\mathbf{H}}$ as approximations of $\mathbf{F}$ and $\mathbf{H}$, respectively.

To use them for a refined projection, we apply the autoencoder first to produce an approximate projection $\tilde{\mathbf{y}}'' = \tilde{\mathbf{H}}(\tilde{\mathbf{y}}') = \tilde{\mathbf{H}}(\tilde{\mathbf{F}}(\tilde{\mathbf{y}}))$. Then, we construct a set of basis vectors $\mathbf{a}_j$ by changing the activation of every individual node j of the coding layer starting from $\tilde{\mathbf{y}}'$:

$$\mathbf{a}_j = \tilde{\mathbf{H}}(\tilde{\mathbf{y}}' + \varepsilon\mathbf{e}_j) - \tilde{\mathbf{H}}(\tilde{\mathbf{y}}') \tag{2}$$

Here, $\mathbf{e}_j$ is the jth standard basis vector and ε determines the length of the vector. ε should be chosen small to ensure a local basis with respect to $\tilde{\mathbf{y}}'$ using the decoder. Because the initial projection is approximate, the distance $||\tilde{\mathbf{H}}(\tilde{\mathbf{y}}') - \mathbf{y}||$ has generally not reached a local minimum regarding variations in $\tilde{\mathbf{y}}'$. If the corresponding distance vector is projected onto the basis vectors $\mathbf{a}_j$, this minimum can be found iteratively. Using the nonorthonormal projection matrix $\mathbf{A} = [\mathbf{a}_1\, \mathbf{a}_2 \cdots \mathbf{a}_S]$, with S being the number of dimensions of the coding subspace, the first step in the subspace is given by

$$\tilde{\mathbf{y}}_1' = \tilde{\mathbf{y}}' + h\varepsilon(\mathbf{A}^T\mathbf{A})^{-1}(\mathbf{y} - \tilde{\mathbf{H}}(\tilde{\mathbf{y}}'))^T\mathbf{A} \tag{3}$$

and the next steps are given by

$$\tilde{\mathbf{y}}_k' = \tilde{\mathbf{y}}_{k-1}' + h\varepsilon(\mathbf{A}^T\mathbf{A})^{-1}(\mathbf{y} - \tilde{\mathbf{H}}(\tilde{\mathbf{y}}_{k-1}'))^T\mathbf{A} \tag{4}$$

The step size h could be set to 1 to progress through the full projection, but because the procedure is iterative, the subspace is nonlinear and the projection is approximate, a smaller h is suggested. A derivation of eqs 3 and 4 can be found in the Supporting Information.

Training Data Generation. To learn the representation of a subspace, the autoencoder is trained on equally distributed data points over the subspace region that will be used for QD calculations. There are many example systems and therefore many different ways to produce the training data set. One general way is to use trajectories to simulate the same process as is going to be simulated using QD and we will exclusively focus on trajectory-based approaches.

For this to work as intended, two criteria must be met. First, the lack of the quantum effects should not have such an impact that the trajectories explore a very different subspace. This is related to a very common problem for grid-based wavepacket QD. Because the motion of the wavepacket is not known beforehand, a guess has to be made to create a grid. In general, trajectories are a good basis for such a guess. It is also possible to incorporate other information on the path, the wavepacket will follow, as we will demonstrate with our example system. Second, the data set should not have very disjoint reaction pathways spanned by different degrees of freedom for the reactions studied. This might result in regions of the subspace located between those pathways that would have to be described without available learning data. However, scenarios where this happens are generally costly for grid-based QD due to the increase in required dimensions and the distinct pathways could in such cases be studied individually. Additionally, this problem could be circumvented using appropriate grids that allow for the corresponding splitting of the wave function. As a result, this generally does not limit the applicability of our approach.

We chose to present a way to create a subspace for reactive QD using trajectories started from the IRC. There are two reasons for this decision. First, this will create an excellent test scenario for our approach, and second, the IRC is one of the most easily available sources of information about a system. A reasonable requirement for the subspace is to capture the curvature of the IRC and to additionally include degrees of freedom with a shallow PES, to allow the wavepacket the most

DOI: 10.1021/acs.jctc.7b01045
J. Chem. Theory Comput. 2018, 14, 55−62

Journal of Chemical Theory and Computation Article

room to move and diverge. Note that in the case of additional critical points one wishes to include, additional trajectory starting points could be included. Staying with the IRC starting points will also provide an important test how well the autoencoder will solve this task. In general, the number of degrees of freedom with a shallow PES is still bigger than the number of reactive coordinates we wish to extract. Therefore, all additional degrees of freedom with a shallow PES that are discarded provide notable noise, because the trajectories will explore them nearly as much as the degrees of freedom that can be included. This will provide an inherent test of the noise resistance of the autoencoder.

To generate data points that enable us to extract the desired subspace, we cannot simply let trajectories run along the IRC, because they will follow its descent and not explore the space orthogonal to it. By incorporating a constraint algorithm like RATTLE,[38] we can restrict the motion along a certain direction. Now, the data points can be produced by choosing equispaced points along the IRC and running a number of trajectories from each point while freezing the motion along the IRC. Because these constraints are of a fairly general kind, they can introduce spurious rotations and translations, which must be avoided by enforcing the Eckart conditions[28,39] for the positions and velocities of the atoms at every time step with reference to the starting point of the trajectory. For the trajectories to explore the configuration space efficiently, they can be randomly initialized with momentum orthogonal to the IRC. Trajectories along degrees of freedom with a shallow PES will run farther and will be better reconstructed by the autoencoder. We suggest a fixed kinetic energy about the size of the activation energy of the reaction. This will help to ensure the construction of a binding PES orthogonal to the IRC. As an illustration, Figure 2 shows a projection of trajectory data points (corresponding to different geometries) produced by the described procedure together with the IRC. For visualization we projected the points on the first two principal components created by a principal component analysis (PCA) of the trajectory data points.

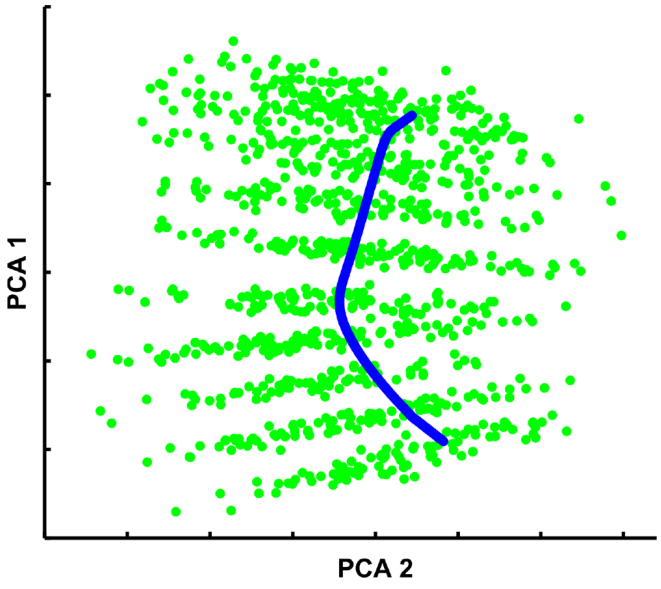

Figure 2. IRC (blue) and training data points (green) projected onto the first two principal components. Even though the IRC is curved in more than three dimensions, the frozen motion of the trajectories parallel to the IRC at their starting point is clearly visible. Every separate slice of points represents trajectory points from their central IRC starting point. The topmost points are in this projection not separable anymore, because the IRC has larger components orthogonal to the first two principal components.

Because we ideally want an equispaced data set, some points of the trajectories starting from the same starting point have to be discarded. This can be done by defining a minimum full-dimensional Euclidean distance between the data points generated and removing all data points that are closer than this distance to any preceding data point. We can use the number of retained points as a function of the number of screened data points to check for convergence. After many trajectory calculations it would be expected that there are only very few new points that are far enough away from all previous points. An example of this trend is shown in Figure 3.

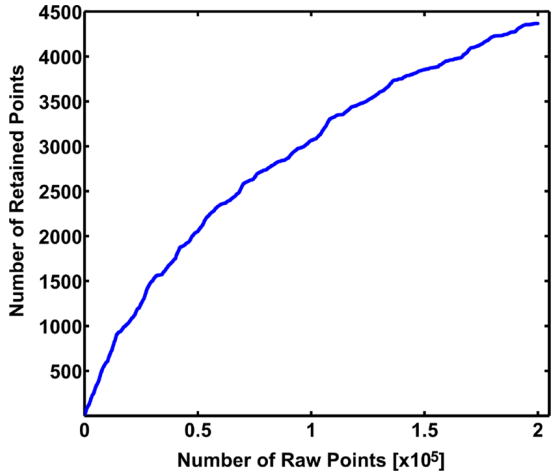

Figure 3. Convergence behavior of the number of retained data points for a single starting point. A point qualified to be retained for the training data set, when it was not closer than a certain threshold to any other retained point. Because there is only a limited configuration space to explore with a fixed amount of energy, the number of retained points converges.

All data points from every IRC starting point are then rescaled so that all components of every input vector lie between 0 and 1. In principal, this data set would be sufficient to train the autoencoder. However, in addition to the pretraining using RBMs it is useful and simple to create a pretraining data set with which to train the RBMs and the autoencoder first. Thereafter we proceed to training the autoencoder on the actual data set. The pretraining data set can be generated by performing a PCA on the actual data set. The number of principal components used equals the number of degrees of freedom of the desired subspace. For each principal component the Cartesian coordinate with the biggest contribution is chosen. These now span a linear Cartesian subspace of the same dimensionality as the desired subspace for the QD calculation and a random distribution of samples with equal variance along all of those Cartesian coordinates is created. These geometry samples thus only vary within the selected Cartesian coordinates. Because the variance along all degrees of freedom is identical and because only a minority of input nodes are required, this is significantly easier to learn. It is also a good starting point, because an overly curved subspace can lead to unphysical results in the QD simulations. As we move to the actual data set during training, additional atomic

DOI: 10.1021/acs.jctc.7b01045
J. Chem. Theory Comput. 2018, 14, 55−62

coordinates and nonlinearities will be introduced until the autoencoder converges.

Grid Construction and G-Matrix. Once we have successfully trained the autoencoder, we have all information about the subspace, but we still have to construct a practical grid. There are several possible approaches to do this. A general strategy is to choose a subspace in which a rectangular grid is easily constructed and that is similar to the subspace found by the autoencoder (see below). The points of the rectangular grid of the simple subspace can then be projected onto the autoencoder subspace. Because we want to use the **G**-matrix formalism for the kinetic energy operator, we have to identify the reactive coordinates of the projected grid. Here, we will first give a short introduction to the **G**-matrix formalism whereas a more extensive presentation can be found in the literature[28,29,40] and thereafter we introduce the grid construction.

Using the **G**-matrix **G**, the kinetic energy operator $\hat{T}_{\mathbf{q}}$ in reactive coordinates **q** is given by

$$\hat{T}_{\mathbf{q}} = -\frac{\hbar^2}{2}\sum_{r=1}^{N_q}\sum_{s=1}^{N_q}\frac{\partial}{\partial q_r}\left[\mathbf{G}_{rs}\frac{\partial}{\partial q_s}\right] \tag{5}$$

G can be calculated via its inverse, whose elements $(\mathbf{G}^{-1})_{rs}$ are given by

$$(\mathbf{G}^{-1})_{rs} = \sum_{i=1}^{3N_{at}} m_i \frac{\partial x_i}{\partial q_r}\frac{\partial x_i}{\partial q_s} \tag{6}$$

The sums in eq 5 run over the number of reactive coordinates that are included in the QD calculation N_q and the sum in eq 6 runs over the number of Cartesian coordinates of all atoms N_{at}. As the masses of the atoms m_i are included in it, the **G**-matrix can be considered a position-dependent reciprocal mass that introduces the necessary coupling between the reactive coordinates. Equation 5 is valid under the assumption that the Jacobian determinant of the coordinate transformation is coordinate independent. As a result, it is good practice to keep the volume change of the reactive coordinates approximately constant with respect to the Cartesian coordinates. The projected grids generally fulfill this reasonably well. Besides that, the reactive coordinates the **G**-matrix can use are very general and as long as we can identify any consistent relation between the change in reactive coordinates and the ordering of the grid points, we can calculate the kinetic energy operator. Because we are focusing on rectangular grids, we can simply assign an reactive coordinate q_r for each direction of our grid and choose arbitrary bounds, e.g., [0, 1].

To construct a rectangular grid to be projected, the PCA can be used again. The principal components of the trajectory training data set can be identified as the directions of a rectangular grid in a linear subspace. The spacing between the grid points should be chosen according to the maximum kinetic energy that has to be represented along all directions on the grid. Using the **G**-matrix of the PCA-based grid, the spacing Δq_r along the different directions q_r should be

$$\Delta q_r < \pi\sqrt{\frac{G_{rr}}{2T_r}} \tag{7}$$

Here, T_r is the kinetic energy along the direction of the rth coordinate that has to be representable. A derivation of eq 7 can be found in the Supporting Information. In practice, the activation energy gives a good idea of the maximum kinetic energy along the reaction coordinate and some value like half or less of the minimum required spacing is chosen. The number of grid points in each direction is then decided by the critical points that have to be included and by the extension of the PES necessary to prevent the wave function from reaching the edges of the grid.

Once the PCA-based rectangular grid is determined, the points can be projected onto the subspace using the autoencoder $\tilde{\mathbf{H}}(\tilde{\mathbf{F}}(\mathbf{y}))$ and eqs 3 and 4. Because every grid point corresponds to a molecular configuration, the PES can be calculated using quantum chemistry methods and **G** can be calculated via finite differences using adjacent grid points and eq 6. The starting wavepacket can be created as in any other grid-based calculation depending mostly on the studied reaction.

EXAMPLE SYSTEM: (*Z*)-HYDROXYACRYLOYL CHLORIDE

We tested our method on the proton transfer reaction in (*Z*)-hydroxyacryloyl chloride. This is an asymmetric variant of the proton transfer in malondialdehyde,[41] where one of the terminal carbon atoms' hydrogen is substituted with chlorine (Figure 4). The protonation of the oxygen on the far side of the chlorine is much more stable. We decided to study the reconstruction of the IRC of this system. Because, for that, this system requires about two to three degrees of freedom to be appropriately described,[3] we created a two-dimensional and a three-dimensional grid on which QD calculations were performed. The number of nodes per layer of the autoencoder used were 18−25−15−7−2 and 18−25−15−7−3. There are 18 input nodes because the model system is planar and nearly stays so during the reaction and has 9 atoms, resulting in 18 degrees of freedom. The data set was created by calculating the IRC with the program package Gaussian09[42] at the DFT (M06-2X,6-31G(d)) level of theory and picking 10 equispaced points. From each point 100 trajectories were started with 2000 time steps of 0.5 fs using the program package NEWTON-X 1.4.,[43] where the gradients were calculated at HF/6-31G(d) level. This was sufficient for the trajectories because they only have to explore the configuration space. Each trajectory was initialized with a randomly directed momentum corresponding to a kinetic energy of 0.345 eV, which is approximately equal to the activation energy of the reaction. All motion parallel to the IRC was removed using

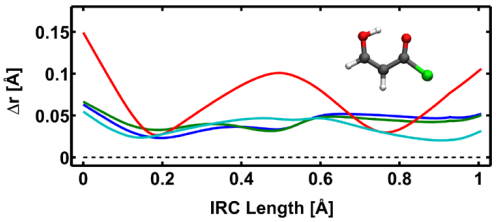

Figure 4. Distances between projected IRCs and the full-dimensional one. The blue and green curves represent projections on 2- and 3-dimensional nonlinear subspaces, respectively. These were created by training the autoencoder on the trajectory data sets. The red and cyan curves represent projections on 2- and 3-dimensional linear subspaces, respectively. These were created using the first two or three principal components of the same data set used for the autoencoders. (*Z*)-Hydroxyacryloyl chloride is shown in the upper right.

DOI: 10.1021/acs.jctc.7b01045
J. Chem. Theory Comput. 2018, 14, 55−62

RATTLE. These two million data points resulted in 38 564 training samples after enforcing a minimum distance of 0.087 Å. The two-dimensional and three-dimensional pretraining data sets consisted of 2166 and 9291 training samples, respectively. For each of the three training data sets, a set consisting of 2000 independent test samples was used.

The RBMs and autoencoders were trained using data in batches of 2000 samples from the three training sets and the number of epochs of training were 50 for the RBMs, 2000 for the autoencoder learning the pretraining data set, and 1000 for the autoencoder learning the actual data set. After the 2000 epochs on the pretraining data set, the two-dimensional and three-dimensional autoencoders reproduced the data points with an average error of 0.1056 and 0.1319 Å, respectively. The reconstruction of the actual data points after 1000 epochs led to an error of 0.1590 and 0.1511 Å, respectively. However, projecting the data points using eqs 3 and 4 lead to more precise reconstructions as can be seen by the deviation of the projected IRCs from the full-dimensional one shown in Figure 4.

Because we used trajectory data points to construct these two autoencoder subspaces, it would not be expected that any low-dimensional projection would reconstruct the IRC exactly. However, we would expect that, as long as an increase in dimensionality is very beneficial for the description, the distance of projected IRCs would decrease significantly. We see this decrease between the projections onto 2-dimensional (red) and 3-dimensional (cyan) linear subspaces in Figure 4. The distances of the nonlinear projections (blue and green) do not differ significantly from the projection onto the 3-dimensional linear subspace. A likely explanation is that two nonlinear or three linear coordinates capture most relevant motions. After this, the description only slowly improves with increasing dimensionality. The most important result is the decrease of distance between the two-dimensional linear subspace (red) and the two-dimensional nonlinear subspace (blue). This clearly shows that our method finds a much better subspace for the reconstruction of the IRC. Given the lack of significant further decrease with increase of dimensionality, this nonlinear two-dimensional subspace might even capture all of the significant motions of the reaction.

Using the autoencoders and eq 7 PES grids of sizes 48 × 17 and 48 × 17 × 24 were constructed as well as a grid of size 100 × 100 for comparison and visualization at the DFT (M06-2X,6-31G(d)) level of theory. A projection of the 2-dimensional nonlinear subspace PES onto the space spanned by the first three principal components is shown in Figure 5. One can see the curvature of the subspace as well as the double minimum structure with the transition state lying inbetween. For this test scenario, a Gaussian wavepacket starting near the transition state was propagated in 500 time steps with a step size of about 0.24 fs using the Chebychev propagation scheme.[44] During this time, the wavepacket reached the minimum and was reflected, as can be seen for the two-dimensional case in Figure 6. The cycle period inside the lower potential well of about 70 fs is approximately half of the cycle period for the full proton transfer of about 120 fs[45] as would be expected. Overall, the propagation in the 2- and 3-dimensional cases did not differ from the ones on more traditional grids in terms of stability or conservation of total energy or norm. The wavepacket ran along the reaction path and showed no unphysical behavior and the time scales of the nuclear motion

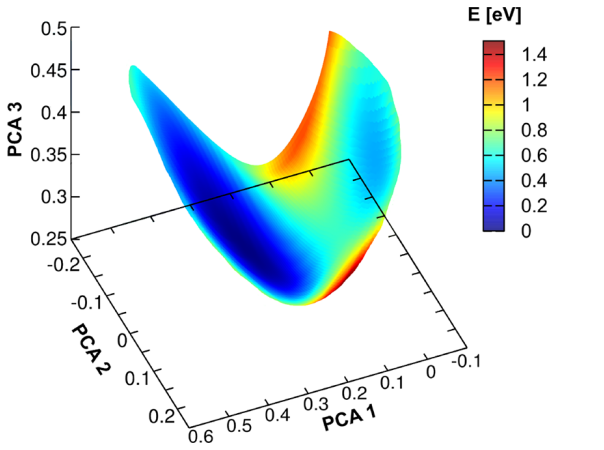

Figure 5. Projection of the two-dimensional potential energy surface generated by our method onto the first three principal components of the training data set. The PCA coordinates are given in relative units. Because all three PCA coordinates contribute significantly to the data set and the IRC, the surface is strongly curved. The depth of the PES is given by color and is not related to the spatial dimensions. It shows the double minimum potential structure typical for derivatives of malondialdehyde. This projection is analogous to an angle coordinate projected onto its x and y components, resulting in a circle, on which a color-coded potential could be represented.

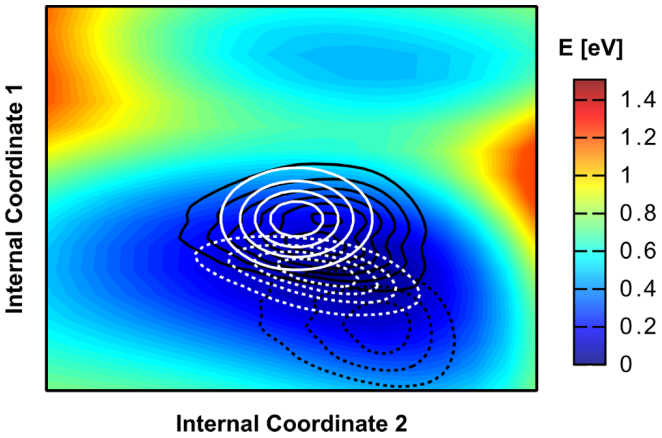

Figure 6. Wavepacket propagation in two reactive coordinates. The PES is shown on a rectangular grid of nonlinear reactive coordinates, constructed using an autoencoder. The wavepacket propagation is shown in snapshots at 0 fs (solid white), 17 fs (dashed white), 31 fs (dashed black), and 68 fs (solid black). The wavepacket travels through the deeper potential minimum and is being reflected.

are consistent with the time scales of the keto−enol switching in malondialdehyde.[46]

SUMMARY AND DISCUSSION

We presented a method for automated nonlinear dimensionality reduction for reactive molecular systems. It uses an autoencoder trained on trajectory data points to create a low-dimensional representation of reactive coordinates. With this approach, trajectories that describe the space of the studied reaction sufficiently well offer a good basis for QD calculations. The autoencoder is able to find a low-dimensional subspace that is close to the configuration space used by the trajectories. We presented all the steps necessary to create the data sets needed, to train the autoencoder and to use it to construct a QD grid by projecting points onto the low-dimensional

DOI: 10.1021/acs.jctc.7b01045
J. Chem. Theory Comput. 2018, 14, 55−62

Journal of Chemical Theory and Computation Article

subspace. To use this grid, we gave a short overview of the G-matrix formalism that is useful to construct a kinetic energy operator for this general type of coordinates.

These steps were then applied to our example system (Z)-hydroxyacryloyl chloride. The high quality of the resulting autoencoder subspaces was demonstrated by their proximity to the IRC. The QD calculations on the resulting grids performed well, without any noticeable unphysical behavior or significant conservation errors in total energy or norm.

There are a few straightforward next steps that could be very beneficial. The first is the application of this method to other systems. There is a huge range of applicable scenarios, but one field that seems especially promising is the laser steering of reactions or optimal control theory as it strongly relies on quantum effects. Classical molecular dynamics can be used to find individual laser pulses that steer reactions for very specific starting conditions and paths, but the pulses differ a lot from each other. However, it is likely that the configuration space used by the individual trajectories is a good predictor for high-quality reactive coordinates used in QD calculations. Thus, this might be an important step to automate the search for efficiently steering laser pulses in complex molecular systems.

Another step is the improvement of the grid creation strategy. Although we are confident that the discovered subspaces are generally of high quality, the projection of a grid in a linear subspace onto the nonlinear subspace might result in very unevenly spaced grid points for highly curved degrees of freedom. However, this problem seems very solvable by developing iterative grid construction algorithms. There are also a number of possible steps to refine the method. For example, it might sometimes be relevant that critical points in the reactive systems are included exactly in the subspace. This might be solved by different kinds of local or global shifts of the created subspace grid in the full configuration space.

Overall, we see our method as very consequential for grid-based approaches. It allows the use of the best affordable trajectory method for a system to identify a very representative subspace in which higher level QD calculations can be performed. Assuming that the number of degrees of freedom involved in a reaction does not grow linearly with the total number of degrees of freedom but has an upper limit, this also offers a way to beat the usual exponential scaling of QD descriptions. In the best case, an implementation could be found that scales roughly linearly with the size of the system, given the existing linear scaling quantum chemistry algorithms and regularization methods for autoencoders. Additionally, the application prospects and the room for simple extensions are very promising.

■ ASSOCIATED CONTENT

Supporting Information

The Supporting Information is available free of charge on the ACS Publications website at DOI: 10.1021/acs.jctc.7b01045.

Short derivation of the iterative projection given by eqs 3 and 4 as well as the derivation of the maximum distance between neighboring grid points as given in eq 7 (PDF)

■ AUTHOR INFORMATION

Corresponding Author

*R. de Vivie-Riedle. E-mail: regina.de_vivie@cup.uni-muenchen.de.

ORCID

Regina de Vivie-Riedle: 0000-0002-7877-5979

Notes

The authors declare no competing financial interest.

■ ACKNOWLEDGMENTS

Financial support by the Deutsche Forschungsgemeinschaft through the SFB749 and the excellence cluster Munich-Centre for Advanced Photonics (MAP) is acknowledged.

■ REFERENCES

(1) Meyer, H.-D.; Manthe, U.; Cederbaum, L. S. The multi-configurational time-dependent Hartree approach. *Chem. Phys. Lett.* **1990**, *165*, 73−78.

(2) Meyer, H.-D.; Worth, G. A. Quantum molecular dynamics: propagating wavepackets and density operators using the multi-configuration time-dependent Hartree method. *Theor. Chem. Acc.* **2003**, *109*, 251−267.

(3) Zauleck, J. P. P.; Thallmair, S.; Loipersberger, M.; de Vivie-Riedle, R. Two New Methods To Generate Internal Coordinates for Molecular Wave Packet Dynamics in Reduced Dimensions. *J. Chem. Theory Comput.* **2016**, *12*, 5698.

(4) Brown, W. M.; Martin, S.; Pollock, S. N.; Coutsias, E. A.; Watson, J.-P. Algorithmic dimensionality reduction for molecular structure analysis. *J. Chem. Phys.* **2008**, *129*, 064118.

(5) Roweis, S. T.; Saul, L. K. Nonlinear Dimensionality Reduction by Locally Linear Embedding. *Science* **2000**, *290*, 2323−2326.

(6) Tenenbaum, J. B.; de Silva, V.; Langford, J. C. A Global Geometric Framework for Nonlinear Dimensionality Reduction. *Science* **2000**, *290*, 2319−2323.

(7) Das, P.; Moll, M.; Stamati, H.; Kavraki, L. E.; Clementi, C. Low-dimensional, free-energy landscapes of protein-folding reactions by nonlinear dimensionality reduction. *Proc. Natl. Acad. Sci. U. S. A.* **2006**, *103*, 9885.

(8) Nguyen, P. H. Complexity of Free Energy Landscapes of Peptides Revealed by Nonlinear Principal Component Analysis. *Proteins: Struct., Funct., Genet.* **2006**, *65*, 898−913.

(9) Antoniou, D.; Schwartz, S. D. Towards identification of the reaction coordinate directly from the transition state ensemble using the kernel PCA method. *J. Phys. Chem. B* **2011**, *115*, 2465−2469.

(10) Amadei, A.; de Groot, B. L.; Ceruso, M.-A.; Paci, M.; Di Nola, A.; Berendsen, H. J. C. A Kinetic Model for the Internal Motions of Proteins: Diffusion Between Multiple Harmonic Wells. *Proteins: Struct., Funct., Genet.* **1999**, *35*, 283−292.

(11) Mansbach, R. A.; Ferguson, A. L. Machine learning of single molecule free energy surfaces and the impact of chemistry and environment upon structure and dynamics. *J. Chem. Phys.* **2015**, *142*, 105101.

(12) Vincent, P.; Larochelle, H.; Lajoie, I.; Bengio, Y.; Manzagol, P.-A. Stacked Denoising Autoencoders: Learning Useful Representations in a Deep Network with a Local Denoising Criterion. *J. Mach. Learn. Res.* **2010**, *11*, 3371−3408.

(13) Sankaran, A.; Vatsa, M.; Singh, R.; Majumdar, A. Group sparse autoencoder. *Image Vision Comput.* **2017**, *60*, 64−74.

(14) Handley, C. M.; Behler, J. Next generation interatomic potentials for condensed systems. *Eur. Phys. J. B* **2014**, *87*, 152.

(15) Blank, T. B.; Brown, S. D.; Calhoun, A. W.; Doren, D. J. Neural network models of potential energy surfaces. *J. Chem. Phys.* **1995**, *103*, 4129−4137.

(16) Manzhos, S.; Carrington, T. Using neural networks to represent potential surfaces as sums of products. *J. Chem. Phys.* **2006**, *125*, 194105.

(17) Manzhos, S.; Carrington, T. A random-sampling high dimensional model representation neural network for building potential energy surfaces. *J. Chem. Phys.* **2006**, *125*, 084109.

DOI: 10.1021/acs.jctc.7b01045
J. Chem. Theory Comput. 2018, 14, 55−62

(18) Behler, J.; Parrinello, M. Generalized neural-network representation of high-dimensional potential-energy surfaces. *Phys. Rev. Lett.* **2007**, *98*, 146401.
(19) Houlding, S.; Liem, S. Y.; Popelier, P. L. A. A polarizable high-rank quantum topological electrostatic potential developed using neural networks: Molecular dynamics simulations on the hydrogen fluoride dimer. *Int. J. Quantum Chem.* **2007**, *107*, 2817.
(20) Pukrittayakamee, A.; Malshe, M.; Hagan, M.; Raff, L. M.; Narulkar, R.; Bukkapatnum, S.; Komanduri, R. Simultaneous fitting of a potential-energy surface and its corresponding force fields using feedforward neural networks. *J. Chem. Phys.* **2009**, *130*, 134101.
(21) Handley, C. M.; Popelier, P. L. A. Potential Energy Surfaces Fitted by Artificial Neural Networks. *J. Phys. Chem. A* **2010**, *114*, 3371−3383.
(22) Behler, J. Neural network potential-energy surfaces in chemistry: a tool for large-scale simulations. *Phys. Chem. Chem. Phys.* **2011**, *13*, 17930−17955.
(23) Nguyen, H. T. T.; Le, H. M. Modified feed-forward neural network structures and combined-function-derivative approximations incorporating exchange symmetry for potential energy surface fitting. *J. Phys. Chem. A* **2012**, *116*, 4629.
(24) Jiang, B.; Guo, H. Permutation invariant polynomial neural network approach to fitting potential energy surfaces. *J. Chem. Phys.* **2013**, *139*, 054112.
(25) Behler, J. Representing potential energy surfaces by high-dimensional neural network potentials. *J. Phys.: Condens. Matter* **2014**, *26*, 183001.
(26) Gastegger, M.; Marquetand, P. High-Dimensional Neural Network Potentials for Organic Reactions and an Improved Training Algorithm. *J. Chem. Theory Comput.* **2015**, *11*, 2187−2198.
(27) Gastegger, M.; Kauffmann, C.; Behler, J.; Marquetand, P. Comparing the accuracy of high-dimensional neural network potentials and the systematic molecular fragmentation method: A benchmark study for all-trans alkanes. *J. Chem. Phys.* **2016**, *144*, 194110.
(28) Wilson, E. B.; Decius, J. C.; Cross, P. C. *Molecular Vibrations: The Theory of Infrared and Raman Vibrational Spectra*; Dover Publications, 1980.
(29) Stare, J.; Balint-Kurti, G. G. Fourier Grid Hamiltonian Method for Solving the Vibrational Schrödinger Equation in Internal Coordinates: Theory and Test Applications. *J. Phys. Chem. A* **2003**, *107*, 7204−7214.
(30) Kowalewski, M.; Mikosch, J.; Wester, R.; de Vivie-Riedle, R. Nucleophilic Substitution Dynamics: Comparing Wave Packet Calculations with Experiment. *J. Phys. Chem. A* **2014**, *118*, 4661−4669.
(31) Thallmair, S.; Roos, M. K.; de Vivie-Riedle, R. Design of specially adapted reactive coordinates to economically compute potential and kinetic energy operators including geometry relaxation. *J. Chem. Phys.* **2016**, *144*, 234104.
(32) Kosloff, D.; Kosloff, R. A Fourier Method Solution for the Time Dependent Schrödinger Equation as a Tool in Molecular Dynamics. *J. Comput. Phys.* **1983**, *52*, 35−53.
(33) Luckhaus, D. 6D vibrational quantum dynamics: Generalized coordinate discrete variable representation and (a)diabatic contraction. *J. Chem. Phys.* **2000**, *113*, 1329.
(34) Luckhaus, D. Multi-arrangement quantum dynamics in 6D: cis-trans isomerization and 1,3-hydrogen transfer in HONO. *Chem. Phys.* **2004**, *304*, 79−90.
(35) Hofmann, A.; de Vivie-Riedle, R. Quantum dynamics of photoexcited cyclohexadiene introducing reactive coordinates. *J. Chem. Phys.* **2000**, *112*, 5054.
(36) Hinton, G. E.; Salakhutdinov, R. R. Reducing the Dimensionality of Data with Neural Networks. *Science* **2006**, *313*, 504.
(37) Rumelhart, D. E.; Hinton, G. E.; Williams, R. J. Learning representations by back-propagating errors. *Nature* **1986**, *323*, 533.
(38) Andersen, H. C. Rattle: A "Velocity" Version of the Shake Algorithm for Molecular Dynamics Calculations. *J. Comput. Phys.* **1983**, *52*, 24−34.
(39) Eckart, C. Some Studies Concerning Rotating Axes and Polyatomic Molecules. *Phys. Rev.* **1935**, *47*, 552.
(40) Schaad, L. J.; Hu, J. The Schrödinger equation in generalized coordinates. *J. Mol. Struct.: THEOCHEM* **1989**, *185*, 203−215.
(41) Matanović, I.; Došlić, N.; Johnson, B. R. Generalized approximation to the reaction path: The formic acid dimer case. *J. Chem. Phys.* **2008**, *128*, 084103.
(42) Frisch, M. J.; Trucks, G. W.; Schlegel, H. B.; Scuseria, G. E.; Robb, M. A.; Cheeseman, J. R.; Scalmani, G.; Barone, V.; Mennucci, B.; Petersson, G. A.; Nakatsuji, H.; Caricato, M.; Li, X.; Hratchian, H. P.; Izmaylov, A. F.; et al. *Gaussian 09*, Revision A.02; Gaussian Inc.: Wallingford, CT, 2009.
(43) Barbatti, M.; Granucci, G.; Ruckenbauer, M.; Plasser, F.; Crespo-Otero, R.; Pittner, J.; Persico, M.; Lischka, H. *NEWTON-X: a package for Newtonian dynamics close to the crossing seam*; 2013; http://www.newtonx.org/.
(44) Tal-Ezer, H.; Kosloff, R. An Accurate and Efficient Scheme for Propagating the Time Dependent Schrödinger Equation. *J. Chem. Phys.* **1984**, *81*, 3967−3971.
(45) do N. Varella, M. T.; Arasaki, Y.; Ushiyama, H.; Takatsuka, K.; Wang, K.; McKoy, V. Real-time observation of intramolecular proton transfer in the electronic ground state of chloromalonaldehyde: An ab initio study of time-resolved photoelectron spectra. *J. Chem. Phys.* **2007**, *126*, 054303.
(46) Wolf, K.; Mikenda, W.; Nusterer, E.; Schwarz, K. Proton motion in malonaldehyde: an ab initio molecular dynamics study. *J. Mol. Struct.* **1998**, *448*, 201−207.

DOI: 10.1021/acs.jctc.7b01045
J. Chem. Theory Comput. 2018, 14, 55−62

Chapter 2

Inclusion of dynamic solvent effects

Liquid solvation is one of the most important processes of applied chemistry and biochemistry. Most reactions require multiple reactants and high collision rates of those reactants are crucial for high reaction rates. In solids, these are difficult to obtain due to immobility. It is also difficult in gases, due to the low particle density at the temperatures and pressures most chemicals can be transferred to a stable gas phase. Liquids offer mobility and high density and are therefore one of the most common substrates in which chemical reactions are carried out. This is even more the case for biological processes, in particular with respect to water and its importance to known life [110, 111].

It is therefore not surprising that with increasing computational abilities, the theoretical study of reactive systems is pushed further and further towards more accurate descriptions of their solvent environments. While there has been tremendous progress in classical and semiclassical MD e.g. with the improvements made to general and specialized force fields [112–116] or with the increasing precision of water models [117–120] describing the probably most important solvent, the inclusion of solvent effects in QD calculations still lacks general models that can be applied to large systems. Instead, there exist various approaches which are suited for specific systems and different effects.

One strategy is to treat the solvent as a continuum. This has the advantage that all of the computationally demanding explicit interactions between the particles can be replaced by implicit effects due to macroscopic quantities such as the viscosity. For QD applications, this was first implemented in the field of heavy ion physics in the 1970s [121–123] and has since been developed further by coupling Bohmian quantum trajectories to an implicit solvent according to the Schrödinger-Langevin equation [124, 125].

The alternative is the explicit description of the solvent. Including the solvent on a quantum mechanical level quickly results in unfeasible computational requirements. However, if the level of precision is low enough, it is still possible. An example for this is the linearized semiclassical initial value representation [126–128], where the quantum behavior for all involved particles can be increased until convergence for the studied observable is reached. This does not always happen within a reasonable time or lead to the required precision of the results [129]. One possible cause are systems where the solute has to be treated with high accuracy, because quantum effects determine the outcome of its dynamics. Here, more asymmetric approaches are useful.

If the QD of the solute is treated with high precision, it is impossible to treat the solvent on equal footing in practice. For many systems, this is not problematic, because the focus lies on the correct description of the solute. As a result, there are several methods to couple the QD of the solute to the classical MD of the solvent. The most straightforward implementation of this is the quantum-classical time-dependent self-consistent field (TDSCF) [130,131], also known as Ehrenfest dynamics [132, 133]. The Ehrenfest method is formally derived from the quantum-quantum TDSCF method [134] by approximating the subsystem of heavier particles as classical.

It has in this fashion been applied to the dissociation of the clusters of rare gases and halogen compounds [135–137], but has also been applied to systems with similar masses such as the relaxation of the cyanide ion in water [138–140].

A related way to include a solvent environment classically is derived from the Liouville-von Neumann equation [141–143] that describes the time evolution of the density matrix. This is once again formally, but not exclusively, done for an environment of heavier particles than the solute and results in the quantum-classical Liouville-von Neumann equation [144–147]. From thereon, the solvent is treated as a classical bath and can be approximated in a number of ways [148–151] that can ultimately lead to simulations of solvated systems of realistic sizes [146].

For this thesis, three methods to include solvent effects into the QD of a system were developed. The first one, the dynamic continuum ansatz, treats the solvent as a continuum and incorporates information about the cavity of the solute in its calculations. It is presented in section 2.1. The second method, the QD/MD approach, treats the environment explicitly and uses snapshots of solvent arrangements for the study of ultrafast processes in the solute. It is presented in section 2.2. The third method, the coupled QD/MD (cQDMD) approach, extends the quantum-classical TDSCF method and aims at constructing a fairly general approach to the lower-level treatment of the solvent. It is presented in section 2.3.

As an example system the first two methods use the photoinduced bond cleavage of diphenylmethyltriphenylphosphonium ion ($Ph_2CH{-}PPh_3^+$) [152]. The resulting diphenylmethyl cation (Ph_2CH^+) can then be used as a reactive intermediates in following reactions. Since this is a common way to produce carbocations and since the influence of the solvent can be decisive for these systems, their correct description is of practical interest. For the cQDMD approach the photodissociation of ICN and the relaxation of uracil after photoexcitation are used as model systems.

2.1 Implicit description of solvents using the dynamic continuum ansatz

The outcome of reactions in many systems depends on whether they take place in solution or in gas phase [27, 28, 153–155]. As an example, the photoactivated bond cleavage of $Ph_2CH{-}PPh_3^+$ can potentially take place via homolysis or heterolysis as is shown in fig. 2.1. If the system is theoretically studied in gas phase by propagating a wavepacket corresponding to a possible initial condition after photoexcitation, homolysis is observed [156]. This conflicts with experimental observations in organic solvents such as acetonitrile and dichloromethane where heterolysis takes place [157].

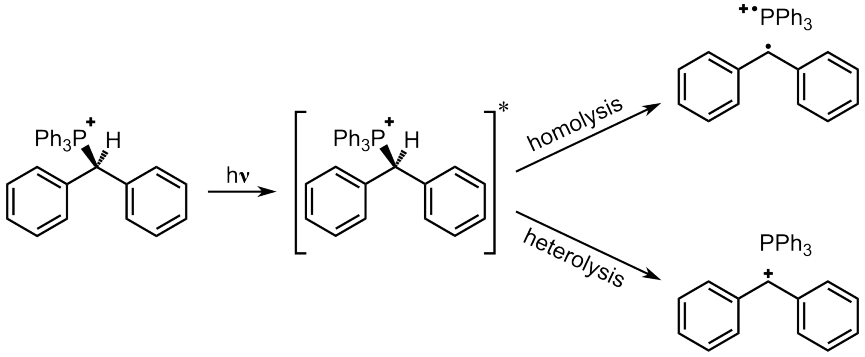

Figure 2.1: Illustration of the two most likely dissociation pathways in $Ph_2CH{-}PPh_3^+$. After photoexcitation, homolysis and heterolysis could take place.

These observations cannot be described with static stabilizations by the solvent, as would be the case for products with different electrostatic charges. Here, in both cases one of the products is positively charged and the other is neutral. In fact, it appears that dynamic effects, i.e. deceleration due to the viscosity of the solvent, play a decisive role for this reaction. This makes $Ph_2CH{-}PPh_3^+$ suited for the dynamic continuum ansatz.

The article "Quantum Dynamics of a Photochemical Bond Cleavage Influenced by the Solvent Environment: A Dynamic Continuum Approach" published in *The Journal of Physical Chemistry Letters* introduces the dynamic continuum ansatz using the example of the photodissociation of $Ph_2CH{-}PPh_3^+$ [29]. The key points of the article are:

- The dynamic effects of the solvent are included by introducing an additional potential term $\hat{V}_{\mathrm{dec}}(\Psi)$ in the solute Hamiltonian $\hat{H}(\Psi)$ that depends on the wavefunction Ψ:

$$\hat{H}(\Psi) = \hat{H}_0 + \hat{V}_{\mathrm{dec}}(\Psi) \ . \tag{2.1}$$

  Here $\hat{H}_0$ is the Hamiltonian that is used for the gas phase. $\hat{V}_{\mathrm{dec}}(\Psi)$ is constructed by calculating a frictional force F_{dec} according to Stokes using the expectation value of the dissociation velocity, the viscosity of the solvent [158], the mass distribution of the fragments after dissociation and information about the deformation of the solvent cavity during the dissociation. The decelerating potential $\hat{V}_{\mathrm{dec}}(\Psi)$ is then obtained by integrating F_{dec}.

- The dynamic continuum ansatz is applied to the photodissociation of $Ph_2CH{-}PPh_3^+$ in acetonitrile and compared to calculations of the gas phase dynamics. To cover the reaction space, two coordinates are needed, a distance coordinate r along the dissociating bond and an angle ϕ describing a concerted motion associated with the relaxation of the molecule along the dissociation. This system has a conical intersection (CoIn), which needs to be reached to assure the relaxation to the electronic ground state and the associated experimentally

observed heterolytic bond cleavage. It is shown that the unhindered accumulation of momentum along the dissociation coordinate causes the wavepacket to miss the CoIn and that the implicit inclusion of the solvent using its viscosity decelerates the wavepacket enough to reach the CoIn.

- The necessary time for the generation of Ph_2CH^+ is calculated by including the non-adiabatic coupling matrix elements in the simulation. After comparison with experimental observations, the results are found to be in good agreement.

In the following, the article "Quantum Dynamics of a Photochemical Bond Cleavage Influenced by the Solvent Environment: A Dynamic Continuum Approach" published in *The Journal of Physical Chemistry Letters* is reprinted with permission from *J. Phys. Chem. Lett.* **5**, 3480-3485 (2014);

THE JOURNAL OF PHYSICAL CHEMISTRY Letters

Letter

pubs.acs.org/JPCL

Quantum Dynamics of a Photochemical Bond Cleavage Influenced by the Solvent Environment: A Dynamic Continuum Approach

Sebastian Thallmair,[†,‡] Markus Kowalewski,[†,§] Julius P. P. Zauleck,[†] Matthias K. Roos,[†] and Regina de Vivie-Riedle*[,†]

[†]Department Chemie, Ludwig-Maximilians-Universität München, D-81377 München, Germany

[‡]Lehrstuhl für BioMolekulare Optik, Ludwig-Maximilians-Universität München, D-80538 München, Germany

Supporting Information

ABSTRACT: In every day chemistry, solvents are used to influence the outcome of chemical synthesis. Electrostatic effects stabilize polar configurations during the reaction and in addition dynamic solvent effects can emerge. How the dynamic effects intervene on the ultrafast time scale is in the focus of this theoretical study. We selected the photoinduced bond cleavage of $Ph_2CH-PPh_3^+$ for which the electrostatic interactions are negligible. Elaborate ultrafast pump−probe studies already exist and serve as a reference. We compared quantum dynamical simulations with and without environment and noticed the necessity to model the influence of the solvent cage on the reactive motions of the solute. The frictional force induced by the dynamic viscosity of the solvent is implemented in the quantum mechanical formalism with a newly developed approach called the dynamic continuum ansatz. Only when the environment is included are the experimentally observed products reproduced on the subpicosecond time scale.

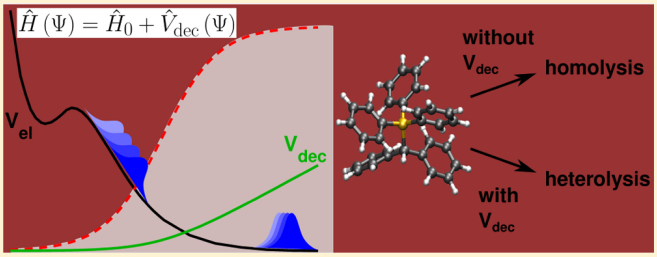

SECTION: Liquids; Chemical and Dynamical Processes in Solution

Solvents play an important role in chemistry.[1] Their polarity and viscosity can change the reaction outcome and rate. The electrostatic contributions become effective when reactants and products possess different dipole moments.[2−4] Here, also the reorientation of the solvent has to be considered if it happens on a similar time scale as the reaction.[5−7] Independent of the presence of electrostatic interactions, dynamic solvent effects may arise that directly interfere with the intramolecular motion. Possible scenarios are photoinduced bond cleavage or formation where ultrafast large amplitude motions occur. The corresponding changes in the molecular structure cause modifications in the shape and volume of the solute's cavity. The surrounding molecules have to be displaced to enable the molecular deformation. This caging effect becomes important, especially, when bulky molecular fragments are involved. For theoretical studies the challenge is to include this effect in the simulations.

Successful realizations were demonstrated for the photodissociation of ICN studied with classical molecular dynamics methods. Benjamin and Wilson used parametrized potentials to simulate the excited state dynamics and showed that the dissociating fragments are decelerated by the surrounding Xe fluid compared to the gas phase.[8] Similar observations were also reported for other solvents.[9−11] Additionally, the slowdown of the rotationally hot $CN^•$ radicals subsequent to photodissociation can be observed. Comparison of classical molecular dynamics simulations with transient pump−probe anisotropy measurements shows that the rotation of the $CN^•$ radicals is decelerated until a larger cavity is formed.[8,12,13] In their enlarged cage, $CN^•$ radicals rotate nearly freely for several picoseconds even in room temperature liquids.[14]

We present an ansatz that incorporates the frictional force from the surrounding solvent cage in the quantum mechanical formalism directly based on the time-dependent Schrödinger equation. It opens a straightforward way to keep the wave packet character to describe the electronic excitation by a laser pulse for coherent control studies[15] in solution and for nonadiabatic processes like population transfer through a conical intersection (CoIn). First quantum mechanical investigations on moving particles that are subject to viscous force were done in the 1970s in heavy ion physics.[16−20] Different approaches using expectation values of the momentum and position[16,17] as well as the phase of the wave function[20] were employed. The effect of rare gas matrices on vibrating diatomics were studied by femtosecond spectroscopy and quantum dynamics simulations.[21]

Our interest lies in photoinduced molecular bond cleavage in organic molecules that generates short-lived reactive intermediates. For these reactions we will demonstrate that already on the short femtosecond time scale the dynamic solvent effect becomes important. Phosphonium salts like $Ph_2CH-PPh_3^+ X^-$

Received: August 14, 2014
Accepted: September 25, 2014
Published: September 25, 2014

The Journal of Physical Chemistry Letters Letter

containing diphenylmethyltriphenylphosphonium ($Ph_2CH-PPh_3^+$) ions are commonly used for the photogeneration of diphenylmethyl cations (Ph_2CH^+) as intermediates in polar and moderately polar solvents like acetonitrile or dichloromethane[22] (see Scheme 1). Experimental investigations using

Scheme 1. Reaction Scheme for the Photochemical Bond Cleavage in Diphenylmethyltriphenylphosphonium Ions $Ph_2CH-PPh_3^+$[a]

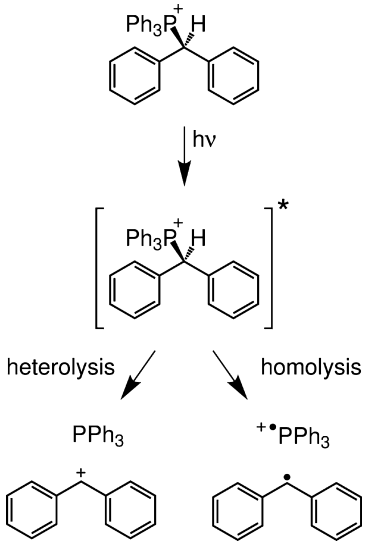

[a]The dissociation character of the ground state is heterolytic leading to the photoproducts Ph_2CH^+ and PPh_3; the first and second excited state have homolytic character generating $Ph_2CH^•$ and $PPh_3^{•+}$.

ultrafast broadband transient absorption spectroscopy demonstrated that, with nonoxidizable counterions X^- (e.g., BF_4^- or SbF_6^-), diphenylmethyl cations are formed almost exclusively.[23] Quantum chemical studies revealed that, after a local $\pi-\pi^*$ excitation on the leaving group PPh_3 and the crossing of a small barrier in the first excited state S_1, the C1−P bond cleavage can take place.[24] In the dissociation limit, the S_1 state describes the homolytic bond cleavage leading to the formation of a radical pair $Ph_2CH^•$ and $PPh_3^{•+}$ (Scheme 1, right channel), whereas in the ground state S_0 the desired Ph_2CH^+ cations (and PPh_3) are built after heterolytic bond cleavage (Scheme 1, left channel). An energetically reachable CoIn was identified, which connects both product channels.[24] Additional to the primary dissociation coordinate, the C1−P distance, an angular coordinate is necessary to reach the CoIn (see Figure 1). Thus, the static quantum chemical results suggest that a wave packet evolving along the dissociation coordinate has to reach the CoIn where the excited state population could be efficiently transferred to the ground state to generate the experimentally observed diphenylmethyl cations.[23]

In order to clarify the reaction mechanism and the role of the CoIn, we first performed quantum dynamical calculations (for details, see Supporting Information (SI)) on the two-dimensional potential energy surface (PES) of the S_1 state, spanned by the two coordinates identified as essential to describe the reaction (see Figure 1). Figure 2 shows the time evolution of the wave packet at selected times after a large part of the wave packet has crossed the barrier in the Franck−Condon (FC) region. The other fraction of the wave packet stays in the local S_1-minimum behind the barrier. The black and white isolines illustrate snapshots at 170 and 290 fs after starting the

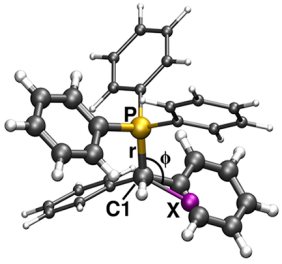

Figure 1. Optimized geometry of $Ph_2CH-PPh_3^+$. For the calculation of the potential energy surface used in the quantum dynamical simulations, the ONIOM method is employed (see SI). The thicker part of $Ph_2CH-PPh_3^+$ shows the high-level system $PhCH_2-PH_2Ph^+$ of the ONIOM calculations; the thinner drawn phenyl rings are only contained in the low-level system $Ph_2CH-PPh_3^+$ and are replaced by hydrogen atoms in the high-level system. The coordinates considered in our quantum dynamical calculations are the C1−P distance r and the angle ϕ between the atoms P, C1 and the dummy atom X, which is introduced to optimally define the angle ϕ.

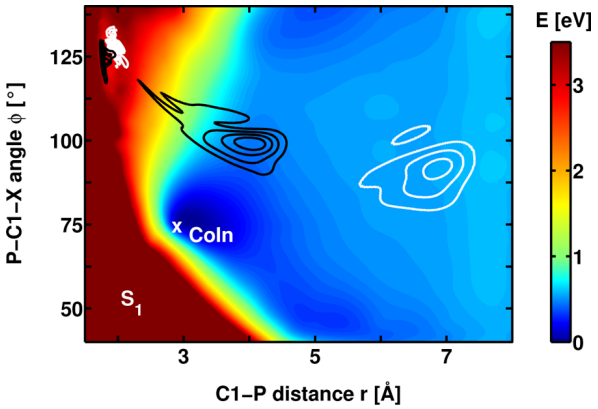

Figure 2. Potential energy surface of the first excited state S_1 of $Ph_2CH-PPh_3^+$ together with dissociating wave packets. Two snapshots are taken at 170 fs (black isolines) and 290 fs (white isolines) after starting the propagation in the FC region. The wave packet clearly misses the CoIn at a C1−P distance r of 2.9 Å and a P−C1−X angle ϕ of 75°.

propagation in the FC region. Evidently the wave packet misses the CoIn, although it lies close to the global minimum of the S_1 - PES. As the gradient in the r direction is larger than the one in the ϕ direction the vibrational wave packet is mainly accelerated in the r direction. The dissociation occurs in the S_1 state and radical pairs are formed after a homolytic bond cleavage. This is clearly in contrast to the experimentally observed heterolytic process.[23] As both dissociation channels have one positively charged fragment, electrostatic solvent effects change neither the energetics of the reaction nor the energetic order of the dissociation channels.[24] Only due to its dynamic impact the solvent is expected to play a decisive role.

We developed a dynamic continuum ansatz that treats the solvent environment in a continuum-like fashion and can be applied when no charges are generated during the reaction. Its decelerating effect is described in the quantum mechanical formalism by means of an additional potential term $\hat{V}_{dec}(\Psi)$ in the Hamiltonian. $\hat{V}_{dec}(\Psi)$ is constructed from a non-conservative force, which depends on the wave function Ψ. Thus, the Hamiltonian is expressed as the sum of the operators for the kinetic energy of the nuclei ($\hat{T}_{nuc}$), the potential energy ($\hat{V}_{el}$), and the decelerating potential ($\hat{V}_{dec}(\Psi)$):

dx.doi.org/10.1021/jz501718t | J. Phys. Chem. Lett. 2014, 5, 3480−3485

$$\hat{H}(\Psi) = \hat{H}_0 + \hat{V}_{dec}(\Psi) = \hat{T}_{nuc} + \hat{V}_{el} + \hat{V}_{dec}(\Psi) \quad (1)$$

The sum of $\hat{T}_{nuc}$ and $\hat{V}_{el}$ is the molecular Hamiltonian $\hat{H}_0$. The negative gradient of $\hat{V}_{dec}(\Psi)$ reflects the decelerating frictional force $\overrightarrow{F_{dec}}$ originating from the surrounding solvent molecules. The time evolution of the wave function Ψ of the system is described by the following nonlinear time-dependent Schrödinger equation:

$$i\hbar\frac{\partial}{\partial t}\Psi = (\hat{H}_0 + \hat{V}_{dec}(\Psi))\Psi \quad (2)$$

In the chosen example $Ph_2CH{-}PPh_3^+$ the bond cleavage process is decelerated. From an atomistic viewpoint, the velocity at which both fragments move apart from each other decreases. The decelerating frictional force $\overrightarrow{F_{dec}}$ is not constant along the C1−P distance r. It is negligible as long as the solute's cavity is not deformed but becomes gradually important with the increase of the cavity. The information how the cavity changes can be obtained by calculating its surface area along the reaction coordinate with the GEPOL algorithm[25,26] as implemented in Gaussian09.[27] Figure 3a shows the cavity surface area (black dots) as a function of r. Around the FC point it stays almost constant. However, with growing r it increases until a constant value is reached when both fragments are separated. The change of the cavity surface can be fitted with a sigmoid function $f_{sig}(r)$ (red solid line in Figure 3a). The step of $f_{sig}(r)$ indicates the onset of the dynamic solvent effect. Its position is determined by r_s; its slope by a_s (see eq 3). When the sigmoid function reaches its plateau, the maximum force $\vec{F}_0(t)$ at time t is experienced by the system (for the detailed definition of $\vec{F}_0(t)$ see eq 4). The product of $\vec{F}_0(t)$ and $f_{sig}(r)$ yields the decelerating force $\overrightarrow{F_{dec}}(r,t)$ which depends on the position along the coordinate r and on the time t:

$$\overrightarrow{F_{dec}}(r,t) = \vec{F}_0(t) f_{sig}(r) = \vec{F}_0(t)\frac{1}{1+\exp(-a_s(r-r_s))} \quad (3)$$

Accordingly, $\overrightarrow{F_{dec}}(r,t)$ is zero for $r \ll r_s$, and the wave packet evolves solely under the influence of the molecular potential. Around r_s, the force $\overrightarrow{F_{dec}}(r,t)$ increases until it reaches its maximum value $\vec{F}_0(t)$ and the wave packet is decelerated. $\vec{F}_0(t)$ is proportional to the expectation value of the velocity $\langle\vec{v}_r(t)\rangle$ of the wave packet along r at which the fragments move apart from each other. A simple model for the frictional force $\vec{F}_0(t)$ in a viscous medium is given by Stokes' law

$$\vec{F}_0(t) = -\gamma\langle\vec{v}_r(t)\rangle = -6\pi\eta R_{eff}\langle\vec{v}_r(t)\rangle, \quad (4)$$

with the experimentally determined dynamic viscosity of the solvent η[28] and the effective radius R_{eff}. The latter takes into account that the momentum along the dissociation coordinate r is equally partitioned between the fragments and that they have different radii R_i and masses m_i:

$$R_{eff} = \frac{R_1 m_2 + R_2 m_1}{m_1 + m_2} \quad (5)$$

In this sense, R_{eff} combines the forces acting on both particles, which have to be calculated individually according to conservation of momentum and Stokes' law.

The radii R_i for the fragments are obtained from quantum chemistry by mapping their cavity volume to the volume of a sphere whose radius then corresponds to R_i. Integration of $-\overrightarrow{F_{dec}}(r,t)$ over r yields the decelerating potential $V_{dec}(r,t)$. In a one-dimensional case, the vector $\overrightarrow{F_{dec}}(r,t)$ becomes scalar: $\overrightarrow{F_{dec}}(r,t) \rightarrow F_{dec}(r,t)$. As $F_0(t)$ is independent of r, it can be moved outside the integral:

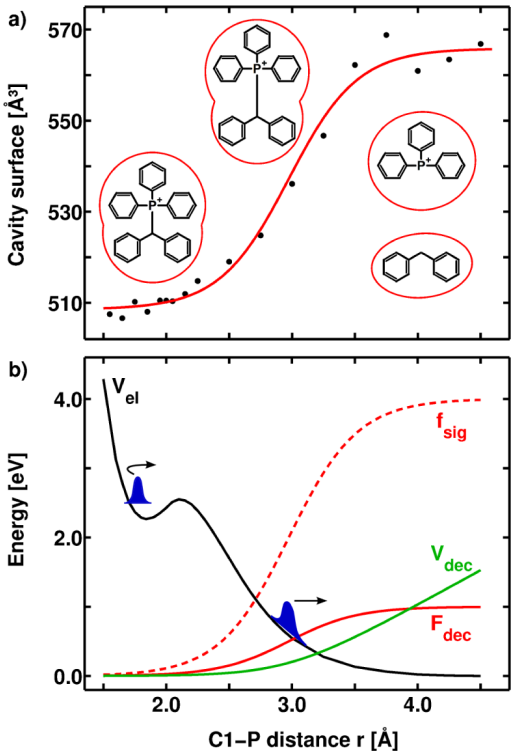

Figure 3. (a) Cavity surface area of the solute $Ph_2CH{-}PPh_3^+$ in acetonitrile (black dots) depending on the C1−P distance calculated for a polarized continuum model. The solid red line shows the fitted sigmoid function f_{sig}. The structural formula illustrates that the cavity surface area increases along the dissociation coordinate until it reaches a constant value when both fragments have separated cavities. (b) Discrimination between a locally trapped (left) and a dissociating part of a wave packet (right) in a molecular potential V_{el} (solid black line) with the help of the sigmoid shape function f_{sig} (dashed red line). The solid red line illustrates the decelerating force $F_{dec}(r,t)$; the solid green line illustrates the decelerating potential $V_{dec}(r,t)$ as a function of the C1−P distance, shown for a specific time t during the propagation. The energy axis relates solely to the molecular potential $\hat{V}_{el}$.

dx.doi.org/10.1021/jz501718t | J. Phys. Chem. Lett. 2014, 5, 3480−3485

The Journal of Physical Chemistry Letters Letter

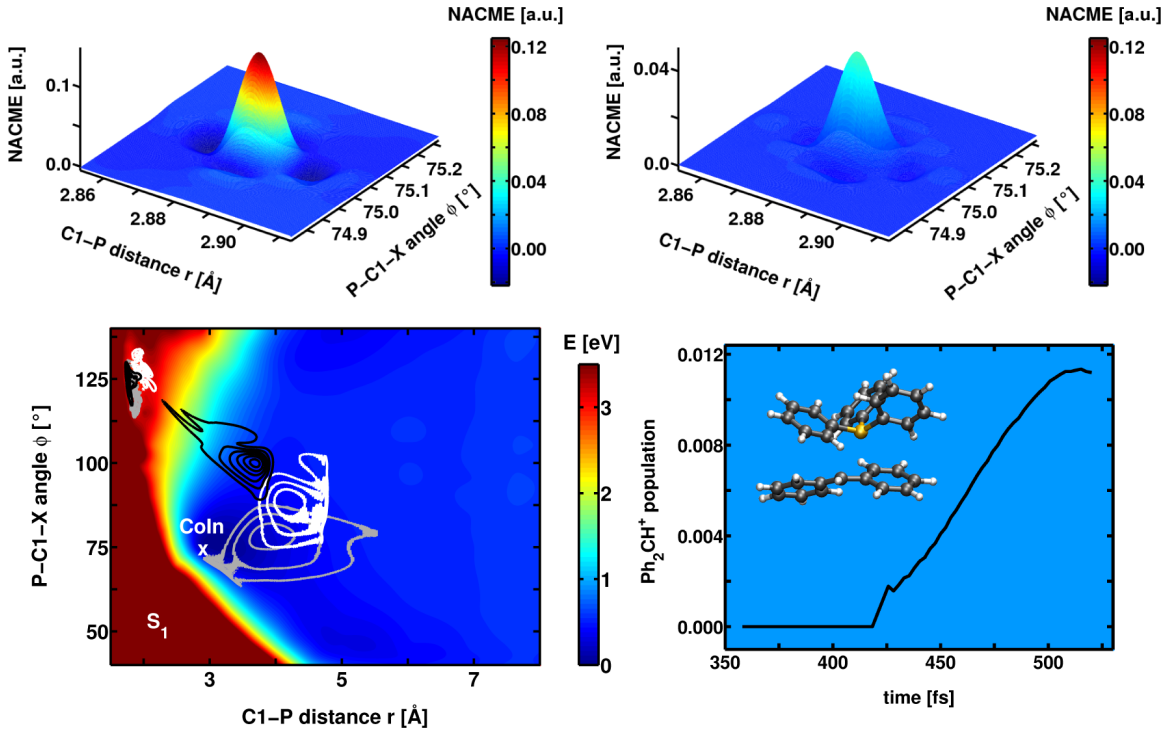

Figure 4. Nonadiabatic coupling matrix elements $\langle\Psi_0|(\partial)/(\partial r)|\Psi_1\rangle$ (top, left) and $\langle\Psi_0|(\partial)/(\partial\phi)|\Psi_1\rangle$ (top, right) for the investigated CoIn in the high-level system $PhCH_2{-}PH_2Ph^+$. Potential energy surface of the first excited state S_1 of $Ph_2CH{-}PPh_3^+$ together with dissociating wave packets propagated with the dynamic continuum ansatz (bottom, left). Three snapshots are taken at 170 fs (black isolines), 290 fs (white isolines) and 390 fs (gray isolines) after starting the propagation in the FC region. In contrast to Figure 2, the wave packet is decelerated and reaches the CoIn with the ground state. Product population of the ground state that was transferred through the CoIn and evolves toward longer bond length, leading to the formation of Ph_2CH^+ cations (bottom, right). The inlay shows the geometry of $Ph_2CH{-}PPh_3^+$ at the CoIn.

$$
\begin{aligned}
V_{\mathrm{dec}}(r,\,t) &= -\int_0^r F_{\mathrm{dec}}(r')\,\mathrm{d}r' \\
&= -F_0(t)\int_0^r \frac{1}{1+\exp(-a_s(r'-r_s))}\,\mathrm{d}r' \\
&= -F_0(t)\left[-\frac{1}{a_s}\ln\left(\frac{\exp(-a_s(r'-r_s))}{1+\exp(-a_s(r'-r_s))}\right)\right]_0^r
\end{aligned}
\tag{6}
$$

Therefore, $V_{\mathrm{dec}}(r,t)$ has the shape of the antiderivative of the sigmoid function with the slope $-F_0(t)$ as shown in Figure 3, panel b (green solid line).

The dissociation dynamics can be divided in three central steps, which are reflected in the sigmoid function. When the wave packet is in the FC region, the dynamics are not influenced by the solvent. Later when the wave packet is split at the barrier along the dissociation coordinate as depicted in panel b of Figure 3, only the part of the wave packet that moves toward larger bond length and passes the step of $f_{\mathrm{sig}}(r)$ is decelerated by the solvent cage. Thus, only the velocity of the outer part of the wave packet contributes to $F_0(t)$. This case is ensured by shaping the wave packet with the sigmoid function $f_{\mathrm{sig}}(r)$ before calculating the velocity $\langle v_{r,\mathrm{out}}(t)\rangle$ of the outer part:

$$
\langle v_{r,\mathrm{out}}(t)\rangle = \frac{1}{\mu_r}\frac{\langle f_{\mathrm{sig}}(r)\Psi(r,\,\phi,\,t)|\hat{p}_r|f_{\mathrm{sig}}(r)\Psi(r,\,\phi,\,t)\rangle}{\langle f_{\mathrm{sig}}(r)\Psi(r,\,\phi,\,t)|f_{\mathrm{sig}}(r)\Psi(r,\,\phi,\,t)\rangle}
\tag{7}
$$

with the reduced mass μ_r. According to the sigmoid function $f_{\mathrm{sig}}(r)$ the decelerating force $F_{\mathrm{dec}}(r,\,t)$ then converges to the maximum force $F_0(t)$ for large values of r. As the wave packet is slowed down $F_0(t)$ decreases until no friction is experienced by the system. Accordingly, the decelerating potential $V_{\mathrm{dec}}(r,\,t)$ flattens until it vanishes.

The limit of our dynamic continuum ansatz is given by the representability of the momentum distribution by its respective expectation value for the considered process. The approach can straightforwardly be extended to higher dimensions. However, it should be noted that the decelerating potential $V_{\mathrm{dec}}(r_1,\,r_2,\,\ldots)$ has to be the antiderivative of all the force functions $\overrightarrow{F_{\mathrm{dec},i}}(r_1,r_2\ldots)$, with i being an enumerator for the number of forces included in the model. This is fulfilled automatically as long as the force functions along different coordinates only depend on that respective coordinate, i.e., $\overrightarrow{F_{\mathrm{dec},i}}(r_1,\,r_2\ldots) = F_{\mathrm{dec},i}(r_j)\vec{e}_j$, with $\vec{e}_j$ being the unit vector in the r_j direction. Once the forces become interdependent, this is not generally the case, and there might not exist a single potential that accounts for all the desired forces.

The dynamic continuum ansatz is suited for our example of the photochemical bond cleavage of $Ph_2CH{-}PPh_3^+$. The quantum dynamical calculations without environment (see Figure 2) have shown that the dominant direction of motion is the r direction because its gradient is larger than the one along ϕ. As shown in eq 4, the maximum force $\vec{F}_0(t)$ along a coordinate is proportional to the corresponding expectation value of the velocity. Thus, the decelerating force in ϕ direction is of minor importance, and we confine the dynamic effects of the solvent to the r direction.

dx.doi.org/10.1021/jz501718t | J. Phys. Chem. Lett. 2014, 5, 3480−3485

Figure 4 (bottom, left) shows the PES of the S_1 state together with three exemplary snapshots of the dissociating wave packet under the influence of the environment. The snapshots are taken at 170 fs (black isolines), 290 fs (white isolines) and 390 fs (gray isolines) after starting the propagation in the FC region. Compared to the dynamics without solvent (see Figure 2) slight differences are already observable for the wave packet at 170 fs (black). The dynamic solvent effect becomes more pronounced as the propagation evolves. At 290 fs the wave packet has slowed down significantly along the r direction and starts moving under the influence of the gradient toward the CoIn, which is close to the global S_1 minimum. Simultaneously, a broadening of the wave packet is observed, as a minor part keeps a small momentum toward the dissociation S_1 channel, while the major part approaches the CoIn. The CoIn is reached for the first time at 390 fs.

In order to observe the population transfer through the CoIn, we calculated the nonadiabatic coupling around the CoIn optimized in the high-level system $PhCH_2-PH_2Ph^+$ at the CASSCF(10,10) level of theory.[24] Figure 4 (top row) shows the nonadiabatic coupling matrix elements $\langle\Psi_0|(\partial/\partial r)|\Psi_1\rangle$ (left) and $\langle\Psi_0|(\partial/\partial\phi)|\Psi_1\rangle$ (right). $\langle\Psi_0|(\partial/\partial r)|\Psi_1\rangle$ is about 3 times larger than $\langle\Psi_0|(\partial/\partial\phi)|\Psi_1\rangle$. Both matrix elements enter into our adiabatic implementation of the quantum dynamics on coupled PES.[29] After coupling through the CoIn, we observe a branching of the wave packet toward the ground state minimum or toward the dissociation channel correlated to the Ph_2CH^+ formation. The increase in the Ph_2CH^+ population is depicted in Figure 4, bottom right. We observe a population rise until about 500 fs, which compares well with the fast initial rise of the Ph_2CH^+ transient absorption signal on the subpicosecond time scale.[23] Geminate recombination as well as diffusional separation occur on a longer time scale and could be treated with an augmented Smoluchowski-type diffusion method.[3]

In summary, we have shown that the dynamic effects of the solvent play a decisive role during the photochemical bond cleavage process in diphenylmethyltriphenylphosphonium ions ($Ph_2CH-PPh_3^+$). We presented an ansatz that treats these effects in a continuum-like fashion within the quantum mechanical formalism. The ansatz does not require fitting of parameters and solely relies on quantum mechanically and dynamically evaluated quantities as well as on the experimentally determined dynamic viscosity of the solvent. The solvent cage decelerates the dissociating wave packet and gives it the opportunity to follow the small gradient toward the CoIn where the branching between diphenylmethyl radicals ($Ph_2CH^\bullet$) radicals and Ph_2CH^+ cations takes place. Only with the solvent environment included is the passage through the CoIn possible and the experimentally observed Ph_2CH^+ cations are formed.

The presented dynamic continuum ansatz is general for any bond cleavage process as the coordinate describing the separation of two fragments is the most essential for this important type of chemical reaction. Its range of application can be extended further to the most general situation of wave packet splitting along multiple reaction pathways. Specially designed shape functions can ensure that the diverse solvent effects experienced along the individual reaction channels are correctly reflected in the simulations. Typical examples are small organic cyclic molecules, like cyclohexadiene, furane and the DNA bases, where the excited state population can relax via photophysical or photochemical channels exhibiting different velocities and structural changes. As long as the expectation value of the momentum of the considered parts of the wave packet is meaningful for the molecular process, the presented dynamic continuum ansatz is applicable.

COMPUTATIONAL METHODS

The potential energy surface of $Ph_2CH-PPh_3^+$ was calculated with the "our own n-layered integrated molecular orbital and molecular mechanics (ONIOM)" method. The thicker drawn part of $Ph_2CH-PPh_3^+$ in Figure 2 indicates the high-level system calculated at the CASSCF(10,10) level of theory with the program package Molpro;[30] the thinner phenyl rings are only contained in the low-level system. It is calculated at the DFT (M06-2X) level of theory using Gaussian09.[27] Throughout all calculations, the basis set 6-31G(d) was employed. The major relaxation processes along the dissociation coordinate r are included in the PES. That is the change of the sp^3 to sp^2 hybridization at the C1 atom of the methyl group and the rotation of the phenyl rings and bond length changes, which come along with the lowering of the hybridization. The nonadiabatic couplings were calculated analytically at the CASSCF(10,10) level of theory for the optimized CoIn in the high-level system $PhCH_2-PH_2Ph^+$, and the projected nonadiabatic coupling matrix elements were shifted to the point of minimal energy difference between S_1 and S_0 on the ONIOM potential at r = 2.9 Å and ϕ = 75°. An energetic comparison of the critical points at the MS-CASPT2 level of theory can be found in the SI. The energetic shifts are too small to change the observed reaction channels and the derived mechanism.

For the quantum dynamical simulations, a homemade program was employed that solves the time-dependent Schrödinger equation on a spatial grid using the Chebychev propagation scheme[31] and the G-matrix method for the kinetic operator $\hat{T}$[32−34] (for details see SI). The vibrational ground state wave function $v = 0$ for the electronic ground state S_0 was placed on the S_1 PES. It was shifted slightly to shorter C1−P distance to ensure that the main part of the wave packet crosses the barrier next to the FC region. This is necessary because the minimal barrier[24] is not included in the two-dimensional coordinate space. To include it a third coordinate would be needed, which would increase the simulation time drastically.

ASSOCIATED CONTENT

Supporting Information

Details about the quantum dynamical simulations, figures of the S_1 PES of $Ph_2CH-PPh_3^+$ and the G-matrix elements, potential energies of the critical points at the MS-CASPT2 level of theory as well as geometries in xyz-format are available in the online version of this article. This material is available free of charge via the Internet at http://pubs.acs.org/.

AUTHOR INFORMATION

Corresponding Author

*E-mail: regina.de_vivie@cup.uni-muenchen.de.

Present Address

[§](M.K.) Department of Chemistry, University of California, Irvine, California 92697−2025, USA

Notes

The authors declare no competing financial interest.

■ ACKNOWLEDGMENTS

Financial support by the Deutsche Forschungsgemeinschaft through the SFB749 and the excellence cluster Munich-Centre for Advanced Photonics (MAP) is acknowledged. We thank Eberhard Riedle for fruitful discussions. We dedicate this publication to the 75th birthday of Dr. Klaus Römer.

■ REFERENCES

(1) Reichardt, C.; Welton, T. *Solvents and Solvent Effects in Organic Chemistry*; Wiley-VCH Verlag GmbH & Co. KGaA: Weinheim, Germany, 2011.
(2) Melo, A.; Alfaia, A. J. I.; Reis, J. C. R.; Calado, A. R. T. Unusual Solvent Effect on a S_N2 Reaction. A Quantum-Mechanical and Kinetic Study of the Menshutkin Reaction between 2-Amino-L-methylbenzimidazole and Iodomethane in the Gas Phase and in Acetonitrile. *J. Phys. Chem. B* **2006**, *110*, 1877−1888.
(3) Sailer, C. F.; Thallmair, S.; Fingerhut, B. P.; Nolte, C.; Ammer, J.; Mayr, H.; de Vivie-Riedle, R.; Pugliesi, I.; Riedle, E. A Comprehensive Microscopic Picture of the Benzhydryl Radical and Cation Photo-Generation and Interconversion through Electron Transfer. *ChemPhysChem* **2013**, *14*, 1423−1437.
(4) Struebing, H.; Ganase, Z.; Karamertzanis, P. G.; Siougkrou, E.; Haycock, P.; Piccione, P. M.; Armstrong, A.; Galindo, A.; Adjiman, C. S. Computer-Aided Molecular Design of Solvents for Accelerated Reaction Kinetics. *Nat. Chem.* **2013**, *5*, 952−957.
(5) Stratt, R. M.; Maroncelli, M. Nonreactive Dynamics in Solution: The Emerging Molecular View of Solvation Dynamics and Vibrational Relaxation. *J. Phys. Chem.* **1996**, *100*, 12981−12996.
(6) Nibbering, E.; Elsaesser, T. Probing Solvation Dynamics with Femtosecond Vibrational Spectroscopy. *Appl. Phys. B: Lasers Opt.* **2000**, *71*, 439−441.
(7) Rosspeintner, A.; Lang, B.; Vauthey, E. Ultrafast Photochemistry in Liquids. *Annu. Rev. Phys. Chem.* **2013**, *64*, 247−271.
(8) Benjamin, I.; Wilson, K. R. Proposed Experimental Probes of Chemical Reaction Molecular Dynamics in Solution: ICN Photodissociation. *J. Chem. Phys.* **1989**, *90*, 4176−4197.
(9) Krylov, A. I.; Gerber, R. B. Photodissociation of ICN in Solid and in Liquid Ar: Dynamics of the Cage Effect and of Excited-State Isomerization. *J. Chem. Phys.* **1994**, *100*, 4242−4252.
(10) Amatatsu, Y.; Morokuma, K. A Theoretical Study on the Photochemical Reaction of ICN in Liquid Ar. *Chem. Phys. Lett.* **1995**, *245*, 469−474.
(11) Winter, N.; Chorny, I.; Vieceli, J.; Benjamin, I. Molecular Dynamics Study of the Photodissociation and Photoisomerization of ICN in Water. *J. Chem. Phys.* **2003**, *119*, 2127−2143.
(12) Moskun, A. C.; Jailaubekov, A. E.; Bradforth, S. E.; Tao, G.; Stratt, R. M. Rotational Coherence and a Sudden Breakdown in Linear Response Seen in Room-Temperature Liquids. *Science* **2006**, *311*, 1907−1911.
(13) Rivera, C. A.; Winter, N.; Harper, R. V.; Benjamin, I.; Bradforth, S. E. The Dynamical Role of Solvent on the ICN Photodissociation Reaction: Connecting Experimental Observables Directly with Molecular Dynamics Simulations. *Phys. Chem. Chem. Phys.* **2011**, *13*, 8269−8283.
(14) Moskun, A. C.; Bradforth, S. E. Photodissociation of ICN in Polar Solvents: Evidence for Long Lived Rotational Excitation in Room Temperature Liquids. *J. Chem. Phys.* **2003**, *119*, 4500−4515.
(15) von den Hoff, P.; Thallmair, S.; Kowalewski, M.; Siemering, R.; de Vivie-Riedle, R. Optimal Control Theory - Closing the Gap Between Theory and Experiment. *Phys. Chem. Chem. Phys.* **2012**, *14*, 14460−14485.
(16) Albrecht, K. A New Class of Schrödinger Operators for Quantized Friction. *Phys. Lett. B* **1975**, *56*, 127−129.
(17) Hasse, R. W. On the Quantum Mechanical Treatment of Dissipative Systems. *J. Math. Phys.* **1975**, *16*, 2005−2011.
(18) Kostin, M. Friction and Dissipative Phenomena in Quantum Mechanics. *J. Stat. Phys.* **1975**, *12*, 145−151.
(19) Hasse, R. W. Approaches to Nuclear Friction. *Rep. Prog. Phys.* **1978**, *41*, 1027−1101.
(20) Stocker, W.; Albrecht, K. A Formalism for the Construction of Quantum Friction Equations. *Ann. Phys.* **1979**, *117*, 436−446.
(21) Ibrahim, H.; Héjjas, M.; Fushitani, M.; Schwentner, N. Phase Sensitive Control of Vibronic Guest-Host Interaction: Br_2 in Ar Matrix. *J. Phys. Chem. A* **2009**, *113*, 7439−7450.
(22) Ammer, J.; Mayr, H. Photogeneration of Carbocations: Applications in Physical Organic Chemistry and the Design of Suitable Precursors. *J. Phys. Org. Chem.* **2013**, *26*, 956−969.
(23) Ammer, J.; Sailer, C. F.; Riedle, E.; Mayr, H. Photolytic Generation of Benzhydryl Cations and Radicals from Quaternary Phosphonium Salts: How Highly Reactive Carbocations Survive Their First Nanoseconds. *J. Am. Chem. Soc.* **2012**, *134*, 11481−11494.
(24) Thallmair, S.; Fingerhut, B. P.; de Vivie-Riedle, R. Ground and Excited State Surfaces for the Photochemical Bond Cleavage in Phenylmethylphenylphosphonium Ions. *J. Phys. Chem. A* **2013**, *117*, 10626−10633.
(25) Pascual-Ahuir, J. L.; Silla, E. GEPOL: An Improved Description of Molecular Surfaces. I. Building the Spherical Surface Set. *J. Comput. Chem.* **1990**, *11*, 1047−1060.
(26) Pascual-Ahuir, J. L.; Silla, E.; Tuñon, L. GEPOL: An Improved Description of Molecular Surfaces. III. A New Algorithm for the Computation of a Solvent-Excluding Surface. *J. Comput. Chem.* **1994**, *15*, 1127−1138.
(27) Frisch, M. J.; Trucks, G. W.; Schlegel, H. B.; Scuseria, G. E.; Robb, M. A.; Cheeseman, J. R.; Scalmani, G.; Barone, V.; Mennucci, B.; Petersson, G. A. et al. *Gaussian 09*, revision A.02; Gaussian, Inc.: Wallingford, CT, 2009.
(28) Kuchling, H. *Taschenbuch der Physik*, 20th ed.; Carl Hanser Verlag: München, Germany, 2010.
(29) Hofmann, A.; de Vivie-Riedle, R. Adiabatic Approach for Ultrafast Quantum Dynamics Mediated by Simultaneously Active Conical Intersections. *Chem. Phys. Lett.* **2001**, *346*, 299−304.
(30) Werner, H.-J.; Knowles, P. J.; Knizia, G.; Manby, F. R.; Schütz, M.; Celani, P.; Korona, T.; Lindh, R.; Mitrushenkov, A.; Rauhut, G. et al. MOLPRO, version 2012.1, A Package of Ab Initio Programs, 2012.
(31) Tal-Ezer, H.; Kosloff, R. An Accurate and Efficient Scheme for Propagating the Time Dependent Schrödinger Equation. *J. Chem. Phys.* **1984**, *81*, 3967−3971.
(32) Wilson Jr., E. B.; Decius, J. C; Cross, P. C. *Molecular Vibrations*; McGraw-Hill: New York, 1955.
(33) Schaad, L.; Hu, J. The Schrödinger Equation in Generalized Coordinates. *J. Mol. Struct: THEOCHEM* **1989**, *185*, 203−215.
(34) Kowalewski, M.; Mikosch, J.; Wester, R.; de Vivie-Riedle, R. Nucleophilic Substitution Dynamics: Comparing Wave Packet Calculations with Experiment. *J. Phys. Chem. A* **2014**, *118*, 4661−4669.

2.2 Explicit treatment of ultrafast processes using frozen solvent arrangements

For some systems an implicit description of the solvent is not enough to capture essential influences of an inhomogeneous environment [159–162]. An example for this are collisions. While the viscosity can describe deceleration, the statistic nature of the possible solvent arrangements is not captured. This can be overcome by an explicit treatment of the solvent. One way to do this in the study of ultrafast processes, is by using frozen solvent arrangements to represent the reaction environment. The solvent arrangements can be generated by propagating the solute by means of classical MD. Since each individual solvent arrangement can induce a certain outcome, several simulations with different initial conditions of the solvent have to be performed. Once enough arrangements are used, the averaged result of the reaction converges and an expected outcome is obtained.

The article "Quantum Dynamics in an Explicit Solvent Environment: A Photochemical Bond Cleavage Treated with a Combined QD/MD Approach" published in *The Journal of Chemical Theory and Computation* illustrates this new QD/MD approach, again using the example of the photodissociation of $Ph_2CH{-}PPh_3^+$ [163]. The key points of the article are:

- The solvent potential $\hat{V}_{\text{solv}}$ is included in the solute Hamiltonian $\hat{H}$:

$$\hat{H} = \hat{T}_{\text{nuc}} + \hat{V}_{\text{mol}} + \hat{V}_{\text{solv}} \ . \tag{2.2}$$

  Here $\hat{T}_{\text{nuc}}$ is the kinetic energy operator of the solute nuclei and $\hat{V}_{\text{mol}}$ the corresponding potential energy surface. $\hat{V}_{\text{solv}}$ is calculated by constructing a library of the potential interaction energy E_{sf} between each of the N_{frag} solute fragments and a single solvent molecule in different orientations. For each of the N_{solv} solvent molecules of each snapshot, E_{sf} is then looked up and added to the total interaction energy. $\hat{V}_{\text{solv}}$ is given by

$$\hat{V}_{\text{solv}} = \sum_{i=1}^{N_{\text{solv}}} \sum_{j=1}^{N_{\text{frag}}} E_{\text{sf}} \left(q_1^{ij}, q_2^{ij}, q_3^{ij}, \ldots, q_6^{ij} \right) \ . \tag{2.3}$$

  The 6 coordinates q_k^{ij} cover all possible orientations two objects in three-dimensional space can have relative to each other. After evaluating their individual importance to the solvent potential by means of a statistical analysis of MD data, the number of coordinates q_k^{ij} is reduced to achieve a feasible computation time.

- The QD/MD approach is applied to the photodissociation of $Ph_2CH{-}PPh_3^+$, which is shown to have two limiting cases. In one, the solvent is in an arrangement that does not block dissociative momentum, resulting in homolytic bond cleavage. In the other, the solvent blocks dissociative momentum and $Ph_2CH{-}PPh_3^+$ reaches the CoIn, resulting in the experimentally observed heterolytic bond cleavage. Using 50 different solvent arrangements gives a converged average of 83 % of the $Ph_2CH{-}PPh_3^+$ reaching the CoIn and the other 17 % leading to homolytic bond cleavage.

In the following, the article "Quantum Dynamics in an Explicit Solvent Environment: A Photochemical Bond Cleavage Treated with a Combined QD/MD Approach" published in *The Journal of Chemical Theory and Computation* is reprinted with permission from *J. Chem. Theory Comput.* **11**, 1987-1995 (2015); copyright 2015 American Chemical Society. For the explicit solvent calculations here and throughout this thesis the program package Gromacs [164] was used. The Supporting Information is reprinted in appendix B.

JCTC Journal of Chemical Theory and Computation Article
pubs.acs.org/JCTC

Quantum Dynamics in an Explicit Solvent Environment: A Photochemical Bond Cleavage Treated with a Combined QD/MD Approach

Sebastian Thallmair,[†,‡] Julius P. P. Zauleck,[†] and Regina de Vivie-Riedle*[,†]

[†]Department Chemie, Ludwig-Maximilians-Universität München, D-81377 München, Germany
[‡]Lehrstuhl für BioMolekulare Optik, Ludwig-Maximilians-Universität München, D-80538 München, Germany

Supporting Information

ABSTRACT: In quantum chemistry methods to describe environmental effects on different levels of complexity are available in the common program packages. Electrostatic effects of a solvent for example can be included in an implicit or explicit way. For chemical reactions with large structural changes additional mechanical effects come into play. Their treatment within a quantum dynamical context is a major challenge, especially when excited states are involved. Recently, we introduced a method that realizes an implicit description. Here, we present an approach combining quantum dynamics and molecular dynamics. It explicitly incorporates the solvent environment, whereby the electrostatic as well as the dynamic effects are captured. This new method is demonstrated for the ultrafast photoinduced bond cleavage of diphenylmethylphosphonium ions ($Ph_2CH-PPh_3^+$), a common precursor to generate reactive carbocations in solution.

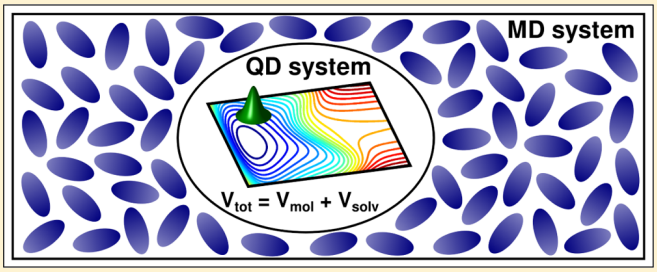

1. INTRODUCTION

Solvents are an important aspect of every day chemistry.[1] While they are often only the reaction medium and do not participate directly in product formation, their electrostatic influence can stabilize or destabilize certain reaction pathways depending on the charge distribution along them.[2,3] In addition, dynamic effects of the solvent environment can emerge.[4,5] The solvent molecules directly interact with the molecular motion of the solute. In the case of ultrafast reactions like photochemical bond cleavage, where strong changes of the molecular structure occur, dynamic solvent effects are particularly important. The solute's fragments, moving apart, push into the solvent cage, and their initial motion is hindered. This can deviate their motion along a path less blocked by solvent molecules, and routes toward smaller energy gradients can come into play. In this way, the dynamics of the molecular system are substantially affected by the forces induced by the solvent cage and hence by its mechanical influence.

From a theoreticians point of view, the challenge is to treat the dynamic solvent effects during quantum dynamics (QD) simulations of photoinduced processes. A solution to treat this caging effect within the quantum mechanical framework in a continuum-like fashion was found recently.[5] The approach uses Stokes' law and the dynamic viscosity of the solvent to include the frictional force exerted on the molecular motion into the QD simulations. It was shown that the deceleration due to the environment is crucial for describing product formation during the bond cleavage of $Ph_2CH-PPh_3^+$. Another possibility for investigating the dynamic effect of the solvent environment is to perform molecular dynamics (MD) simulations of the reactant in a box of solvent molecules. For photoinduced bond cleavage in ICN, parametrized potentials are available to simulate the excited state dynamics and to compare the gas phase with the behavior in different fluids, e.g., Xe,[6] Ar,[7,8] or H_2O.[9] Moskun et al. derived a microscopic picture of the rotational deceleration of $CN^•$ radicals after photochemical bond cleavage in liquid Ar by comparing classical MD simulations and transient pump−probe anisotropy measurements.[10]

Here, we present a new method that includes an explicit, atomistically modeled solvent environment in QD simulations on quantum chemical potential surfaces. The method is demonstrated for QD on a regular grid, which offers high flexibility in its applications. We use the photoinduced bond cleavage of $Ph_2CH-PPh_3^+$ as an example. The selected solvent, acetonitrile (MeCN), does not react with the solute or its photoproducts. MD simulations are used to evaluate the solvent environment and to deduce the minimum number of coordinates required to describe the interaction between solvent and solute by means of a statistical analysis. The resulting solute solvent interaction energy is then calculated for each point of the ab initio potentials based on a quantum chemically precalculated database. Quantum dynamics are performed for many solvent arrangements, and their average leads to the overall picture of the bond cleavage.

Received: January 19, 2015
Published: March 20, 2015

DOI: 10.1021/acs.jctc.5b00046
J. Chem. Theory Comput. 2015, 11, 1987−1995

Journal of Chemical Theory and Computation Article

This article is structured as follows: The description of our new QD/MD approach and the statistical rating of the coordinates for the solute solvent interaction are given in Section 2. This is followed by a brief summary of the computational details of the calculations (Section 3). The application of the QD/MD method to the photochemical bond cleavage of $Ph_2CH-PPh_3^+$ and the discussion of the results are presented in Section 4.

2. INCLUDING THE EXPLICIT ENVIRONMENT INTO QUANTUM DYNAMICS

2.1. Calculation of the Solvent Potential. Our new QD/MD approach combines QD with an atomistic modeling of the solvent environment. The surrounding of the reactant enters the QD via an additional potential term $\hat{V}_{solv}$ in the Hamiltonian, comparable to the dynamic continuum ansatz.[5] $\hat{V}_{solv}$ contains the interaction energy between the reactant and its ambient solvent molecules. Thus, the Hamiltonian $\hat{H}$ encompasses the operators for the kinetic energy of the nuclei ($\hat{T}_{nuc}$), the molecular potential energy ($\hat{V}_{mol}$), and the solvent potential ($\hat{V}_{solv}$)

$$\begin{aligned}\hat{H} &= \hat{T}_{nuc} + \hat{V}_{mol} + \hat{V}_{solv} \\ &= \hat{T}_{nuc} + \hat{V}_{tot}\end{aligned} \tag{1}$$

The sum of $\hat{V}_{mol}$ and $\hat{V}_{solv}$ is the total potential $\hat{V}_{tot}$. The time evolution of the wave function Ψ of the system is described by the time-dependent Schrödinger equation

$$i\hbar\frac{\partial}{\partial t}\Psi = (\hat{T}_{nuc} + \hat{V}_{mol} + \hat{V}_{solv})\Psi \tag{2}$$

The solvent potential $\hat{V}_{solv}$ is the sum of all individual interaction energies E_{sf} between the N_{solv} solvent molecules and the reactant described by the wave function Ψ. Consistent with a standard force field, $\hat{V}_{solv}$ is described by two-body interactions. The reactant is partitioned into N_{frag} fragments, which, approximately, do not change their shape during the process. They are chosen to reflect the chemistry of the system, which means separation or reordering of the fragments model the major structural changes during the reaction. Each fragment contributes to $\hat{V}_{solv}$

$$\hat{V}_{solv} = \sum_{i=1}^{N_{solv}} \sum_{j=1}^{N_{frag}} E_{sf}(q_1^{ij}, q_2^{ij}, q_3^{ij}, ..., q_6^{ij}) \tag{3}$$

E_{sf} depends on the relative orientation of the considered pair of solvent molecule i and fragment j and is a function of six degrees of freedom q_n^{ij} with $n \in \{1, 2, ..., 6\}$, i.e., one distance and five angular coordinates (Figure 1). This is the number necessary to describe the relative orientation of two three-dimensional objects in a three-dimensional space. Each object requires three noncollinear rotational axes (R_{A1}, R_{A2}, R_{A3} and R_{B1}, R_{B2}, R_{B3}) which can be chosen arbitrarily. If one axis of each object is collinear with the connecting vector between both centers of mass, which is the case for R_{A2} and R_{B2} in Figure 1, then one redundant degree of freedom can be removed. In addition, the distance between the centers of mass is necessary. Thus, altogether, six degrees of freedom fully describe the relative orientation of the solvent molecule i and the fragment j and constitute the orientation space.

The potential landscape for the arrangement of the solvent environment around a solute is very flat and has a large number of energetically accessible regions around local minima at room temperature. This makes it nearly impossible to optimize a representative number of configurations around a medium-sized molecule. A convenient way to cover the thermodynamically accessible configuration space is to perform MD simulations of the reactant in a box of solvent molecules. From these, a sufficiently large number of snapshots along the trajectories represents the surrounding solvent. The MD simulations should be carried out for the reactant in its electronic ground state. This is also reasonable for the initial setting of the excited state dynamics, especially if ultrashort laser pulses are used for excitation. On this time scale, the nuclei of the solvent molecules cannot react to the electronic changes of the solute.[11,12] For each snapshot of the MD trajectories, the solvent potential V_{solv} has to be calculated, which is then used for a QD simulation. In addition, the QD simulations require the potential energy surfaces V_{mol} of the reactant, which are set up on a grid of selected coordinates. The Hamiltonian in eq 1 allows the setup in full dimensions; in our working example, we will follow the reaction in specially designed reactive coordinates ξ_i. For each grid point, the interaction energy E_{sf} between reactant and solvent molecules is evaluated in the six-dimensional orientation space by reading the current structure of the reactant and placing it at the respective position in the solvent box for the given snapshot (Figure 2). To include not only the steric, i.e., mechanical, but also electrostatic effects of the solvent, E_{sf} is calculated quantum chemically. The sum of all E_{sf} yields the solvent potential V_{solv} for this grid point (eq 3). This procedure is repeated for the whole grid, leading to a V_{solv} mapped to the coordinate space of the potential energy surface V_{mol}. The sum of both yields the total potential V_{tot} for the reaction in solution. To permit the quantum chemical calculation of E_{sf}, we precalculate the interaction between the reactant and one solvent molecule for all possible relative orientations on a regular space grid in the six-dimensional orientation space. The energy for any arbitrary orientation is then obtained by interpolation.

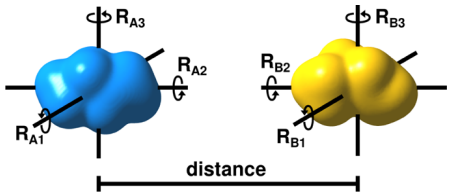

Figure 1. Illustration of the coordinates necessary to describe the relative orientation of two three-dimensional objects in three-dimensional space. One of the two rotational axis, R_{A2} and R_{B2}, can be left out if they are collinear with the connecting vector of both objects. Altogether, six degrees of freedom describe the relative orientation of both objects.

The QD calculations are carried out on all thus-constructed V_{tot} individually. The average of all QD simulations reflects the impact of the solvent surrounding on the investigated process. It is calculated by summation of the absolute squares of the propagated wave functions Ψ_i using the different solvent potentials of the N_{snap} snapshots

$$|\Psi_{av}|^2 = \frac{1}{N_{snap}} \sum_{i=1}^{N_{snap}} |\Psi_i|^2 \tag{4}$$

An important issue to consider is the ratio of the time scales for the motion of the reactant and the motion of the solvent

DOI: 10.1021/acs.jctc.5b00046
J. Chem. Theory Comput. 2015, 11, 1987−1995

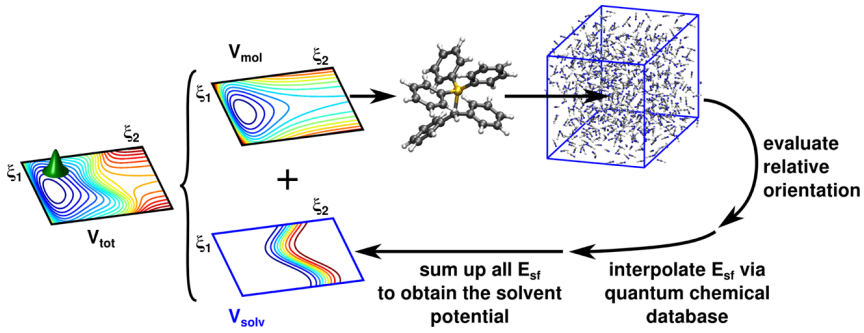

Figure 2. Flowchart visualizing the procedure to calculate the solvent potential V_{solv} based on the reactive coordinates ξ_i of the ab initio molecular potential V_{mol}. For all combinations of ξ_1 and ξ_2, a solute molecule is placed into the cavity in the solvent box, the relative orientation between the solvent molecules and the fragments is evaluated, and E_{sf} is interpolated via the quantum chemical database. Finally, all E_{sf} are summed for each (ξ_1, ξ_2) to yield V_{solv}, which is then added to V_{mol}. The resulting V_{tot} is used for the QD simulations.

molecules. In general, three different scenarios are possible: Either the molecular reaction is much faster than the motion of the solvent molecules or vice versa or the dynamics of both systems happens on a comparable time scale. In the first two cases, one can take advantage of the separation of time scales. In case one, the position of the solvent molecules at the beginning of the molecular reaction is decisive for the whole process and, as a first approximation, the solvent motion is negligible. This is the case for ultrafast photoinduced processes on the hundreds of femtoseconds time scale, like photochemical bond cleavage[5,13−15] or photoisomerization.[16,17] In the second case, one can average over the solvent dynamics. Thus, only one solvent potential V_{solv} is experienced by the reactant. In the third case, when both dynamics are comparably fast, no separation of time scales is possible and both systems have to be propagated in parallel. An example for this case are vibrationally mediated processes involving ladder climbing[18,19] or bimolecular processes in the ground state.[20]

2.2. Evaluating the Coordinates Relevant for the Relative Orientation of Solvent and Fragment. The MD simulations can be used not only to take the snapshots needed for a statistical solvent description but also to facilitate rating the five rotational axes with regard to their importance for the interaction energy E_{sf}. The decisive criterion for their rating is the standard deviation σ_{q_n} of the probability distribution of E_{sf} for each coordinate q_n. The larger σ_{q_n}, the more important is the coordinate q_n. Note that the standard deviation depends on the temperature T, as each MD simulation sketches a Boltzmann distribution. Thus, the obtained rating is valid only for the given temperature T.

The standard deviation σ_{q_n} for a chosen coordinate q_n can be calculated starting from the empirical distribution function $F_m(q_n)$ for a random sample of m elements[21]

$$F_m(q_n) = \frac{1}{m}\sum_{i=1}^{m} 1\{q_{ni} \le q_n\} \tag{5}$$

with q_{ni} being the coordinate values from the random sample. $F_m(q_n)$ is the fraction of the m elements of the sample that fulfill the condition $q_{ni} \le q_n$. For the case of an infinite sample size, the derivative of $F_m(q_n)$ is the probability distribution $P(q_n)$

$$P(q_n) = \frac{\partial}{\partial q_n} F_m(q_n) \tag{6}$$

With the integral $\int_{q_0}^{q_0+\Delta q} P(q_n)\, dq_n$, the probability for q_n to take a value within the interval $[q_0; q_0 + \Delta q]$ can be evaluated. The probability distribution $P(q_n)$ is Boltzmann distributed, as it is extracted from an MD simulation at a particular temperature T

$$P(q_n) = \frac{1}{Z_{q_n}} \exp\left(-\frac{E_{sf}(q_n)}{k_B T}\right) \tag{7}$$

with $1/Z_{q_n}$ being the normalization factor and Z_{q_n} the canonical partition function. The usual degeneracy factor is not present in eq 7 because, first, it is already included due to the explicit dependence of E_{sf} on the coordinate q_n, which compensates for orientations with the same E_{sf} value. Second, all coordinate-dependent degeneracies can be removed beforehand by ensuring that each orientation is uniquely defined in the orientation space. To obtain $E_{sf}(q_n)$, we take the logarithm of eq 7. As for the coordinate rating, we are interested only in the relative variation of $E_{sf}(q_n)$ along q_n and not in the absolute values, the expression can be simplified by shifting $E_{sf}(q_n)$ by $\ln(Z_{q_n})\, k_B T$

$$\begin{aligned} E'_{sf}(q_n) &= E_{sf}(q_n) + \ln(Z_{q_n})\, k_B T \\ &= -\ln(P(q_n)) k_B T \end{aligned} \tag{8}$$

Equation 8 provides an elegant way to obtain the potential landscape for the interaction energy $E'_{sf}(q_n)$ from the MD simulation without explicit calculation. The accessibility of the different energy states depends on the temperature. Thus, the next step is the transformation of $E'_{sf}(q_n)$ into the probability distribution $P(E'_{sf})$. The probability that a specific energy state is occupied is given by the Boltzmann distribution, where the density of states $n(E'_{sf})$ takes the place of the degeneracy factor

$$P(E'_{sf}) = \frac{1}{Z_{E'_{sf}}} \exp\left(-\frac{E'_{sf}}{k_B T}\right) n(E'_{sf}) \tag{9}$$

with $Z_{E'_{sf}}$ being the canonical partition function. The density of states is the sum of the reciprocal absolute gradients of $E'_{sf}(q_n)$ at all values of q_n for which $E'_{sf}(q_n) = E'_{sf}$ multiplied by $N(q_n)$

$$n(E'_{sf}) = \sum_{E'_{sf}(q_n)=E'_{sf}} \left|\frac{\partial E'_{sf}(q_n)}{\partial q_n}\right|^{-1} N(q_n) \tag{10}$$

$N(q_n)$ is a coordinate-dependent degeneracy factor. For the spherical coordinates, as used here to describe the relative

DOI: 10.1021/acs.jctc.5b00046
J. Chem. Theory Comput. 2015, 11, 1987−1995

orientation between the fragments and the solvent, the factor takes into account the different accessible surface areas of a sphere depending on the polar angle.

Figure 3a shows an exemplary probability distribution $P(q_n)$ along an angular coordinate q_n. Following eq 8, we extract the

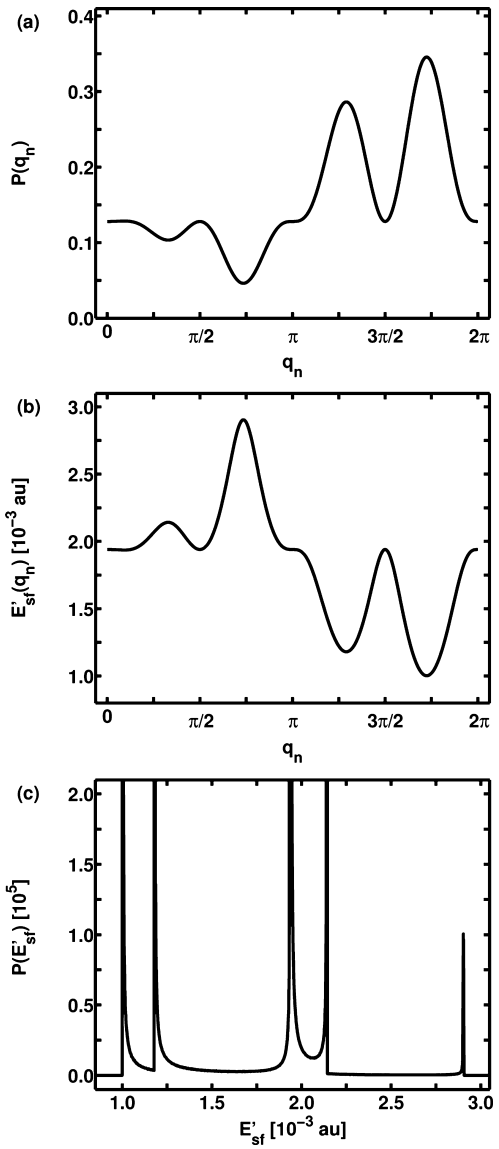

Figure 3. (a) Probability distribution $P(q_n)$ along an angular coordinate q_n. (b) $E'_{sf}(q_n)$ along q_n calculated from $P(q_n)$ at a temperature of T = 298 K according to eq 8. As expected, the maxima in the probability distribution $P(q_n)$ correspond to minima in $E'_{sf}(q_n)$. (c) Probability distribution for the energy $P(E'_{sf})$ resulting from $E'_{sf}(q_n)$ depicted in (b) at T = 298 K determined according to eq 9.

underlying $E'_{sf}(q_n)$ (Figure 3b). As expected, the maxima in $P(q_n)$ correspond to minima in $E'_{sf}(q_n)$. The probability distribution $P(E'_{sf})$ is calculated from eq 9 and depicted in Figure 3c. It shows the typical structure of a density of states. The stationary points of $E'_{sf}(q_n)$ lead to the poles of $P(E'_{sf})$ due to the reciprocal absolute gradient in eq 10. The broader the energy range of $P(E'_{sf})$, the larger the standard deviation σ_{q_n} gets. In Figure 3c, the most relevant range is from 1×10^3 to 2.2×10^3 au. With the expectation value of the energy $\overline{E'_{sf}}$

$$\overline{E'_{sf}} = \int_{-\infty}^{\infty} E'_{sf} \cdot P(E'_{sf})\, dE'_{sf} \tag{11}$$

finally, the standard deviation σ_{q_n} can be calculated as the square root of the variance $\mathrm{Var}(E'_{sf})$

$$\sigma_{q_n} = \sqrt{\mathrm{Var}(E'_{sf})} = \sqrt{\int_{-\infty}^{\infty} (E'_{sf} - \overline{E'_{sf}})^2 P(E'_{sf})\, dE'_{sf}} \tag{12}$$

3. COMPUTATIONAL DETAILS

For all MD simulations, the program package Gromacs[22,23] (version 3.3.2) was used. The solute $Ph_2CH-PPh_3^+$ was described by the all-atom version of the OPLS (optimized potentials for liquid simulations) force field.[24] The atomic charges were determined quantum chemically (DFT, M06-2X, 6-31G(d)) with the program package Gaussian09.[25] For the liquid MeCN, force field parameters developed by Edwards et al.[26] were used that reproduced the viscosity of MeCN well.[27] We used a cubic simulation box with an edge length of 40 Å containing 709 MeCN molecules. The time evolution was calculated using a time step of 1 fs. The temperature was kept constant at 298 K by a Berendsen thermostat. After propagating the system for 10 ps while monitoring the temperature to ensure successful equilibration, snapshots were taken every 200 fs.

The interaction energy E_{sf} between a fragment and a MeCN molecule was evaluated quantum-chemically at the DFT (M06-2X, 6-31G(d)) level of theory with the program package Gaussian09.[25] The molecular potential $\hat{V}_{mol}$ of $Ph_2CH-PPh_3^+$ was calculated with the our own *n*-layered integrated molecular orbital and molecular mechanics (ONIOM) method.[28−30] The high-level system (thicker drawn part of $Ph_2CH-PPh_3^+$ in Figure 4, top) was calculated at the CASSCF(10,10) level of theory with the program package Molpro;[31] the low-level system additionally contains the thinner phenyl rings and is calculated at the DFT (M06-2X) level of theory using Gaussian09.[25] Throughout all calculations, the basis set 6-31G(d) was employed. This approach was already employed and tested in ref 5. The coordinates for the quantum dynamical calculations are the C1−P distance r and the angle ϕ between the atoms P, C1, and the dummy atom X, which is introduced to ensure that the conical intersection (CoIn) lies in the coordinate space. Along the dissociation coordinate r, which describes the distance between the phosphorus atom P and the carbon atom C1 (Figure 4, top), the potential energy surface accounts for the major relaxation processes. Those are given by the lowering of the hybridization from sp^3 to sp^2 at the C1 atom of the methyl group as well as the rotation of the phenyl rings and bond length changes.

The quantum dynamical simulations were carried out by a homemade program that solves the time-dependent Schrödinger equation on a spatial grid using the Chebychev propagation scheme[32] and the G-matrix method for the kinetic operator $\hat{T}$[33−35] (for details, see the Supporting Information). At the beginning of the propagation, the vibrational ground state wave function v = 0 of the electronic ground state S_0 was placed on the S_1 state. It was shifted slightly to a shorter C1−P distance to ensure that the main part of the wave packet crosses the barrier next to the Franck−Condon (FC) region in the gas phase. This is necessary because the two-dimensional coordinate space does not include the minimal barrier.[36] To include it, a third coordinate would be required, which would lead to an enormous increase in the simulation time.

DOI: 10.1021/acs.jctc.5b00046
J. Chem. Theory Comput. 2015, 11, 1987−1995

Journal of Chemical Theory and Computation Article

4. BOND CLEAVAGE OF $Ph_2CH-PPh_3^+$ IN AN EXPLICIT SOLVENT ENVIRONMENT

Our interest lies in the photochemistry of medium-sized organic molecules, in particular in photoinduced dissociative processes. A well-suited example for the significance of the dynamic solvent effect is the bond cleavage of $Ph_2CH-PPh_3^+$ in MeCN[4,5] for which we apply our new QD/MD approach. Salts like $Ph_2CH-PPh_3^+X^-$ are common precursors for the generation of diphenylmethyl cations (Ph_2CH^+) as intermediates in polar and moderately polar solvents (Figure 4).[37]

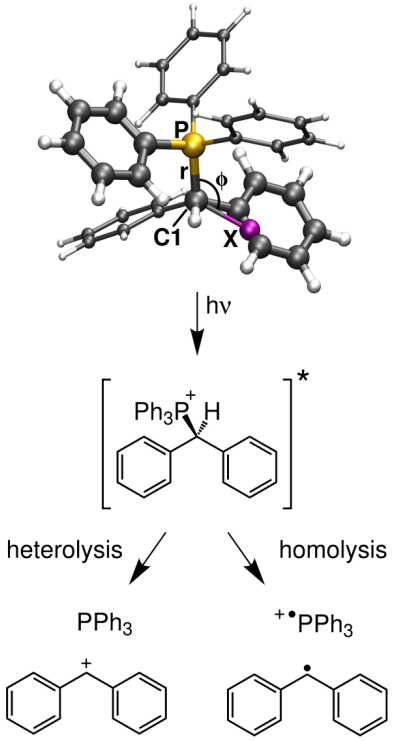

Figure 4. Reaction scheme for the photochemical bond cleavage in diphenylmethyltriphenylphosphonium ions $Ph_2CH-PPh_3^+$. The ground state has heterolytic dissociation character, leading to Ph_2CH^+ and PPh_3 as photoproducts; the character of the first and second excited state is homolytic, generating $Ph_2CH^\bullet$ and $PPh_3^{\bullet+}$. The optimized geometry of $Ph_2CH-PPh_3^+$ is depicted at the top. The potential energy surface used in the quantum dynamical simulations is calculated at the ONIOM level of theory. The high-level system $PhCH_2-PH_2Ph^+$ of the ONIOM calculations contains the thicker drawn part of $Ph_2CH-PPh_3^+$; in the low-level system $Ph_2CH-PPh_3^+$, the thinner drawn phenyl rings are taken into account additionally. The coordinates for the quantum dynamical calculations are the C1–P distance r and the angle ϕ between the atoms P, C1, and the dummy atom X, which is introduced to ensure that the CoIn lies in the coordinate space.

Ultrafast broadband transient absorption experiments revealed that almost exclusively diphenylmethyl cations are formed if the counterion X^- is nonoxidizable (e.g., BF_4^- or SbF_6^-).[38] Quantum chemical investigations showed that after a local $\pi-\pi^*$excitation on the PPh_3 moiety the C1–P bond cleavage can take place by crossing a small barrier in the first excited state S_1.[36] In the dissociation limit, the S_1 state leads to the formation of a radical pair $Ph_2CH^\bullet$ and $PPh_3^{\bullet+}$ (homolytic bond cleavage), whereas in the ground state S_0, the desired Ph_2CH^+ cations and PPh_3 are generated (heterolytic bond cleavage). QD simulations clarified that for the bond cleavage in $Ph_2CH-PPh_3^+$ ions the dynamic solvent effect is essential. By including the frictional force of the solvent implicitly, we were able to explain the experimentally observed initial product formation on the several hundreds of femtoseconds time scale.[4,5,38] The applied dynamic continuum ansatz combines Stokes' law with the dynamic viscosity of the solvent to model the deceleration by the solvent cage.[5] This enables the system to reach a CoIn, which connects both product channels and allows the fast generation of Ph_2CH^+ cations.[5]

The presented QD/MD approach goes one step further and includes an atomistic modeling of the solvent cage. Here, the MeCN solvent cage is obtained from MD simulations, during which the methyl group of MeCN is treated as a united atom.[26] If the bending is neglected, then MeCN can be treated as linear. One advantage of this simplification is that the number of coordinates in the orientation space can be reduced to five if one of the rotational axes of MeCN is selected to be collinear with the molecular axis. During the QD calculations, the positions of the solvent molecules around the solute $Ph_2CH-PPh_3^+$ are frozen, as in scenario one (introduced in Section 2.1). This is legitimized by the fact that the bond cleavage takes place within 200–300 fs and is faster than the motion of the solvent molecules in the thermodynamic equilibrium. Thus, the initially experienced solvent potential V_{solv} is crucial for the time evolution of the wave packet, although the shape of the solvent cage will change during the reaction process.

The five coordinates $|\vec{r}_{sf}|$, α_s, α_f, β_s, and β_f to describe E_{sf} in the orientation space are presented in Figure 5. $|\vec{r}_{sf}|$ is the

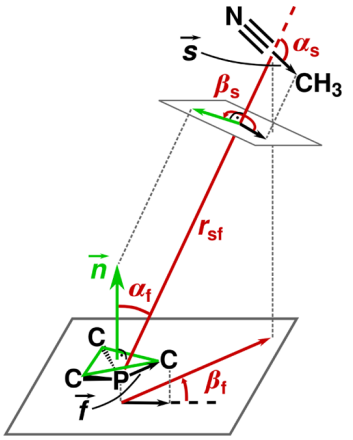

Figure 5. Definition of the five coordinates r_{sf}, α_s, α_f, β_s, and β_f describing the relative orientation of one MeCN and the PPh_3 moiety. For the sake of simplicity, only the C atoms of the phenyl rings that are bound to the P atom are shown; the remaining atoms are omitted.

length of the connecting vector between the center of mass of MeCN and the central atom of the two fragments: the P atom in the case of PPh_3 and the methyl C atom for Ph_2CH. The remaining four coordinates are angles describing the rotation of the fragment (α_f, β_f) and of the solvent (α_s, β_s). In detail, α_f specifies the angle between $\vec{r}_{sf}$ and the normal vector $\vec{n}$ of the plane (green triangle) defined by the three C atoms attached to the P atom. It is defined in the interval $[0;\pi]$. β_f characterizes the rotation of the PPh_3 fragment around $\vec{n}$. To this, we use the auxiliary vector $\vec{f}$, which points from the P atom to one C atom. β_f is then defined as the angle (counterclockwise) between the projections of the vectors $\vec{r}_{sf}$ and $\vec{f}$ into the

DOI: 10.1021/acs.jctc.5b00046
J. Chem. Theory Comput. 2015, 11, 1987–1995

C−C−C plane. The angle β_f takes values between $[0;2\pi[$. α_s is the angle between $\vec{r}_{sf}$ and the vector $\vec{s}$, which points from the center of mass of MeCN to its methyl group. The angle α_s is defined in the interval $[0;\pi]$. β_s indicates the rotation of MeCN around $\vec{r}_{sf}$ and is defined in the interval $[0;2\pi[$. It is calculated projecting the vectors $\vec{s}$ and $\vec{n}$ into a plane perpendicular to $\vec{r}_{sf}$. The angle between these projected vectors (again in counterclockwise direction) is β_s. For the second fragment, Ph_2CH, generated in the bond cleavage, the methyl C atom replaces the P atom and one atom of the C−C−C plane is exchanged by the H atom. The selected coordinates are orthogonal and guarantee that each position in the orientation space is uniquely defined by one coordinate quintuple.

In the next step, the importance of the five coordinates for the interaction energy E_{sf} has to be evaluated. The significance of the distance coordinate is obvious; the rating of the four angular coordinates has to be determined according to the standard deviations σ_{q_n}. For this, 2500 snapshots along MD trajectories were analyzed. The orientations of all MeCN molecules with a maximum distance of 8.0 Å between the two nearest atoms of the fragment and the solvent molecule were calculated. Beyond 8.0 Å, no influence of the structure of the solute on the solvent orientation was observed. As E_{sf} depends on all five coordinates, orientational effects along one coordinate can be compensated by another one. This happens when the preferred value for one coordinate depends systematically on the value of one or more other coordinates. To ensure that no compensation of orientations occurs for the tested coordinate, we divided the interval of the remaining angular coordinates in half and compared the shape of the obtained probability distributions $P(q_n)$ of both parts with each other and the initial shape. If they are similar enough, then no further dividing is necessary; if they are not, then the procedure is repeated for both halves. When convergence of the shape is reached in step i, the $(i-1)$th partitioning is used to calculate the m related standard deviations $\sigma^j_{q_n}$ for the m resulting intervals with $j \in \{1, 2, ..., m\}$. The standard deviation σ_{q_n} for the whole domain of definition is calculated via the average of the variances $(\sigma^j_{q_n})^2$ weighted by the proportion of elements N_j/N_0 in the interval j according to

$$\sigma_{q_n} = \sqrt{\sum_{j=1}^{m} \frac{N_j}{N_0} (\sigma^j_{q_n})^2} \tag{13}$$

where N_j is the number of elements in the interval j and $N_0 = \sum_{j=1}^{m} N_j$ (for details, see the Supporting Information). As the probability distributions are quite noisy, a comparison of the raw data is difficult. Thus, $P(q_n)$ was smoothed by applying a low-pass Butterworth filter before being normalized. Additionally, we calculated the integral of the absolute difference of the normalized probability distributions to check that the absolute deviations are not too large. All values were below 12% (for details, see the Supporting Information).

The values of the standard deviations σ_{q_n} along the four angular coordinates calculated following eq 13 are given in Table 1. Their values are between 7.21×10^{-5} and 2.71×10^{-4} au. In general, the ones for the PPh_3 moiety are slightly larger than the ones for Ph_2CH. This could be due to the less sterically demanding H atom that replaces one phenyl ring, which leads to a flatter potential around the H atom and thus

Table 1. Standard Deviation σ_{q_n} of the Interaction Energy between the Molecular Fragment and MeCN along the Four Angular Coordinates α_s, β_s, α_f, and β_f

fragment	σ_{α_s} (au)	σ_{β_s} (au)	σ_{α_f} (au)	σ_{β_f} (au)
PPh_3	1.58×10^{-4}	7.61×10^{-5}	1.62×10^{-4}	2.71×10^{-4}
Ph_2CH	1.28×10^{-4}	7.21×10^{-5}	1.03×10^{-4}	1.34×10^{-4}

reduces the standard deviation in the probability distributions $P(E_{sf})$. We carefully checked the influence of the filtering process on the values of σ_{q_n}. They change slightly, but the observed trends are fairly robust.

For the PPh_3 moiety, σ_{β_s} has the smallest value. The other values are at least twice as large; the largest one is observed for σ_{β_f}. A similar picture is obtained for the Ph_2CH moiety. Here also, σ_{β_s} has the smallest value. Since for both fragments σ_{β_s} has the smallest value, β_s is the least important coordinate for the interaction energy E_{sf}. As the E_{sf} values entering the QD simulations are evaluated quantum chemically, the reduction of its degrees of freedom from $n = 5$ to $n = 4$ leads to a significant reduction in computational time. Thus, the solvent potential $\hat{V}_{solv}(r,\phi)$ is approximated as

$$\hat{V}_{solv}(r,\phi) = \sum_{i=1}^{N_{solv}} \sum_{j=1}^{2} E_{sf}\left(\left|\vec{r}^{ij}_{sf}(r,\phi)\right|, \alpha^{ij}_s(r,\phi), \alpha^{ij}_f(r,\phi), \beta^{ij}_f(r,\phi)\right) \tag{14}$$

We calculated $V_{solv}(r,\phi)$ for 50 snapshots of the MD trajectories with a time interval of 200 fs between the snapshots and simulated the bond cleavage process quantum dynamically for each of the obtained V_{tot}. For reference, we show the molecular potential $V_{mol}(r,\phi)$ of the first excited state S_1 without any solvent influence in Figure 6. The FC point is

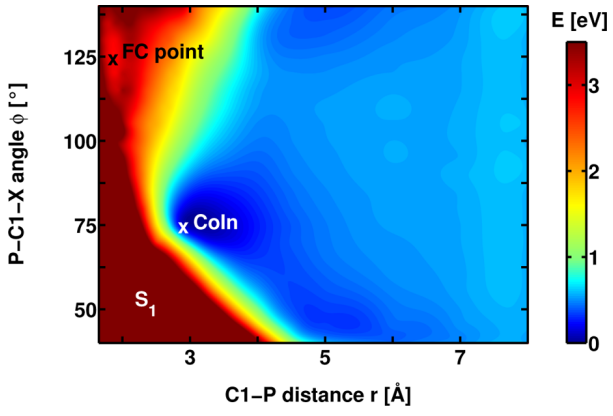

Figure 6. Molecular potential V_{mol} of the first excited state S_1 of $Ph_2CH{-}PPh_3^+$ calculated at the ONIOM (CASSCF(10,10)/M06-2X/6-31G(d)) level of theory. The potential is shown up to a C1−P distance of $r = 8.0$ Å to clarify that V_{mol} has no barrier along the r direction.

located at a C1−P distance of $r = 1.87$ Å and a P−C1−X angle of $\phi = 125°$, the S_0/S_1 CoIn at $r = 2.9$ Å and $\phi = 75°$,[5] and the global S_1 minimum next to the S_0/S_1 CoIn.

The left column of Figure 7 depicts two selected MD snapshots. The solute $Ph_2CH{-}PPh_3^+$ is drawn in a space-filling representation; the MeCN solvent molecules are shown in a ball and stick representation. The white ball represents the

DOI: 10.1021/acs.jctc.5b00046
J. Chem. Theory Comput. 2015, 11, 1987−1995

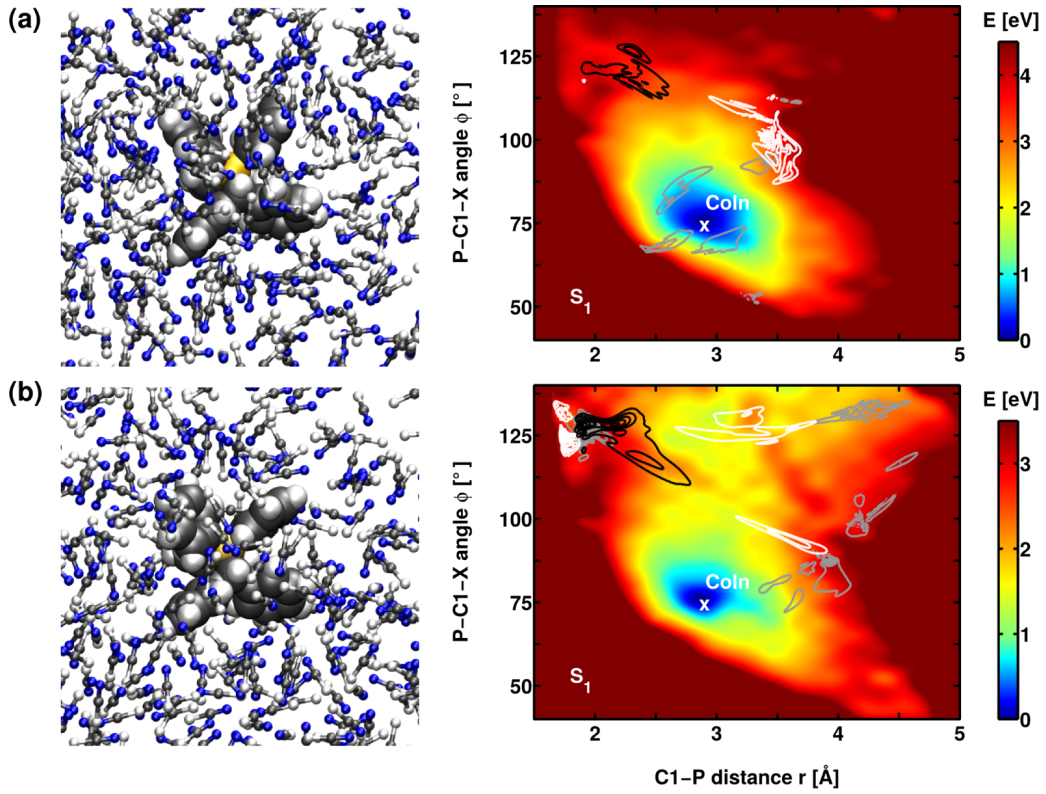

Figure 7. Two selected snapshots of $Ph_2CH{-}PPh_3^+$ in a box of MeCN taken from the MD simulation (left column). The solute $Ph_2CH{-}PPh_3^+$ is drawn in a space-filling representation; the MeCN solvent molecules are shown in a ball and stick representation. The white ball represents the methyl group, the gray one the C atom and the blue one the N atom. The corresponding total potentials $V_{tot}(r,\phi)$ are depicted in the right column together with three snapshots of the propagated wave packets. For (a), they are taken at 90 fs (black isolines), 180 fs (white isolines), and 240 fs (gray isolines), and for (b), at 90 fs (black isolines), 160 fs (white isolines), and 240 fs (gray isolines) after starting the propagation in the FC region. In the total potential V_{tot} shown in (a), the whole wave packet explores the channel toward the global minimum and oscillates around the CoIn. In contrast, the wave packet in V_{tot} depicted in (b) splits and explores both offered dissociation pathways.

methyl group, the gray one the C atom and the blue one the N atom. The right column of Figure 7 shows the total potential V_{tot} of the first excited state S_1 for the depicted solvent arrangements together with three snapshots from the wave packet evolution. The snapshots in Figure 7a are taken at 90 fs (black isolines), 180 fs (white isolines), and 240 fs (gray isolines), and in Figure 7b, at 90 fs (black isolines), 160 fs (white isolines), and 240 fs (gray isolines) after starting the propagation in the FC region of the S_1 state.

First, we focus on the two resulting V_{tot}, which exhibit significant differences in their topography. The solvent potential generates a barrier at large C1−P distances of approximately r = 3.5 Å, where the dissociating fragments approach the solvent cage. This leads to the steep rise of the total potential, which is not present in the purely molecular potential V_{mol} (Figure 6). The first V_{tot} (Figure 7a, right) has one valley pointing toward the CoIn. In contrast, the second V_{tot} (Figure 7b, right) offers two reaction channels. One points toward the CoIn, and the other one leads away from the CoIn. These examples represent the two limiting cases found in the 50 snapshots taken from the MD trajectories. The first case occurs about two times more often than the second.

The quantum dynamics of the bond cleavage is visualized by the selected snapshots from the wave packet propagation. In Figure 7a, the wave packet leaves the FC area about 90 fs after the propagation has been started (black isolines). Subsequently, it hits the potential barrier of the solvent cage at about r = 3.7 Å and ϕ = 100° (white isolines). Then, it evolves toward the CoIn and oscillates back and forth around the global minimum of V_{tot}. The time evolution of the wave packet in the second solvent arrangement (Figure 7b) differs fundamentally. After 90 fs, a part of the wave packet crosses the barrier in the FC region and moves toward a larger C1−P distance (black isolines). Compared to the propagation in Figure 7a, a significant fraction stays in the FC minimum. The part overcoming the barrier already reveals a splitting toward the two reaction channels. At 160 fs, the branching of the wave packet is completed (white isolines). The upper fraction moves toward larger ϕ values and dissociates in the first excited state, leading to the formation of radicals (gray isolines). The lower part hits the potential barrier at around r = 4.0 Å and ϕ = 90° and is guided toward the CoIn with the ground state.

The two examples demonstrate the importance of the individual arrangement of the solvent cage. It has a significant impact on the direction in which the wave packet evolves and whether a splitting occurs. The second reaction channel opens when no solvent molecules hinder the motion of the reactant along that channel. This situation can be captured only by a microscopic description of the solvent environment, as provided by our QD/MD ansatz.

For an overall picture of the bond cleavage, we averaged the wave packet propagations for the 50 different environments according to eq 4. As we found convergence in the population dynamics, 50 snapshots proved to be a sufficiently large number (for details, see the Supporting Information). To analyze the population distribution, we separated the two-dimensional

DOI: 10.1021/acs.jctc.5b00046
J. Chem. Theory Comput. 2015, 11, 1987−1995

potentials in three areas. They correspond to the FC region ($r \leq 2.1$ Å and $\phi > 105°$; gray rectangle in the inset of Figure 8),

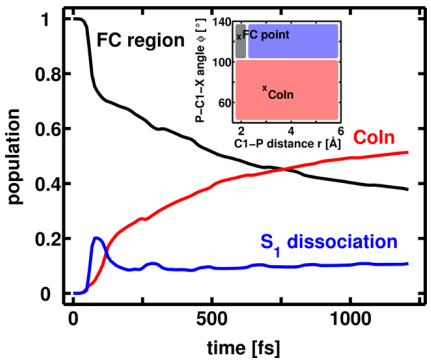

Figure 8. Population dynamics for the QD simulation of the bond cleavage of $Ph_2CH{-}PPh_3^+$ averaged over 50 different solvent arrangements taken from MD trajectories. The population in the FC region (black line) is located in the gray rectangle in the inset, the population in the S_1 dissociation area (blue line) in the blue rectangle, and the population around the CoIn (red line) in the red rectangle.

the dissociation channel in the S_1 state ($r > 2.1$ Å and $\phi > 105°$; blue rectangle), and the area around the CoIn ($\phi \leq 105°$; red rectangle). To start the propagation, the vibrational ground state wave function $v = 0$ is transferred to the S_1 state. Accordingly, the population in the FC region is one at $t = 0$ fs (black line). Within the first 70 fs, 30% of the population leave the FC region with an initial momentum along the r direction, observable in the sudden increase of population in the S_1 dissociation channel (blue line). At about 100 fs, the averaged wave packet is deflected toward the CoIn. Correspondingly, the population now increases in this area (red line). This increase continues moderately while the S_1 dissociation channel stays constant. After 1200 fs, the population is distributed as follows: 40% is still located in the FC region, 10% dissociated in the first excited state, and 50% reached the CoIn, from where the population can relax to the ground state[5,36] to form the experimentally observed Ph_2CH^+ cations. The explicit treatment of the solvent provides a passage toward the CoIn similar to the results from the dynamic continuum ansatz.[5] Furthermore, it captures the individual arrangements of the solvent cage and, based on this, reveals the formation of different reaction channels.

5. SUMMARY AND CONCLUSIONS

We presented our newly developed QD/MD method to include the explicit solvent environment in reactive QD simulations. The method merges MD simulations of the reactant in a box of solvent molecules with QD calculations of the reactant's dynamics. The interaction between the QD system and the solvent molecules is incorporated in the Hamiltonian for the QD calculations. The interaction energy E_{sf} between the reactant and a solvent molecule depends on their relative orientation, which, in general, can be described by six degrees of freedom q_n with $n \in \{1, 2, ..., 6\}$ in the orientation space. We showed that MD trajectories also provide the necessary information to calculate the standard deviation σ_{q_n} of the interaction energy $E_{sf}(q_n)$ as a decisive criterion for rating the coordinates q_n. With this procedure, the least relevant degrees of freedom can be eliminated to reduce the computational cost for the precalculation of the quantum chemical database.

To demonstrate the impact of the solvent cage treated explicitly with our new QD/MD approach, we chose the photoinduced bond cleavage of $Ph_2CH{-}PPh_3^+$. It has been shown that consideration of dynamic solvent effects during the quantum dynamical simulation of the process is crucial to explain the experimentally observed heterolytic bond cleavage generating Ph_2CH^+ cations.[5,38] We performed MD simulations of one $Ph_2CH{-}PPh_3^+$ in a box of MeCN. The rating of the coordinates in the orientation space led to four necessary coordinates: the distance coordinate r_{sf} and three angular coordinates α_s, $\alpha_{\bar{p}}$ and β_f. With them, we calculated the solvent potential $V_{solv}(r,\phi)$ for 50 snapshots of the MD simulations and performed QD simulations for each of the obtained total potentials $V_{tot}(r,\phi)$. The solvent cage hinders the free dissociation in the S_1 state. In the microscopic description, two different dissociation channels emerged. One leads to dissociation in the S_1 state and homolytic bond cleavage, and the other one leads to a S_0/S_1 CoIn, where the system can relax to the ground state, which has heterolytic dissociation character. The average over all QD simulations gives the overall picture of the photoinduced bond cleavage. 83% of the excited state population that leaves the FC region approaches the CoIn, where the formation of Ph_2CH^+ cations can take place. The remaining 17% pass through the second dissociation channel of the homolytic bond cleavage. Thus, our new QD/MD approach provides a passage toward the CoIn similar to the results from the dynamic continuum ansatz[5] and explains the experimental observations for the initial product formation.[38] Compared to the dynamic continuum ansatz, it goes one step further and gives a more detailed microscopic picture of the whole process. It allows for the description of different reaction channels reflecting the individual arrangements of the solvent cage. Furthermore, the flexibility of the solvent cage with temperature and solvent composition can be modeled.

The presented results demonstrate encouragingly that a combination of MD and QD simulations is an appropriate tool to describe photoinduced ultrafast molecular processes in a complex environment. The next step for future development is the inclusion of the feedback of the QD system on the motion of the classically treated solvent molecules. This will further broaden the application range to reactions where the dynamics of the reactant and solvent are on a comparable time scale.

■ ASSOCIATED CONTENT

Supporting Information

Details of the quantum dynamical simulations, the partitioning of the coordinates in the orientation space to calculate the probability distributions $P(q_n)$, the convergence of the population dynamics, a qualitative comparison of the required computing time, and geometries in *xyz* format. This material is available free of charge via the Internet at http://pubs.acs.org.

■ AUTHOR INFORMATION

Corresponding Author

*E-mail: regina.de_vivie@cup.uni-muenchen.de.

Funding

Financial support by the Deutsche Forschungsgemeinschaft through SFB749 and the excellence cluster Munich-Centre for Advanced Photonics (MAP) is acknowledged.

DOI: 10.1021/acs.jctc.5b00046
J. Chem. Theory Comput. 2015, 11, 1987−1995

Notes

The authors declare no competing financial interest.

■ ACKNOWLEDGMENTS

We thank Eberhard Riedle for fruitful discussions and Andrea Kreppel for carrying out first test calculations. S.T. thanks the Dr. Klaus Römer-Stiftung for financial support.

■ REFERENCES

(1) Reichardt, C.; Welton, T. *Solvents and Solvent Effects in Organic Chemistry*; Wiley-VCH: Weinheim, Germany, 2011.
(2) Sailer, C. F.; Thallmair, S.; Fingerhut, B. P.; Nolte, C.; Ammer, J.; Mayr, H.; de Vivie-Riedle, R.; Pugliesi, I.; Riedle, E. *ChemPhysChem* **2013**, *14*, 1423−1437.
(3) Struebing, H.; Ganase, Z.; Karamertzanis, P. G.; Siougkrou, E.; Haycock, P.; Piccione, P. M.; Armstrong, A.; Galindo, A.; Adjiman, C. S. *Nat. Chem.* **2013**, *5*, 952−957.
(4) Thallmair, S.; Kowalewski, M.; Fingerhut, B.; Sailer, C.; de Vivie-Riedle, R. *EPJ Web Conf.* **2013**, *41*, 05043−1−05043−3.
(5) Thallmair, S.; Kowalewski, M.; Zauleck, J. P. P.; Roos, M. K.; de Vivie-Riedle, R. *J. Phys. Chem. Lett.* **2014**, *5*, 3480−3485.
(6) Benjamin, I.; Wilson, K. R. *J. Chem. Phys.* **1989**, *90*, 4176−4197.
(7) Krylov, A. I.; Gerber, R. B. *J. Chem. Phys.* **1994**, *100*, 4242−4252.
(8) Amatatsu, Y.; Morokuma, K. *Chem. Phys. Lett.* **1995**, *245*, 469−474.
(9) Winter, N.; Chorny, I.; Vieceli, J.; Benjamin, I. *J. Chem. Phys.* **2003**, *119*, 2127−2143.
(10) Moskun, A. C.; Jailaubekov, A. E.; Bradforth, S. E.; Tao, G.; Stratt, R. M. *Science* **2006**, *311*, 1907−1911.
(11) Horng, M. L.; Gardecki, J. A.; Papazyan, A.; Maroncelli, M. *J. Phys. Chem.* **1995**, *99*, 17311−17337.
(12) Caricato, M.; Mennucci, B.; Tomasi, J.; Ingrosso, F.; Cammi, R.; Corni, S.; Scalmani, G. *J. Chem. Phys.* **2006**, *124*, 124520-1−124520-13.
(13) Moskun, A. C.; Bradforth, S. E. *J. Chem. Phys.* **2003**, *119*, 4500−4515.
(14) Sailer, C. F.; Krebs, N.; Fingerhut, B. P.; de Vivie-Riedle, R.; Riedle, E. *EPJ Web Conf.* **2013**, *41*, 05042-1−05042-3.
(15) Cui, G.; Thiel, W. *Angew. Chem., Int. Ed.* **2013**, *52*, 433−436.
(16) Nenov, A.; Cordes, T.; Herzog, T. T.; Zinth, W.; de Vivie-Riedle, R. *J. Phys. Chem. A* **2010**, *114*, 13016−13030.
(17) Weingart, O.; Lan, Z.; Koslowski, A.; Thiel, W. *J. Phys. Chem. Lett.* **2011**, *2*, 1506−1509.
(18) Gollub, C.; Kowalewski, M.; Thallmair, S.; de Vivie-Riedle, R. *Phys. Chem. Chem. Phys.* **2010**, *12*, 15780−15787.
(19) von den Hoff, P.; Thallmair, S.; Kowalewski, M.; Siemering, R.; de Vivie-Riedle, R. *Phys. Chem. Chem. Phys.* **2012**, *14*, 14460−14485.
(20) Fingerhut, B. P.; Sailer, C. F.; Ammer, J.; Riedle, E.; de Vivie-Riedle, R. *J. Phys. Chem. A* **2012**, *116*, 11064−11074.
(21) Bronstein, I. N.; Semendjajew, K. A.; Musiol, G.; Mühlig, H. *Taschenbuch der Mathematik*, 7th ed.; Wissenschaftlicher Verlag Harri Deutsch GmbH: Frankfurt am Main, Germany, 2008.
(22) Lindahl, E.; Hess, B.; van der Spoel, D. *J. Mol. Model.* **2001**, *7*, 306−317.
(23) van der Spoel, D.; Lindahl, E.; Hess, B.; Groenhof, G.; Mark, A. E.; Berendsen, H. J. C. *J. Comput. Chem.* **2005**, *26*, 1701−1718.
(24) Jorgensen, W. L.; Maxwell, D. S.; Tirado-Rives, J. *J. Am. Chem. Soc.* **1996**, *118*, 11225−11236.
(25) Frisch, M. J.; Trucks, G. W.; Schlegel, H. B.; Scuseria, G. E.; Robb, M. A.; Cheeseman, J. R.; Scalmani, G.; Barone, V.; Mennucci, B.; Petersson, G. A.; Nakatsuji, H.; Caricato, M.; Li, X.; Hratchian, H. P.; Izmaylov, A. F.; Bloino, J.; Zheng, G.; Sonnenberg, J. L.; Hada, M.; Ehara, M.; Toyota, K.; Fukuda, R.; Hasegawa, J.; Ishida, M.; Nakajima, T.; Honda, Y.; Kitao, O.; Nakai, H.; Vreven, T.; Montgomery, J. A., Jr.; Peralta, J. E.; Ogliaro, F.; Bearpark, M.; Heyd, J. J.; Brothers, E.; Kudin, K. N.; Staroverov, V. N.; Kobayashi, R.; Normand, J.; Raghavachari, K.; Rendell, A.; Burant, J. C.; Iyengar, S. S.; Tomasi, J.; Cossi, M.; Rega, N.; Millam, J. M.; Klene, M.; Knox, J. E.; Cross, J. B.; Bakken, V.; Adamo, C.; Jaramillo, J.; Gomperts, R.; Stratmann, R. E.; Yazyev, O.; Austin, A. J.; Cammi, R.; Pomelli, C.; Ochterski, J. W.; Martin, R. L.; Morokuma, K.; Zakrzewski, V. G.; Voth, G. A.; Salvador, P.; Dannenberg, J. J.; Dapprich, S.; Daniels, A. D.; Farkas, O.; Foresman, J. B.; Ortiz, J. V.; Cioslowski, J.; Fox, D. J. *Gaussian 09*, revision A.02; Gaussian, Inc.: Wallingford, CT, 2009.
(26) Edwards, D. M.; Madden, P. A.; McDonald, I. R. *Mol. Phys.* **1984**, *51*, 1141−1161.
(27) Mountain, R. D. *J. Chem. Phys.* **1997**, *107*, 3921−3923.
(28) Svensson, M.; Humbel, S.; Froese, R. D. J.; Matsubara, T.; Sieber, S.; Morokuma, K. *J. Phys. Chem.* **1996**, *100*, 19357−19363.
(29) Bearpark, M. J.; Larkin, S. M.; Vreven, T. *J. Phys. Chem. A* **2008**, *112*, 7286−7295.
(30) Fingerhut, B. P.; Oesterling, S.; Haiser, K.; Heil, K.; Glas, A.; Schreier, W. J.; Zinth, W.; Carell, T.; de Vivie-Riedle, R. *J. Chem. Phys.* **2012**, *136*, 204307.
(31) Werner, H.-J.; Knowles, P. J.; Knizia, G.; Manby, F. R.; Schütz, M.; Celani, P.; Korona, T.; Lindh, R.; Mitrushenkov, A.; Rauhut, G.; Shamasundar, K. R.; Adler, T. B.; Amos, R. D.; Bernhardsson, A.; Berning, A.; Cooper, D. L.; Deegan, M. J. O.; Dobbyn, A. J.; Eckert, F.; Goll, E.; Hampel, C.; Hesselmann, A.; Hetzer, G.; Hrenar, T.; Jansen, G.; Köppl, C.; Liu, Y.; Lloyd, A. W; Mata, R. A.; May, A. J.; McNicholas, S. J.; Meyer, W.; Mura, M. E.; Nicklass, A.; O'Neill, D. P.; Palmieri, P.; Peng, D.; Pflüger, K.; Pitzer, R.; Reiher, M.; Shiozaki, T.; Stoll, H.; Stone, A. J.; Tarroni, R.; Thorsteinsson, T.; Wang, M. *MOLPRO*, version 2012.1, 2012.
(32) Tal-Ezer, H.; Kosloff, R. *J. Chem. Phys.* **1984**, *81*, 3967−3971.
(33) Wilson, E. B., Jr.; Decius, J. C.; Cross, P. C. *Molecular Vibrations*; McGraw-Hill: New York, USA, 1955.
(34) Schaad, L.; Hu, J. *J. Mol. Struct.: THEOCHEM* **1989**, *185*, 203−215.
(35) Kowalewski, M.; Mikosch, J.; Wester, R.; de Vivie-Riedle, R. *J. Phys. Chem. A* **2014**, *118*, 4661−4669.
(36) Thallmair, S.; Fingerhut, B. P.; de Vivie-Riedle, R. *J. Phys. Chem. A* **2013**, *117*, 10626−10633.
(37) Ammer, J.; Mayr, H. *J. Phys. Org. Chem.* **2013**, *26*, 956−969.
(38) Ammer, J.; Sailer, C. F.; Riedle, E.; Mayr, H. *J. Am. Chem. Soc.* **2012**, *134*, 11481−11494.

DOI: 10.1021/acs.jctc.5b00046
J. Chem. Theory Comput. 2015, 11, 1987−1995

2.3 Explicit description of solvents using a quantum-classical TDSCF approach

If processes of more similar timescales for solute and solvent are studied, the use of frozen solvent arrangements misses important effects. This can be seen in collisions, where the reaction of a solvent molecule influences the solute's motion. Coupling the time evolution of the solvent to the time evolution of the solute offers a general improvement.

For this, a quantum-classical TDSCF [130–133] can be used. Here, the time evolution of the solute is treated using QD and the evolution of the solvent using classical mechanics. The interaction between the two subsystems is contained in their respective potential energies on the other system or the corresponding forces. For grid based QD, an illustration can be seen in fig. 2.2. Regarding the classical system (fig. 2.2.a), the potential energy or force acting on it due to the solute is weighted using the probability density $|\Psi|^2$ of the solute at each grid point, effectively using an expectation value. For the quantum system (fig. 2.2.b), at each point on its grid the potential energy to every solvent molecule is calculated and is added to the solutes internal PES.

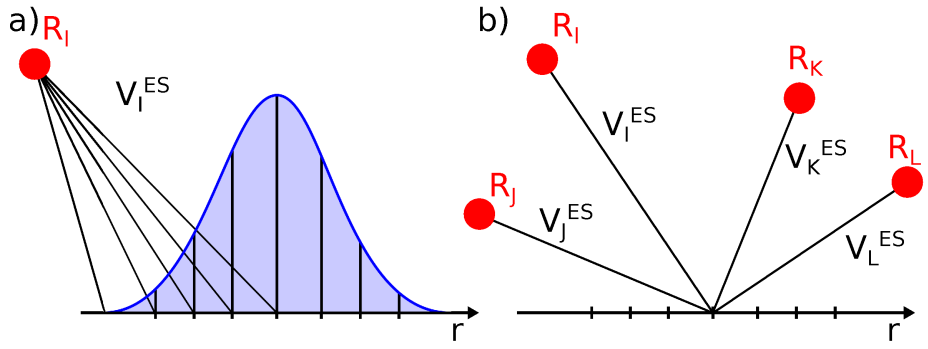

Figure 2.2: Schematic overview of the interactions between the quantum and classical subsystem. a) shows the weighted forces acting on the classical particles and b) shows the influences of four classical particles on the PES of the quantum system. The V_I^{ES} and the R_I are the interaction potentials between the Ith solvent particle and the solute and coordinates of the Ith solvent particle, respectively. r is a reactive coordinate of the solute.

For the dynamics simulations, once again enough different initial solvent arrangements have to be used to reach convergence in the averaged results. With the use of multiple calculations comes the possibility to study decoherence. Two different ways to do this are explored, using the density matrix in the basis of vibrational eigenstates and the Wigner function.

The article "Reactive quantum dynamics coupled to classical solvent dynamics using an extended quantum-classical TDSCF approach" submitted to *The Journal of Physical Chemistry A* illustrates the cQDMD approach, using the examples of the photodissociation of ICN and the photorelaxation of uracil. The key points of the article are:

- The working equations for the solute QD and the solvent MD according to quantum-classical TDSCF are given by

$$i\frac{\partial \Psi^{\mathrm{S}}}{\partial t} = \left(T^{\mathrm{S}} + V^{\mathrm{S}}_{\mathrm{PES}} + \sum_I V_I^{\mathrm{ES}} \right) \Psi^{\mathrm{S}} \tag{2.4}$$

  and

$$M_I \ddot{R}_I = -\nabla_I \sum_J V^{\mathrm{E}}_{IJ} - \nabla_I \langle \Psi^{\mathrm{S}} | V_I^{\mathrm{ES}} | \Psi^{\mathrm{S}} \rangle \ , \tag{2.5}$$

respectively. Here Ψ^{S} is the wavefunction of the solute, T^{S} and $V^{\mathrm{S}}_{\mathrm{PES}}$ are the same as $\hat{T}_{\mathrm{nuc}}$ and $\hat{V}_{\mathrm{solv}}$ in section 2.2, namely the kinetic and potential energy operators of the solute on its PES and V^{E}_{IJ} is the interaction potential between the Ith and Jth solvent particle. To be able to include translational and rotational degrees of freedom of the solute in the grid based calculations, which are restricted to low dimensionality, a virtual rigid classical solute (VRCS) system is introduced as an extension to the TDSCF approach. This efficiently allows for rotation and translation of the solute using classical mechanics.

- The cQDMD approach is applied to the model system of the photodissociation of ICN in liquid argon. Using 49 different solvent arrangements leads to converged results. The percentage of undissociated ICN increases from 3 % in gas phase to 45 % in liquid argon. Conservation of total energy is achieved to a precision of the order of $10^{-6}\,\mathrm{E_h}$.

- Decoherence caused by the liquid solvent is studied for the same system using slightly different, non-dissociative initial conditions for ICN. The influence is shown by means of the Wigner function and a decoherence time comparable to similar systems is found.

- The cQDMD approach is also applied to the more complex system of the photorelaxation of uracil in water, which is important in the study of the prevention of photodamage in RNA. Using 35 solvent arrangements, the influence of the initial conditions on the relaxation time is shown. While the average relaxation time remains almost the same, the individual solvent arrangements can accelerate or decelerate the relaxation notably.

In the following, the article “Reactive quantum dynamics coupled to classical solvent dynamics using an extended quantum-classical TDSCF approach” submitted to *The Journal of Physical Chemistry A* is reprinted with permission from *J. Chem. Theory Comput.*; The Supporting Information is reprinted in appendix B.

Reactive quantum dynamics coupled to classical solvent dynamics using an extended quantum-classical TDSCF approach

Julius P. P. Zauleck, Martin T. Peschel, Florian Rott, Sebastian Thallmair, and Regina de Vivie-Riedle*

Department of Chemistry, Ludwig-Maximilians-Universität München, D-81377 München, Germany

E-mail: regina.de_vivie@cup.uni-muenchen.de

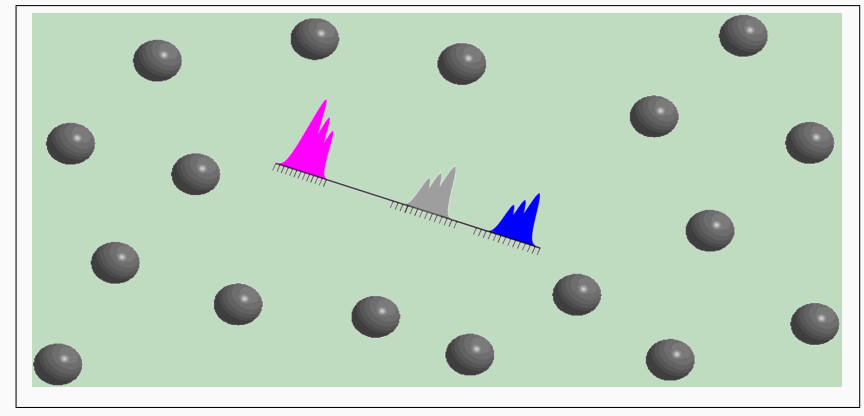

*To whom correspondence should be addressed

Abstract

The inclusion of solvent effects in the theoretical analysis of molecular processes becomes increasingly important. Currently, it is not feasible to directly include the solvent on the quantum level. We present an approach advancing the time-dependent self-consistent field method by combining quantum and classical dynamics. The classical dynamics of the solvent is coupled to the wavepacket dynamics of the solute and rotational and translational degrees of freedom of the solute are included classically. This allows quantum dynamics simulations that are decided by environment interactions without explicit separation of time scales. We show the application to the dissociation of ICN in liquid Ar as a proof of principal system and to the more applied example of uracil in water.

Introduction

Solvents play an important role in molecular processes. They are the medium in which a majority of reactions take place and influence the course of reactions directly or indirectly. While most catalytic effects of the solvent can be qualitatively described very well and then be modeled accordingly,[1] the more subtle influences like viscosity or electrostatic interaction are often more difficult to include.[2,3] However, they sometimes are decisive to the outcome of a reaction.[4–9] One way this can happen is by electrostatic stabilization of certain reaction pathways, thereby favoring their respective products.[5,6] Other possibilities are dynamic solvent effects[7,8,10] that can for example deflect dissociative motions, because solvent molecules have to be pushed away. This can favor one of several competing pathways as well. Further complexity is added if quantum effects such as tunneling and passing through conical intersections (CoIn)[11,12] occur. Then, quantum dynamics (QD) simulations are most suited.

There exist a number of strategies to describe a mixed quantum-classical interaction for different systems. Examples are the polarizable continuum models[13–15] that allow to approximate solvent effects in quantum chemical calculations using an implicit description, the linearized semiclassical initial value representation,[16–19] which describes all particles of a system with increasing

quantum behavior until convergence is reached and the use of the Liouville-von Neumann equation[20–23] for a quantum-classically coupled approach[24–26] which introduces the environment as a classically treated bath and can with approximations be applied to systems with environments of realistic sizes.[26] We are interested in a description suited for general reaction dynamics where the focus lies on the solute that has to be treated quantum dynamically. In this direction we developed two methods for modeling solvent effects in QD simulations, either implicitly in a continuum model by the use of a friction force[7] or explicitly by using molecular dynamics (MD) snapshots of the solvent.[8] Both approaches cover many scenarios involving solute-solvent interaction, but not all. As the former calculates the interaction as Stokes' friction caused by viscosity, cases where collisions between solute and solvent atoms deflect the internal momentum of the solute are not taken into account. Those collisions are included in the latter method, but as it relies on frozen snapshots, the response of the solvent to the motion of the solute is not included. For some systems this is sufficient as basic repulsion by the solvent cage can introduce the required deceleration. In the case of more complex reactions a response of the solvent cage is desirable. For example, if the shape of the solute changes considerably due to the formation of a new bond, the solvent environment has to rearrange accordingly. In case of a frozen snapshot, the solute will prevent the reaction and additional information about the system is necessary for a meaningful interpretation. If the solvent is allowed to respond, the solvent cage can make space for the expanding solute in real time. Thus, the natural next step is to explicitly include the solvent dynamics to enable a fully coupled QD/MD (cQDMD) description.

The method we present here accomplishes this. It treats selected nuclear degrees of freedom of the solute using quantum mechanical wavepackets while the nuclei of the solvent are represented classically. In doing so, it propagates a grid based QD solute system on its intrinsic potential energy surface and simultaneously propagates the solvent classically by extending the time-dependent self-consistent field (TDSCF) approach to larger, reactive environments and a multidimensional description of the solute using selected active degrees of freedom. The TDSCF approach was previously applied to the much smaller or less reactive systems, such as the dissociation of the clusters

I_2Ne,[27] I_2He,[28] XeHI[29] and ArHCl[30] in gas phase or the vibrational relaxation of a cyanide ion in water.[31,32] Our method is to some extent related to an approach by Yamada et al.,[33] which propagates a solute quantum dynamically in its eigenstate representation and couples it to a semi-classical solvent using a fewest switches algorithm but is restricted to a single degree of freedom for the solute. The grid based character of the approach we are presenting allows for more general applications, including molecular processes like chemical reactions that move far away from equilibrium structures and for more degrees of freedom for the quantum system. To our knowledge, we are the first to apply this approach in this general extend to grid based QD with all its advantages. It also allows the inclusion of translational and rotational motion of the solute and offers an approach towards describing decoherence. In each step, the interaction between solvent and solute is treated using a quantum-classical TDSCF,[34,35] also known as Ehrenfest dynamics.[36,37] While first physical interpretations can be made, the main focus of this work lies on presenting a method that fulfills our requirements and to present the study of first applications.

In the following section we present the theoretical background of our approach and introduce an extension of quantum-classical TDSCF allowing for translation and rotation of the solute. We then present the application to two example systems. One is the dissociation of electronically excited ICN in liquid argon where the QD can be reduced to a one-dimensional grid along the carbon-iodine bond. As a second example we discuss the ultrafast relaxation of uracil in liquid water after photoexcitation during its first few hundred femtoseconds which can be well described by the dynamics on a two dimensional PES[38] before we conclude.

TDSCF formulation to couple a nuclear wavepacket to classical nuclei

As a first step, the nuclear and electronic degrees of freedom of the solute are separated by means of the Born-Oppenheimer approximation or a post-Born-Oppenheimer approach. Next, the nuclear degrees of freedom to be used in the QD are chosen and the corresponding grid based potential

energy surface (PES) of the solute in the gas phase is calculated. This can be done with any number of electronic states. The expected initial structure of the solute is then placed in a random orientation of the classically treated solvent environment, followed by an equilibration of the solvent while keeping the solute frozen using a constraint algorithm. Equilibration of the solvent can be achieved with a gradient descent algorithm, ensuring the absence of unphysically small distances.

As a result, we obtain a possible initial condition for the full system, once the solvent arrangement reaches a relative minimum. There are several choices for the constraint algorithm, we chose to use RATTLE[39] throughout our work. As a last step, before initiating the cQDMD approach, the solvent system is brought to the desired temperature using a thermostat.

The initial wavepacket on the solute PES has now to be coupled to the MD of the solvent to be propagated. This can be accomplished by the use of quantum-classical TDSCF also known as Ehrenfest dynamics. It starts by treating the total wavefunction Ψ of a system as the product of the wavefunctions of two subsystems. This results in the quantum-quantum TDSCF method,[40] yielding coupled equations to propagate both systems using QD:

$$i\hbar\frac{\partial\Psi^{\mathrm{E}}}{\partial t} = \left(T^{\mathrm{E}} + V^{\mathrm{E}} + \langle\Psi^{\mathrm{S}}|V^{\mathrm{ES}}|\Psi^{\mathrm{S}}\rangle\right)\Psi^{\mathrm{E}} \tag{1}$$

$$i\hbar\frac{\partial\Psi^{\mathrm{S}}}{\partial t} = \left(T^{\mathrm{S}} + V^{\mathrm{S}} + \langle\Psi^{\mathrm{E}}|V^{\mathrm{ES}}|\Psi^{\mathrm{E}}\rangle\right)\Psi^{\mathrm{S}} \tag{2}$$

T and V are kinetic and potential energy operators, respectively, the superscripts E and S indicate that a quantity belongs to the environment or the solute and ES means it belongs to both. At this point usually the subsystems are separated based on their mass in a system of light and a system of heavy particles. The light subsystem then continues to be treated using QD while the heavier one is approximated using MD.[37]

We do not distinguish light from heavy subsystems but realize that we are mainly interested in a highly precise description of the dynamics of the solute whereas the dynamics of the solvent are of minor interest. The major purpose of the inclusion of the solvent environment is rather to cover its effect on the solute behavior. Hence, we approximate the solvent as classical particles. While

this misses quantum effects in the solvent and correlational interaction between the solute and the solvent, those effects cannot be included explicitly due to the size of such a system. The resulting working equations[36] are given by

$$M_I \ddot{R}_I = -\nabla_I \sum_J V_{IJ}^{\mathrm{E}} - \nabla_I \langle \Psi^{\mathrm{S}} | V_I^{\mathrm{ES}} | \Psi^{\mathrm{S}} \rangle \tag{3}$$

as the equations of motion for the solvent and by

$$i\hbar \frac{\partial \Psi^{\mathrm{S}}}{\partial t} = \left(T^{\mathrm{S}} + V_{\mathrm{PES}}^{\mathrm{S}} + \sum_I V_I^{\mathrm{ES}} \right) \Psi^{\mathrm{S}} \tag{4}$$

as the Schrödinger equation for the solute. The form of the potential operator V_I^{ES} in eq. 3 and 4 results from the wavefunction of the solvent being a Dirac delta function in the classical limit. The indices I and J refer to the Ith and Jth atom of the solvent respectively, M_I is the mass of the Ith atom and R_I its position vector. $V_{IJ}^{\mathrm{E}}(R_I, R_J)$ is the interaction potential between the particles of the solvent environment and $V_I^{\mathrm{ES}}(R_I, r)$ is the interaction potential between the solvent particles and the solute which together with $\Psi^{\mathrm{S}}(r)$ results in a mean field in eq. 3. The mean field is a function of the degrees of freedom r of the solute. Eq. 4 uses the kinetic energy operator $T^{\mathrm{S}}(r)$ and the PES $V_{\mathrm{PES}}^{\mathrm{S}}(r)$ of the solute as well as $V_I^{\mathrm{ES}}(R_I, r)$. The potentials V_{IJ}^{EE} and V_I^{ES} can for example be calculated using force fields or to some extent using quantum chemistry.[7] Figure 1 illustrates the construction of V_I^{ES}. Note that for each point of the PES represented on a spatial grid the corresponding geometry of the solute has to be used to calculate V_I^{ES}. To calculate the force acting on a solvent particle, every interaction potential between the solute at grid coordinate r and the solvent is calculated and weighed according to its population density. For the solute, the interaction potentials from the solvent particles are summed at every grid point, resulting in the sum of the interaction potentials $\sum_I V_I^{\mathrm{ES}}$. It is also worth pointing out that the interaction potential between the solvent and the solute in the QD calculation has the form of a changing external potential.[7,8] Equations 3 and 4 can be solved using the standard propagation tools of QD and MD. We used the Split-Operator method[41] for the QD of ICN, the Chebychev propagation scheme[42]

for the QD of uracil and the velocity Verlet integrator[43] for the MD throughout this work.

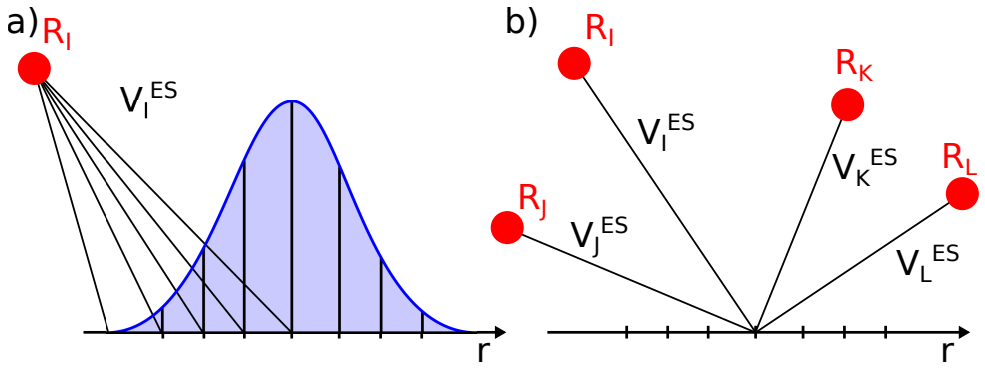

Figure 1: Schematic representation of the interaction potential V_I^{ES} construction from two perspectives. a) illustrates the solute acting on solvent particle I. Using the example of a Gaussian wavepacket, every interaction potential between the solute at grid coordinate r and the solvent is calculated and weighed according to the population density $|\Psi^S|^2$ shown. b) illustrates four solvent particles acting on the solute. This interaction is shown for one exemplary grid point, corresponding to a point in the configuration space of the solute. The interaction potentials from the solvent particles are summed and such a sum has to be calculated for every grid point, resulting in an energy surface for the interaction potential on the grid.

Thus far, the time evolution of the solute is restricted to the QD of the selected degrees of freedom. In addition, rotation and translation can easily be included using a classical approach. The main motivation for this is the difference in the distributions of collisions that are experienced by the solute with and without these external degrees of freedom. This is especially relevant for light solutes as they, according to the Maxwell-Boltzmann distribution, have larger velocities. Ideally, one would like to have the same interaction potential in both directions between the solute and the solvent system. Thus, since a force, weighted according to the population on a grid point corresponding to a certain solute geometry, acts on the solvent, the identically weighted counter force should act on exactly this geometry. While this could be realized by adding the rotational and translational degrees of freedom to the QD simulation, the computational cost of this gain in accuracy is unreasonably large. Instead, as an approximation we use a single geometry on which the counter force is acting, corresponding to the classical treatment of these degrees of freedom.

To achieve this, we include an additional step while discretizing the time. As we progress one time step according to eqs. 3 and 4, we also propagate a virtual rigid classical solute (VRCS) system where all internal degrees of freedom are frozen using a constraint algorithm. It replaces the quantum system for the MD step and is propagated classically using the aforementioned counter forces. Afterwards, the rotation and translation of the VRCS is transferred to the quantum system by means of changing the location and orientation of the spatial grid with respect to the solvent box.

To construct the VRCS, a single solute structure has to be found that approximates the relevant dynamical properties best. One way is by simply using the geometry corresponding to the position expectation values of the wavepacket given by $r_i^{\mathrm{VRCS}} = \langle \Psi^{\mathrm{S}} | r_i^{\mathrm{S}} | \Psi^{\mathrm{S}} \rangle$ for the ith internal coordinate r_i. Another way to do this is by enforcing that the VRCS system has the same center of mass and most similar moment of inertia ($I = \sum_i m_i x_i^2$ along a principal axis) as the respective expectation values of the quantum system. After testing both, we found that the error in energy conservation resulting from the former way is an order of magnitude smaller and decided to use this one. Since finding a structure with a moment of inertia that is most similar to the expectation value of the moment of inertia introduces additional complications, such as the ambiguity of these structures in higher-dimensional internal coordinate spaces, the use of the position expectation value is a justified simplification. Note that the latter approximation might result in a slightly better conservation of angular momentum. After the propagation of this VRCS system, the space grid of the QD system is translated by the same distance and rotated by the same angles within the classical solvent environment.

These considerations allow us to formulate a propagation step using the same time increment for all systems. The QD of the solute require the interaction potential V_I^{ES} and the PES. The solvent atoms require forces between themselves and between themselves and the solute. Again, the solvent-solute forces have to be calculated for every geometry corresponding to a grid point and weighted according to the population on that grid point before being summed up. The VRCS gets its forces on the individual atoms as population weighted forces over all geometries, summed

over all solvent atoms:

$$\mathbf{F}_i^{\mathrm{VRCS}} = \sum_I \int |\Psi^S(r)|^2 \mathbf{F}_{iI}(r) dr \tag{5}$$

Both, QD and MD system are then propagated using these interactions and their previous positions, velocities or wavefunctions depending on the propagation algorithm. For the solvent this finalizes the step. The QD solute system in addition has to be updated according to the changes in center of mass and angular orientation in the VRCS system. An illustration of this algorithm can be found in Figure 1 in the Supporting Information.

A simple test case: ICN in liquid Ar

We implemented this cQDMD approach using a QD program of our own design coupled to Gromacs[44] performing the calculation of the interaction energies and forces and the MD of the solvent. The time evolution after electronic excitation of ICN in liquid argon at 84 K and 1 bar was chosen as example system. This was simulated using the one-dimensional excited spin-orbit state S_1 as described by Goldfield et al.[45] as the internal PES for the solute. It was placed in a periodic box with side lengths of 21.17 Å, 200 Ar atoms and a van der Waals cutoff of 10 Å. The initial wavepacket is given by a stationary Gaussian with its center at a distance of 2.12 Å and a standard deviation of 0.121 Å unless stated otherwise. This corresponds to the vibrational ground state of the S_0 state and can therefore be considered as a first approximation of a laser excitation from the electronic ground state. The potentials for the solvent-solvent and solvent-solute interaction have been used as given by Benjamin et al.[46] The initial conditions of the QD system are also illustrated in Figure 2 and 3 in the Supporting Information. For each simulation the initial condition of the solvent was created by equilibrating a random orientation of the argon atoms. The system was propagated with the Split-Operator method[41] using time steps of 0.1 fs.

Given that the energy expectation value of the initial wavepacket lies well above the dissociation energy (7.3 times as much), dissociation is expected when no environment is present. This

is also the result of a QD simulation in vacuum shown in the upper panel of Figure 2 (black line) with an undissociated fraction of only 3 % after 700 fs. We define parts of the wavepacket with an iodine-carbon distance $r_{IC} > 6.5$ Å as dissociated and remove them using a negative imaginary potential, since after this distance the chance of recombination is negligible. What happens in the solvent environment? The averages of 49 cQDMD simulations with random solvent arrangements are shown in the upper panel of Figure 2 (red line) together with the results of two exemplary simulations (green and blue lines). Note that a small number of initial conditions for the solvent environment is sufficient to reach convergence in the observables of the quantum system, as can be seen in the lower panel of Figure 2. The reason is that the interaction potential with the solvent environment is essentially projected on the low-dimensional space of the quantum system and then further reduced to a single scalar value. The results of the simulations suggest that the dissociation pathway is still accessible in a liquid argon environment, however, the dissociation is delayed and a significant part of the wavepacket gets trapped inside the solvent cage. Hence, the percentage of undissociated ICN raises to 45 % in liquid argon, which is about 15 times higher than in vacuum.

The energy of the two subsystems including rotation and translation of the QD system is shown in Figure 3. Here we used another set of starting conditions with a lower, non dissociative energy of the initial wavepacket, a stationary Gaussian with its center at a distance of 2.74 Å and a standard deviation of 0.079 Å (see Figure 3 in the Supporting Information). It can be seen that the energy exchange between the QD (red line) and the MD system (blue line) has a very small relative error (black line). The error in energy conservation is depicted magnified in the subplot of Figure 3. In the case of the full system without rotational and translational degrees of freedom of the solute the fluctuations are on the order of 10^{-8} E_h which can be attributed to numerical errors. This is to be expected since the TDSCF approach by itself is energy conserving.[47] As we include the translational and rotational degrees of freedom of the solute, the fluctuations increase up to the order of 10^{-6} E_h. This is consistent with our expectations of the introduction of small errors due to the use of the position expectation values used for the propagation of the VRCS.

For the computation time we expect the typical algorithm-dependent scaling behavior for the

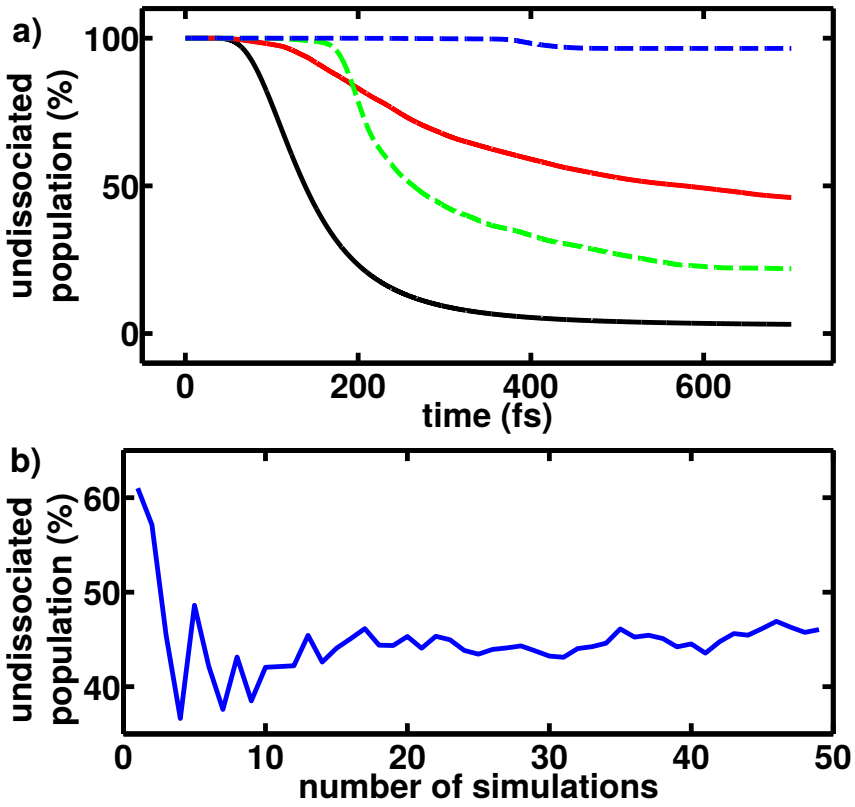

Figure 2: Percentage of undissociated ICN after time t and convergence behavior of dissociation percentage. a) shows a reference system without solvent (black solid), two example simulations with different initial solvent arrangements (green and blue dashed) and the averaged result over 49 simulations using different initial solvent arrangements (red solid). b) shows the percentage of the undissociated population at 700 fs as a function of the number simulations with different initial conditions. Convergence is achieved after about 20 simulations.

subsystems.[48] In our case, having no Coulomb interactions and using a cutoff, this is $O(m)$ for the MD with the number of solvent atoms m and $O(n \log n)$ for the QD due to the use of the fast Fourier transform with n being the number of grid points used for the solute. Calculating the interaction between the subsystems is $O(n)$ as the interaction potential is calculated for every grid point. For our calculations, we observed linear scaling with the number of grid points used, up to a maximum of $n = 2048$. This means that the higher scaling of the QD algorithms has not taken over yet, which is explained by the large number of potential calculations between the n solute structures and the

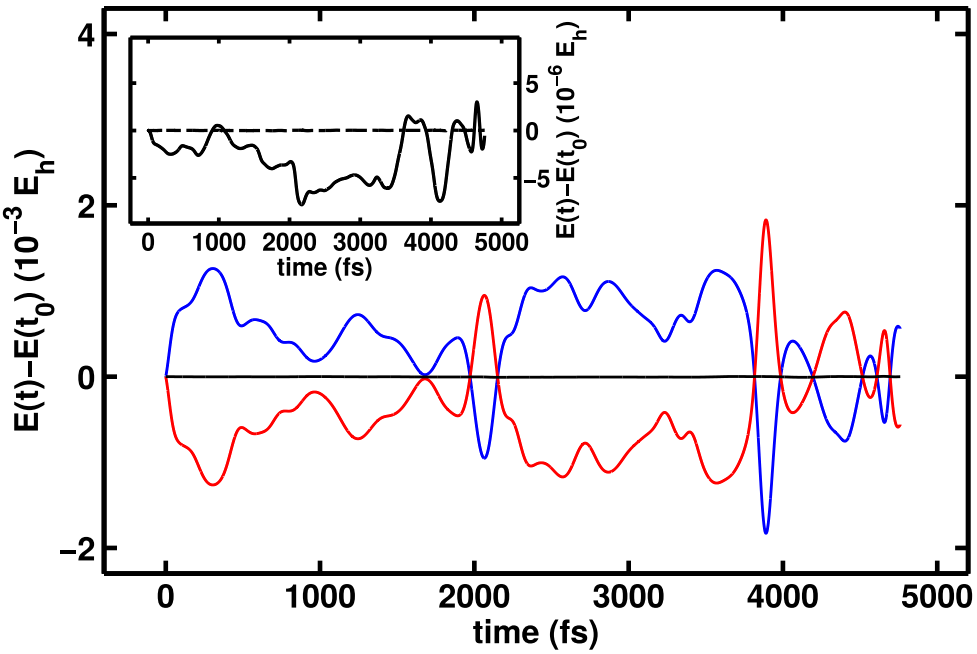

Figure 3: Change in energy for the QD (red solid) and the MD (blue solid) system during a single simulation for the low energy initial conditions. The errors in energy conservation introduced together with translational and rotational degrees of freedom (black solid) are negligible in comparison to the exchanged energy. The interaction potential energy is included in the quantum system. The subplot compares the error in total energy conservation over time without (black dashed) and with (black solid) translational and rotational degrees of freedom of the QD system.

solvent atoms closer than the cutoff radius.

Another phenomenon that should be observable in this scenario is decoherence. Since we performed simulations starting from an ensemble of different initial conditions, we are able to make physical predictions e.g. estimate decoherence times. We chose to calculate the decrease of the coherence $\gamma = \sum_{i \neq j} |\rho_{ij}|$. Here $\rho = \frac{1}{N} \sum_{i=1}^{N} \rho^i$ where ρ^i is the density matrix in the basis of vibrational eigenstates of the ith initial condition of the solvent taking into account $N = 21$ initial conditions. An exponential decrease with a time constant $\tau = 380\,\mathrm{fs}$ is observed. This is comparable to decoherence times in similar systems.[49,50] Figure 4 a) shows the evolution of the coherence $\gamma(t)$ together with the exponential fit. There might be decoherence on a substantially longer timescale leading to a better description by a multiexponential fit. However, a monoexponential fit describes

the decay well on the studied timescale. Another way to observe decoherence is to compare the density matrix ρ for the low energy initial conditions for the wavepacket. The Wigner function of a wavepacket propagated in the gas phase and the Wigner function of the sum of the wavepackets propagated in the environment which are shown in Figure 4 b) and c), respectively. It can be seen that the interference pattern simplifies in the solvent environment with the loss of phase relation due to the varying impact of the different environment arrangements. The convergence behavior for all shown quantities as well as the decrease of purity over time is shown in the Supporting Information.

A real life example: Uracil in water

To examine the performance of our method in a more complex test case, we decided to study the excited state dynamics of uracil in an aqueous environment.

The photorelaxation of uracil is key to understanding the photostability of RNA, since it can provide insight into the main mechanism by which photodamage is prevented. As a range of pump-probe experiments have shown, it is a complex multi-step process in the gas phase[51–53] as well as in solution.[54–56] In general, these studies have identified a biexponential decay from which two lifetimes can be extracted. The first short one τ_1 is around 105 fs in the gas phase[53] and 120 fs in solution for the related 1-Cyclohexyluracil[54] while the second one τ_2 longer than 1 ps in the gas phase as well as in solution. Here, we are focusing on the first step, which has been attributed to an ultrafast decay from the bright S_2 state with $\pi\pi^*$ character to the dark S_1 state with $n\pi^*$ character via a CoIn.[57,58]

Our system consists of a central uracil molecule and 217 water molecules embedded in a periodic box with side lengths of 19 Å. We use the AMBER14SB[59,60] force field for the VRCS of uracil and the interaction potential and TIP3P[61] for the MD of water. For the van der Waals and Coulomb interactions a cutoff of 7 Å was used. Long-range Coulomb interactions were taken into account by the reaction-field mechanism implemented in Gromacs. The system was equilibrated at 298.15 K

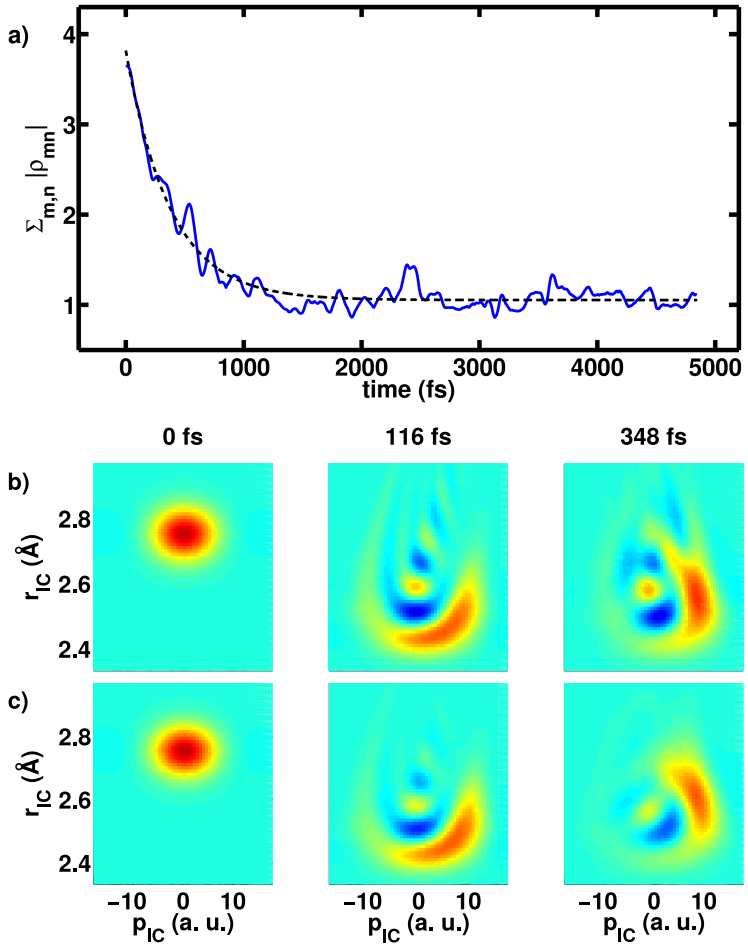

Figure 4: Decrease of coherence of the system with the low energy initial conditions. a) shows the coherence traced over 21 randomly chosen starting conditions as a function of time (blue solid) together with the monoexponential fit (black dotted). b) shows the Wigner function of a simulation in the gas phase at 0, 116 and 348 fs. c) shows the Wigner function for the sum of all 21 simulations in the liquid argon environment at the same times. The red areas indicate a positive sign and the blue areas a negative sign.

and 1 bar while keeping the uracil molecule frozen in its ground state geometry. Then, during a time evolution of 200 ps frames were extracted every 5 ps as starting points for the cQDMD simulations. Out of the resulting 40 arrangements, 35 were randomly chosen as initial conditions. For the internal degrees of freedom of uracil we used a two dimensional two state model. Uracil is represented in a configuration space spanned by the vector connecting the Franck-Condon point

with the small S_2 minimum ($q_{FC\rightarrow S_2min}$) and the vector, connecting the Franck-Condon point with the S_2/S_1 CoIn ($q_{FC\rightarrow CoIn}$). The optimization of the corresponding structures, the construction of the gas phase S_2 PES and the construction of the non-adiabatic coupling matrix elements in these coordinates on the MRCI(12,9) level of theory is described elsewhere.[38,57,62] A negative imaginary potential represents the S_1 PES and we approximate the non-adiabatic coupling as being solvent independent. As the starting wavepacket, the lowest vibrational eigenstate of the ground state was transferred to the S_2 state. The dynamics in the gas phase that result from this starting condition are comparable to an excitation by a simple probe pulse.[38] 35 cQDMD trajectories were propagated with a time step of 0.1 fs using the Chebychev propagator.[42]

In the gas phase, the wavepacket oscillates twice in the S_2 minimum before parts of it cross the barrier between the S_2 minimum and the CoIn at around 100 fs leading to relaxation to the S_1 state (Figure 5 a). In all 35 simulations in water, a similar behavior is observed, with an example shown in Figure 5 b. The influence of the water environment clearly shows in the time dependence of the potential energy surface. These effects lead to slightly different relaxation behaviors in the individual trajectories, but no deviation from the general scheme. A process that influences relaxation is the collision of the wavepacket with solvent molecules during its oscillations in the S_2 minimum. We also observe periodic increases or decreases in the height of the barrier due to the interaction with the water molecules. However, within this theoretical description using the AMBER14SB force field the influence of these two factors is rather minute and over different trajectories, they accelerate as well as decelerate the relaxation. Hence, in the mean of all 35 simulations, no significant deviation from the gas phase relaxation is observed (Figure 6). Overall, this means that the cavity of the uracil molecule does not need to change much to allow for the motions associated with the relaxation process.

These findings are in line with experiments[54] that show only little solvent dependence of τ_1 and only a small difference to the gas phase. They also compare well with previous theoretical studies by Doltsinis *et al.* using non-adiabatic ab initio dynamics on TDDFT level[63] that focus on the S_1 state in solution and show no qualitative difference governing non-radiative decay in the gas phase

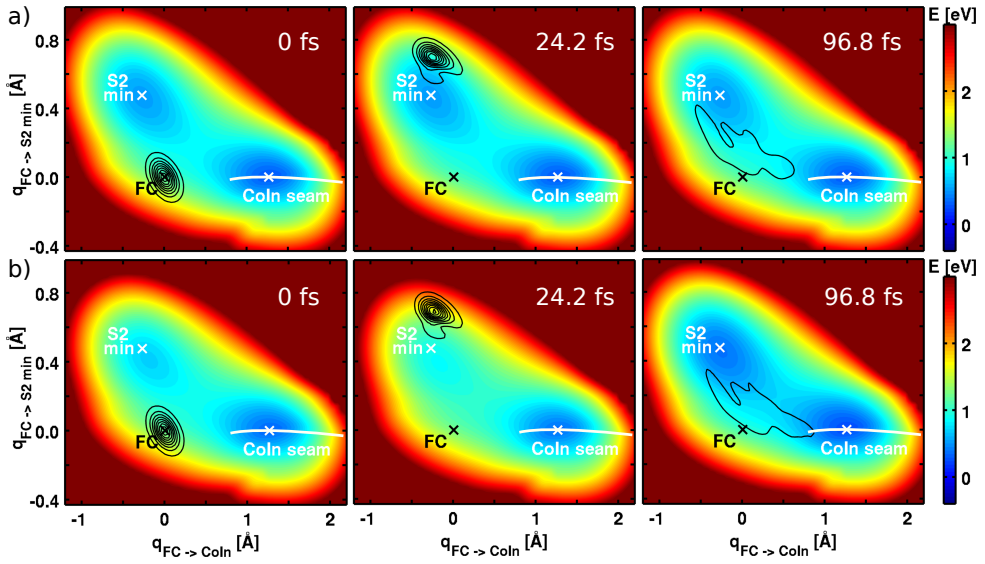

Figure 5: Wavepacket propagation on the S_2 surface of uracil. The surface is spanned by the Franck-Condon point, the local S_2 minimum and the S_2/S_1 CoIn. Nonadiabatic coupling takes place along the CoIn seam indicated by the curved white line. a) shows the propagation in the gas phase, b) shows an exemplary calculation in water, where the relaxation speed is slightly increased due to a collision solvent molecules at around 24.2 fs.

and in aqueous solution. On a longer time scale, associated with S_1/S_0 relaxation, transient UV absorption spectra have shown characteristics of vibrational cooling in the aqueous environment.[56] With the approach presented here, we might be able to investigate these in the future.

Conclusions

We presented an approach that is an extension of our recently presented QD/MD approach[8] and builds on the quantum-classical TDSCF scheme. It captures environmental effects onto reactive systems by simultaneously propagating a quantum solute system coupled to a classical solvent system using a TDSCF. As the quantum system is propagated on a spatial grid, this method is generally applicable to most PES which makes it especially suited for reactive scenarios where the solvent has an important influence on the outcome. It also allows the inclusion of classical

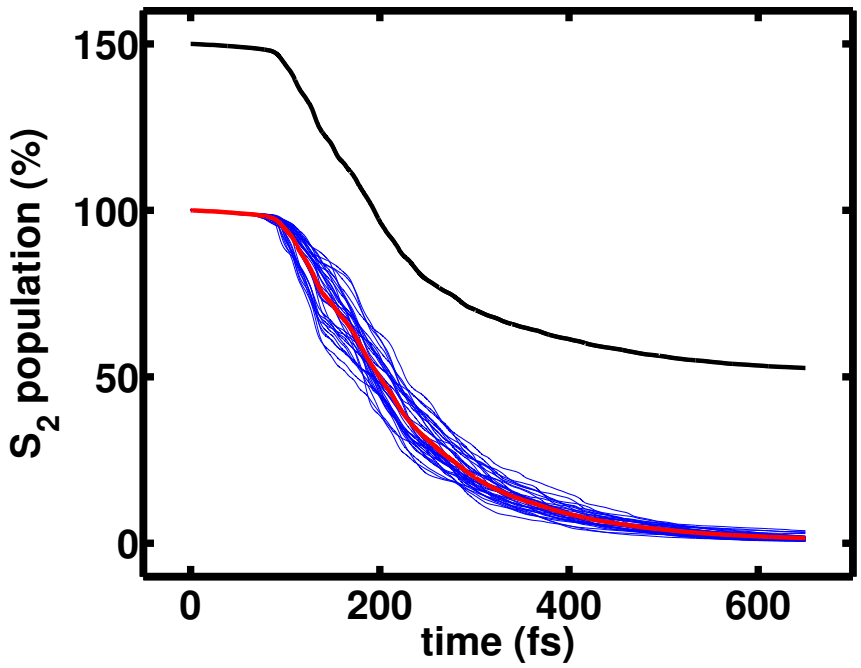

Figure 6: Decrease of S_2 population in the gas phase (black line, shifted by 50 %) and of 35 cQDMD simulations in water (blue lines). The red line marks the average of the simulations in water.

rotational and translational degrees of freedom of the solute, leading to a more accurate simulation of collisions. While our approach is fairly general with respect to the solvation scenario, it is limited in the extreme by cases where significant parts of the wavefunction are widely separated during the propagation. We presented the dissociation of ICN in liquid argon as an example system and examined the observable decoherence in our simulations.

There are a few directions for further development. One is the possible decoupling of the time step size of the two subsystems. In principle, each subsystem could use its own appropriate step size and usually the step size of the MD system could be increased relative to the QD system. It might also be worth to explore the use of MCTDH instead of a grid based approach for scenarios where the MCTDH excels. Additionally, it is straightforward to move to a larger test system that will allow us to challenge our approach.

Acknowledgement

We gratefully acknowledge support by the DFG via the Cluster of Excellence: The SFB749 and Munich Centre for Advanced Photonics.

Supporting Information Available

The Supporting Information contains a flowchart illustrating our algorithm and plots of the different initial conditions for the QD calculations of ICN presented. It also contains the time evolution of the purity of the ICN system together with the convergence behavior of the other decoherence measures studied.

This material is available free of charge via the Internet at `http://pubs.acs.org`.

References

(1) Kohen, A.; Klinman, J. P. *Acc. Chem. Res.* **1998**, *31*, 397–404.

(2) Stratt, R. M.; Maroncelli, M. *J. Phys. Chem.* **1996**, *100*, 12981–12996.

(3) Moskun, A. C.; Jailaubekov, A. E.; Bradforth, S. E.; Tao, G.; Stratt, R. M. *Science* **2006**, *311*, 12981–12996.

(4) Li, X.; Maroncelli, M. *J. Phys. Chem. A* **2010**, *73*, 3746–3754.

(5) Sailer, C. F.; Thallmair, S.; Fingerhut, B. P.; Nolte, C.; Ammer, J.; Mayr, H.; de Vivie-Riedle, R.; Pugliesi, I.; Riedle, E. *Chem. Phys. Chem.* **2013**, *14*, 1423–1437.

(6) Struebing, H.; Ganase, Z.; Karamertzanis, P. G.; Siougkrou, E.; Haycock, P.; Piccione, P. M.; Armstrong, A.; Galindo, A.; Adjiman, C. S. *Nature Chem.* **2013**, *5*, 952–957.

(7) Thallmair, S.; Kowalewski, M.; Zauleck, J. P. P.; Roos, M. K.; de Vivie-Riedle, R. *J. Phys. Chem. Lett.* **2014**, *5*, 3480–3485.

(8) Thallmair, S.; Zauleck, J. P. P.; de Vivie-Riedle, R. *J. Chem. Theory Comput.* **2015**, *11*, 1987–1995.

(9) Kumpulainen, T.; Lang, B.; Rosspeinter, A.; Vauthey, E. *Chem. Rev.* **2016**, 10.1021/acs.chemrev.6b00491.

(10) Denys, I. B.; Cabrera, R.; Campos, A.; Mukamel, S.; Rabitz, H. A. *J. Phys. Chem. Lett.* **2016**, *7*, 1632–1637.

(11) Burghardt, I.; Cederbaum, L. S.; Hynes, J. T. *Faraday Discuss.* **2004**, *127*, 395–411.

(12) Cederbaum, L. S.; Gindensperger, E.; Burghardt, I. *Phys. Rev. Lett.* **2005**, *94*, 113003.

(13) Cossi, M.; Rega, N.; Scalmani, G.; Barone, V. *J. Comput. Chem.* **2003**, *24*, 669–681.

(14) Tomasi, J.; Mennucci, B.; Cammi, R. *Chem. Rev.* **2005**, *105*, 2999–3094.

(15) Caricato, M. *Comput. Theor. Chem.* **2014**, *1040*, 99–105.

(16) Shi, Q.; Geva, E. *J. Phys. Chem. A* **2003**, *107*, 9059–9069.

(17) Ka, B. J.; Geva, E. *J. Phys. Chem. A* **2006**, *110*, 13131–13138.

(18) Liu, J.; Miller, W. H. *J. Chem. Phys.* **2007**, *127*, 114506.

(19) Liu, J.; Miller, W. H.; Paesani, F.; Zhang, W.; Case, D. A. *J. Chem. Phys.* **2009**, *131*, 164509.

(20) Fano, U. *Rev. Mod. Phys.* **1957**, *29*, 74–93.

(21) Lindblad, G. *Comm. Math. Phys.* **1973**, *33*, 305–322.

(22) Lindblad, G. *Comm. Math. Phys.* **1974**, *39*, 111–119.

(23) Lindblad, G. *Comm. Math. Phys.* **1976**, *48*, 119–130.

(24) Wong, K. F.; Rossky, P. J. *J. Chem. Phys.* **2002**, *116*, 8418–8428.

(25) Rekik, N.; Hsieh, C.-Y.; Freedman, H.; Hanna, G. *J. Chem. Phys.* **2013**, *138*, 144106.

(26) Martinez, F.; Hanna, G. *Mol. Simul.* **2015**, *41*, 107–122.

(27) Gerber, R. B.; Buch, V.; Ratner, M. A. *J. Chem. Phys.* **1982**, *77*, 3022–3030.

(28) Bisseling, R. H.; Kosloff, R.; Gerber, R. B.; Ratner, M. A.; Gibson, L.; Cerjan, C. *J. Chem. Phys.* **1987**, *87*, 2760–2765.

(29) Alimi, R.; Gerber, R. B.; Hammerich, A. D.; Kosloff, R.; Ratner, M. A. *J. Chem. Phys.* **1990**, *93*, 6484–6490.

(30) García-Vela, A.; Gerber, R. B.; Valentini, J. J. *J. Chem. Phys.* **1992**, *97*, 3297–3306.

(31) Bastida, A.; Cruz, C.; Zúñiga, J.; Requena, A.; Miguel, B. *J. Chem. Phys.* **2007**, *126*, 014503.

(32) Bastida, A.; Zúñiga, J.; Requena, A.; Miguel, B. *J. Chem. Phys.* **2008**, *129*, 154501.

(33) Yamada, A.; Kojima, H.; Okazaki, S. *J. Chem. Phys.* **2014**, *141*, 084509.

(34) Wang, L.; Mccoy, A. B. *Phys. Chem. Chem. Phys.* **1999**, *1*, 1227–1235.

(35) Whittier, G. S.; Light, J. C. *J. Chem. Phys.* **1999**, *110*, 4280–4290.

(36) Tully, J. C. *Faraday Discuss.* **1998**, *110*, 407.

(37) Marx, D.; Hutter, J. *Modern Methods and Algorithms of Quantum Chemistry*, 2nd ed.; John von Neumann Institute for Computing: Jülich, North Rhine-Westphalia, Germany, 2000; Vol. 3, pp 301–449.

(38) Keefer, D.; Thallmair, S.; Matsika, S.; de Vivie-Riedle, R. *J. Am. Chem. Soc.* **2017**, *139*, 5061–5066.

(39) Andersen, H. C. *J. Comput. Phys.* **1983**, *52*, 24 – 34.

(40) Dirac, P. A. M. *Math. Proc. Cambridge* **1930**, *26*, 376–385.

(41) Feit, M. D.; Fleck, J. A., Jr.; Steiger, A. *J. Comput. Phys.* **1982**, *47*, 412.

(42) Tal-Ezer, H.; Kosloff, R. *J. Chem. Phys.* **1984**, *81*, 3967–3971.

(43) Swope, W. C.; Andersen, H. C.; Berens, P. H.; Wilson, K. R. *J. Chem. Phys.* **1982**, *76*, 637.

(44) Hess, B.; Kutzner, C.; Van Der Spoel, D.; Lindahl, E. *J. Chem. Theory Comput.* **2008**, *4*, 435–447.

(45) Goldfield, E. M.; Houston, P. L.; Ezra, G. S. *J. Chem. Phys.* **1986**, *84*, 3120.

(46) Benjamin, I.; Wilson, K. R. *J. Chem. Phys.* **1989**, *90*, 4176.

(47) Micha, D. A. *J. Chem. Phys.* **1983**, *78*, 7138–7145.

(48) Greengard, L.; V., R. *J. Comput. Phys.* **1987**, *73*, 325.

(49) Rector, K. D.; Fayer, M. D. *J. Chem. Phys.* **1998**, *108*, 1794–1803.

(50) Stenger, J.; Madsen, D.; Hamm, P.; Nibbering, E. T. J.; Elsaesser, T. *Phys. Rev. Lett.* **2001**, *87*, 027401.

(51) Kang, H.; Lee, K. T.; Jung, B.; Ko, Y. J.; Kim, S. K. *J. Am. Chem. Soc.* **2002**, *124*, 12958–12959.

(52) Ullrich, S.; Schultz, T.; Zgierski, M. Z.; Stolow, A. *Phys. Chem. Chem. Phys.* **2004**, *6*, 2796–2801.

(53) Canuel, C.; Mons, M.; Piuzzi, F.; Tardivel, B.; Dimicoli, I.; Elhanine, M. *J. Chem. Phys.* **2005**, *122*, 074316.

(54) Hare, P. M.; Crespo-Hernández, C. E.; Kohler, B. *J. Phys. Chem. B* **2006**, *110*, 18641–18650.

(55) Gustavsson, T.; Sarkar, N.; Lazzarotto, E.; Markovitsi, D.; Improta, R. *Chem. Phys. Lett.* **2006**, *429*, 551 – 557.

(56) Hua, X.; Hua, L.; Liu, X. *Phys. Chem. Chem. Phys.* **2016**, *18*, 13904–13911.

(57) Matsika, S. *J. Phys. Chem. A* **2004**, *108*, 7584–7590.

(58) Richter, M.; Mai, S.; Marquetand, P.; Gonzalez, L. *Phys. Chem. Chem. Phys.* **2014**, *16*, 24423–24436.

(59) Cornell, W. D.; Cieplak, P.; Bayly, C. I.; Gould, I. R.; Merz, K. M.; Ferguson, D. M.; Spellmeyer, D. C.; Fox, T.; Caldwell, J. W.; Kollman, P. A. *J. Am. Chem. Soc.* **1995**, *117*, 5179–5197.

(60) Zgarbová, M.; Otyepka, M.; Šponer, J.; Mládek, A.; Banáš, P.; Cheatham, T. E.; Jurečka, P. *J. Chem. Theory Comput.* **2011**, *7*, 2886–2902.

(61) Jorgensen, W. L.; Chandrasekhar, J.; Madura, J. D.; Impey, R. W.; Klein, M. L. *J. Chem. Phys.* **1983**, *79*, 926–935.

(62) Yoshikawa, A.; Matsika, S. *Chem. Phys.* **2008**, *347*, 393 – 404.

(63) Nieber, H.; Doltsinis, N. L. *Chem. Phys.* **2008**, *347*, 405 – 412.

Chapter 3

Small improvements to QD calculation efficiency

In addition to the automation of the coordinate construction and the inclusion of dynamic solvent effects, there are two minor topics presented here that can improve QD calculations to a lesser extent.

The first improvement is a study of the effects of an approximation in the Wilson G-matrix formalism [30–32], mentioned in chapter 1.2 and potential strategies to reduce introduced errors and is included in section 3.1. The second one covers the potential use of undersampling in QD calculations in order to reduce the number of grid points needed and hence increase computational speed. It is presented in section 3.2.

3.1 Examining an approximation in the Wilson G-matrix formalism

It is unreasonable to expect a perfect understanding of every decision made in the process of scientific work and in practice this understanding is often replaced by intuition or in more conscious cases by consensus [165]. This regularly leads to misjudgments and misuse of methods and formalisms. While this is an unavoidable byproduct of the scientific method and in most cases does not indicate individual failure, there still is need to re-evaluate critical steps in our understanding in order to improve them and the efficiency of practical applications.

In this context, the focus in this section lies on the use of the Wilson G-matrix formalism [30–32]. It offers a simple way to formulate the kinetic energy operator in arbitrary coordinates, which is the most difficult part in transforming the coordinates for a QD calculation. Using the elements $\mathbf{G}_{rs}$ of the G-matrix $\mathbf{G}$, the kinetic energy operator $\hat{T}_{\mathbf{q}}$ in reactive coordinates $\mathbf{q}$ is given by

$$\hat{T}_{\mathbf{q}} \approx -\frac{1}{2}\sum_{r=1}^{N_{\mathbf{q}}}\sum_{s=1}^{N_{\mathbf{q}}}\frac{\partial}{\partial q_r}\left[\mathbf{G}_{rs}\frac{\partial}{\partial q_s}\right] \ . \tag{3.1}$$

Here, $N_{\mathbf{q}}$ is the number of reactive coordinates used. The G-matrix elements are given by

$$\mathbf{G}_{rs} = \sum_{i=1}^{3N}\frac{1}{m_i}\frac{\partial q_r}{\partial x_i}\frac{\partial q_s}{\partial x_i} \ , \tag{3.2}$$

with m_i being the masses and x_i being the Cartesian coordinates of the ith atom.

The draft "Revisiting an approximation in the Wilson G-matrix formalism and its impact on molecular quantum dynamics" focuses on the consequences of the approximation implied in eq. 3.1. The key points of the article are:

- A coordinate transformation for a model system is introduced that exhibits notable errors as a result of the approximation studied and its time evolution is presented.
- A thought experiment is used to illuminate the usual conflation of the error resulting from the discussed approximation and the reduction of dimensionality common in grid based approaches. This is used to construct a general strategy to avoid all errors introduced due to the approximation in eq. 3.1. An alternate approach is suggested to allow the use of an exact formulation of the kinetic energy operator given the reduction to reactive coordinates.

In the following, the draft "Revisiting an approximation in the Wilson G-matrix formalism and its impact on molecular quantum dynamics" is included.

Revisiting an approximation in the Wilson G-matrix formalism and its impact on molecular quantum dynamics

Julius P. P. Zauleck

Department Chemie, Ludwig-Maximilians-Universität München, Butenandtstr. 13, 81377 München, Germany

Sebastian Thallmair

Groningen Biomolecular Sciences and Biotechnology Institute and The Zernike Institute for Advanced Material, University of Groningen, Nijenborgh 7, 9747 AG Groningen, Netherlands

Regina de Vivie-Riedle

Department Chemie, Ludwig-Maximilians-Universität München, Butenandtstr. 13, 81377 München, Germany

Quantum dynamics simulations of reactive molecular processes are commonly performed in a low-dimensional space spanned by highly optimized reactive coordinates. Usually, these sets of reactive coordinates consist of non-linear coordinates. The Wilson G-matrix formalism allows to formulate the Hamiltonian in arbitrary coordinates. In our present work, we revisit an approximation in this formalism, namely the assumption that the Jacobian determinant is constant. We show that the approximation can introduce an error and illustrate it for a harmonic oscillator. Finally, we present a strategy to prevent this error.

The reduction of coordinates is an important aspect in molecular quantum dynamics (QD)[1,2]. This naturally comes along with the search for the most important coordinates to describe the molecular process of interest[3–9]. Often Z-matrix coordinates or linear combinations of them are chosen because they represent molecular motions in an intuitive way. As these Z-matrix coordinates include e.g. angles they are non-linear which in turn complicates the kinetic part of the Hamiltonian.[10] A straightforward way to deal with this is the Wilson G-matrix formalism[11–13]. It allows to transform the kinetic Hamiltonian from the Cartesian space to arbitrary coordinates. The G-matrix gives access to the kinetic couplings along the non-linear coordinates and its diagonal elements can be interpreted as position dependent inverse reduced mass[6].

The G-matrix formalism was first introduced by B. Podolsky[11] to reformulate the quantum mechanical Hamiltonian. Later, it became a common tool for the description and interpretation of vibrational spectra where the Hamiltonian had to be expressed in normal mode coordinates[12,14,15]. In its common formulation, the G-matrix formalism comes along with an approximation assuming that the Jacobian determinant $j = \det|\mathbf{J}|$ is constant. This approximation is usually justified by arguing that the position dependence of the G-matrix is more pronounced than that of the Jacobian determinant. To the best of our knowledge, this approximation and its effect has never been checked for molecular QD. Thus, we revisit this approximation in our present work. While a transformation into linear coordinates, e.g. normal modes that are often used for small displacements around equilibrium structures, assures a constant Jacobian determinant j and introduces no error, this is not the case for non-linear coordinates. We investigate if a certain setup of the chosen subspace coordinates can reduce the error due to approximating the Jacobian determinant as constant or if it might be even possible to avoid this error at all. In doing so, we first introduce the approximation typically applied within the G-matrix formalism. Then, we demonstrate for an example of a simple coordinate transformation for a harmonic oscillator when the approximation leads to an obvious error. Finally, we present a strategy how to deal with a molecular system for which the dimensionality reduction and the approximation of a constant Jacobian determinant are applied at the same time. Note that all equations are written in atomic units.

To describe the time evolution of the nuclear wavefunction $\Psi(x,t)$ of a molecular system,

the time-dependent Schrödinger equation of the nuclei has to be solved:

$$i\frac{\partial}{\partial t}\Psi\left(x,t\right) = \hat{H}\Psi\left(x,t\right) \tag{1}$$

$$= \left(\hat{T}+\hat{V}\right)\Psi\left(x,t\right) \ . \tag{2}$$

with the Hamiltonian $\hat{H}$ being the sum of the kinetic operator $\hat{T}$ and the potential operator $\hat{V}$. For an appropriate description of molecular processes, the Schrödinger equation is commonly transformed into reactive coordinates $\mathbf{q}$[13,16]. The multiplicative potential operator $\hat{V}$ can be transformed easily. This is not the case for the kinetic operator $\hat{T}$. The Wilson G-matrix formalism opens a way to reformulate the kinetic energy operator in a general set of coordinates. Its exact formulation is given by

$$\hat{T}_{\mathbf{q}} = -\frac{1}{2}\sum_{r=1}^{N_{\mathbf{q}}}\sum_{s=1}^{N_{\mathbf{q}}} j^{-\frac{1}{2}}\frac{\partial}{\partial q_r}\left[j\mathbf{G}_{rs}\frac{\partial}{\partial q_s}j^{-\frac{1}{2}}\right] \tag{3}$$

with the G-matrix elements $\mathbf{G}_{rs}$ being

$$\mathbf{G}_{rs} = \sum_{i=1}^{3N}\frac{1}{m_i}\frac{\partial q_r}{\partial x_i}\frac{\partial q_s}{\partial x_i} \ . \tag{4}$$

Assuming that the Jacobian determinant j is constant, all derivatives acting on j can be ignored[17], resulting in

$$\hat{T}_{\mathbf{q}} \approx -\frac{1}{2}\sum_{r=1}^{N_{\mathbf{q}}}\sum_{s=1}^{N_{\mathbf{q}}}\frac{\partial}{\partial q_r}\left[\mathbf{G}_{rs}\frac{\partial}{\partial q_s}\right] \ . \tag{5}$$

This approximation is often disregarded and thus not treated carefully enough which may result in a misunderstanding in grid based approaches for QD. It might lead to sets of reactive coordinates $\mathbf{q}$ which inherit an error that can be easily removed.

Figure 1 illustrates a simple scenario where this approximation causes a notable error. Here, a Gaussian wavepacket of the mass of a proton with a small initial momentum is propagated inside a harmonic potential (blue) using the Split-Operator method[18]. The upper panel of Figure 1 shows the correct time evolution of the system in a Cartesian coordinate x (or in other coordinates according to Eq. 3). The lower panel shows the time evolution on a coordinate y with non-constant Jacobian determinant j with respect to x using the kinetic energy operator of Eq. 5. To introduce a significant nonlinearity around 0 Å, the coordinate transformation is given by $x = a\,\mathrm{erf}(by) + y$ with the error function erf, $a = -0.4$

and $b = 1.5$. This leads to a compressed coordinate y with respect to x around 0 Å. The propagation is shown at time 0 fs (green), 30 fs (red) and 54 fs (cyan). It can be seen that the error is introduced as the wavepacket crosses the nonlinearity in y and the resulting error is most easily visible at 54 fs, where an additional Gaussian shaped wavepacket appears left of the nonlinearity. As the propagation continues and the wavepacket crosses the nonlinearity again, the error accumulates.

However, approaching the error generally from a theoretical perspective is difficult because j is only defined for a coordinate transformation of equal numbers of coordinates. Since most grid based QD approaches rely on reducing the number of reactive coordinates $\mathbf{q}$, the approximation of a constant j gets easily conflated with the error introduced by removing all non-reactive coordinates not relevant for the studied system. There are two important steps to unravel this combined error related therewith. The first one is to clarify, under which conditions j is actually constant. The second one is to quantify and reduce the error which is introduced by the removal of (non-reactive) coordinates but associated with the first step[6,17].

A straightforward way to argue the first step is to take a look at the meaning of the Jacobian determinant j. It describes the volume change during a coordinate transformation. If we stay in the space of continuous well-behaved coordinate spaces that we need for our QD calculations to work well, we can ensure this constancy for all cases where the dimensionality of a system is reduced. As the change in volume will also be continuous along the different coordinates and as long as there is a single non-reactive coordinate which we do not include in our subspace, we can simply define this additional coordinate as ensuring a constant j. One can think of the additional coordinate as stretching when the volume of the included reactive coordinates shrink and compressing when their volume grows.

Thus for all practical purposes j can already be considered being constant under the assumption that the not included non-reactive coordinates take care of this by construction. However, it is not yet clear, which kind of error is introduced by the removal of those coordinates. In what follows, we will investigate this error further. Therefore we propose the following model scenario. If we construct a system whose dimensionality could be reduced without introducing any error, we can ensure that any error occurring due to a flawed reduction procedure is not an intrinsic effect of the dimensionality reduction itself. In other words, any error introduced to the correctly reduced system must also be present in an

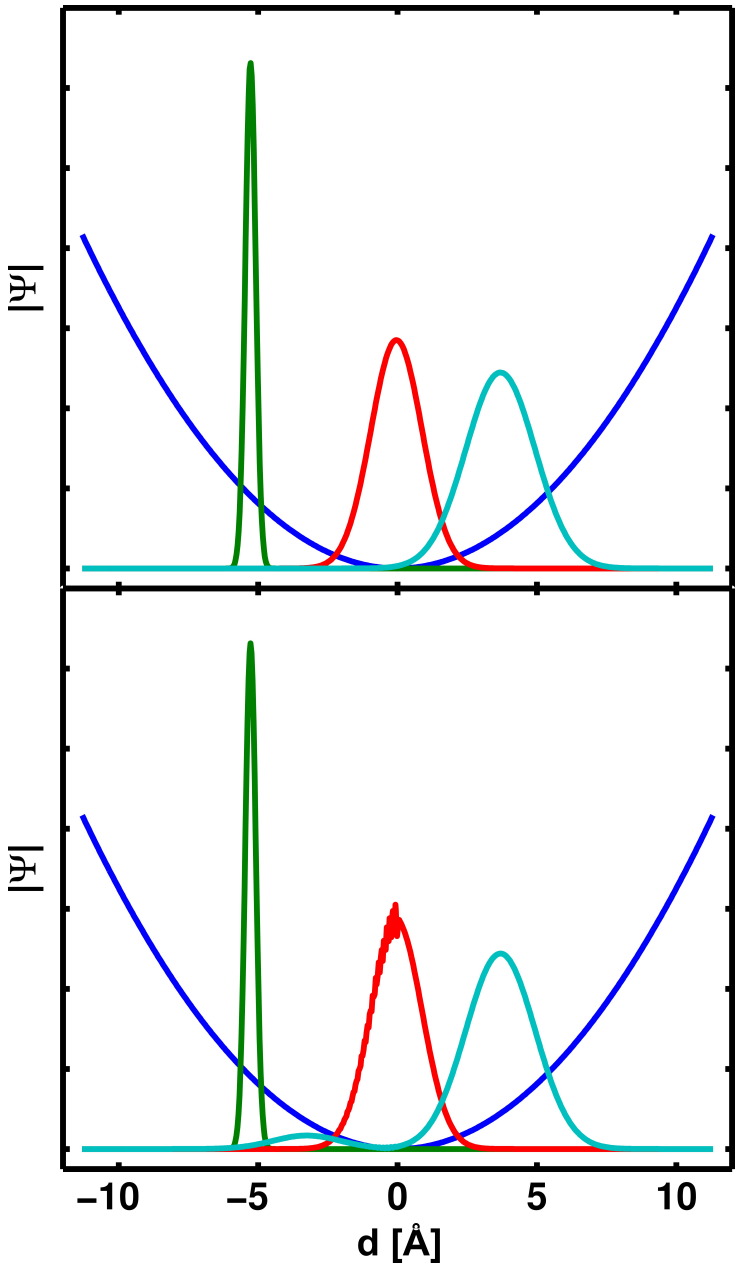

FIG. 1. Error introduced by approximating a constant Jacobian determinant j. The time evolution of a wavepacket inside a harmonic potential (blue) is shown at time 0 fs (green), 30 fs (red) and 54 fs (cyan). The upper panel shows the correct propagation on a Cartesian coordinate x, whereas the lower panel shows a erroneous propagation according to Eq. 5 on a nonlinear coordinate y. For visualization consistent with the coordinate x, the propagation on y in the lower panel is illustrated according to the transformation $\Psi(y)j(y)^{-\frac{1}{2}}$.

identical system that was created by reducing the dimensionality of the full system in a non-optimal way. This will allow us to isolate the error introduced by reducing different sets of coordinates.

The wavefunction Ψ_0 of our chosen full-dimensional system can be described by a product ansatz:

$$\Psi_0 = \Psi_{\mathbf{x}}\Psi_{\mathbf{y}} \ . \tag{6}$$

Here $\mathbf{x}$ denotes the part of coordinates that will be kept in the system of reduced dimensionality and $\mathbf{y}$ the part that will be removed. The Hamiltonian H can be written as a sum of two separate Hamiltonians – one for each coordinate subset $\mathbf{x}$ and $\mathbf{y}$:

$$H = H_{\mathbf{x}} + H_{\mathbf{y}} \ . \tag{7}$$

That the product ansatz works can be seen by inserting Eqs. 6 and 7 into the Schrödinger equation (Eq. 1) and separating the variables, leading to

$$\frac{1}{\Psi_{\mathbf{y}}}\left(i\frac{\partial}{\partial t}\Psi_{\mathbf{y}} - H_{\mathbf{y}}\Psi_{\mathbf{y}}\right) = C = -\frac{1}{\Psi_{\mathbf{x}}}\left(i\frac{\partial}{\partial t}\Psi_{\mathbf{x}} - H_{\mathbf{x}}\Psi_{\mathbf{x}}\right) \ . \tag{8}$$

Since C has to be a coordinate independent constant it is equivalent to some constant potential, which is irrelevant to the time evolution of the subsystems. From Eq. 8 we can derive two separate Schrödinger equations, propagating the subsystems $\mathbf{x}$ and $\mathbf{y}$ independently. Now, for all observables that only focus on results in the $\mathbf{x}$ subspace, we can write

$$\langle\Psi|O_{\mathbf{x}}|\Psi\rangle = \langle\Psi_{\mathbf{x}}|O_{\mathbf{x}}|\Psi_{\mathbf{x}}\rangle \langle\Psi_{\mathbf{y}}|\Psi_{\mathbf{y}}\rangle \ . \tag{9}$$

Since in Eq. 9 all observables only depend on the $\mathbf{x}$ subsystem, the dimensionality reduction to only the coordinates $\mathbf{x}$ can be performed without introducing any error. As a result, we can now make the aforementioned comparison.

Case 1: We start from the reduced subsystem $\mathbf{x}$ and introduce a coordinate transformation to an reactive coordinate set $\mathbf{s}$. Since we do not reduce the dimensionality any further, any error introduced by j not being constant is just the difference between Eq. 3 and Eq. 5.

Case 2: We start from the full system and introduce a coordinate transformation between $\mathbf{x}$ and $\mathbf{s}$. This also results in a coordinate transformation between the full coordinate space in its original coordinates and the full chosen set of reactive and non-reactive coordinates,

including those that ensure a constant j. Now the dimensionality is reduced by removing all degrees of freedom not included in $\mathbf{s}$.

In both cases the initial conditions for the propagation are identical and the time evolution after correctly performing the coordinate transformation will also be. We can therefore conclude that the easily quantifiable error in case 1 is indeed the error that will occur due to a non-constant j. This error could be eliminated by ensuring the transformation between $\mathbf{x}$ and $\mathbf{s}$ has a constant j.

For molecular cases there are at least two view points. Since j represents the change in volume due to the coordinate transformation, one way would be to rescale reactive coordinates so that the volume spanned by equispaced grid points remains constant at all positions. Let us consider an easy example with a bond distance d and an angular coordinate α. If d and α are equidistantly spaced, the volume segments of the reactive coordinate space grid will increase linearly with d. In this case rescaling the distance coordinate d to $\widetilde{d} = d^2$ will remove the errors by making j constant. This example is visualized in Figure 2. It can be seen that in a) the volume elements spanned by the grid points differ in size, whereas they are all equal in b). In this example, it is obvious that the rescaling does not change the subspac. Thus, errors due to a non-constant j are removed. A more rigorous treatment would be by ensuring that the Jacobian determinant j between the reactive coordinates and its locally tangential Cartesian subspace remains constant. The benefits of this approach can be seen in cases where the tangential Cartesian subspace changes along the reactive coordinates. An example for this is a reactive subspace spanned by a bond angle and a corresponding dihedral angle. There is no single two-dimensional tangential space for this subspace and for every grid point the volume change under coordinate transformation has to be considered relative to its locally tangential Cartesian subspace. This volume change would then again needed to be kept constant using the appropriate rescaling procedures of the coordinates.

In summary, we showed that the approximation of a constant Jacobian determinant in the Wilson G-matrix formalism can lead to errors using non-linear coordinates in molecular QD. However, the actual source of the error is hard to find as the coordinate reduction is commonly performed in the same step as the investigated approximation of a constant Jacobian determinant j. We presented a simple and straightforward solution to this problem: By ensuring a constant Jacobian determinant for the chosen subspace of the reactive

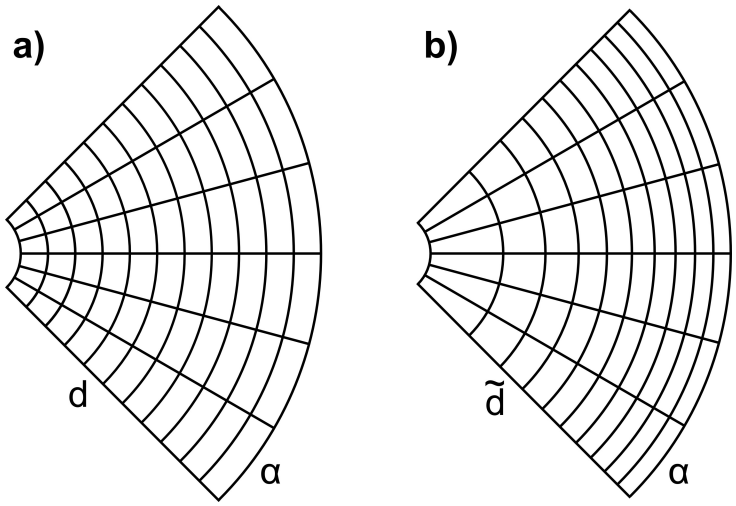

FIG. 2. Two types of coordinates sampling a distance and an angle. a) shows an equidistantly spaced grid using an angle α and a distance d that does not have a constant j. b) shows an equidistantly spaced grid using the same angle α and another distance variable $\widetilde{d}$ transformed according to $\widetilde{d} = d^2$. In this case j is constant.

coordinates $\mathbf{q}$ with respect to its tangential Cartesian subspace the approximation can be fulfilled and the only remaining error occurs due to the coordinate reduction itself.

In examples of molecular reactions, where a constant Jacobian determinant is not feasible – e.g. due to limitations on the number of grid points to $\sim 10^9$ – a solution might be to keep the Jacobian determinant between the non-linear reactive coordinate space and its locally tangential Cartesian subspace position dependent and to use it to substitute the full Jacobian determinant. We plan to investigate this hypothesis in more detail in the future.

ACKNOWLEDGEMENT

J.P.P.Z. and R.d.V.-R. thank the Deutsche Forschungsgemeinschaft for support via the excellence cluster Munich-Centre for Advanced Photonics (MAP) and the SFB749. S.T. thanks the European Commission for support via a Marie Skłodowska-Curie Individual Fellowship (project code 748895).

REFERENCES

[1]G. Nyman and H.-G. Yu, Int. Rev. Phys. Chem. **32**, 39–95 (2013), http://dx.doi.org/10.1080/0144235X.2012.735863.

[2]G. Nyman, Int. J. Quantum Chem. **114**, 1183–1198 (2014), ISSN 1097-461X, http://dx.doi.org/10.1002/qua.24661.

[3]K. Yagi, T. Taketsugu, and K. Hirao, J. Chem. Phys. **115**, 10647 (2001).

[4]C. Iung and F. Gatti, Int. J. Quantum Chem. **106**, 130 (2006).

[5]L. Joubert-Doriol, B. Lasorne, F. Gatti, M. Schröder, O. Vendrell, and H.-D. Meyer, Comput. Theor. Chem. **990**, 75 (2012).

[6]S. Thallmair, M. K. Roos, and R. de Vivie-Riedle, J. Chem. Phys. **144**, 234104 (2016), http://dx.doi.org/10.1063/1.4953667.

[7]J. P. P. Zauleck, S. Thallmair, M. Loipersberger, and R. de Vivie-Riedle, J. Chem. Theory Comput. **12**, 5698–5708 (2016), http://dx.doi.org/10.1021/acs.jctc.6b00800.

[8]X. Li, Y. Xie, D. Hu, and Z. Lan, J. Chem. Theory Comput. **13**, 4611 (2017).

[9]J. P. P. Zauleck and R. de Vivie-Riedle, arXiv(2017), https://arxiv.org/abs/1710.04535.

[10]M. R. Brill, F. Gatti, D. Lauvergnat, and H.-D. Meyer, Chemical Physics **338**, 186 (2007), ISSN 0301-0104.

[11]B. Podolsky, Phys. Rev. **32**, 812–816 (1928).

[12]E. B. Wilson Jr., J. C. Decius, and P. C. Cross, *Molecular Vibrations* (McGraw-Hill, New York, 1955).

[13]L. J. Schaad and J. Hu, J. Mol. Struct.: THEOCHEM **185**, 203–215 (1989).

[14]E. B. Wilson Jr., J. Chem. Phys. **7**, 1047 (1939).

[15]F. Ribeiro, C. Iung, and C. Leforestier, J. Chem. Phys. **123**, 054106 (2005).

[16]D. J. Tannor, *Introduction to Quantum Mechanics: A Time-Dependent Perspective* (University Science Books, Sausalito, California, USA, 2007).

[17]V. Alexandrov, D. M. A. Smith, H. Rostkowska, M. J. Nowak, L. Adamowicz, and W. McCarthy, J. Chem. Phys. **108**, 9685–9693 (1998).

[18]M. D. Feit, J. J. A. Fleck, and A. Steiger, J. Comput. Phys. **47**, 412 (1982).

3.2 Undersampling as a tool to reduce the grid point density

There are several possible directions to improve the computational efficiency of grid based QD calculations. Optimizing the dimensionality reduction beforehand has been discussed in chapter 1 and in the last bit of section 3.1 an unevenly spaced grid has been implied that could allow for more efficient sampling. The associated reduction in number of grid points due to the latter would in turn reduce the computation cost. In fact, much research has been done on the topic of grids with adaptive point densities for this reason [17, 166–169]. However, undersampling [170, 171], which can have a similar effect on the reduction of grid points and which is compatible with the DFM in contrast to the adaptive grids, has not been touched in the context of QD to the authors knowledge.

The basic idea in undersampling is to use additional information to avoid the limit on grid point density as given by the Nyquist-Shannon sampling theorem [172, 173]. Since the point density of a spatial grid is proportional to the maximum representable range in momentum space, this works well for localized wavepackets in momentum space, as will be demonstrated in the following. An illustration is given in fig. 3.1. It shows three wavepackets in momentum space that cannot be distinguished for a given grid spacing of Δx. Decreasing the spacing to $\Delta x/3$ allows to distinguish all three wavepackets. In this case however, large parts of the momentum space are not used. In fact, the small momentum space captures almost all information about each wavepacket, except for the position of its center. This can be introduced as an external piece of information and the small momentum space resulting from the original grid spacing of Δx can be used. It should be noted that the PES that is used by the wavepacket has to be accurately represented by the grid point density as well. This makes undersampling most suited for parts of the PES with a small curvature.

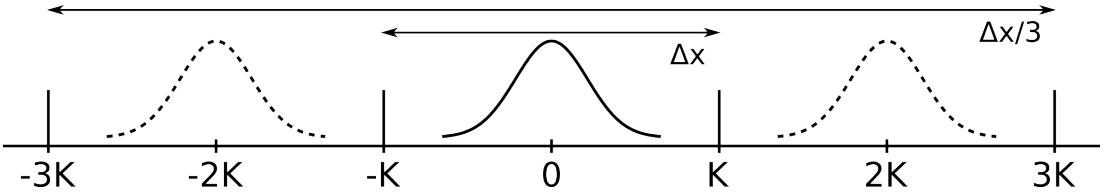

Figure 3.1: Illustration of the wavefunction in momentum space for grids with different spacing. For a grid with a spacing of Δx, the momentum space reaches from $-K$ to K. Due to the periodic boundary conditions, the solid and dashed wavefunctions cannot be distinguished in this case. If the grid spacing is decreased to $\Delta x/3$ and the length of the momentum space thus tripled, all three cases are distinguishable.

Undersampling is easy to implement within the DFM, since the additional information about the wavepacket in the momentum space can be included in the application of the kinetic energy operator to the wavefunction Ψ after applying the Fourier transform. Here, the second derivative is applied using the Fourier transform $\mathcal{F}()(k)$ and the inverse Fourier transform $\widetilde{\mathcal{F}}()(x)$ according to

$$\frac{\partial^2}{\partial x^2}\Psi(x) = \widetilde{\mathcal{F}}\big(-k^2\mathcal{F}(\Psi(x))(k)\big)(x) \ , \tag{3.3}$$

denoting the position by x and the wavenumber by k, which is the same as the momentum with the use of atomic units. To use undersampling, the wavefunction can be shifted so that its momentum expectation value lies at $k = 0$ via

$$\Psi_\mathrm{s}(k) = \Psi(k - k_\mathrm{s}) \ , \tag{3.4}$$

while keeping track of the shift k_s. This allows to restrict the minimum and maximum representable momentum. In order to still correctly apply the kinetic energy operator to the shifted

wavefunction Ψ_s, eq. 3.3 is updated to

$$\frac{\partial^2}{\partial x^2}\Psi_\mathrm{s}(x) = \widetilde{\mathcal{F}}\big(-(k-k_\mathrm{s})^2\mathcal{F}(\Psi_\mathrm{s}(x))(k)\big)(x) \ . \tag{3.5}$$

In the representation on a grid, the necessary operations, namely the testing whether a shift is needed, calculation of the size of the shift and the application of the shift to k, scale at most $O(n)$ with the number of grid points while requiring very few additions and multiplications every few time steps. The fast Fourier transform scales $O(n \log n)$ and dominates the computational cost at the system sizes at which savings become relevant. Thus, if the number of grid points can be halved using the mentioned additional $O(n)$ computations, the computation time will approximately also be halved.

The functionality is best illustrated using a small model system. One may consider a compact wavepacket continuously accelerated on a linear, steep potential. This can be described using a grid with a point density that can represent the biggest momentum, i.e. the momentum at the end of the propagation. This point density can be reduced significantly using undersampling. This is shown in fig. 3.2 together with a propagation using a high point density. A system with the same mass as the reduced mass of the $Ph_2CH{-}PPh_3^+$ system and potential with a constant gradient of 2 eV/Å, which is similar to the gradient in $Ph_2CH{-}PPh_3^+$, has been used.

The initial wavepacket is centered at 5 Å and allowed to accelerate until it reaches 20 Å. The red system uses 2048 grid points without undersampling and the blue system uses 80 grid points with undersampling. This is done by shifting the wavepacket by k_s to the center of the momentum space, once the expectation value of k reaches 5 Å^{-1}. Fig. 3.2.b shows how little momentum space is necessary for a correct description using undersampling. For the first part (0-147 fs), the red system behaves physically correct, as is expected. Up to this point it can be understood as a reference for the undersampling system, which performs well. As the wavepacket of the red system then reaches the limits of its momentum space, its momentum gets effectively inversed and it turns around, which is also to be expected. However, the blue systems still evolves in the physically expected way as can be seen at 210 fs in fig. 3.2.a. In this example, the blue system using undersampling thus performs better than the red system of high grid density, that is limited by its momentum space. Additionally, the number of grid points is reduced from 2048 to 80 using undersampling.

As has been demonstrated, undersampling can provide enormous savings in computational cost for some systems. The benefits depend strongly on the compactness of the wavefunction in momentum space and the structure of the potential. One scenario encountered in practice is the dissociation of a molecule into relatively heavy fragments due to photoexcitation. Here the PES can be sufficiently steep and even, accelerating the wavepacket fast enough that dispersion does not occur significantly. All in all, the application to different realistic systems would be an important next step to test the use of this approach.

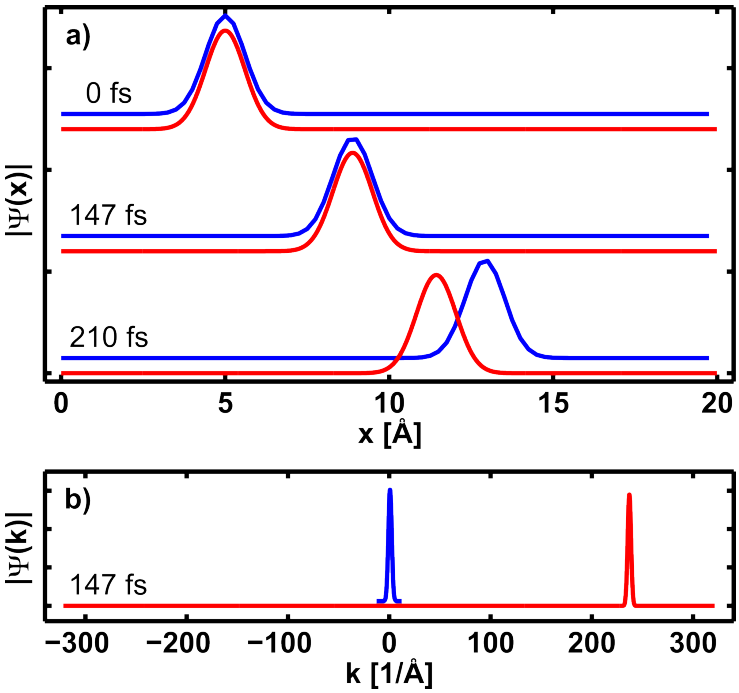

Figure 3.2: Comparison of propagations with and without the use of undersampling. a) shows the propagation in position space at the times of 0 fs, 147 fs and 210 fs. Both systems span the same position space but differ in points density. The red system uses 2048 grid points without, whereas the blue system uses undersampling to reduce the number of grid points to 80. At 210 fs, the red system has reached the edge of the momentum space and produced incorrect results. b) shows the momentum space at 147 fs for both systems. It can be seen that the momentum space for the system with undersampling (blue) is much smaller. For visibility the red and blue curves are slightly shifted against each other in y-direction.

Chapter 4

Summary and outlook

For quantum dynamics (QD), the dynamic Fourier method (DFM) with its pseudo-spectral grid basis is an important tool, because of its accuracy and generality for systems, which can be described with a reduced number of coordinates. Consequentially, its further development in terms of efficiency and scope is desirable. In the present work efficiency improvements concerning the reduction of coordinates, the more accurate treatment of a common approximation in the G-matrix formalism and the use of undersampling were presented as well as an extension of the method to include classically treated solvent environments.

The first chapter discussed strategies to automate the dimensionality reduction for reactive systems that is required in order to apply QD calculations using the DFM to systems of realistic sizes. Altogether three approaches were presented. The first (IBA) begins by spanning the subspace containing the critical points of the reaction. Additionally, points along the IRC are used to further increase the dimensionality of the subspace. The resulting subspaces, one for each combination of IRC points, are compared according to their ability to reconstruct the IRC and its energy profile and the best one is chosen for prospective QD calculations. In a similar fashion, the TBA also starts from the degrees of freedom describing the critical points, but then uses classical molecular dynamics (MD) trajectories that approximately follow the reaction path to extract additional degrees of freedom that are most descriptive of the trajectories. The resulting subspace is also linear and can be compared to the one created by the IBA. Both approaches were applied to two example systems, the proton transfer in (Z)-hydroxyacryloyl chloride and the methylization of cyclohexanone using trimethylaluminum. It was demonstrated that both approaches yield similar results, which indicates, given their independence from each other, that both approaches discover high-quality subspaces.

Extending the dimensionality reduction to nonlinear subspaces, the third approach uses an autoencoder to find a low-dimensional embedding of MD trajectory data. It was shown how this can be used to set up a grid and how a Hamiltonian can be constructed. The approach was tested on the proton transfer in (Z)-hydroxyacryloyl chloride, where the increased accuracy of the constructed nonlinear subspace compared to linear ones was demonstrated. All three developed methods are best suited for slightly different systems. The IBA may be very useful for systems whose dynamics stay close to the IRC and are mostly described by linear coordinates such as bond distances. In this case, only the IRC is required and offers a relatively lightweight option to approach the QD. The TBA seems to be a valuable tool to gain quick access to first QD results, when MD trajectories are easily attainable. It can be applied using very few trajectories and the computational overhead associated with the identification of the reactive coordinates can be neglected.

The nonlinear subspaces created by using an autoencoder have the potential to become the standard basis for this kind of grid based QD whenever most emphasis lies on the accuracy of the results. While they require notable computational effort, they allow for the use of any desired

level of classical or semiclassical trajectories to screen the reactive subspace and use them as construction guidelines. The resulting nonlinear subspaces require less dimensions than linear ones and thus push the limitations in system size. An illustration of this is shown in fig. 4.1 for the proton transfer reaction in (Z)-hydroxyacryloyl chloride. Here, three linear coordinates, i.e. the principal components, are very relevant to the reactive space, but a curved subspace allows for the essential motions to be covered using two nonlinear coordinates that constitute the potential energy surface (PES). In the bigger picture, this reduced dimensional approach could possibly lead to a quadratic or lower scaling of the computation time with the number of atoms of a molecule. The number of processes studied where this will be useful is immense. One example that illustrates this especially well is the laser steering of reactions. Here, trajectory calculations can be done to design laser pulses that enable individual reactant geometries to be guided to the desired product. However, these pulses vary significantly with different initial geometries. QD calculations are suited to overcome this, since they intrinsically work with distributions. As a result, the trajectory calculations might be very useful to identify the reactive space that describes the reaction one wishes to enable. This reactive space can then be used to calculate the required laser pulses using accurate QD calculations.

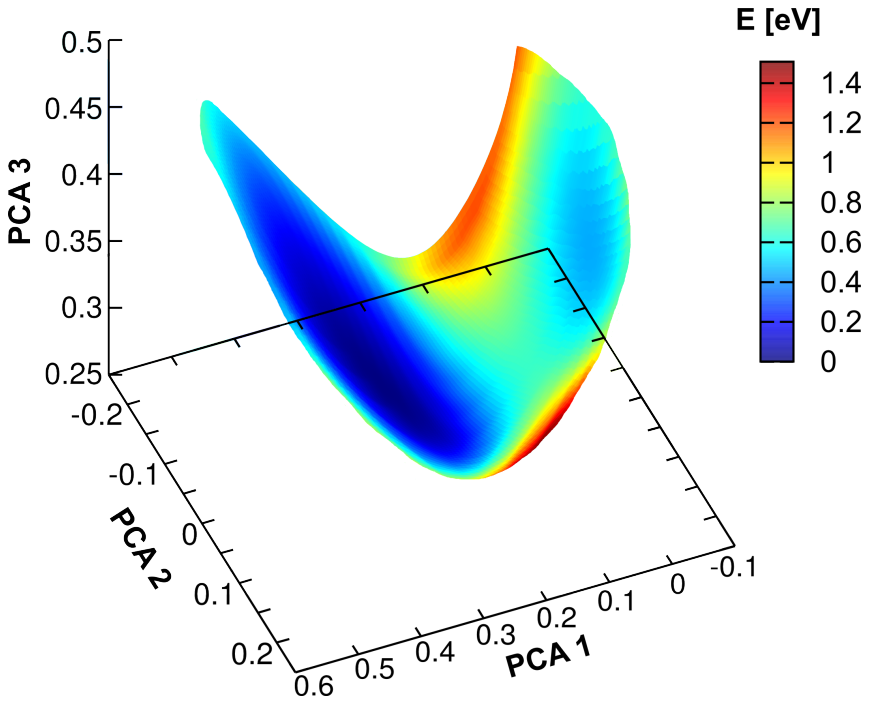

Figure 4.1: Projection of the two-dimensional potential energy surface generated using an autoencoder onto the first three principal components of the MD data. Since all three PCA coordinates contribute significantly to the data set and the IRC the surface is strongly curved. The depth of the PES is given by color and is not related to the spatial dimensions. It shows the double minimum potential structure typical for derivatives of malondialdehyde. This projection is analogous to an angle coordinate projected onto its x and y components, resulting in a circle, on which a color coded potential could be represented. The PCA coordinates are given in relative units.

In the second chapter, the inclusion of dynamic environment effects in the grid based QD of solvated systems was studied. Three methods with increasing complexity were presented. The first, the dynamic continuum ansatz, treats the solvent of dissociative systems implicitly. It uses the experimentally determined viscosity of the solvent, a distance function representing the deformation of the solvent cavity and the wavefunction to calculate a decelerating potential acting on the dissociating fragments. The second method, the combined QD/MD approach, uses frozen

MD snapshots of the solvent to explicitly calculate external potentials for ultrafast processes of the solute. With the use of enough different solvent arrangements, the overall results converge. Along with this, a procedure was introduced to calculate the interaction potential between solute and solvent molecules using a reduced number of relative coordinates. Both approaches have been applied to simulate the photodissociation of $Ph_2CH{-}PPh_3^+$. In this system the dynamic effects of the solvent are decisive for the prediction of the formation of the experimentally observed products. Both methods were shown to be able to predict the experimental results correctly. The third method, the cQDMD, extends the quantum-classical TDSCF to the simultaneous propagation of solute and solvent, where the grid based QD of the solute are complemented with classical degrees of freedom for translation and rotation. Accordingly, the cQDMD can be understood as a direct improvement of the combined QD/MD approach. Within its limits, the cQDMD can also be used to study decoherence, as has been demonstrated.

Of the resulting approaches, the dynamic continuum ansatz is the more specialized one. While it is clearly very computationally efficient, care must be taken that the dynamic solvent effects can be described reasonably well without explicit effects such as collisions that result in opposite momentum. If this is the case, as for example in large dissociating fragments, the dynamic continuum ansatz can prove useful. The cQDMD approach is more costly but also far more generally applicable. Its major limitations are scenarios where quantum effects of the solvent become important and systems, where parts of the wave function become widely spatially separated. Given present computational abilities, both limits are in principal avoidable, but would require further research.

The third chapter focused on two minor improvements to grid based QD. The first is a re-evaluation of an approximation commonly made in the Wilson G-matrix formalism. It was shown how the approximation can introduce errors and how they can be avoided using a low-dimensional alternative to the Jacobian determinant. Besides the resulting increased accuracy, the alternative to the Jacobian determinant might also be useful for constructing more efficient grids by avoiding the studied approximation.

The other improvement was demonstrated for systems whose wavefunctions have a low variance in momentum, while having big momentum expectation values. It was demonstrated how undersampling can be used in these cases to reduce the number of grid points needed for propagation. One potential application is the study of dissociative systems with an evenly structured PES, where this may enable an increase in the dimensionality of the reactive subspace in which the system is to be studied using similar computation times.

Appendix A

Supporting information for chapter 1.2

Constructing grids for molecular quantum dynamics using an autoencoder – Supporting Information

Julius P. P. Zauleck and Regina de Vivie-Riedle*

Department Chemie, Ludwig-Maximilians-Universität München, D-81377 München, Germany

E-mail: regina.de_vivie@cup.uni-muenchen.de

Approximate Projection onto Nonlinear Subspaces

This projection assumes that the point $\mathbf{y}$ to be projected is close enough to the subspace and the subspace is not pathologically curved. Otherwise the algorithm will only find relative projection optima. It also assumes that the imperfect projection $\widetilde{\mathbf{H}}(\widetilde{\mathbf{F}}())$ does not change drastically with small changes in its argument. In practice, this assumption holds.

We now have a set of non orthonormal basis vectors $\mathbf{a}_j$, comprising a nonorthonormal projection matrix $\mathbf{A} = [\mathbf{a}_1\ \mathbf{a}_2 \cdots \mathbf{a}_N]$. These give us a basis of the tangential space of the nonlinear subspace at the point $\widetilde{\mathbf{H}}(\widetilde{\mathbf{y}}')$. If we find a projection onto this tangential space, we can project the distance between the point to be projected $\mathbf{y}$ and the current approximation of its projection $\widetilde{\mathbf{H}}(\widetilde{\mathbf{y}}')$ onto it. This projection is approximately the distance vector between the approximate projection and the actual projection. Thus, if we deduct it from $\widetilde{\mathbf{H}}(\widetilde{\mathbf{y}}')$ and iteratively do this with an appropriately small step size, we reach the actual projection.

The last thing missing is an expression for a projection using a nonorthonormal basis. To derive

*To whom correspondence should be addressed

this, we start with the most general representation of a vector $\mathbf{x}$ in this basis:

$$\mathbf{x} = \sum_i a_i \mathbf{a}_i \tag{1}$$

Here a_i is the coefficient of its ith basis vector. Those coefficients tell us how the vector $\mathbf{x}$ looks in our basis $\mathbf{a_i}$ and we want to find a vector $\mathbf{b} = [a_1\ a_2 \cdots a_N]$ composited of these coefficients a_i.

To get there we multiply $\mathbf{x}$ with an $\mathbf{a}_j^T$:

$$\mathbf{a}_j^T \mathbf{x} = \sum_i a_i \mathbf{a}_j^T \mathbf{a}_i \tag{2}$$

If this is considered to be the jth element of a vector, we can write this as

$$[\mathbf{a}_1^T \mathbf{x}\ \ \mathbf{a}_2^T \mathbf{x}\ \ \cdots\ \ \mathbf{a}_N^T \mathbf{x}]^T = \mathbf{x}^T \mathbf{A} = \mathbf{A}^T \mathbf{A} \mathbf{b}\ . \tag{3}$$

If we isolate $\mathbf{b}$ we obtain

$$\mathbf{b} = \left(\mathbf{A}^T \mathbf{A}\right)^{-1} \mathbf{x}^T \mathbf{A}\ . \tag{4}$$

Grid Spacing

We begin with the classical expression of the kinetic energy T in terms of the G-matrix $\mathbf{G}$ and the momentum vector $\mathbf{p}$:[1]

$$T = \frac{1}{2} \mathbf{p}^T \mathbf{G} \mathbf{p} \tag{5}$$

Now, a relationship between the kinetic energy and the momentum along a single coordinate is needed. In the worst case all of the kinetic energy is contained within a single directional momentum $p_{r,\max}$, which represents the maximum momentum that is classically possible in this direction. This means that the the momentum vector $\mathbf{p}$ has only one non zero entry at index r. If we insert

this in Eq. 5, it becomes

$$T = \frac{1}{2} p_{r,\max}^2 \mathbf{G}_{rr} \, . \tag{6}$$

Since the nyquist frequency determines the upper bound for the spacing Δq_r in order to represent a certain momentum via

$$\Delta q_r < \frac{\pi}{p_{r,\max}} \, , \tag{7}$$

we can now derive the relationship between the spacing and the kinetic energy along a certain direction as

$$\Delta q_r < \pi \sqrt{\frac{\mathbf{G_{rr}}}{2T}} \, . \tag{8}$$

In practice the kinetic energy T will almost never be close to completely in coordinates orthogonal to the IRC. Therefore the kinetic energy T_r along the different directions r also differs, resulting in

$$\Delta q_r < \pi \sqrt{\frac{G_{rr}}{2T_r}} \, . \tag{9}$$

References

(1) Wilson, E. B.; Decius, J. C.; Cross, P. C. *Molecular Vibrations: The Theory of Infrared and Raman Vibrational Spectra*; Dover Publications, 1980.

Appendix B

Supporting information for chapter 2.2

Supporting information for: Quantum Dynamics in an Explicit Solvent Environment: A Photochemical Bond Cleavage Treated with a Combined QD/MD Approach

Sebastian Thallmair,[†,‡] Julius P. P. Zauleck,[†] and Regina de Vivie-Riedle[*,†]

Department Chemie, Ludwig-Maximilians-Universität München, D-81377 München, Germany, and Lehrstuhl für BioMolekulare Optik, Ludwig-Maximilians-Universität München, D-80538 München, Germany

E-mail: regina.de_vivie@cup.uni-muenchen.de

[*]To whom correspondence should be addressed

[†]Department Chemie, Ludwig-Maximilians-Universität München, D-81377 München, Germany

[‡]Lehrstuhl für BioMolekulare Optik, Ludwig-Maximilians-Universität München, D-80538 München, Germany

1 Partition of the coordinates to calculate the probability distributions $P(q_n)$

To analyze the standard deviation σ_{q_n} of the interaction energy, the probability distributions $P(q_n)$ for the angular coordinates in the orientation space have to be evaluated. To this, $P(q_n)$, calculated according to eq 6 in the manuscript, has to be smoothed. We Fourier transformed $P(q_n)$, applied a low-pass butterworth filter $F(\omega)$ and then performed an inverse

Table S1: Partition of the coordinates and relative deviation D of the normalized resulting probability distributions for the calculation of the standard deviation σ_{q_n} of the interaction energy with respect to the four angular coordinates α_s, β_s, α_f and β_f. The values are given for the two fragments PPh_3 and Ph_2CH in which $Ph_2CH{-}PPh_3{}^+$ is partitioned.

coordinate q_n	partition	partition	partition	σ_{q_n} [au]
	D	D	D	
$\alpha_s(PPh_3)$	$\frac{\beta_s}{2}$	$\frac{\alpha_f}{2}$	$\frac{\beta_f}{2}$	$1.58 \cdot 10^{-4}$
	0.038	0.047	0.049	
$\beta_s(PPh_3)$	$\frac{\alpha_s}{2}$	$\frac{\alpha_f}{2}$	$\frac{\beta_f}{2}$	$7.61 \cdot 10^{-5}$
	0.044	0.032	0.055	
$\alpha_f(PPh_3)$	$\frac{\alpha_s}{2}$	$\frac{\beta_s}{2}$	$\frac{\beta_f}{2}$	$1.62 \cdot 10^{-4}$
	0.058	0.039	0.029	
$\beta_f(PPh_3)$	$\frac{\alpha_s}{2}$	$\frac{\beta_s}{2}$	$\frac{\alpha_f}{4}$	$2.71 \cdot 10^{-4}$
	0.095	0.060	0.097 / 0.116	
$\alpha_s(Ph_2CH)$	$\frac{\beta_s}{2}$	$\frac{\alpha_f}{2}$	$\frac{\beta_f}{2}$	$1.28 \cdot 10^{-4}$
	0.020	0.035	0.012	
$\beta_s(Ph_2CH)$	$\frac{\alpha_s}{2}$	$\frac{\alpha_f}{2}$	$\frac{\beta_f}{2}$	$7.21 \cdot 10^{-5}$
	0.047	0.059	0.057	
$\alpha_f(Ph_2CH)$	$\frac{\alpha_s}{2}$	$\frac{\beta_s}{2}$	$\frac{\beta_f}{2}$	$1.03 \cdot 10^{-4}$
	0.020	0.021	0.034	
$\beta_f(Ph_2CH)$	$\frac{\alpha_s}{2}$	$\frac{\beta_s}{2}$	$\frac{\alpha_f}{2}$	$1.34 \cdot 10^{-4}$
	0.085	0.085	0.107	

Fourier transformation. $F(\omega)$ reads

$$F(\omega) = \frac{1}{1 + \left(\frac{\omega}{\omega_0}\right)^n}, \tag{1}$$

with the central frequency ω_0 and the order n. We used the values $\omega_0 = 0.1$ and $n = 100$. To ensure that no compensation of orientations occurs for the tested coordinate we divided the interval of the other angular coordinates in half and compared the shape of the obtained probability distributions of both parts with each other and with the initial shape. If they are similar enough no further dividing is necessary, if not the procedure is repeated for both halves. In Table S1 the relative deviation D, i.e. the integral of the absolute difference of the normalized probability distributions $P^j(q_n)$ for each interval j, for the final partitioning are given. All D values lie below 12% and are sufficiently small.

Figure S1 shows the normalized probability distributions $P(\alpha_s)$ for the PPh_3 fragment. The intervals of all remaining angular coordinates are divided into halves ((a) β_s; (b) α_f; (c) β_f). The corresponding relative deviations D are given in the second row of Table S1. In the depicted case the probability distributions are quite similar so no further partitioning of the coordinates is necessary.

To calculate the standard deviations σ_{q_n} for the interaction energy along the angular coordinates, the m standard deviations $\sigma_{q_n}^j$ for the partitions $j \in \{1, 2, \ldots, m\}$ have to be averaged according to eq 13 in the main text. Here we briefly want to explain the origin of the weighting factor $\frac{N_j}{N_0}$ in this equation.

The variance $\mathrm{Var}_A(x) = (\sigma_{A,x})^2$ of the elements $x \in A$ of a set A is

$$\mathrm{Var}_A(x) = \sum_{x \in A} \left(x - \overline{x_A}\right)^2 P_A(x), \tag{2}$$

with the mean value of x in A being $\overline{x_A}$ and the discrete probability distribution $P_A(x)$ of the elements in A. The set A can now be divided into two subsets B and C. Each element

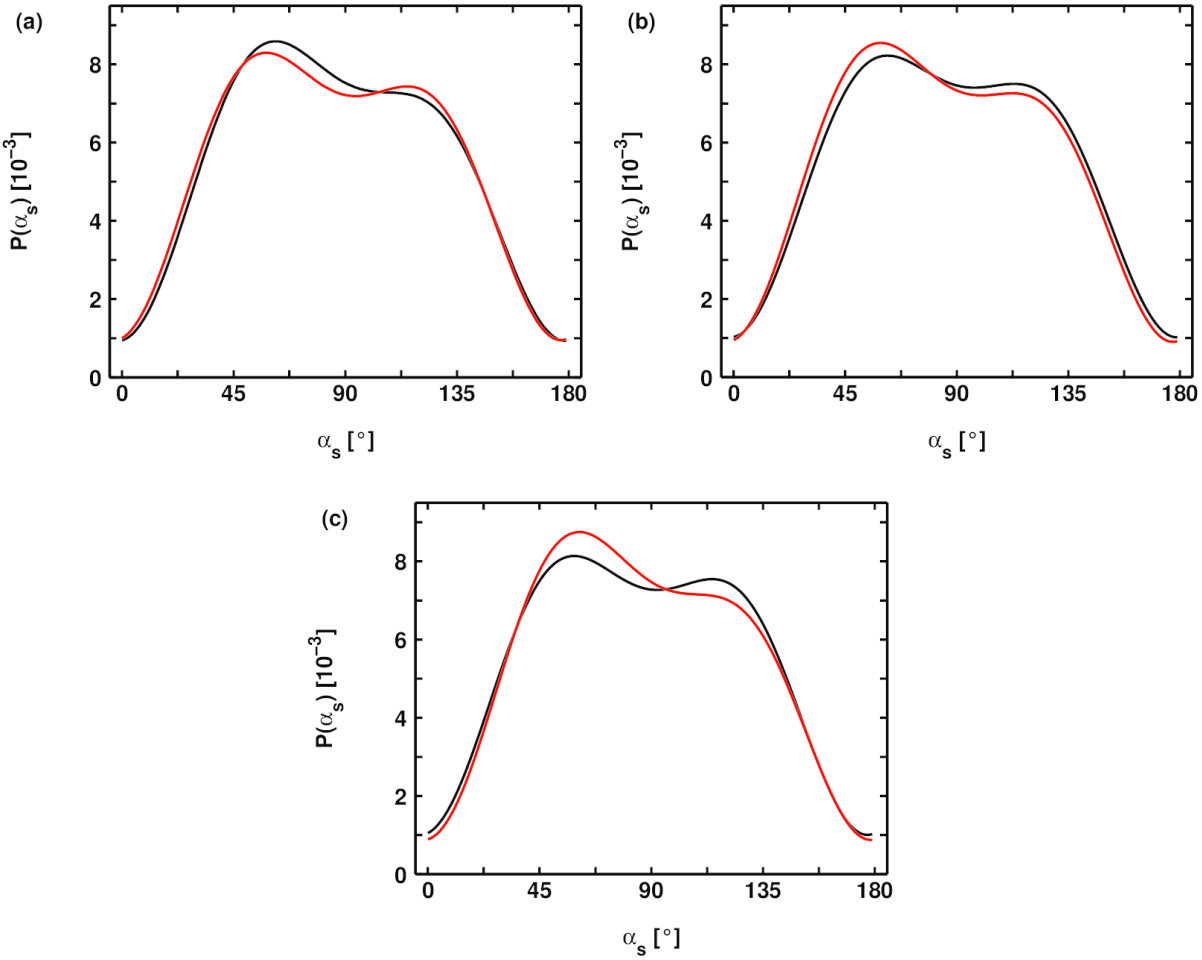

Figure S1: Normalized probability distributions $P(\alpha_s)$ evaluated for the halved interval of the remaining angular coordinates for the PPh_3 fragment. (a) Intervals for β_s: $[0;180[$ (black) and $[180;360[$ (red). (b) Intervals for α_f: $[0;45[$ (black) and $[45;90[$ (red). (c) Intervals for β_f: $[0;180[$ (black) and $[180;360[$ (red).

of A is either an element of B or of C. Thus eq 2 can be transformed to

$$\mathrm{Var}_A(x) = \sum_{x\in B} (x - \overline{x_A})^2 \frac{N_B}{N_A} P_B(x) + \sum_{x\in C} (x - \overline{x_A})^2 \frac{N_C}{N_A} P_C(x). \tag{3}$$

Here N_A, N_B and N_C are the number of elements in the set A, B and C, respectively. In the case, the mean values in the subsets B and C ($\overline{x_B}$ and $\overline{x_C}$) are the same as $\overline{x_A}$ eq 3 can

be rewritten:

$$\begin{aligned} \mathrm{Var}_A(x) &= \frac{N_B}{N_A} \sum_{x \in B} (x - \overline{x_B})^2 \, P_B(x) + \frac{N_C}{N_A} \sum_{x \in C} (x - \overline{x_C})^2 \, P_C(x) \\ &= \frac{N_B}{N_A} \mathrm{Var}_B(x) + \frac{N_C}{N_A} \mathrm{Var}_C(x). \end{aligned} \tag{4}$$

In eq 13 in the main text we also use the proportion of elements in the each subset (here $\frac{N_B}{N_A}$ and $\frac{N_C}{N_A}$) as weighting factors for the squares of the standard deviations $\sigma_{q_n}^j$ like in eq 4 above.

2 Quantum dynamics

The quantum dynamics (QD) were performed on a regular space grid with 1024 points in r direction and 512 points in ϕ direction. The size of the spatial grid was $r \in [1.65\,\text{Å}, 6.00\,\text{Å}]$ and $\phi \in [40°, 140°]$. The time evolution of the system was calculated by solving the time-dependent Schrödinger equation numerically with the Chebychev propagation scheme.[S1] We used a time step of 100 au (1.42 fs). The vibrational ground state eigenfunction $v = 0$ of the electronic ground state was determined propagating in imaginary time.[S2] To express the kinetic operator $\hat{T}$ in the chosen two-dimensional coordinate space, the G-matrix method was used:[S3–S5]

$$\hat{T} = -\frac{1}{2} \sum_{r=1}^{M} \sum_{s=1}^{M} \frac{\partial}{\partial q_r} \left[G_{rs} \frac{\partial}{\partial q_s} \right] \tag{5}$$

$$\text{with} \quad G_{rs} = \sum_{i=1}^{3N} \frac{1}{m_i} \frac{\partial q_r}{\partial x_i} \frac{\partial q_s}{\partial x_i} \; . \tag{6}$$

Here M is the total number of internal coordinates and N is the number of atoms in the considered molecule.

The G-matrix method allows the use of arbitrary orthogonal coordinates for the quantum dynamical propagations. For details about the G-matrix elements see reference S6 and its supporting information.

3 Convergence of population dynamics

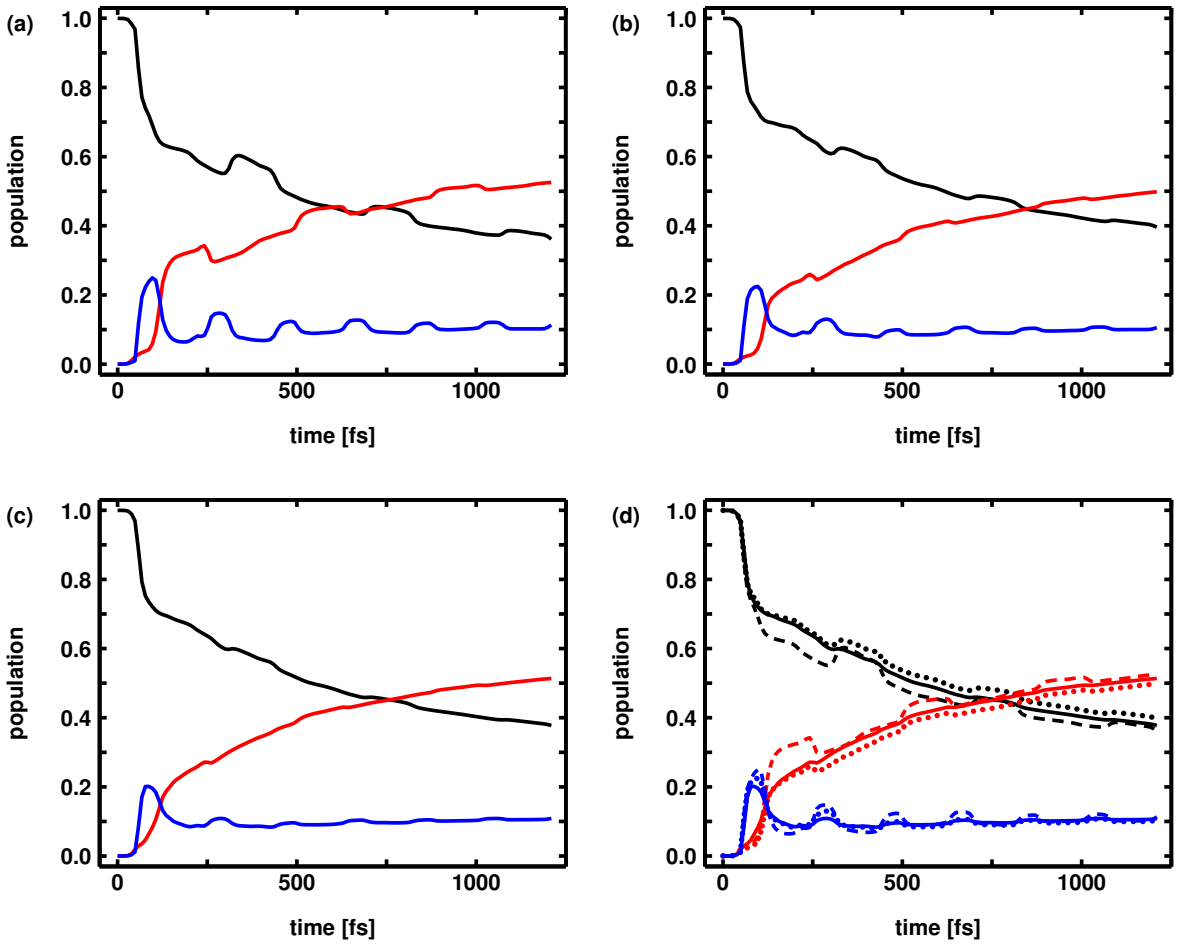

Figure S2: Population dynamics for the QD simulation of the bond cleavage of $Ph_2CH{-}PPh_3^+$ averaged over (a) 12, (b) 25 and (c) 50 different solvent arrangements taken from MD trajectories. The black line represents the population in the FC region, the blue line the population in the S_1 dissociation area and the red line the population around the CoIn. The three areas are depicted in the inlay in Figure 8 in the manuscript. (d) shows the overlay of the three graphs (dashed: 12 snapshots, dotted: 25, solid: 50).

A convenient way to cover the thermodynamically accessible configuration space of a solvent environment around a solute is to perform MD simulations of the system. From these a sufficient large number of snapshots along the trajectories represents the solvent surrounding. For an overall picture of the bond cleavage of $Ph_2CH{-}PPh_3^+$ we averaged the wave packet propagations in the different solvent surroundings according to eq 4 in the manuscript. Figure S2 shows the convergence in the population dynamics increasing the number of MD snapshots from $N_{\mathrm{snap}} = 12$ (a) over $N_{\mathrm{snap}} = 25$ (b) to $N_{\mathrm{snap}} = 50$ (c). The black line represents the population in the FC region, the blue line the population in the S_1 dissociation area and the red line the population around the CoIn. In Figure S2(d) the three graphs of Figure S2(a)–(c) are overlaid (dashed line: 12 snapshots, dotted: 25, solid: 50). This showed 50 to be a sufficient large number of MD snapshots.

4 Qualitative comparison of the required computing time

The presented QD/MD approach requires several different computational steps to simulate the influence of the solvent environment on the QD of the solute. To estimate the effort behind the different computations table S2 lists the required computing time for the dif-

Table S2: Qualitative comparison of computing time for simulation of the photoinduced bond cleavage of $Ph_2CH{-}PPh_3^+$ using the presented QD/MD approach. The computing time is given for one CPU although some computations were performed parallel. Note that not all computations were performed on the same machine. The fourth column specifies how often the computation has been performed for the presented bond cleavage of $Ph_2CH{-}PPh_3^+$.

computation of	method	computing time [s]	number
$V_{\mathrm{mol}}(r, \phi)$	QC (ONIOM)	$3.4 \cdot 10^6$	1
solvent dynamics	MD	$3.7 \cdot 10^4$	1
$P(q_n)$	evaluation of orientations	$3.2 \cdot 10^3$	1
$E_{\mathrm{sf}}(\lvert\overrightarrow{r_{\mathrm{sf}}}\rvert, \alpha_{\mathrm{s}}, \alpha_{\mathrm{f}}, \beta_{\mathrm{f}})$	QC (DFT)	$1.8 \cdot 10^7$	1
$V_{\mathrm{solv}}(r, \phi)$	evaluation of orientations	$2.1 \cdot 10^2$	50
solute dynamics	QD	$4.4 \cdot 10^4$	50

ferent calculations in the case of the photoinduced bond cleavage of $Ph_2CH{-}PPh_3{}^+$. The computing time is given for one CPU although some computations were performed parallel. Note that not all computations were performed on the same machine. The fourth column specifies how often the corresponding computation has been performed for the investigation of the bond cleavage of $Ph_2CH{-}PPh_3{}^+$.

For the calculation of $V_{\mathrm{mol}}(r, \phi)$ 483 single point calculations on the "our own n-layered integrated molecular orbital and molecular mechanics (ONIOM)" level of theory (CASSCF(10, 10)/M06-2X) were performed; for the quantum chemical database of $E_{\mathrm{sf}}(|\overrightarrow{r_{\mathrm{sf}}}|, \alpha_{\mathrm{s}}, \alpha_{\mathrm{f}}, \beta_{\mathrm{f}})$ 21780 single points at the DFT level of theory (M06-2X).

5 Optimized geometries

In the following the optimized geometry of the ground state minimum of $Ph_2CH{-}PPh_3{}^+$ (DFT, B3LYP / 6-31g(d)) and the structure with the minimal energy difference between S_1 and S_0 at the ONIOM level of theory, where the S_1/S_0 CoIn is located, are given in xyz-format (all coordinates are given in Å):[S6]

S_0 minimum of $Ph_2CH-PPh_3^+$							
C	-0.857563	-0.363243	2.740120	C	-3.904048	1.193641	-1.825089
C	-0.857563	-0.363243	4.136624	C	-4.758800	0.209656	-1.326982
C	-0.857563	0.841154	4.841799	C	-4.361545	-0.552605	-0.227744
C	-0.856673	2.048881	4.142127	C	-3.115493	-0.342429	0.364361
C	-0.851032	2.049395	2.747461	H	-2.013596	2.184599	-1.623796
C	-0.853155	0.846224	2.026641	H	-4.209166	1.808742	-2.666574
C	-0.880912	0.923931	0.505055	H	-5.732204	0.049228	-1.780938
P	0.553877	-0.001046	-0.330103	H	-5.027687	-1.305911	0.182917
C	0.517185	0.439117	-2.096536	H	-2.843546	-0.924442	1.237017
C	0.599261	1.797043	-2.459860	C	-0.700253	-2.495806	-0.620834
C	0.592713	2.163352	-3.803077	C	-0.775043	-3.880705	-0.482911
C	0.506237	1.182728	-4.795959	C	0.270872	-4.586815	0.116795
C	0.437019	-0.164062	-4.442198	C	1.398748	-3.906729	0.577736
C	0.445454	-0.540090	-3.097451	C	1.485457	-2.520941	0.446454
H	-0.846940	-1.312929	2.215166	H	-1.519025	-1.963354	-1.091187
H	-0.859334	-1.308491	4.671702	H	-1.651438	-4.407711	-0.847813
H	-0.860511	0.838254	5.927692	H	0.207297	-5.665973	0.220175
H	-0.858520	2.992397	4.679905	H	2.216089	-4.452555	1.038998
H	-0.851139	2.996680	2.213670	H	2.367591	-2.003812	0.806828
H	-0.618846	1.954488	0.234810	C	2.399308	0.648467	1.716078
H	0.686844	2.570247	-1.701169	C	3.650060	1.051488	2.181513
H	0.658404	3.212488	-4.074981	C	4.669060	1.373368	1.283123
H	0.500526	1.470915	-5.842909	C	4.438939	1.285321	-0.090196
H	0.379884	-0.928828	-5.210685	C	3.191926	0.885547	-0.568494
H	0.401473	-1.591562	-2.837609	H	1.627922	0.392578	2.430697
C	-2.239750	0.631801	-0.138374	H	3.825451	1.112398	3.251277
C	0.433997	-1.804790	-0.150298	H	5.640696	1.687494	1.652754
C	2.156330	0.570647	0.331175	H	5.229081	1.526783	-0.794606
C	-2.658817	1.403261	-1.233867	H	3.031528	0.819900	-1.638206

S_1/S_0 CoIn of $Ph_2CH-PPh_3^+$							
C	0.294154	-1.602203	1.912734	C	-2.255969	-0.595800	-2.928832
C	0.621997	-1.826153	3.251610	C	-3.147218	-1.542878	-2.423208
C	1.007022	-0.763660	4.070578	C	-3.003787	-1.987426	-1.108301
C	1.063701	0.527240	3.542836	C	-1.971752	-1.498803	-0.306080
C	0.741769	0.750568	2.204326	H	-0.550484	0.641117	-2.531738
C	0.351269	-0.307908	1.371052	H	-2.368740	-0.225073	-3.943419
C	0.000000	0.000000	0.000000	H	-3.955918	-1.919045	-3.042749
P	2.819669	-0.677408	0.024219	H	-3.705104	-2.707433	-0.696474
C	2.782977	-0.237245	-1.742214	H	-1.901171	-1.834719	0.721734
C	2.865053	1.120681	-2.105538	C	1.565539	-3.172168	-0.266512
C	2.858505	1.486990	-3.448755	C	1.490749	-4.557067	-0.128589
C	2.772029	0.506366	-4.441637	C	2.536664	-5.263177	0.471117
C	2.702811	-0.840424	-4.087876	C	3.664540	-4.583091	0.932058
C	2.711246	-1.216452	-2.743129	C	3.751249	-3.197303	0.800776
H	0.007998	-2.446541	1.294024	H	0.746767	-2.639716	-0.736865
H	0.573669	-2.834330	3.652918	H	0.614354	-5.084073	-0.493491
H	1.258603	-0.940196	5.112078	H	2.473089	-6.342335	0.574497
H	1.360123	1.362210	4.170841	H	4.481881	-5.128917	1.393320
H	0.788979	1.760803	1.804978	H	4.633383	-2.680174	1.161150
H	0.355952	0.978807	-0.344955	C	4.665100	-0.027895	2.070400
H	2.952636	1.893885	-1.346847	C	5.915852	0.375126	2.535835
H	2.924196	2.536126	-3.720659	C	6.934852	0.697006	1.637445
H	2.766318	0.794553	-5.488587	C	6.704731	0.608959	0.264126
H	2.645676	-1.605190	-4.856363	C	5.457718	0.209185	-0.214172
H	2.667265	-2.267924	-2.483287	H	3.893714	-0.283784	2.785019
C	-1.058458	-0.559590	-0.808639	H	6.091243	0.436036	3.605599
C	2.699789	-2.481152	0.204024	H	7.906488	1.011132	2.007076
C	4.422122	-0.105715	0.685497	H	7.494873	0.850421	-0.440284
C	-1.224458	-0.108012	-2.127500	H	5.297320	0.143538	-1.283884

References

(S1) Tal-Ezer, H.; Kosloff, R. *J. Chem. Phys.* **1984**, *81*, 3967–3971.

(S2) Kosloff, R.; Tal-Ezer, H. *Chem. Phys. Lett.* **1986**, *127*, 223–230.

(S3) Wilson Jr., E. B.; Decius, J. C.; Cross, P. C. *Molecular Vibrations*; McGraw-Hill: New York, 1955.

(S4) Schaad, L.; Hu, J. *J. Mol. Struct.: THEOCHEM* **1989**, *185*, 203–215.

(S5) Kowalewski, M.; Mikosch, J.; Wester, R.; de Vivie-Riedle, R. *J. Phys. Chem. A* **2014**, *118*, 4661–4669.

(S6) Thallmair, S.; Kowalewski, M.; Zauleck, J. P. P.; Roos, M. K.; de Vivie-Riedle, R. *J. Phys. Chem. Lett.* **2014**, *5*, 3480–3485.

Appendix C

Supporting information for chapter 2.3

Reactive quantum dynamics coupled to classical solvent dynamics using an extended quantum-classical TDSCF approach – Supporting Information

Julius P. P. Zauleck, Florian M. Rott, Martin T. Peschel, Sebastian Thallmair, and Regina de Vivie-Riedle*

Department Chemie, Ludwig-Maximilians-Universität München, D-81377 München, Germany

E-mail: regina.de_vivie@cup.uni-muenchen.de

*To whom correspondence should be addressed

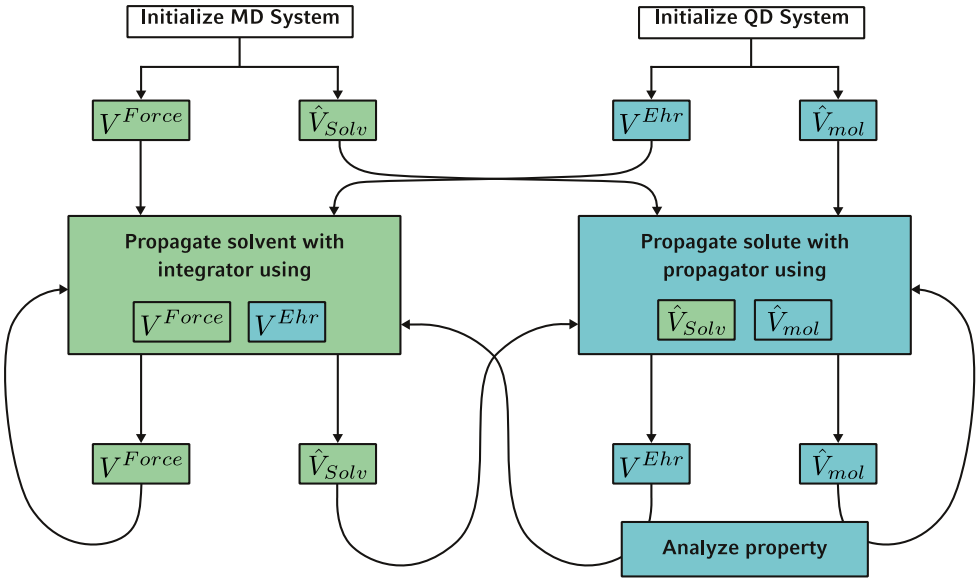

Figure 1: Flowchart illustrating the complete dynamic algorithm. First, both subsystems are initialized. Each subsystem is then propagated. The classical MD system requires the interaction between the classical particles V^{force} and the mean field potential of the quantum system V^{Ehr}. The QD system requires the PES of the solute $\hat{V}_{mol}$ and the potential created by the solvent molecules $\hat{V}_{Solv}$. At any point in time information can be extracted from the QD solute system.

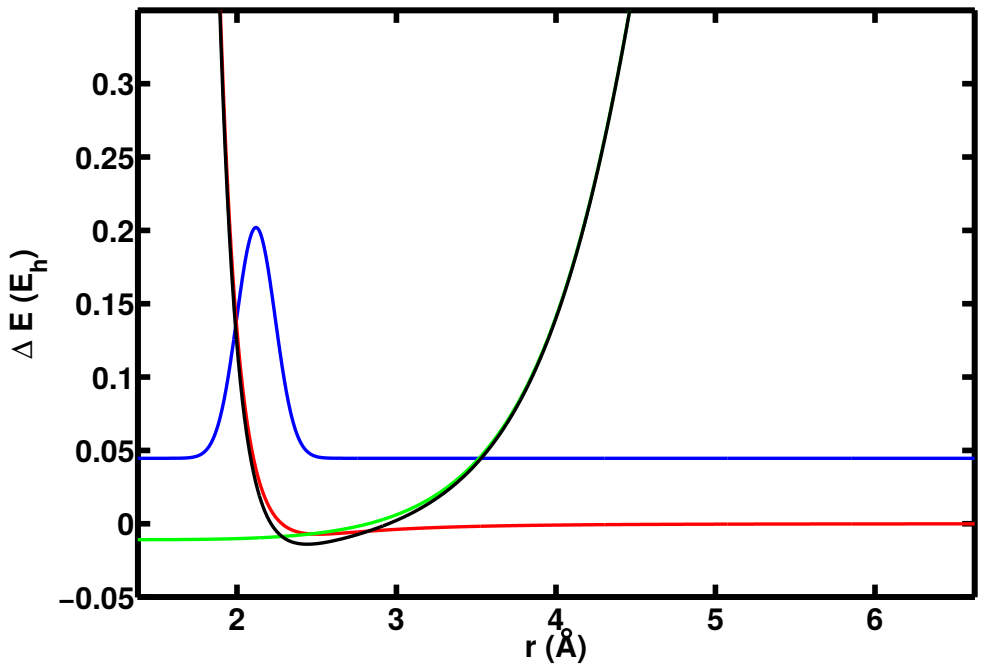

Figure 2: Initial conditions corresponding to excitation from the vibrational groundstate in S0. Shown are the initial wave function (blue), the S1 potential (red), the solvent potential acting on the solute (green) and the sum of both potentials (black) for a random solvent orientation.

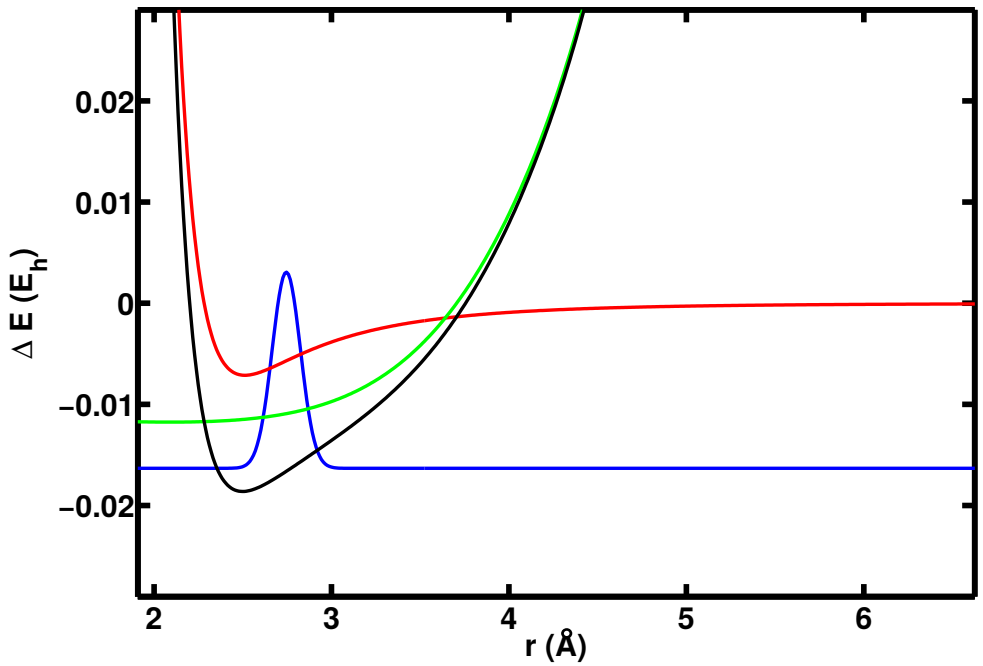

Figure 3: Initial conditions corresponding to the non dissociative initial wave packet of the solute. Shown are the initial wave function (blue), the S1 potential (red), the solvent potential acting on the solute (green) and the sum of both potentials (black) for a random solvent orientation.

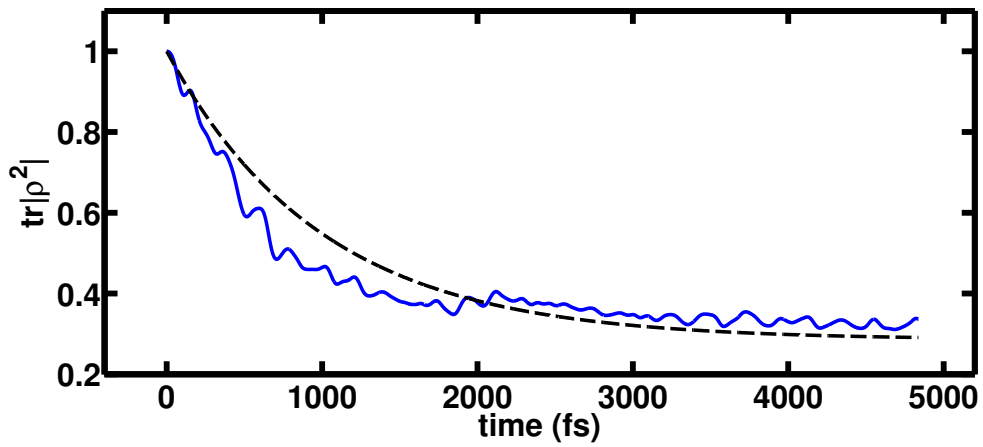

Figure 4: Decrease of coherence of the system with the low energy initial conditions. The purity over 21 randomly chosen starting conditions as a function of time is shown.

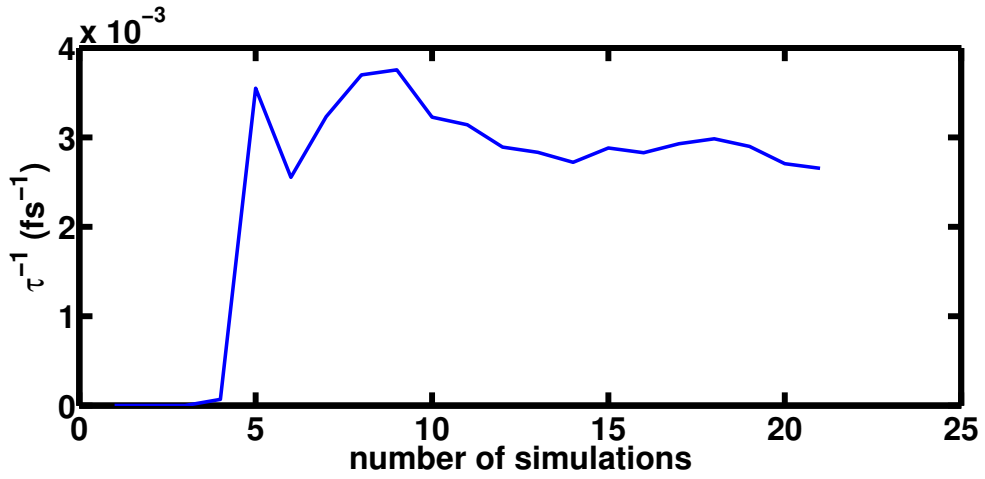

Figure 5: Convergence of the time constant of the decrease of coherence of the system with the low energy initial conditions. The shown time constant was calculated for the decoherence measure introduced in the main article.

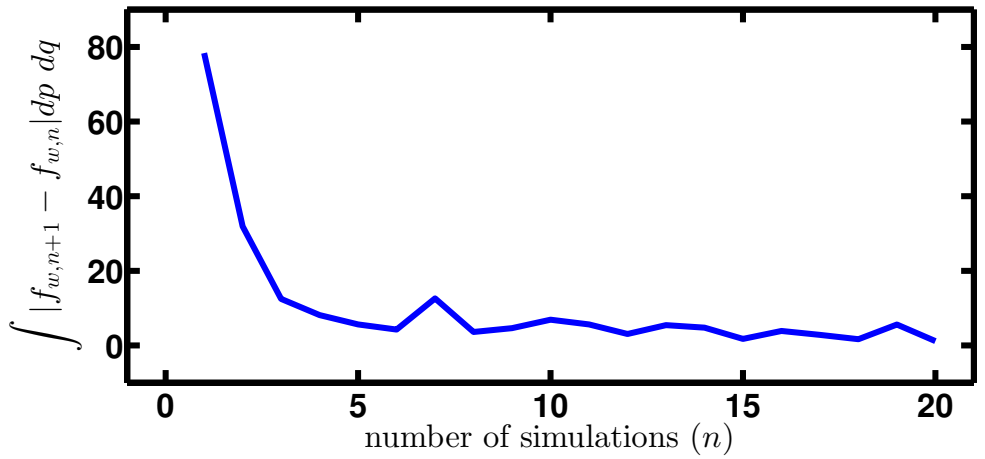

Figure 6: Convergence of the phase space volume covered by the Wigner function f_w at 116 fs. It is calculated via the integral over the absolute values of the difference between the successive Wigner functions generated by incrementating the number of simulations n.

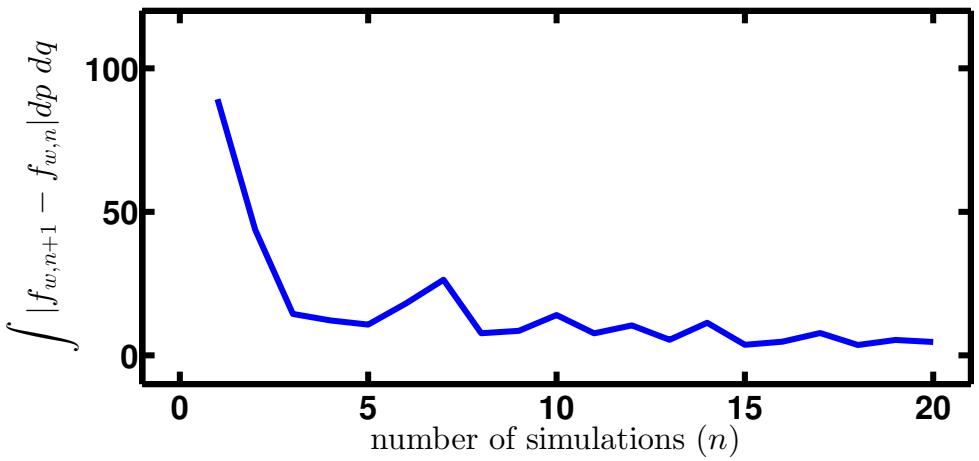

Figure 7: Convergence of the phase space volume covered by the Wigner function f_w at 348 fs. It is calculated via the integral over the absolute values of the difference between the successive Wigner functions generated by incrementating the number of simulations n.

List of abbreviations

CoIn conical intersection

PES potential energy surface

IBA IRC-based approach

TBA trajectory-based approach

PCA principal component analysis

IRC intrinsic reaction coordinate

QD quantum dynamics

MD molecular dynamics

cQDMD coupled QD/MD

TDSCF time-dependent self-consistent field

VRCS virtual rigid classical solute

DFM dynamic Fourier method

$\mathbf{Ph_2CH{-}PPh_3^+}$ diphenylmethyltriphenylphosphonium ion

$\mathbf{Ph_2CH^+}$ diphenylmethyl cation

Bibliography

[1] E. Runge and E. K. U. Gross, *Phys. Rev. Lett.* **52**, 997 (1984).

[2] H.-D. Meyer, U. Manthe and L. Cederbaum, *Chem. Phys. Lett.* **165**, 73 (1990).

[3] M. Cossi and V. Barone, *J. Chem. Phys.* **115**, 4708 (2001).

[4] H. Wang and M. Thoss, *J. Chem. Phys.* **119**, 1289 (2003).

[5] D. Kosloff and R. Kosloff, *J. Comput. Phys.* **52**, 35 (1983).

[6] H. Tal-Ezer and R. Kosloff, *J. Chem. Phys.* **81**, 3967 (1984).

[7] R. Kosloff, *J. Phys. Chem.* **92**, 2087 (1988).

[8] S. A. Orszag, *Phys. Fluids* **12**, II (1969).

[9] S. A. Orszag, *Stud. Appl. Math.* **51**, 253 (1972).

[10] C. F. Gauss, *Königliche Gesellschaft der Wissenschaften zu Göttingen* pp. 265–303 (1866), Nachlass (Unpublished manuscript). Werke (in Latin and German). 3.

[11] J. Cooley and J. W. Tukey, *Math. Comput.* **19**, 297 (1965).

[12] H.-D. Meyer, *WIREs Comput. Mol. Sci.* **2**, 351 (2012).

[13] M. Bonfanti, B. Jackson, K. H. Hughes, I. Burghardt and R. Martinazzo, *J. Chem. Phys.* **143**, 124703 (2015).

[14] F. Lin and J. Muckerman, *Comput. Phys. Commun.* **63**, 538 (1991).

[15] G. Katz, K. Yamashita, Y. Zeiri and R. Kosloff, *J. Chem. Phys.* **116**, 4403 (2002).

[16] E. Kieri, S. Holmgren and H. O. Karlsson, *J. Chem. Phys.* **137**, 044111 (2012).

[17] K. Kormann, *Communications in Computational Physics* **20**, 60 (2016).

[18] H. R. Larsson, B. Hartke and D. J. Tannor, *J. Chem. Phys.* **145**, 204108 (2016).

[19] A. Hofmann and R. de Vivie-Riedle, *J. Chem. Phys.* **112**, 5054 (2000).

[20] S. Thallmair, M. K. Roos and R. de Vivie-Riedle, *J. Chem. Phys.* **144**, 234104 (2016).

[21] M. Kirby, *Geometric Data Analysis*, Wiley, New York, first edn. (2001).

[22] J. A. Lee and M. Verleysen, *Nonlinear Dimensionality Reduction*, Springer-Verlag, Berlin, first edn. (2007).

[23] W. M. Brown, S. Martin, S. N. Pollock, E. A. Coutsias and J.-P. Watson, *J. Chem. Phys.* **129**, 064118 (2008).

[24] L. van der Maaten, E. O. Postma and H. J. van den Herik, *Dimensionality Reduction: A Comparative Review* (2008).

[25] G. E. Hinton and R. R. Salakhutdinov, *Science* **313**, 504 (2006).

[26] M. Cossi, N. Rega, G. Scalmani and V. Barone, *J. Comput. Chem.* **24**, 669 (2003).

[27] H. Heitele, *Angew. Chem. Int. Ed.* **32**, 359 (1993).

[28] P. Rossky and J. Simon, *Nature* **370**, 263 (1994).

[29] S. Thallmair, M. Kowalewski, J. P. P. Zauleck, M. K. Roos and R. de Vivie-Riedle, *J. Phys. Chem. Lett.* **5**, 3480 (2014).

[30] B. Podolsky, *Phys. Rev.* **32**, 812 (1928).

[31] E. B. Wilson Jr., J. C. Decius and P. C. Cross, *Molecular Vibrations*, McGraw-Hill, New York (1955).

[32] L. J. Schaad and J. Hu, *J. Mol. Struct.: THEOCHEM* **185**, 203 (1989).

[33] C. E. Dateo, V. Engel, R. Almeida and H. Metiu, *Comput. Phys. Commun.* **63**, 435 (1991).

[34] N. Marković and G. D. Billing, *Chem. Phys. Lett.* **195**, 53 (1992).

[35] D. Wexler, J. I. Zink and C. Reber, *Spectroscopic manifestations of potential surface coupling along normal coordinates in transition metal complexes*, pp. 173–203, Springer Berlin Heidelberg, Berlin, Heidelberg (1994).

[36] H. Müller and H. Köppel, *Chem. Phys.* **183**, 107 (1994).

[37] Y. Zhao and O. Kühn, *J. Phys. Chem. A* **104**, 4882 (2000).

[38] R. Schork and H. Köppel, *Theor. Chem. Acc.* **100**, 204 (1998).

[39] A. Hofmann and R. de Vivie-Riedle, *Chem. Phys. Lett.* **346**, 299 (2001).

[40] H. Guo, K. Q. Lao, G. C. Schatz and A. D. Hammerich, *J. Chem. Phys.* **94**, 6562 (1991).

[41] H. Guo, *J. Chem. Phys.* **96**, 6629 (1992).

[42] S. Thallmair, B. P. Fingerhut and R. de Vivie-Riedle, *J. Phys. Chem. A* **117**, 10626 (2013).

[43] M. Kowalewski, J. Mikosch, R. Wester and R. de Vivie-Riedle, *J. Phys. Chem. A* **118**, 4661 (2014).

[44] A. Alijah and E. E. Nikitin, *Mol. Phys.* **96**, 1399 (1999).

[45] R. Schork and H. Köppel, *J. Chem. Phys.* **115**, 7907 (2001).

[46] Z. Lan, A. Dupays, V. Vallet, S. Mahapatra and W. Domcke, *J. Photochem. Photobiol. A: Chem.* **190**, 177 (2007).

[47] K. Yagi, T. Taketsugu and K. Hirao, *J. Chem. Phys.* **115**, 10647 (2001).

[48] K. Giese and O. Kühn, *J. Chem. Phys.* **123**, 054315 (2005).

[49] I. Matanović, N. Došlić and B. R. Johnson, *J. Chem. Phys.* **128**, 084103 (2008).

[50] T. B. Blank, S. D. Brown, A. W. Calhoun and D. J. Doren, *J. Chem. Phys.* **103**, 4129 (1995).

[51] S. Manzhos and T. Carrington, *J. Chem. Phys.* **125**, 194105 (2006).

[52] J. Behler and M. Parrinello, *Phys. Rev. Lett.* **98**, 146401 (2007).

[53] C. M. Handley and J. Behler, *Eur. Phys. J. B* **87**, 152 (2014).

[54] P. Dönnes and A. Elofsson, *BMC Bioinformatics* **3**, 25 (2002).

[55] L. Jacob and J.-P. Vert, *Bioinformatics* **24**, 2149 (2008).

[56] P. Wang, J. Sidney, Y. Kim, A. Sette, O. Lund, M. Nielsen and B. Peters, *BMC Bioinformatics* **11**, 568 (2010).

[57] H. Li, C. Y. Ung, C. W. Yap, Y. Xue, Z. R. Li, Z. W. Cao and Y. Z. Chen, *Chem. Res. Toxicol.* **18**, 1071 (2005).

[58] R. Olivares-Amaya, C. Amador-Bedolla, J. Hachmann, S. Atahan-Evrenk, R. S. Sánchez-Carrera, L. Vogt and A. Aspuru-Guzik, *Energy Environ. Sci.* **4**, 4849 (2011).

[59] A. Lusci, G. Pollastri and P. Baldi, *J. Chem. Inf. Model.* **53**, 1563 (2013).

[60] G. Montavon, M. Rupp, V. Gobre, A. Vazquez-Mayagoitia, K. Hansen, A. Tkatchenko, K.-R. Müller and O. A. von Lilienfeld, *New J. Phys.* **15**, 095003 (2013).

[61] J. Hert, P. Willett, D. J. Wilton, P. Acklin, K. Azzaoui, E. Jacoby and A. Schuffenhauer, *J. Chem. Inf. Model.* **46**, 462 (2006).

[62] M. J. Keiser, B. L. Roth, B. N. Armbruster, P. Ernsberger, J. J. Irwin and B. K. Shoichet, *Nat. Biotechnol.* **25**, 197 (2007).

[63] R. Klinger, C. Kolářik, J. Fluck, M. Hofmann-Apitius and C. M. Friedrich, *Bioinformatics* **24**, i268 (2008).

[64] J. Hert, M. J. Keiser, J. J. Irwin, T. I. Oprea and B. K. Shoichet, *J. Chem. Inf. Model.* **48**, 755 (2008).

[65] H. Stamati, C. Clementi and L. E. Kavraki, *Proteins: Struct., Funct., Bioinf.* **78**, 223 (2010).

[66] V. Spiwok and B. Králová, *J. Chem. Phys.* **135**, 224504 (2011).

[67] A. M. Virshup, J. Chen and T. J. Martnez, *J. Chem. Phys.* **137**, 22A519 (2012).

[68] M. Bonomi, G. T. Heller, C. Camilloni and M. Vendruscolo, *Curr. Opin. Struct. Biol.* **42**, 106 (2017).

[69] J. B. Tenenbaum, V. d. Silva and J. C. Langford, *Science* **290**, 2319 (2000).

[70] S. T. Roweis and L. K. Saul, *Science* **290**, 2323 (2000).

[71] R. R. Coifman, S. Lafon, A. B. Lee, M. Maggioni, B. Nadler, F. Warner and S. W. Zucker, *Proc. Natl. Acad. Sci. U.S.A.* **102**, 7426 (2005).

[72] T. Kohonen, *Biol. Cybern.* **43**, 59 (1982).

[73] T. Noguti and N. Gō, *Biopolymers* **24**, 527 (1985).

[74] A. Amadei, A. B. M. Linssen and H. J. C. Berendsen, *Proteins: Struct., Funct., Bioinf.* **17**, 412 (1993).

[75] A. Amadei, A. B. Linssen, B. L. de Groot, D. M. van Aalten and H. J. Berendsen, *J. Biomol. Struct. Dyn.* **13**, 615 (1996).

[76] A. Amadei, B. de Groot, M.-A. Ceruso, M. Paci, A. Di Nola and H. Berendsen, *Proteins: Struct., Funct., Bioinf.* **35**, 283 (1999).

[77] J. B. Clarage, T. Romo, B. K. Andrews, B. M. Pettitt and G. N. Phillips, *Proc. Natl. Acad. Sci. U.S.A.* **92**, 3288 (1995).

[78] B. R. Brooks, D. Janežič and M. Karplus, *J. Comput. Chem.* **16**, 1522 (1995).

[79] D. Janežič and B. R. Brooks, *J. Comput. Chem.* **16**, 1543 (1995).

[80] D. Janežič, R. M. Venable and B. R. Brooks, *J. Comput. Chem.* **16**, 1554 (1995).

[81] B. L. de Groot, A. Amadei, R. M. Scheek, N. A. J. van Nuland and H. J. C. Berendsen, *Proteins: Struct., Funct., Bioinf.* **26**, 314 (1996).

[82] L. S. D. Caves, J. D. Evanseck and M. Karplus, *Protein Science* **7**, 649 (1998).

[83] A. Kitao and N. Go, *Curr. Opin. Struct. Biol.* **9**, 164 (1999).

[84] R. Abseher and M. Nilges, *Proteins: Struct., Funct., Bioinf.* **39**, 82 (2000).

[85] A. Altis, P. H. Nguyen, R. Hegger and G. Stock, *J. Chem. Phys.* **126**, 244111 (2007).

[86] M. Zacharias, *Proteins: Struct., Funct., Bioinf.* **54**, 759 (2004).

[87] B. Qian, A. R. Ortiz and D. Baker, *Proc. Natl. Acad. Sci. U.S.A.* **101**, 15346 (2004).

[88] D. Mustard and D. W. Ritchie, *Proteins: Struct., Funct., Bioinf.* **60**, 269 (2005).

[89] O. F. Lange and H. Grubmüller, *J. Chem. Phys.* **124**, 214903 (2006).

[90] M. Stepanova, *Phys. Rev. E* **76**, 051918 (2007).

[91] V. Spiwok, P. Lipovová and B. Králová, *J. Phys. Chem. B* **111**, 3073 (2007).

[92] C. F. Wong and H. Rabitz, *J. Phys. Chem.* **95**, 9628 (1991).

[93] P. H. Nguyen, *Proteins: Struct., Funct., Bioinf.* **65**, 898 (2006).

[94] R. Laatikainen, J. Saarela, K. Tuppurainen and T. Hassinen, *Biophys. Chem.* **73**, 1 (1998).

[95] J. T. A. Saarela, K. Tuppurainen, M. Peräkylä, H. Santa and R. Laatikainen, *Biophys. Chem.* **95**, 49 (2002).

[96] S. Mesentean, S. Fischer and J. C. Smith, *Proteins: Struct., Funct., Bioinf.* **64**, 210 (2006).

[97] G. G. Maisuradze, A. Liwo and H. A. Scheraga, *J. Mol. Biol.* **385**, 312 (2009).

[98] I. Horenko, J. Schmidt-Ehrenberg and C. Schütte, *Set-Oriented Dimension Reduction: Localizing Principal Component Analysis Via Hidden Markov Models*, pp. 74–85, Springer Berlin Heidelberg, Berlin, Heidelberg (2006).

[99] P. Ivanov, *J. Mol. Struct.* **1009**, 3 (2012).

[100] E. Bertram, R. Shetty, S. C. O. Glover, R. S. Klessen, J. Roman-Duval and C. Federrath, *Mon. Notices Royal Astron. Soc.* **440**, 465 (2014).

[101] B. Fresch and F. Remacle, *An Atomistic View of DNA Dynamics and Its Interaction with Small Binders: Insights from Molecular Dynamics and Principal Component Analysis*, pp. 17–33, Springer International Publishing, Cham (2015).

[102] J. P. P. Zauleck, S. Thallmair, M. Loipersberger and R. de Vivie-Riedle, *J. Chem. Theory Comput.* **12**, 5698 (2016).

[103] C. Eckart, *Phys. Rev.* **47**, 552 (1935).

[104] S. M. Ferigle and A. Weber, *Am. J. Phys.* **21**, 102 (1953).

[105] M. L. Teodoro, G. N. Phillips and L. E. Kavraki, *J. Comput. Biol.* **10**, 617 (2004).

[106] O. F. Lange and H. Grubmüller, *Proteins: Struct., Funct., Bioinf.* **62**, 1053 (2006).

[107] D. Meng, Y. Leung and Z. Xu, *Neurocomputing* **74**, 941 (2011).

[108] M. Balasubramanian and E. L. Schwartz, *Science* **295**, 7 (2002).

[109] X. Lu, Y. Tsao, S. Matsuda and C. Hori, *Proc. INTERSPEECH ISCA* pp. 436–440 (2013).

[110] M. F. Chaplin, *Biochem. Mol. Biol. Educ.* **29**, 54 (2001).

[111] P. Ball, *Chem. Rev.* **108**, 74 (2008).

[112] J. Wang, R. M. Wolf, J. W. Caldwell, P. A. Kollman and D. A. Case, *J. Comput. Chem.* **25**, 1157 (2004).

[113] K. Vanommeslaeghe, E. Hatcher, C. Acharya, S. Kundu, S. Zhong, J. Shim, E. Darian, O. Guvench, P. Lopes, I. Vorobyov and A. D. Mackerell, *J. Comput. Chem.* **31**, 671 (2010).

[114] K. Vanommeslaeghe and A. D. MacKerell, *J. Chem. Inf. Model.* **52**, 3144 (2012).

[115] A. C. T. van Duin, S. Dasgupta, F. Lorant and W. A. Goddard, *J. Phys. Chem. A* **105**, 9396 (2001).

[116] K. Chenoweth, A. C. T. van Duin and W. A. Goddard, *J. Phys. Chem. A* **112**, 1040 (2008).

[117] J. L. F. Abascal and C. Vega, *J. Chem. Phys.* **123**, 234505 (2005).

[118] G. S. Fanourgakis and S. S. Xantheas, *J. Chem. Phys.* **128**, 074506 (2008).

[119] S. Habershon, T. E. Markland and D. E. Manolopoulos, *J. Chem. Phys.* **131**, 024501 (2009).

[120] J. F. Ouyang and R. P. A. Bettens, *CHIMIA* **69**, 104 (2015).

[121] M. D. Kostin, *J. Chem. Phys.* **57**, 3589 (1972).

[122] M. Kostin, *J. Stat. Phys.* **12**, 145 (1975).

[123] W. Stocker and K. Albrecht, *Ann. Phys.* **117**, 436 (1979).

[124] C.-C. Chou, *Ann. Phys. (N. Y.)* **362**, 57 (2015).

[125] C.-C. Chou, *Ann. Phys. (N. Y.)* **377**, 22 (2017).

[126] Q. Shi and E. Geva, *J. Phys. Chem. A* **107**, 9059 (2003).

[127] B. J. Ka and E. Geva, *J. Phys. Chem. A* **110**, 13131 (2006).

[128] J. Liu and W. H. Miller, *J. Chem. Phys.* **127**, 114506 (2007).

[129] H.-H. Teh and Y.-C. Cheng, *J. Chem. Phys.* **146**, 144105 (2017).

[130] L. Wang and A. B. Mccoy, *Phys. Chem. Chem. Phys.* **1**, 1227 (1999).

[131] G. S. Whittier and J. C. Light, *J. Chem. Phys.* **110**, 4280 (1999).

[132] J. C. Tully, *Faraday Discuss.* **110**, 407 (1998).

[133] D. Marx and J. Hutter, *Modern Methods and Algorithms of Quantum Chemistry*, vol. 3, John von Neumann Institute for Computing, Jülich, North Rhine-Westphalia, Germany, second edn. (2000).

[134] P. A. M. Dirac, *Math. Proc. Cambridge* **26**, 376 (1930).

[135] R. H. Bisseling, R. Kosloff, R. B. Gerber, M. A. Ratner, L. Gibson and C. Cerjan, *J. Chem. Phys.* **87**, 2760 (1987).

[136] R. Alimi, R. B. Gerber, A. D. Hammerich, R. Kosloff and M. A. Ratner, *J. Chem. Phys.* **93**, 6484 (1990).

[137] A. Garca-Vela, R. B. Gerber and J. J. Valentini, *J. Chem. Phys.* **97**, 3297 (1992).

[138] R. B. Gerber, V. Buch and M. A. Ratner, *J. Chem. Phys.* **77**, 3022 (1982).

[139] A. Bastida, C. Cruz, J. Ziga, A. Requena and B. Miguel, *J. Chem. Phys.* **126**, 014503 (2007).

[140] A. Bastida, J. Ziga, A. Requena and B. Miguel, *J. Chem. Phys.* **129**, 154501 (2008).

[141] J. von Neumann, *Göttinger Nachr.* pp. 245–272 (1927).

[142] J. von Neumann, *Göttinger Nachr.* pp. 273–291 (1927).

[143] U. Fano, *Rev. Mod. Phys.* **29**, 74 (1957).

[144] K. F. Wong and P. J. Rossky, *J. Chem. Phys.* **116**, 8418 (2002).

[145] N. Rekik, C.-Y. Hsieh, H. Freedman and G. Hanna, *J. Chem. Phys.* **138**, 144106 (2013).

[146] F. Martinez and G. Hanna, *Mol. Simul.* **41**, 107 (2015).

[147] R. Kapral, *J. Phys. Condens. Matter* **27**, 073201 (2015).

[148] A. McLachlan, *Mol. Phys.* **8**, 39 (1964).

[149] S. Bonella and D. F. Coker, *J. Chem. Phys.* **118**, 4370 (2003).

[150] H. Kim, A. Nassimi and R. Kapral, *J. Chem. Phys.* **129**, 084102 (2008).

[151] A. V. Akimov, R. Long and O. V. Prezhdo, *J. Chem. Phys.* **140**, 194107 (2014).

[152] S. Thallmair, B. P. Fingerhut and R. de Vivie-Riedle, *J. Phys. Chem. A* **117**, 10626 (2013).

[153] G. Rothenberger, D. K. Negus and R. M. Hochstrasser, *J. Chem. Phys.* **79**, 5360 (1983).

[154] P. W. Fenimore, H. Frauenfelder, B. H. McMahon and F. G. Parak, *Proc. Natl. Acad. Sci. U.S.A.* **99**, 16047 (2002).

[155] S. Mukherjee and M. A. Vannice, *J. Catal.* **243**, 108 (2006).

[156] S. Thallmair, B. P. Fingerhut and R. de Vivie-Riedle, *J. Phys. Chem. A* **117**, 10626 (2013).

[157] J. Ammer, C. F. Sailer, E. Riedle and H. Mayr, *JACS* **134**, 11481 (2012).

[158] Thallmair, S., Kowalewski, M., Fingerhut, B. P., Sailer, C. F. and de Vivie-Riedle, R., *EPJ Web. Conf.* **41**, 05043 (2013).

[159] B. Roux and T. Simonson, *Biophys. Chem.* **78**, 1 (1999).

[160] B. Mennucci, J. Tomasi, R. Cammi, J. R. Cheeseman, M. J. Frisch, F. J. Devlin, S. Gabriel and P. J. Stephens, *J. Phys. Chem. A* **106**, 6102 (2002).

[161] R. Zhou, *Proteins: Struct., Funct., Bioinf.* **53**, 148 (2003).

[162] N. A. Baker, *Curr. Opin. Struct. Biol.* **15**, 137 (2005).

[163] S. Thallmair, J. P. P. Zauleck and R. de Vivie-Riedle, *J. Chem. Theory Comput.* **11**, 1987 (2015).

[164] B. Hess, C. Kutzner, D. Van Der Spoel and E. Lindahl, *J. Chem. Theory Comput.* **4**, 435 (2008).

[165] R. L. Wilder, *Science* **156**, 605 (1967).

[166] I. Babuvška and W. C. Rheinboldt, *SIAM J. Numer. Anal.* **15**, 736 (1978).

[167] R. Becker and R. Rannacher, *East-West J. Numer. Math.* **4**, 237 (1996).

[168] W. Dörfler, *Numer. Math.* **73**, 419 (1996).

[169] R. Bermejo and J. Carpio, *SIAM J. Sci. Comput.* **31**, 3324 (2009).

[170] K. Arfanakis, A. A. Tamhane, J. G. Pipe and M. A. Anastasio, *Magn. Reson. Med.* **53**, 675 (2005).

[171] D. L. Donoho and J. Tanner, *Proc. IEEE* **98**, 913 (2010).

[172] H. Nyquist, *Trans. Am. Inst. Elect. Eng.* **47**, 617 (1928).

[173] C. E. Shannon, *Proc. IRE* **37**, 10 (1949).

Danksagung

Zunächst und vor allem möchte ich meiner Chefin, Prof. de Vivie-Riedle, ganz herzlich für die Möglichkeit danken, meine Projekte so frei zu gestalten, wie ich es konnte. Ich habe das nie als selbstverständlich wahrgenommen und besonders in Gesprächen mit anderen Doktoranden ist mir das Ausmaß dieser Freiheit immer wieder klar geworden. Dazu kommt das angenehme Arbeitsklima in der gesamten Gruppe, welches mich einerseits in meiner Produktivität unterstützt hat und andererseits immer wieder geholfen hat, all die kleinen Frustrationen schnell zu überwinden. An dieser Stelle gilt natürlich mein Dank auch allen Kollegen, die in dieser Zeit zu der Atmosphäre beigetragen haben. Also damit vielen Dank an Artur, Patrick, Robert, Keefer, Flo, Thomas, Franziska, Martin und Sebastian. Im Speziellen möchte ich noch Philipp und Markus für die Unterstützung in meiner Anfangszeit, Thali für die reichliche und fruchtbare Zusammenarbeit, Sven für die vielen hilfreichen und interessanten Gespräche und die Administration und Matthias für die vielen kleinen organisatorischen Hilfen danken.

Außerhalb der Gruppe gilt noch ein ganz besonderer Dank Gerold Doyen (und der damaligen Interessengemeinschaft aus dem Arbeitskreis von Prof. Ebert) und seinen Vorlesungen, die sich zumeist mit den Extremen der theoretischen Physik beschäftigt haben. Zum einen haben diese mich ungeheuer für die Forschung motiviert und zum anderen darauf vorbereitet, immer wieder meinen eigenen Wissenshorizont zu erweitern und Skepsis an meinem Grundwissen anzubringen. Ich rechne diese Fähigkeiten zu den wichtigsten für mich als Theoretiker und hätte diese durch das Chemiestudium allein nicht ausreichend erlernt.

Zusätzlich möchte ich noch Charly danken, die ich während meiner Promotion kennengelernt und geheiratet habe und die mich seither inspiriert hat und mir zu reichlich Antrieb verholfen hat, meine Dissertation abzuschließen. In diesem persönlichen Kontext gilt mein Dank auch allen Freunden und Bekannten, die mein Leben bereichern.